

ISBN 978-91-7473-301-3
LUNFD6/(NFFL-7234)2012

Transition Radiation Tracker calibration, searches beyond the Standard Model and multiparticle correlations in ATLAS

Thesis submitted for the degree of
Doctor of Philosophy
by

Alejandro Alonso



LUND
UNIVERSITY

DEPARTMENT OF PHYSICS
LUND, 2012

Thesis Advisor: Oxana Smirnova
Faculty Opponent: Ulrik Egede

To be presented, with the permission of the Faculty of Science of Lund University, for public criticism in lecture hall b of the Department of Physics on Friday, the 20th of April 2012, at 13.00.

CERN-THESIS-2012-056
20/05/2012



Organization LUND UNIVERSITY Department of Physics Lund University Box 118 SE-221 00 Lund SWEDEN		Document name DOCTORAL DISSERTATION
		Date of issue March, 2012
		CODEN LUNFD6/(NFFL-7234)2012
Author(s) Alejandro Alonso		Sponsoring organisation
Title and subtitle Transition Radiation Tracker calibration, searches beyond the Standard Model and multiparticle correlations in ATLAS		
Abstract This thesis contains two different aspects of my research work towards physics in proton-proton collisions in the ATLAS experiment at the LHC. The first part is focused on the understanding and developing of a calibration system to obtain the best possible charged particle reconstruction in the Transition Radiation Tracker. The method explained in this thesis is the current calibration technique used in the TRT and it is applied to all the data collected by ATLAS. Thanks to the method developed, the detector design resolution is achieved, and even improved in the central region of the TRT. In the second part, three different analyses are presented. Due to my interest in tracking and thanks to the new energy range available at the LHC, the first analysis is the study of multiparticle correlations at 900 GeV and 7 TeV. This analysis is performed with the first ATLAS data collected during 2010. Two different aspects are studied: the high order moments and an attempt to measure the normalized factorial moments in η bins. The other two data analyses described in this thesis are focused on the discovery of physics Beyond Standard Model. The search of same-sign top quarks and b-like fourth generation quarks is one of them. For this analysis the probability to reconstruct a lepton with the wrong charge measurement is studied in detail. New data-driven methods are developed, of which a likelihood technique has shown a good performance, and it is adopted by other analysis in ATLAS. This search shows that data is in agreement with the Standard Model expectations. The last analysis is the search for Supersymmetry with two leptons in the final state and large missing transverse energy. A detailed description of the diboson production, which is one of the main backgrounds of this analysis, is presented. The final measurement shows no excess with respect to the Standard Model expectations.		
Key words: LHC, ATLAS, Beyond Standard Model, Supersymmetry, Inner Detector calibration, Tracking ,QCD, TRT, Drift tubes, Same-sign top production, Fourth family of quarks		
Classification system and/or index terms (if any)		
Supplementary bibliographical information:		Language English
ISSN and key title:		ISBN 978-91-7473-301-3
Recipient's notes	Number of pages 214	Price
	Security classification	

Distribution by (name and address)

Alejandro Alonso
Department of Physics
Div. of Experimental High-Energy Physics
Box 118, SE-221 00 Lund, SWEDEN

I, the undersigned, being the copyright owner of the above-mentioned dissertation, hereby grant to all reference sources permission to publish and disseminate the abstract of the above-mentioned dissertation.



Signature _____

Date 10/03, 2012

ISBN 978-91-7473-301-3
LUNFD6/(NFFL-7234)2012

Transition Radiation Tracker calibration, searches beyond the Standard Model and multiparticle correlations in ATLAS

Thesis submitted for the degree of
Doctor of Philosophy
by

Alejandro Alonso



LUND
UNIVERSITY

DEPARTMENT OF PHYSICS
LUND, 2012

To my Family

Contents

Preface	i
1 The LHC and the ATLAS experiment	1
1.1 The Large Hadron Collider	1
1.1.1 The LHC performance	4
1.2 The ATLAS experiment	5
1.2.1 Magnet System	7
1.2.2 Inner Detector	8
1.2.3 Calorimeters	10
1.2.4 Muon Spectrometer	11
1.2.5 Trigger and data acquisition	13
1.2.6 Luminosity measurements and beam monitors	14
2 The ATLAS Transition Radiation Tracker	17
2.1 Drift tubes, principles of operation	18
2.1.1 Ionization from charged particles	19
2.1.2 Electron and ion transport and amplification	23
2.1.3 Transition radiation	26
2.2 Detailed picture of the ATLAS TRT	29
2.2.1 The TRT straw tube	31
2.2.2 Gas mixture	32
2.2.3 Barrel and end-caps	34
2.2.4 Electronics	37
2.2.5 Cooling	41
3 Calibration of the ATLAS Transition Radiation Tracker	43
3.1 Tracking with the TRT	44
3.1.1 Introduction to tracking	44
3.1.2 The TRT Hits	47
3.1.3 Figures of merit	48
3.2 Calibration principles	51
3.2.1 T_0 calibration	51
3.2.2 r-t calibration	52
3.2.3 Granularity of the calibration	56

3.2.4	24h Calibration ATLAS policy	57
3.3	Cosmic Results	58
3.3.1	Event phase	59
3.3.2	T_0 calibration	60
3.3.3	Barrel r - t calibration	62
3.3.4	Barrel performance	63
3.4	Calibration with collision data	65
3.4.1	r - t calibration	66
3.4.2	T_0 calibration	70
3.4.3	Calibration of simulated data	76
3.4.4	TRT performance	78
3.4.5	Heavy Ions calibration	85
3.5	TRT hit error definition	86
3.6	Conclusion and outlook	88
4	Multiparticle correlations in proton-proton collisions	89
4.1	Quantum Chromodynamics	90
4.2	Multiparticle production in proton-proton collisions	92
4.2.1	Parton showers	95
4.2.2	Hadronization	95
4.2.3	Monte Carlo generators	96
4.3	The charged particle multiplicity distribution and its correlations	100
4.3.1	Analytical QCD prediction	101
4.3.2	Phenomenological descriptions	101
4.4	Normalized factorial moments and intermittency	104
4.5	Summary	106
5	High Order Moments and Factorial Moments in ATLAS	107
5.1	Event selection	108
5.2	Monte Carlo samples	109
5.3	High order moments	110
5.3.1	Correction procedure for the charge multiplicity distribution	110
5.3.2	Charged particle multiplicity	115
5.3.3	Statistical uncertainties for high order moments	119
5.3.4	Systematic effects for high order moments	120
5.3.5	High order moments at reconstructed level	121
5.3.6	High order moments at particle level	122
5.3.7	Interpretation	123
5.4	Study of normalized factorial moments in η bins	125
5.4.1	Statistical uncertainties	125
5.4.2	Systematic uncertainties	125
5.4.3	Correction procedure	128
5.4.4	Results at reconstructed level	132
5.5	Summary and outlook	135

6	Same-sign top and b' searches	137
6.1	Same-sign top search	138
6.2	Fourth family of quarks	140
6.3	Object definition	141
6.4	Event selection and signal region	143
6.5	Background contribution	144
6.6	Charge mis-identification	145
6.6.1	Monte Carlo samples	145
6.6.2	Electron charge mis-identification	146
6.6.3	Muon charge mis-identification	162
6.6.4	Extrapolation for high momentum leptons charge mis-identification	166
6.7	Conclusions and outlook	166
7	Diboson estimation for SUSY analysis	177
7.1	Supersymmetry, MSSM and mSUGRA	178
7.1.1	Dilepton and large missing transverse energy	180
7.2	Object reconstruction	181
7.3	Event selection and signal regions	182
7.4	Background contributions	182
7.5	Diboson background estimation	183
7.6	Conclusion and results	190
8	Summary and outlook	195
9	Acknowledgements	197

Preface

This thesis reflects in many ways the *classical* evolution of the startup of a new particle physics experiment. The ATLAS [8] experiment started, with an ambitious R&D program and design phase, long time before I got involved. By early 2008, when I started to work in the ATLAS collaboration, the detector was fully built and the commissioning phase was ongoing. This phase was focused on cosmic rays and Monte Carlo simulations to understand the main properties of the detector. The great expectations we had for collisions were truncated in September 2008, when a large quench forced the experiments to wait longer than a year to measure the first proton-proton interactions. Once collisions arrived in late 2009, the data era started. Running at low luminosity, the aim of this phase was to understand QCD at the new energy and to measure well-known processes such as vector boson production [1]. In 2011, the amount of collisions per second increased incredibly, accumulating more data than ever expected at this early stage. This motivated the execution of several analyses looking for new physics, such as Higgs boson, SUSY and completely new processes like same-sign top production.

I started my work in ATLAS when the only data samples were Monte Carlo and cosmic rays. I focused my technical work in understanding the Transition Radiation Tracker (TRT) and developing the best calibration system for it. A large effort was done in order to get ready for the first collisions. We reached the startup of ATLAS with a great framework and a good understanding of the TRT tracking capabilities thanks to the detailed studies performed with cosmic rays and Monte Carlo. When luminosity started to get accumulated, the TRT was in place to get the best position resolution. During the first year of data taking, the calibration method was fine-tuned and several studies were performed to improve the final resolution. I presented the performance and calibration of the TRT with early collisions in the Summer of 2010, at the IPRD conference [2].

In the chapter 2 of this thesis I review the principles of operation of the ATLAS Transition Radiation Tracker, which is based in drift straws. In the same chapter a detailed overview of the TRT is presented, including the basic straw design, the gas mixture, the straw arrangement and the electronics systems used. The chapter 3, which is the core of my work for the TRT, presents the calibration algorithm together with the tracking performance achieved. The results for the current calibration have been published in [3]. A detailed publication for the TRT performance, which includes part of the results shown in this thesis, is currently under preparation [4].

With my expertise on tracking, I decided to study the multiparticle correlations. This was a completely new field for me, with new challenges. The target was to study factorial

moments and high order moments. Both methods allow to look into the genuine correlations, removing the Poissonian noise and revealing the nature behind. The work was first done at Monte Carlo (MC) level, where the MC generators were used to understand the properties of the methods and the predictions of QCD at collision energies \sqrt{s} of 900 GeV and 7 TeV. Once this was understood, the time for the real data came. The principles of Quantum Chromodynamics, together with the different methods used to measure multiparticle correlation, are presented in chapter 4. In chapter 5 the results for multiparticle correlations obtained by ATLAS at $\sqrt{s} = 900$ GeV and 7 TeV are shown.

In 2011, after a short shutdown, LHC started to accumulate data at 7 TeV. This time, the rise in the luminosity was incredibly fast, and just few months of operation in 2011 more data than in whole 2010 was accumulated. The instantaneous luminosity was increasing in such a way that before summer the first inverse nano-barn was ready to be analyzed. This encouraged the collaboration to initialize a large search for new physics, physics not predicted in the Standard Model. Due to the interesting phenomenology and the exciting implications in case of existence of such phenomena, I began to collaborate in searches for Supersymmetry and same-sign top quark production. Both involve the searches with two leptons in the final state, both with completely different physics meaning but with similar representations in nature.

My task in the search of same-sign top quarks and fourth family of b-quarks was to understand the background produced by the leptons with wrong reconstructed charge. During my studies I realized that the methods used traditionally by other analysis groups were not suitable for our analysis. I developed new methods [5], which improved the performance and now are used by other analysis groups. In chapter 6, an introduction to the same sign top quarks search is given. After this, the chapter is focused on the different methods created for this analysis and their performance to measure the charge flip in muons and electrons. These methods are used and reported in final analysis [6], and the conclusion of the chapter presents the results of the same-sign top search.

The chapter 7 starts with an introduction to Supersymmetry and an explanation why it is a good candidate for new physics. My involvement in this analysis was studying the different Monte Carlo predictions for two vector boson production modes. This result is included in the final analysis reported in [7]. The conclusions of this search are explained at the end of the chapter.

In the LHC programme, a long road is ahead, with several places to visit, with several models to search for, with billions of collisions that can hide something unexpected. That is what was pursued in this work, study the detector to make sure we get the best detector performance, study the soft-QCD processes to know what we can expect from the Standard Model, how QCD looks like in ATLAS and then, try to look if the nature wants to surprise us.

Chapter 1

The LHC and the ATLAS experiment

Since the first experiments in particle physics until nowadays, the size and complexity of experimental setups have increased substantially. In order to look for the smaller components of the matter, more powerful particle accelerators have been built and larger detectors have been created to detect all the particles produced in the collisions.

The work presented in this thesis is based on the data measured by the ATLAS detector [8]. This detector operates at the Large Hadron Collider (LHC), at CERN¹ in Geneva. The LHC collides beams of protons and lead ions at very high energy. In this chapter, a brief overview on the design specifications and the performance of the LHC is given. In the second part, a review of the ATLAS detector and its components is presented.

1.1 The Large Hadron Collider

The Large Hadron Collider (LHC) [9] belongs to the latest generation of particle accelerators and is the most powerful particle collider ever built. In 1994 its construction was approved to take place in the 27 km circular tunnel where the LEP [10] accelerator was situated. The LHC is designed to accelerate proton beams and collide them at a center of mass energy, \sqrt{s} , of 14 TeV. This is a factor of seven more energy than the previous most energetic accelerator, the Tevatron [11]. In addition to protons, the LHC is designed to collide heavy ion beams of lead (Pb) at $\sqrt{s_{NN}} = 5.5$ TeV.

The main motivation to build the LHC is the search of the elusive Higgs boson that was predicted more than 40 years ago [12] and has not been found yet. Other motivations have been the search of Physics Beyond Standard Model (BSM) and the measurements of the Standard Model with higher precision for such processes as Top quark physics and B-quark physics. The production of Higgs boson is largely enhanced when the collision energy increases. A similar effect is predicted for the top quark production. Figure 1.1 shows the cross-section of a selected number of processes depending on the center of mass energy of the collider. The LHC design center-of-mass energy is shown together with the Tevatron

¹Organisation européenne pour la recherche nucléaire, cern.ch

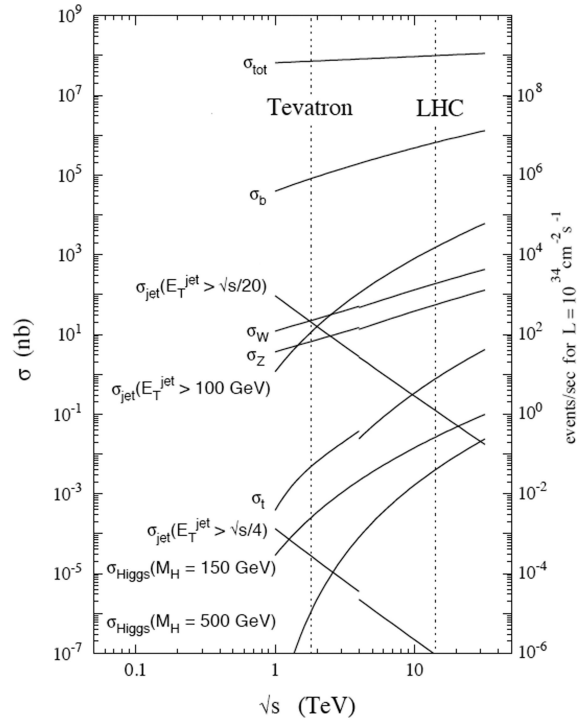


Figure 1.1: Cross-section for various processes as a function of the center of mass energy. The Tevatron and the LHC design center of mass energies are shown, with a great increase in the expected number of events for the LHC [8].

one. A large increases in the top and bottom quark, W, Z and Higgs bosons cross sections can be expected. As we can see, the increase of the total proton-proton cross-section with the energy is very small, which enhances the ratio of signal over background for the processes of interest.

The LHC ring contains two beam pipes with counter-rotating beams. The rings are divided in 8 sectors, each of which is made of a straight and a curved section. The straight sections are 528 m long and in four of them the beams are collided and the different experiments are placed in their interaction points. The remaining straight sections are used for the radio frequency (RF) cavities to accelerate the particles, for the collimation systems performing the cleaning of the beams and for the systems to dump the beams. The curved sections, also known as arcs, are done of magnetic dipoles, quadrupoles, sextupoles and octupoles. The LHC has 1232 dipoles and 392 quadrupoles in total. Each dipole is 14.3 m length and they are designed to provide a 8.65 T magnetic field to bend and keep 7 TeV protons in their circular orbit. The dipoles are made of superconducting Niobium-Titanium alloy which is placed in a cryostat and cooled with liquid helium at 1.9K. The quadrupoles are used to focus the beams.

In addition to the center of mass energy, the number of proton-proton interactions per second increases the probability to observe events with low production rates. The number

of produced events for a specific process with cross-section σ is given by:

$$n = \sigma \cdot \int \mathcal{L} dt \quad (1.1)$$

Where \mathcal{L} is the accelerator luminosity^{II}. The LHC design luminosity is $10^{34} \text{ cm}^{-2}\text{s}^{-1}$. In order to reach it, a total of 2808 bunches, with 1.14×10^{11} protons each, are circulated in every beam. The bunch separation is 25 ns or 7.5 m, so the collisions are produced at a frequency rate of 40 MHz with a luminosity lifetime of 15 hours per fill. Under these conditions, the total accumulated energy in the proton beams will be around 362 MJ.

The proton bunches are injected into the LHC through a series of accelerators which shape and accelerate them in different steps. The elements of this injection chain, from the proton production to the interaction points, are illustrated in Figure 1.2. Electrons from initial hydrogen atoms are stripped off and the remaining protons are accelerated to 50 MeV in the Linac2. Then, the protons are injected into the Proton Synchrotron Booster (PSB), where they acquire an energy of 1.4 GeV. The beams are sent to the Proton Synchrotron (PS) and boosted to 26 GeV. In the next stage, the protons are transferred to the Super Proton Synchrotron (SPS), a 7 km circumference accelerator in which they are accelerated to 450 GeV. Finally, the protons are passed into the LHC, which is designed to accelerate each beam to 7 TeV, producing proton-proton collisions in the four interaction points.

In order to analyze the collision data produced by the LHC, four main experiments, or detectors, have been constructed and placed underground in the four beam interaction points. Two of them, ATLAS and CMS, are designed as general purpose-detector, covering similar physics goals. This allows to independently confirm the results of each other. The other two experiments, ALICE and LHCb, are focused on different areas of interest open in particle physics:

1. CMS (Compact Muon Solenoid) [13]: It is one of the two general-purpose detectors designed to look for a wide range processes such as Higgs boson production, Top physics and new physics beyond the Standard Model.
2. ATLAS (A Toroidal LHC AparatuS) [8]: It is the second general-purpose detector. More details will be given later in this chapter.
3. ALICE (A Large Ion Collider Experiment) [14]: It is designed to explore the quark-gluon plasma (QGP) produced in heavy ion collision. The QGP reproduces the first instants of the Universe when matter was in its primordial state, a 'soup' of quarks and gluons.

^{II}The luminosity \mathcal{L} refers to the number of particles per unit area per unit time. It is determined by the accelerator design parameters:

$$\mathcal{L} = F \frac{N_1 N_2 n_b f_r \gamma}{\beta \epsilon} \quad (1.2)$$

Where F is the geometric luminosity reduction factor due to the crossing angle at the IP, N_1 and N_2 are the number of particles in each bunch, γ is the relativistic factor of the colliding particles, n_b is the total number of bunches, f_r is the revolution frequency, ϵ is the normalized transverse beam emittance and β is the beta function at the collision point.

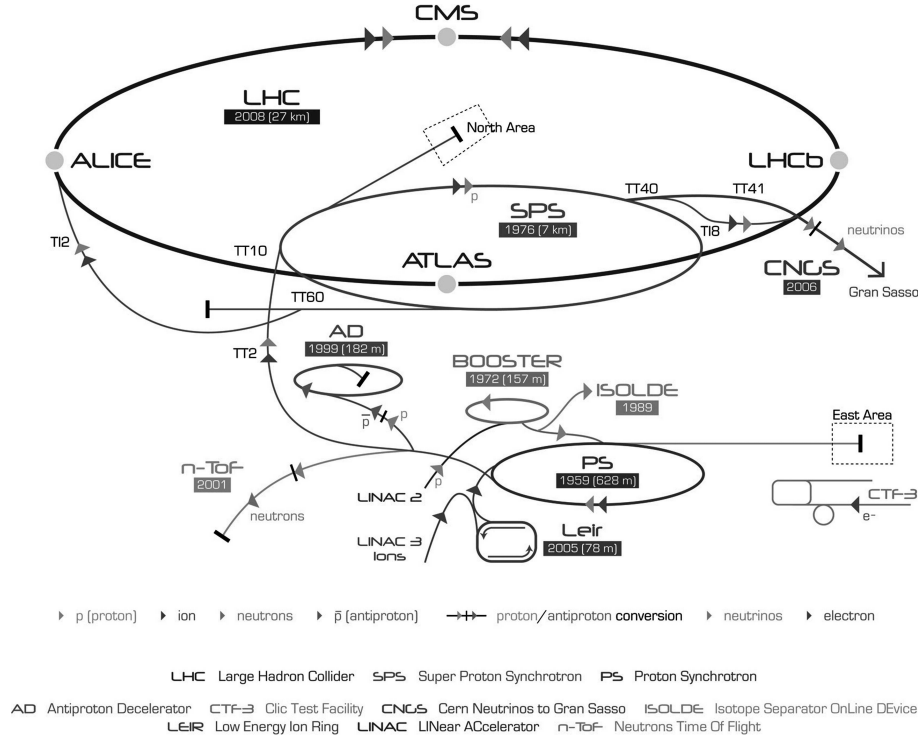


Figure 1.2: Schematic view of the Large Hadron Collider, the different injection facilities and the detector situations [9].

4. LHCb [15]: It is specialized in the physics of the b-quark, with a focus on the problem of the imbalance of matter versus antimatter in the Universe.

1.1.1 The LHC performance

The first proton beam circulation took place on 10 September 2008. The beams were injected with an energy of 450 GeV each and were circulated in the LHC ring without accelerating them. The commissioning was going as planned until the 19 September 2008, when a failure in the electric joint between two superconducting magnets produced a large quench. Over 50 superconducting magnets were damaged and the vacuum pipe was contaminated. After a bit more than a year of work to fix them and to improve the operation safety of the magnets, on 20 November 2009, the proton beams were successfully circulated again. The first LHC proton-proton collisions were produced and successfully recorded by the different experiments on 23 November 2009. The initial collisions were done at the injection energy, 450 GeV, giving a center of mass energy $\sqrt{s} = 900$ GeV. On 30 March 2010 the first collision at center of mass energy of 7 TeV was produced. The accelerator has been operating at this energy, 3.5 TeV per beam, during 2010 and 2011 and it is planned to run at $\sqrt{s} = 8$ TeV during 2012 data-taking. To reach the design collision energy, a shutdown until 2014 is foreseen in which the machine will be upgraded to safely accelerate each beam to 7 TeV.

The total luminosity delivered during 2010 at $\sqrt{s} = 7$ TeV for proton-proton collisions was around 50 pb^{-1} for ATLAS and CMS. Several data analyses were performed by the different experiments. During the 2011 operation, the LHC machine increased the instantaneous luminosity by an order of magnitude. By 26 October 2011, when the 2011 proton-proton run finished, the instantaneous luminosity achieved was $3.65 \times 10^{33} \text{ cm}^{-2}\text{s}^{-1}$. At this luminosity, the maximum number of proton-proton interactions in each bunch crossing observed is 32. The total accumulated luminosity by the ATLAS and CMS detectors during 2011 was larger than 5.0 fb^{-1} in each detector. With the amount of data collected, the LHC experiments started a search for new physics, with a great success in setting upper mass limits for the Higgs boson (which has not been found yet) and several BSM models. The performance of the LHC machine during its first two years of operation exceeds by far the most optimistic expectations made during the initial commissioning.

In addition to the proton-proton program, between 8 November 2010 and 6 December 2010 the first heavy ion run took place, colliding two beams of lead (Pb) at an energy of 2.76 TeV per nucleon. During 2011, a second heavy ion run took place from the 5 November until 7 December, reaching an instantaneous luminosity of $4.5 \times 10^{26} \text{ cm}^{-2}\text{s}^{-1}$. The delivered luminosity during 2011 was around $150 \mu\text{b}^{-1}$, which is almost a factor of 15 larger than the data delivered during 2010.

1.2 The ATLAS experiment

The ATLAS detector [8] is the largest multi-purpose detector operating at the Large Hadron Collider. It has been designed to study multiple physics processes at the TeV mass scales, such as Higgs searches, the possible existence of physics beyond Standard Model and precision measurements of Standard Model parameters, top-quark physics and CP violation in b-hadrons.

As an example, the Higgs boson, which is expected to have several possible decay modes, was largely used as benchmark to optimize the detector requirements. At low Higgs hypothetical masses, its most interesting decay is into two photons, so in ATLAS a very good photon resolution is needed. Not only the total energy of the photons needs to be precisely measured, but also their direction to assure that photons are produced in the primary vertex. For larger Higgs masses, other decay modes become dominant, such as to two W or Z bosons. The W bosons decay to a lepton and a neutrino, so the calorimetry needs to be very sensitive to missing transverse energy in order to detect the energy of the neutrinos leaving the detector. For the W and Z reconstruction, the identification of high momentum electrons and muons and their momentum measurement is fundamental. In addition to Higgs searches, several new physics models, such as Supersymmetry or extra-dimensions, predict the existence of weakly interacting particles, which will leave the detector without depositing energy, having a final state with large missing transverse energy. The measurement of b-jets and τ leptons, which decay very close to the primary vertex, requires a high resolution for secondary vertex determination. For top physics, a good b-tagging efficiency is needed, together with a large efficiency of electron and muon identification.

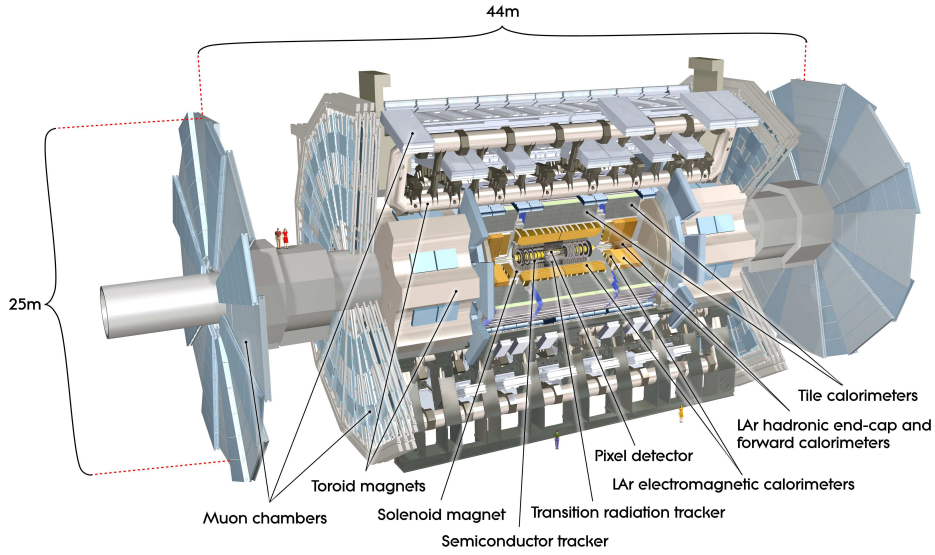


Figure 1.3: Schematic view of the ATLAS detector [8].

The basic design criteria for the ATLAS detector to be sensitive to a wide range of final states can be summarized as:

- A large acceptance in pseudorapidity (η^{III}) and full coverage in the azimuthal angle (ϕ) measured around the beam axis.
- Excellent electromagnetic calorimetry for electron and photon identification and energy measurements.
- Hermetic jet calorimetry providing full coverage for accurate jet and missing transverse energy measurements.
- Very efficient tracking at high luminosity with high resolution for high momentum lepton measurements, τ -leptons and heavy flavor tagging, enhancing the electron and photon identification and vertexing capabilities at high luminosity.
- Muon identification and high precision measurement of its transverse momentum at the highest luminosity.
- Triggering capabilities for low transverse momentum particles providing high efficiency for most physics processes of interest.

In addition to the physics requirements, the ATLAS detector has to operate at very high interaction rate and large radiation dose, so the systems must be fast and radiation hard.

^{III}Pseudorapidity, η , is related to the polar angle by: $\eta = -\ln \tan(\theta/2)$, where θ is the angle from the beam axis (z direction)

The final design of the ATLAS detector is presented in Figure 1.3. It has a cylindrical shape with an overall length of 44 m and 25 m of diameter, forward-backward symmetric with respect to the interaction point. To achieve the different goals, the detector is divided into different systems depending on the distance to the interaction point. The tracking of charged particles is handled by the Inner Detector, which is placed around the collision point. This tracking device has a very high granularity, which allows to reconstruct tracks with very good resolution in environments with high density of particles. In addition to the momentum measurement, thanks to the magnetic field provided by the central solenoid, it provides vertex measurements and electron identification. To measure the electron and photon energies, a high granularity calorimeter is placed after the Inner Detector. This calorimeter is optimized to fully absorb the electrons and photons produced, and its performance is determinant for searches of Higgs boson in the channels $H \rightarrow \gamma\gamma, H \rightarrow 2Z \rightarrow 4e, H \rightarrow WW \rightarrow 2e2\nu$. A hadronic calorimeter, surrounding the electromagnetic calorimeter, provides a large coverage for jet and missing transverse energy measurement. Finally, a large muon spectrometer is responsible for the muon identification and stand-alone momentum measurement using a toroidal magnetic field, which bends the muon tracks. The performance required for the different systems to achieve the physics goals in ATLAS is summarized in Table 1.1. Extensive documentation of the different ATLAS subdetectors, the physics program and the expected performance is available in [8], [16] and [17].

Table 1.1: General performance goals of the ATLAS detector [8].

<i>Detector Component</i>	<i>η coverage</i>		<i>Required resolution</i>
	Measurement	Trigger	
Tracking	± 2.5		$\sigma_{p_T}/p_T = 0.05\%p_T \oplus 1\%$
EM calorimetry	± 3.2	± 2.5	$\sigma_E/E = 10\%/\sqrt{E} \oplus 0.7\%$
Hadronic calorimetry :			
Barrel and end-caps	± 3.2	± 3.2	$\sigma_E/E = 50\%/\sqrt{E} \oplus 3\%$
Forward region	$3.1 < \eta < 4.9$	$3.1 < \eta < 4.9$	$\sigma_E/E = 100\%\sqrt{E} \oplus 10\%$
Muon spectrometer	± 2.7	± 2.4	$\sigma_{p_T}/p_T = 10\%$ at $p_T = 1$ TeV

1.2.1 Magnet System

In high energy physics detectors, very strong magnetic fields are used to bend tracks of charged particles. The ATLAS detector has two systems of superconducting magnets. A central solenoid magnet located between the Inner Detector and the Calorimeters provides a 2T axial magnetic field parallel to the beam pipe (z direction). This field is fundamental for the momentum measurement done by the Inner Detector and at the same time is designed to minimize the material in front of the electromagnetic calorimeter. The axial length of the solenoid is 5.8 m and the inner diameter is 2.46 m. It is constructed as a single-layer coil of 0.1 m thickness, resulting in 0.66 radiation lengths.

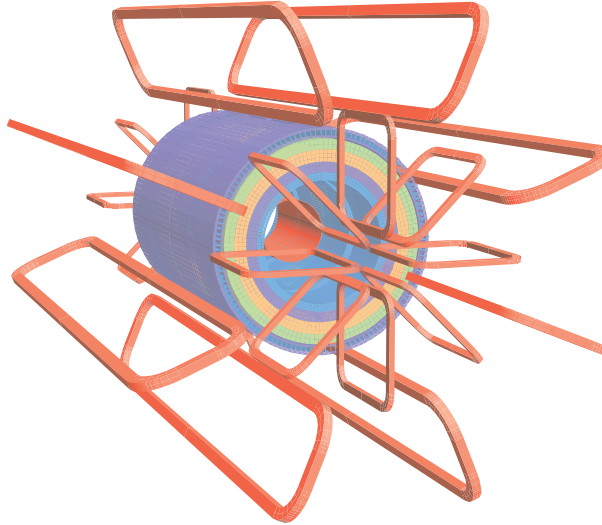


Figure 1.4: Geometry of the magnet windings and the tile calorimeter steel. The eight barrel toroid coils with the end-cap coils interleaved are visible. The solenoid winding lies inside the calorimeter volume. The tile calorimeter is modeled by four layers of materials with different magnetic properties and an outside return yoke [8].

In the muon spectrometer, the magnetic field is produced by a toroidal magnet made of three elements, a barrel and two end-caps, as shown in Figure 1.4. The barrel toroid, made of eight identical coils with air core encased in individual cryostats, provides 0.5 T in the ATLAS central region: $|\eta| < 1.4$. Each of the two end-cap toroids is made of eight coils, all of them encased in a single cryostat, assembled radially and symmetrically around the beam axis. They are inserted at the end of the barrel toroids and lined up with the central solenoids. The end-caps toroids create a field of 1T in the region $1.6 < |\eta| < 2.7$. Each barrel coil measures $25.5 \text{ m} \times 5.4 \text{ m}$, while the end-cap coils dimensions are $4 \text{ m} \times 4.5 \text{ m}$.

1.2.2 Inner Detector

The Inner Detector (ID) plays a crucial role for the momentum determination of charged particles and primary and secondary vertex determination in a dense particle environment. It is also important for electron identification.

A high granularity silicon pixel detector (Pixel) is located close to the interaction point. In the outer region of the Pixel, a silicon microstrip (SCT) detector is placed. Pixel detector together with SCT is often referred to as the Silicon detector, due to the semiconductor technology used in them. The outer part of the Inner Detector is the Transition Radiation Tracker (TRT) made of straw tubes in combination with material causing transition radiation to identify electrons. The Inner detector is 6.2 m long and 2.1 m of diameter, covering the region $|\eta| < 2.5$. It is embedded in the 2T magnetic field created by the central solenoid. An overview of the Inner Detector and its three subdetectors is presented

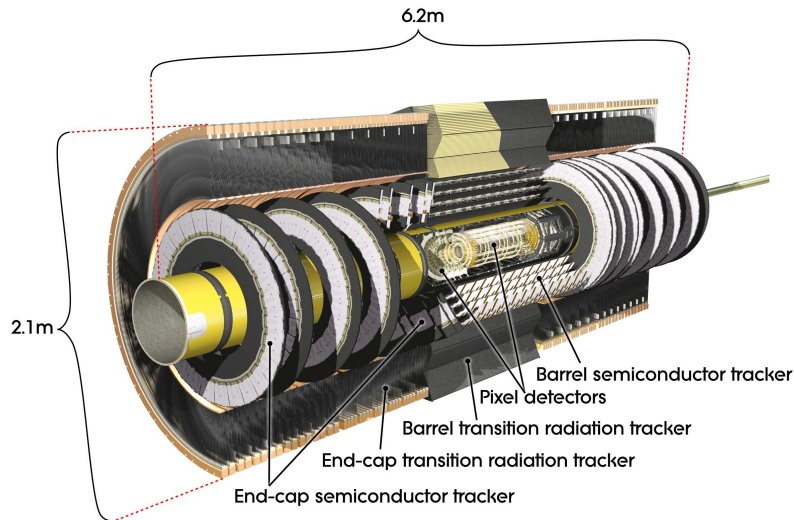


Figure 1.5: Schematic view of the Inner Detector.

in Figure 1.5. In Figure 1.6 a transverse view of a quarter section of the Inner Detector is shown with detailed information on the different systems position and size. The total number of measurement layers must be limited because of the material they introduce. The estimated material budget is less than $0.5X_0$ ^{IV} in the central region and it exceeds $2X_0$ around $|\eta| = 1.5$. This dependence has a direct influence in the electron charge measurement, which will be discussed later in this thesis.

The Pixel detector provides a very high granularity around the interaction point. The sensors are arranged in three concentric cylinders in the barrel and three disks perpendicular to the beam pipe in the end-caps. The barrel layer closer to the beam pipe is at radius 50.5 mm and is referred as the b-layer. The b-layer plays an important role in search for short-lived particles like b-hadrons and τ leptons as well as photons converting to electron-positron pairs. The pixel sensors have a minimum pixel size of $50 \times 300 \mu\text{m}^2$ in $R - \phi \times z$ with an intrinsic resolution of $12 \mu\text{m}$ in $R - \phi$ and 66 in z for the barrel. In total 80 millions of readout channels are available.

The SCT barrel is made of four layers of double-sided silicon strips arranged in four cylindrical layers for the barrel and in nine disks for the end-cap region providing at least eight precision coordinates per track. The strip pitch is $80 \mu\text{m}$, leading to an intrinsic resolution of $17 \mu\text{m}$ in $R - \phi$ and $580 \mu\text{m}$ in z (R) for the barrel (end-cap). The SCT contains around 61 m^2 of silicon detector with 6.2 million of read-out channels.

A large fraction on my work for ATLAS and therefore of this thesis is focused on the Transition Radiation Tracker. The TRT consists on straw tubes of 2 mm of radius. Between the straws, a radiator is placed which produces X-ray photons when high momentum electrons traverse it. These X-rays are absorbed in the straw gas, producing larger signals that are used for electron identification. The straws are arranged in parallel to the beam

^{IV} X_0 is the radiation length: the mean distance over which a high-energy charged particle reduces its energy by $1/e$.

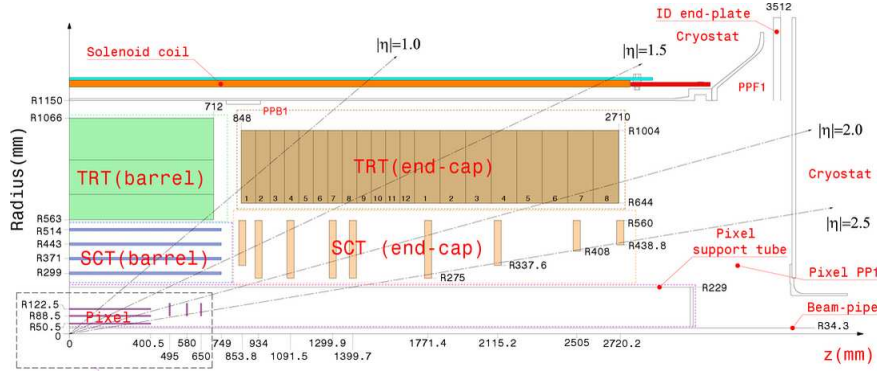


Figure 1.6: Schematic view of a quarter-section of the ATLAS Inner Detector showing each of the major elements with its active dimensions [8].

pipe in the central region and radially in the end-cap wheels. The design intrinsic resolution of the straws is $130 \mu\text{m}$ but this relatively poor resolution is compensated with a large number of measurements on each track. The TRT provides continuous tracking with a much less material per measurement than silicon detectors. A very detailed explanation of the operation principles, the TRT layout and its performance and calibration are given later in this thesis.

1.2.3 Calorimeters

The ATLAS Calorimeters cover the range $|\eta| < 4.9$ with different technologies. An electromagnetic calorimeter (EM) with fine granularity placed over the η region covered by the Inner Detector is designed to measure the electrons and photons. The hadronic calorimeter situated after the EM has a coarser granularity optimized for the jet reconstruction and the measure of missing transverse energy. The EM is based on a technique that uses liquid argon (LAr) as active element for the energy measurement, while the hadronic calorimeters uses LAr and scintillating tile techniques depending on the η region. In Figure 1.7 a cut-away view of the calorimeter components is shown. The figure shows the electromagnetic LAr calorimeter, the hadronic tile calorimeter, the LAr hadronic end-cap (HEC) and the LAr Forward Calormeter (FCal).

The Electromagnetic calorimeter is a sampling calorimeter with an accordion geometry made of lead and liquid argon. This geometry provides a complete ϕ symmetry without azimuthal cracks. The barrel part of the EM extends in the range $|\eta| < 1.475$ and the end-caps in the region $1.375 < |\eta| < 3.2$. The central region, $|\eta| < 2.5$, is devoted to high precision measurements and it is segmented in three sections depending on the distance to the beam pipe. The remaining regions are segmented in two sections with coarser granularity. The first layer is around 4 radiation lengths (X_0) and allows extracting shower shape variables to separate electrons and photons from hadronic objects. Most of the energy of the electrons and photons is deposited in the second layer, which is $16 X_0$. The outer layer, which is $2 X_0$, is used to correct for the tails of very large momentum photons and

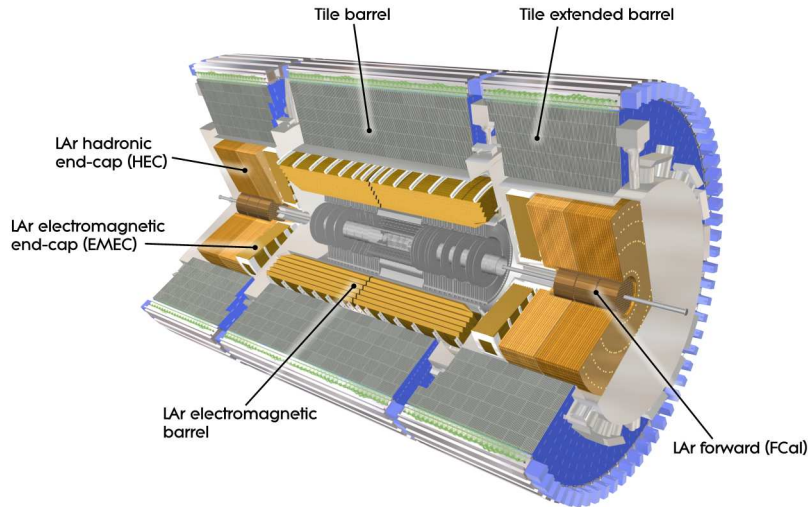


Figure 1.7: Cut-away view of the ATLAS electromagnetic and hadronic calorimeters [8].

electrons. The total thickness in the EM calorimeter is more than 22 (24) radiation lengths for barrel (end-cap) and the total number of read-out cells is about 180000.

A presampler (PS) is placed in front of the electromagnetic calorimeters in the region $|\eta| < 1.8$. It is used to estimate the energy lost in front of the electromagnetic calorimeters. The PS consists on an active LAr layer of thickness 1.1 cm in the barrel and 0.5 cm in the end-caps.

The hadronic calorimeter in the central region, $|\eta| < 1.7$, is provided by a scintillator-tile assembly placed directly outside the LAr calorimeter envelope. The tile calorimeter is a sampling calorimeter that uses steel as absorber and tiles of scintillating plastic as active material. The tile barrel covers the region $|\eta| < 1.0$ and two extended barrels are aimed to extend from 0.8 to 1.7 in $|\eta|$. The scintillating tiles are arranged in three layers in depth of approximately 1.5, 4.1 and 1.8 interaction lengths (λ) for the barrel and 1.5, 2.6 and 3.3 λ in the extended barrels. Each of the two Hadronic End-Cap calorimeters are made of two independent wheels using LAr as active element and copper plates as passive medium. They are placed after the electromagnetic calorimeter end-caps covering the region $1.5 < |\eta| < 3.2$. The hadronic calorimeter is about 10 interaction lengths (λ), adequate to provide a good energy resolution of highly energetic jets.

In the forward regions, the LAr Forward calorimeter provides electromagnetic and hadronic energy measurement in $3.1 < |\eta| < 4.9$. The FCal is a liquid argon sampling calorimeter with copper and tungsten as absorbers. The FCal is also reducing the background radiation in the muon spectrometer.

1.2.4 Muon Spectrometer

The muon spectrometer (MS) is the largest tracking system and the outermost part of the ATLAS detector. It is designed to detect and measure the momentum of muons exiting

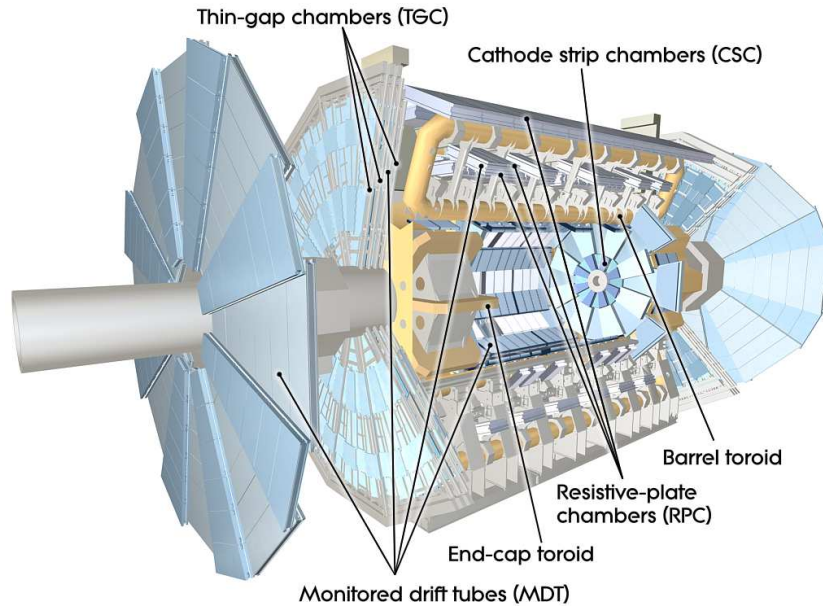


Figure 1.8: Cut-away view of the ATLAS muon spectrometer system [8].

the calorimeters in the range $|\eta| < 2.7$. The magnetic field needed for bending the muon tracks is provided by the toroid magnets, which provide a field mostly orthogonal to the muon trajectory. A view of the muon spectrometer systems is presented in Figure 1.8.

The Monitored Drift Tubes (MDT) are responsible to provide the precision measurement of the position. The MDTs sensitive elements are drift tubes of 60 mm diameter filled with an $Ar - CO_2$ gas mixture, providing a resolution around $35 \mu\text{m}$. Electrons produced in the drift tube can take up to 700 ns before the anode collects them. The MDTs are arranged in three cylindrical layers around the beam axis for the barrel region at radius 5, 7.5 and 10 m. The first layer is 8 tubes deep and the other two are 6 tubes deep. For the end-cap regions, the chambers are installed in planes perpendicular to the beam, at $|z| \sim 13.5$ and $|z| \sim 20$ m. Closer to the interaction point and at larger pseudorapidities ($2.0 < |\eta| < 2.7$) Cathode Strip Chambers (CSC) with higher granularity are used. The CSCs are multiwire proportional chambers where the wires are oriented in the radial direction and the cathodes are segmented into strips. The overall stand-alone momentum resolution of the muon spectrometer is better than 10 % for 1 TeV muons.

In addition to tracking-dedicated chambers, the muon spectrometer has a fast trigger system covering the region $|\eta| < 2.4$: the Resistive Plate Chambers (RPCs) in the barrel and the Thin Gap Chambers (TGCs) in the end-cap regions. The RPCs are gaseous parallel electrode-plate detectors with a distance between plates of 2 mm. The TGCs are multiwire proportional chambers operating in a quasi-saturate mode with a wire to cathode distance of 1.4 mm and a wire to wire distance of 1.8 mm. The muon trigger chambers are designed to provide bunch-crossing identification, well defined transverse momentum thresholds and to complement the MDTs measurements adding the orthogonal coordinate to the precision measurement. Table 1.2 summarizes the performance goals of the four

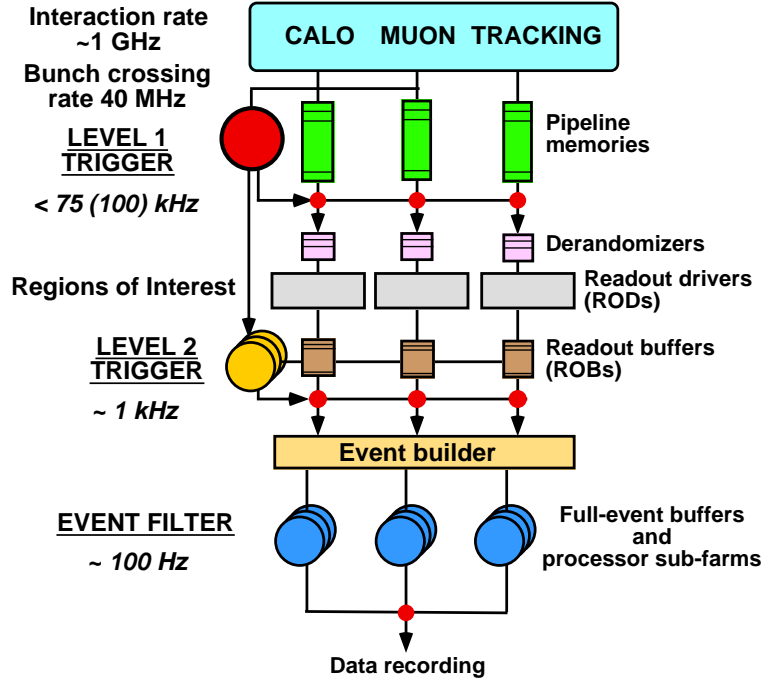


Figure 1.9: Diagram of the ATLAS trigger and DAQ systems [8].

systems used for the muon spectrometer,

Table 1.2: Parameters of the four different muon spectrometer components [8].

Type	Function	Chamber resolution in			Measurements/track		Number of	
		z/R	ϕ	time	barrel	end-cap	chambers	channels
MDT	Tracking	$35 \mu\text{m}$ (z)	-	-	20	20	1088	339k
CSC	Tracking	$40 \mu\text{m}$ (R)	5 mm	7 ns	-	4	32	30.7k
RPC	Trigger	10 mm (z)	10 mm	1.5 ns	6	-	544	359k
TGC	Trigger	40 mm (R)	3-7 mm	4 ns	-	9	3588	318k

1.2.5 Trigger and data acquisition

At the LHC design luminosity, there will be a bunch crossing every 25 ns, each of them with more than 20 proton-proton interactions. In each event, the ATLAS detector produces 1.3 Mbyte of information which requires at least few seconds to be fully processed. At 40 MHz collision rate, the amount of data to store and process is too large and just a fraction of all the collisions produced contain interesting events. It is essential to filter out the background with a large rejection factor while keeping an efficiency for selecting interesting physics as close as possible to 1.

The ATLAS detector has a three level trigger to select the potentially interesting events which reduces the event rate to 200 Hz. The data distribution between the different trigger systems and the mass storage is handled by the Data Acquisition System (DAQ). The different level triggers together with their event rates and the DAQ system are presented in Figure 1.9.

The hardware base Level 1 trigger (L1) receives and buffers the event data from the read-out electronics. The information is used to take a decision in less than $2.5 \mu\text{s}$, reducing the event rate to about 75 kHz. To identify muons online, the Resistive Plate Chambers and the Thin-Gap Chambers are used. The electron, photon and jet decisions are based on calorimeter information. Using simple approaches and high detector granularities, the L1 trigger is able to find high momentum electrons, muons, photons, jets, τ -jets and large missing transverse energy. In each event, the L1 trigger defines Regions of Interest (RoI's) with the geometrical coordinates of areas in the detector where candidates for different processes are found. The trigger decision is distributed to the detector front-end and read-out electronics via the Timing, Trigger and Control (TTC) interface.

The software-based High Level Trigger (HLT) includes the Level 2 (L2) trigger and the event filter (EF). They run in a large computing farm adjacent to the ATLAS experimental cavern to avoid signal delays. The L2 uses the full detector information but only in the RoI's selected by the L1. Using fast algorithms and simplified selections, it reduces the event rate to around 3.5 kHz. The L2 is able to perform a fast tracking in the Inner Detector, which the L1 cannot. The processing time per event is 40 ms. The EF receives the events accepted by the L2 and it has access to the full information of the event, not just the RoI's. The EF is able to run full reconstruction and applies very similar selection to that used in the offline processing. With a processing time per event of 4s, the EF reduces the event rate to around 200 Hz. In the current trigger implementation, around 500 EF definitions are used. The selected events are classified by the EF into a predefined set of event *streams*. These streams are stored to be processed offline once the calibration of the different systems has been fine tuned.

1.2.6 Luminosity measurements and beam monitors

A set of detectors are dedicated to measure the luminosity delivered in ATLAS and to monitor the beams to assure their quality:

- BCM: the Beam Condition Monitor is made of two stations placed close to the beam pipe at $|z| = 1.84 \text{ m}$ and $r = 55 \text{ mm}$ ($|\eta| = 4.2$). It is designed to detect if the beams hit the collimators designed to protect the detectors and if needed to abort the data-taking. In addition, it provides measurement of bunch by bunch luminosities.
- LUCID: the LUMinosity measurement using Cherenkov Integrating Detector, is located at $z = \pm 17 \text{ m}$, close to the beam pipe ($|\eta| \sim 5.8$). It is the main luminosity monitor in ATLAS. It measures the inelastic proton-proton scattering and uses it to estimate the relative luminosity.

-
- MBTS: the Minimum Bias Trigger Scintillators consist on 32 scintillator tiles arranged in 2 disks placed perpendicular to the beam pipe at $z = \pm 3.65$ m covering $2.09 < |\eta| < 3.84$. It provides an interaction trigger when the beam conditions are not optimal and other detectors as the Inner Detector cannot be used. This system has been largely used for triggering during the 2010 collisions program due to its high efficiency.
 - ZDC: the Zero Degree Calorimeter consists on four modules on each side of the interaction point at $z = \pm 140$ m, $|\eta| > 8.3$ designed to detect neutrons. They are mainly used to estimate the centrality in heavy ion collisions.
 - ALFA: The Absolute Luminosity For ATLAS consists of roman pots installed at $z = \pm 240$ m. ALFA determines the absolute luminosity by measuring the elastic scattering at small angles ($\sim 0.3 \mu\text{rad}$).

Chapter 2

The ATLAS Transition Radiation Tracker

The ATLAS Transition Radiation Tracker (TRT) is the outermost and largest of the three sub-systems of the ATLAS Inner Detector [26]. It is designed to operate in the 2T solenoidal magnetic field at the LHC design luminosity ($L = 10^{34} \text{cm}^2 \text{s}^{-1}$). It is made of thin-walled straw drift tubes with a single hit design resolution of $130 \mu\text{m}$. TRT detector geometry gives on average 30 two-dimensional space-points for charged particles with $|\eta| < 2$ and $p_T > 0.5 \text{ GeV}/c$. In addition to a significant contribution to the precision of the momentum measurement due to the track-length measured, the TRT provides particle identification making use of the transition radiation produced by electrons when they traverse different dielectric media.

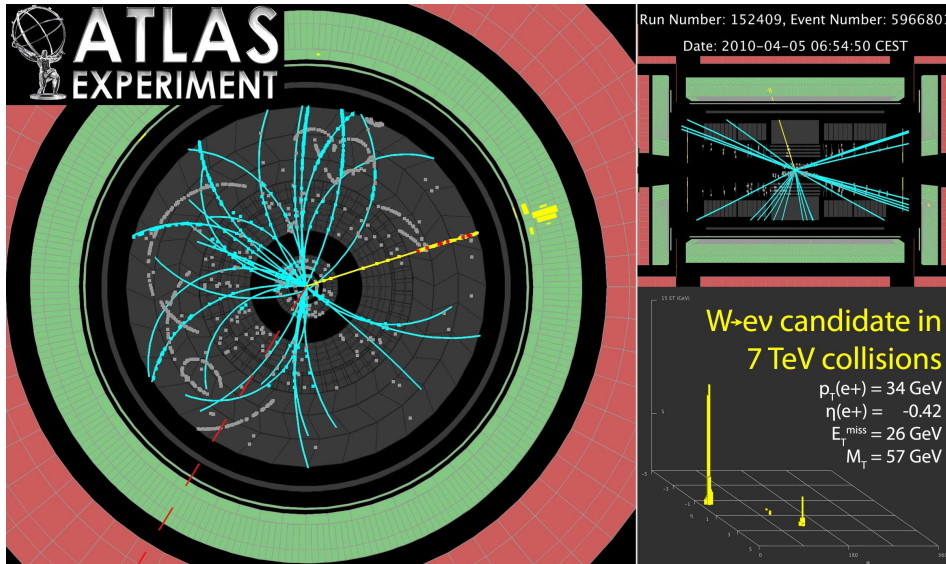


Figure 2.1: Candidate event to $W \rightarrow e\nu$. The red dots are high threshold hits of the TRT, showing the particle is likely to be an electron.

In this chapter, a review of the principles of operation of the drift tubes is given. A detailed description of the ionization, the electron transport and amplification in the presence of electric and magnetic field is given. More details can be found in [18] and [19]. Also, the production and absorption of transition radiation, to separate electrons from heavier particles, is explained but, for further details: [20] and [21]. In the second part of this chapter, the layout of the TRT together with its gas mixture properties and electronics are detailed.

2.1 Drift tubes, principles of operation

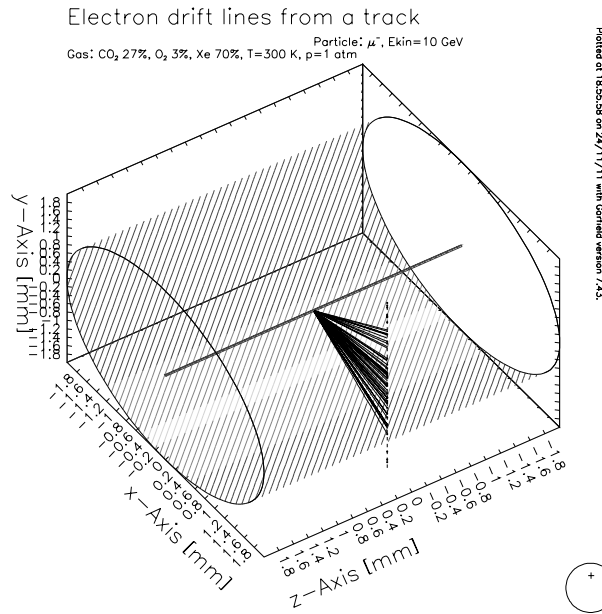


Figure 2.2: Schematic view of a drift tube corresponding to an external radius of 2 mm and a central wire of 0.03 mm. The dashed line corresponds to a muon of energy 10 GeV. The electrons drifting from the ionization clusters to the central wire are shown. The simulation was performed with the Garfield program [22] using as gas mixture 70%He 27%CO₂ 3%O₂.

A drift tube is made of a cylindrical container with conducting walls and filled with a suitable gas. In the axis of the cylinder, a conducting wire is placed with a positive voltage applied relative to the walls producing an electric field. The field created is radial:

$$E = \frac{1}{r} \frac{V_0}{\ln(b/a)} \quad (2.1)$$

where r is the radial distance, V_0 the voltage applied on the wire and a and b the radius of the central wire and the cylinder respectively.

When a charged particle goes through the cylinder, the electromagnetic interaction with the atoms of the gas produces a number of electron-ion pairs (ionization). The number of

pairs created is proportional to the energy loss in the medium. Due to the electric field, the ions will be accelerated toward the cathode (cylinder wall) and the electrons toward the anode (central wire). Depending on the field strength, the electrons will get enough energy to produce more ionization in the gas. Since close to the wire the field is stronger, a cascade or avalanche will be produced, delivering a signal large enough to be measured. The drift tubes operate in the so-called proportional mode, where the collected charge in the wire is directly proportional to the number of the ionizations produced by the incident particle. A simulation of a drift tube with similar characteristics as the TRT drift tube is shown in Figure 2.2. The simulation has been done with Garfield [22], a simulation package for gas detectors. This program allows to do detailed simulations of the different processes involved.

In order to improve the spatial information returned by the detector, the drift time of the electrons produced by the ionization of the incident particle is measured. Assuming a good timing between the different drift tubes and the trigger system and a known drift velocity of the electrons in the medium, then the closest approach to the central wire is known. This drift radius will be defined with a very good precision. In the case of the TRT, with straws of radius 2 mm, the single hit resolution measured is 130 μm .

In the TRT, the straws are surrounded with layers of materials with different dielectric constants (radiator). When a charged particle crosses a boundary between 2 media with different dielectric constants, photons in the X-ray region are emitted collinear to the incident particle. This is the so-called transition radiation and it is only produced for ultra-relativistic particles. This favors electrons to produce a measurable amount of X-rays. The radiation created by the electrons will penetrate into the drift tube and will be absorbed by the gas producing a charge deposition larger than just the ionization of the charged particle. Using this fact, it is possible to distinguish electrons from heavier particles such as charged pions.

2.1.1 Ionization from charged particles

The mean energy loss per unit of path-length of a heavy particle¹ with charge z is described by the Bethe-Bloch formula [105]:

$$-\left\langle \frac{dE}{dx} \right\rangle = 2\pi N_a r_e^2 m_e c^2 \rho \frac{Z}{A} \frac{z^2}{\beta^2} \left(\ln \frac{2m_e c^2 \beta^2 \gamma^2 T_{max}}{I^2} - \beta^2 - \frac{\delta(\beta\gamma)}{2} \right) \quad (2.2)$$

Where N_a is the Avogadro's number, m_e is the mass of the electron and r_e is its classical radius. Z and A are the atomic number and the atomic mass number of the absorber respectively. β is the velocity of the incident particle normalized to the speed of light ($\beta = v/c$). $\gamma = 1/\sqrt{1-\beta^2}$. The parameter I is the mean excitation potential of the absorber and it is tabulated for different materials. δ is the density effect correction which is relevant for particles of large momentum. Finally, T_{max} corresponds to the maximum kinetic energy that can be transferred to a free electron in a collision. For a particle of

¹Bethe-Bloch formula cannot be applied to electrons due to their low mass, the contribution from bremsstrahlung gets very relevant.

mass M it is given by:

$$T_{max} = \frac{2m_e c^2 \beta^2 \gamma^2}{1 + 2\gamma m_e/M + (m_e/M)^2} \quad (2.3)$$

The Equation 2.2, for a given charge, depends mainly on the $\beta\gamma$ of the incident particle with a small dependence on M in T_{max} , so different particles will have almost the same energy losses for equal $\beta\gamma$ values.

The energy loss for some different materials is presented in Figure 2.3. When the momentum of the incident particle increases, the energy loss decreases until reaching the minimum at $\gamma\beta \sim 3.5$. This point is referred to as the Minimum Ionization Particle (MIP) region. For larger momentum, the relativistic region rise takes effect. In this region, the energy loss increases logarithmically until it saturates in the Fermi Plateau. This saturation happens because the medium gets polarized by the charged particles reducing the influence of collisions at large distances.

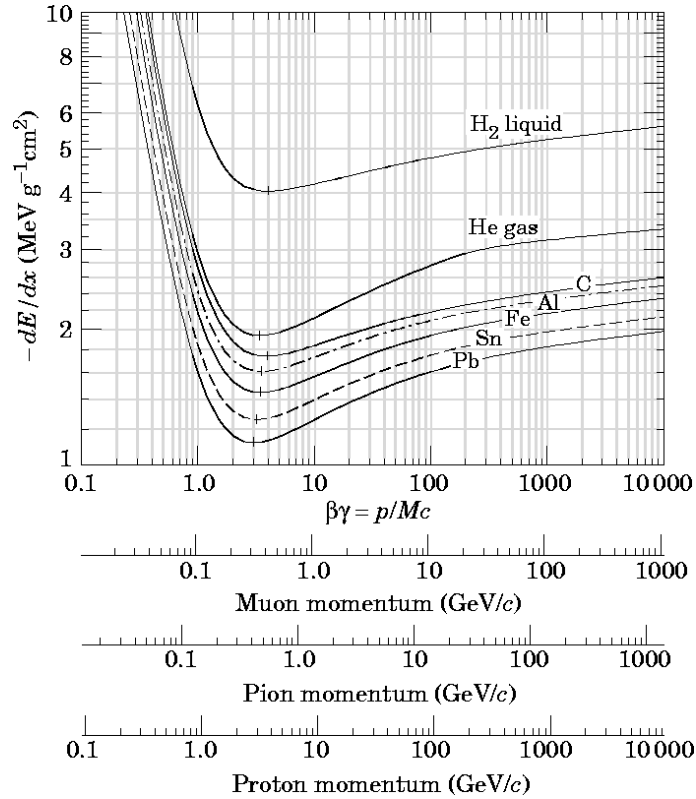


Figure 2.3: The energy loss dE/dx of a charged particle in a range of materials calculated with the Bethe-Bloch equation [105].

The Bethe-Bloch formula describes the mean energy loss for pions with energies between 6 MeV and 6 GeV in most of the materials with a precision of $\sim 1\%$. In the case of drift tubes, the active gas volume is rather thin, so the energy loss is described by a Landau distribution (Figure 2.4). This distribution produces a long tail when the energy loss

increases, known as Landau tail. This long tail is due to the large fluctuations in very few energy deposits along the particle path inside the drift tube. For larger absorber thicknesses the Landau distribution gets more symmetric.

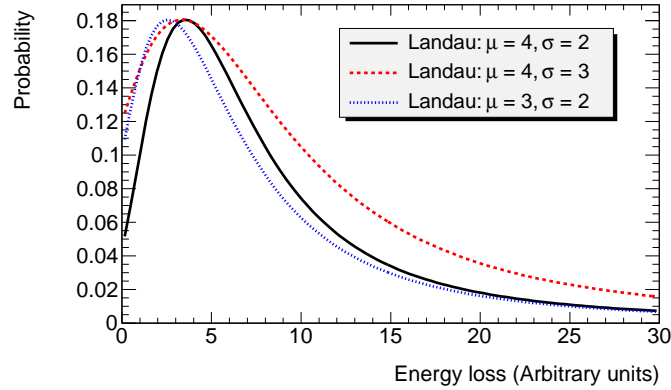


Figure 2.4: Landau distribution for different mean peak values (μ) and widths (σ). The characteristic long tail can be seen.

The energy loss estimated by the Bethe-Bloch formula describes mainly 2 processes: excitation and ionization. The excitation occurs in the process: $He + p \rightarrow He^* + p$ where the Helium atom and p is a charged particle that interacts with the atom exciting it. The ionization process is: $He + p \rightarrow He^+ + e^- + p$. In this case, the atom is ionized by a charged particle, producing a positive ion and a free electron (electron-ion pair). In addition to primary ionization, if there are high energy (δ) electrons in the ionization, they can interact with atoms generating more ion-electron pairs. This can keep going until the energy of the electrons is very low so no more ionization is produced. Another secondary mechanism of ionization is the Penning effect, where an excited state is unable to de-excite emitting a photon due to large spin-parity difference, so it collides with a second atom, that will be ionized, for example: $Xe + CO_2^* \rightarrow Xe^+ + CO_2 + e^-$.

For understanding the performance of a drift tube we have to know the ionization processes. The electron-ion pairs will drift toward the wire and the drift chamber walls producing the measured signal. For this reason the number of pairs produced and their energy is of main interest. The probability density for the energy transfer in each collision inside the gas is not yet fully understood, models based on slightly different approaches are available. The model most widely used is the PAI model (Photo-Absorption Ionization) [24]. This is a semiclassical model that starts from the Maxwell's equations for a charged particle moving inside a medium to estimate the energy loss from the field induced. The

final result of the PAI model is:

$$\begin{aligned} \left\langle \frac{dE}{dx} \right\rangle = & -\frac{\alpha}{\beta^2 \pi} \int_0^\infty d\omega \left[\frac{n_e}{Z} \sigma(\omega) \ln \left[(1 - \beta^2 \epsilon_1)^2 + \beta^4 \epsilon_2^2 \right]^{-1/2} \right. \\ & + \omega \left(\beta^2 - \frac{\epsilon_1}{|\epsilon_2|} \right) \Theta + \frac{n_e}{Z} \sigma(\omega) \ln \left[\frac{2m_e \beta^2}{\omega} \right] \\ & \left. + \frac{1}{\omega} \int_0^\infty d\omega' \frac{\sigma(\omega')}{Z} \right] \end{aligned} \quad (2.4)$$

Here Z is the atomic number, $\Theta = \arg(1 - \epsilon\beta^2)$ is responsible for the Cerenkov radiation, $\epsilon(\omega) = \epsilon_1 + i\epsilon_2$ is the dielectric constant, than can be expressed in terms of the photo absorption cross-section:

$$\epsilon_1(\omega) = 1 + \frac{2n_e}{\pi Z} \int_0^\infty d\omega' \frac{\sigma(\omega')}{\omega'^2 - \omega^2} \quad (2.5)$$

$$\epsilon_2(\omega) = \frac{n_e}{\omega Z} \sigma(\omega) \quad (2.6)$$

The Equation 2.4 can be rewritten as discrete number of collisions with an energy transfer of ω :

$$\left\langle \frac{dE}{dx} \right\rangle = - \int_0^\infty d\omega n_e \omega \frac{d\sigma}{d\omega} \quad (2.7)$$

Where the differential cross-section is then given by:

$$\begin{aligned} \frac{d\sigma}{d\omega} = & -\frac{\alpha}{\beta^2 \pi} \left[\frac{\sigma\omega}{\omega Z} \ln \left[(1 - \beta^2 \epsilon_1)^2 + \beta^4 \epsilon_2^2 \right]^{-1/2} \right. \\ & + \frac{1}{n_e} \left(\beta^2 - \frac{\epsilon_1}{|\epsilon_2|} \right) \Theta + \frac{\sigma(\omega)}{Z} \ln \left[\frac{2m_e \beta^2}{\omega} \right] \\ & \left. + \frac{1}{\omega^2} \int_0^\infty d\omega' \frac{\sigma(\omega')}{Z} \right] \end{aligned} \quad (2.8)$$

The mean free path (λ) for a charged particle traversing a gas volume is the average number of collisions per unit length. This is described by a Poisson distribution with mean value inversely proportional to the total cross section:

$$\lambda = \frac{A}{N_A \sigma} \quad (2.9)$$

where A is the atomic number of the medium, N_A the Avogadro's number and

$$\sigma = \int_{I_i}^{\omega_{max}} \frac{d\sigma(\omega')}{d\omega'} d\omega' \quad (2.10)$$

with I_i being the first minimum ionization potential and ω_{max} the maximum energy transfer per interaction. Garfield simulation package can do an estimate of this parameter and for the TRT gas it is of the order: $\lambda \approx 53 \text{ cm}^{-2}$.

2.1.2 Electron and ion transport and amplification

The equation of motion for a charged particle moving inside an electric (\mathbf{E}) and magnetic (\mathbf{B}) field is given by:

$$m \frac{d\mathbf{u}}{dt} = e\mathbf{E} + e(\mathbf{u} \times \mathbf{B}) \quad (2.11)$$

where \mathbf{u} is the velocity vector of the particle, m is its mass and e is its electric charge. The charged particles, when moving inside a gas, will collide with the molecules and atoms of the gas, losing energy and changing the drift direction. In absence of magnetic field, the velocity acquired by an electron between two collisions with the molecules of the gas is given by:

$$u = |\mathbf{u}| = \frac{e|\mathbf{E}|}{m} \tau \quad (2.12)$$

where τ is the average time between collisions. This velocity will appear macroscopically as the drift velocity. The equation is often written in terms of mobility μ :

$$\mu = \frac{e\tau}{m} = \frac{\mathbf{u}}{\mathbf{E}} \quad (2.13)$$

$$\mathbf{u} = \mu\mathbf{E} \quad (2.14)$$

For ions, the drift velocity is reduced compared to electrons due to their large mass. Usual drift velocities for electrons are of the order of $\sim 10^6$ cm/s (~ 10 $\mu\text{m/ns}$) while for ions they are $\sim 10^4$ cm/s (~ 0.1 $\mu\text{m/ns}$). A detailed microscopic picture of the charged particle drift can be found in [18].

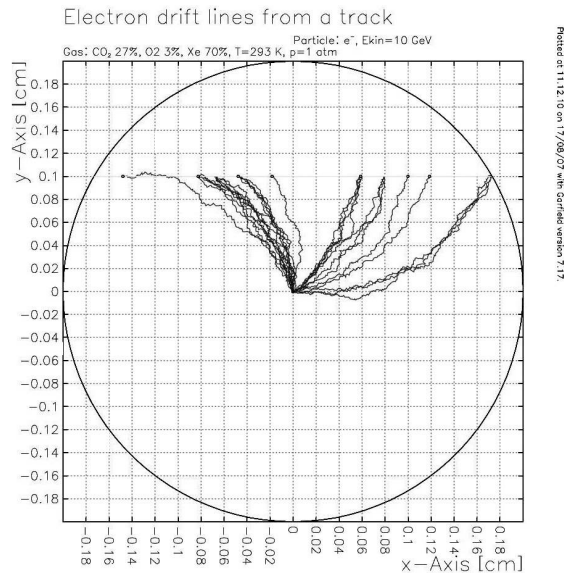


Figure 2.5: Electron drift lines with magnetic field parallel to the central wire [35].

If a magnetic field is present, the last term in Equation 2.11 must be taken into account. In case the magnetic field is orthogonal to the electric field: $\mathbf{E} = (E, 0, 0)$ and $\mathbf{B} = (0, 0, B)$, the equations of motion are:

$$\begin{aligned}\frac{du_x}{dt} &= \frac{E}{m} + \frac{B}{m}u_y \\ \frac{du_y}{dt} &= -\frac{B}{m}u_x \\ \frac{du_z}{dt} &= 0\end{aligned}\tag{2.15}$$

The solution for the system of equations is:

$$\begin{aligned}u_x(t) &= \frac{E}{m} \sin \frac{B}{m}t \\ u_y(t) &= \frac{E}{m} \left(\cos \frac{B}{m}t - 1 \right) \\ u_z(t) &= 0\end{aligned}\tag{2.16}$$

This shows that the trajectory of the charged particle is bent in the plane transversal to the magnetic field. When the magnetic field is parallel to the electric field, no transverse force will appear and the charged particle trajectory remains the same as without field.

In the Figure 2.5 an example of the electron drift toward the anode produced by a charged particle is shown. In the simulation, 2T magnetic field parallel to the central wire and therefore perpendicular to the electric field, is included. This magnetic field bends the path of the electrons as presented in the figure, increasing the collecting time on the anode.

In case of charged particles moving inside a gas volume without the presence of electric or magnetic field, they collide with the gas molecules and atoms, losing energy until they get in thermal equilibrium with the gas. This effect is known as diffusion. The thermal velocity of a particle is given by:

$$v = \sqrt{\frac{8kT}{\pi m}}\tag{2.17}$$

here k is the Boltzmann's constant, T is the temperature of the gas and m is the mass of the ion or the electron moving. This random movement is superimposed onto the drift velocity, increasing the traveled path. In Figure 2.5, this effect can be appreciated, where the electrons drift toward the anode suffering from multiple collisions affecting the final path length. Depending on the magnitude of the diffusion, the time and spatial resolution can get affected. A special case is when the magnetic and electric fields are parallel. In this case the diffusion is minimized improving the spatial resolution, and this field orientation has been largely used in Time Projection Chambers (TPCs) [25].

Using the simplest case where the deviation is the same in all directions, the distribution of charges after diffusing a time t is described by a Gaussian distribution:

$$N = \left(\frac{1}{\sqrt{4\pi Dt}} \right)^3 \exp \left(-\frac{x^2}{4Dt} \right)\tag{2.18}$$

Where D is the diffusion constant. From this distribution, the spread produced by the diffusion effect after traveling a certain time t , is given by:

$$\sigma_x^2 = 2Dt \quad (2.19)$$

This can be rewritten in terms of the travel distance (L) using the mobility (μ) inside an electric field E :

$$\sigma_x^2 = \frac{2DL}{\mu E} \quad (2.20)$$

In the case of the ions, the diffusion is orders of magnitude smaller than for electrons in the same field. For the drifting lengths within the TRT straw, in which the maximum distance to the wire is 2 mm, the electron diffusion width is of the order of ~ 0.01 mm and can be neglected.

Amplification and collected signal

As we have seen, electrons will move much faster than ions towards the anode (central wire). As shown in Equation 2.1, the field will increase dramatically when close to the wire. Once the electric field is above 10^4 V/cm, the electrons can gain enough energy to produce new ionization between collisions. The primary and the secondary electrons will keep drifting toward the wire, producing more and more electron-ion pairs in an avalanche effect.

The probability of ionization per unit length ($\alpha = 1/\lambda$), also known as the first Townsend coefficient, relates the number of electron-ion pairs (dn) produced in a path (dx):

$$\frac{dn}{n} = \alpha n dx \quad (2.21)$$

The ionization probability depends on the electric field, and in our case it is not uniform, so:

$$n = n_0 e^{\int \alpha(x) dx} \quad (2.22)$$

Where n_0 is the original number of electrons. The total gas gain (M) is defined as:

$$M = \frac{n}{n_0} = e^{\int \alpha(x) dx} \quad (2.23)$$

In the case of the drift tube, the voltage used is optimized to run in the so-called proportional mode. In this mode, the total collected charge in the anode is proportional to the ionization produced by the incident particle. The avalanche is produced very close to the wire, creating a large amount of free electrons that are collected in the anode in a short time (order of ns). These electrons produce a very fast rise of the signal. On the other hand, the ion drift toward the straw walls is much slower than for the electrons. These ions in motion induce a negative charge in the central wire, leading to a very long tail in the signal pulse. In the Figure 2.6 both parts of the signal can be clearly appreciated. The full time for the collection of the charge induced by ions can be several μs , which is much larger than the LHC bunch crossing time (25-50 ns). For this reason, a dedicated tail cancellation mechanism was implemented in the TRT electronics.

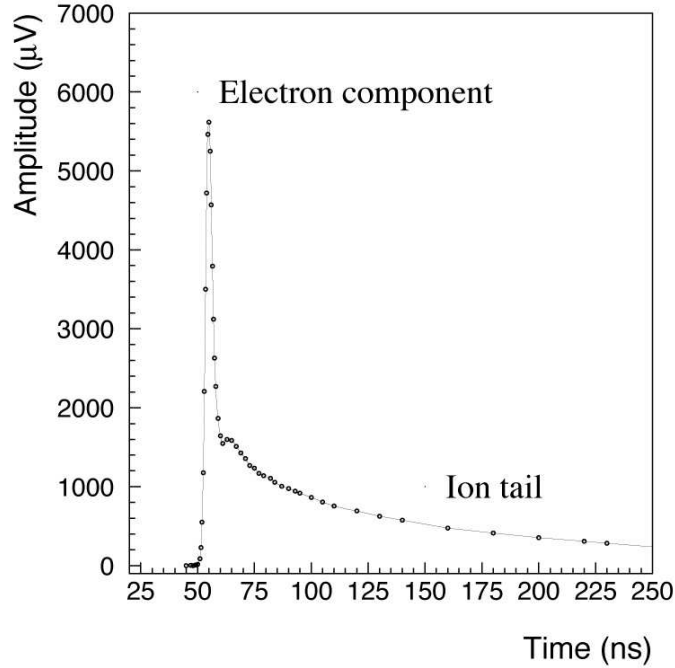


Figure 2.6: Signal measured in the wire in the straw. The electron and the ion components are shown [35].

In the avalanche, photons are as abundant as electrons because the cross-sections are of the same order. Some of these photons will have enough energy to also ionize the gas. They can travel further leaving the original avalanche and starting a new full avalanche that again can produce new avalanches in different regions. This can cause the breakage-down of the drift tube. Free electrons are created by the photoelectric effect when photons, which can travel even further, reach the cathode surface. In order to absorb these photons, a quench gas has to be added to the mixture. Quench gases have large photo-absorption coefficients over a wide wavelengths range and they deexcite by changing rotational and vibrational states.

2.1.3 Transition radiation

When a charged particle crosses a surface between two media with different dielectric constants, a boundary condition in the solution of Maxwell equations for the field induced by the moving charge is created. The solution for this new condition is the emission of extra radiation, the transition radiation, where fields reorganize radiating photons. For a particle of charge z crossing from vacuum to another medium, the emitted radiation (R_{rad}) is given by:

$$R_{rad} = \frac{\alpha z^2 \gamma \hbar \omega_p}{3} \quad (2.24)$$

Where α is the fine structure constant ($\approx 1/137$), $\gamma = 1/\sqrt{1-\beta^2}$ and ω_p is the plasma frequency of the medium given by:

$$\omega_p = \sqrt{4\pi N_e r_e^3 m_e c^2 / \alpha} \quad (2.25)$$

N_e is the electron density of the medium and r_e is the classical radius of the electron. The photons emitted are very forward peaked with an angle given by $\theta \sim 1/\gamma$ with respect to the charged particle direction.

In the drift tube, the low energy photons will not be measured, so a lower energy threshold (E_{cutoff}) has to be requested for the final spectrum. Applying this condition, the number of photons emitted per surface transition is distributed following a Poisson distribution with mean value:

$$N_\gamma(E_\gamma > E_{cutoff}) = \frac{\alpha z^2}{\pi} \left[\left(\ln \frac{\gamma \hbar \omega_p}{E_{cutoff}} - 1 \right)^2 + \frac{\pi^2}{12} + 1 \right] \quad (2.26)$$

In general, the order of magnitude of the number of photons produced can be roughly estimated by: $N_\gamma \sim \alpha = 1/137$. To give an idea on the capabilities for electron-pion separation, in case an electron of energy 50 GeV crosses a boundary between polypropylene ($\omega_p \approx 20$ eV) and air, the average number of photons with energy larger than 1 keV ($E_{cutoff} = 1$ keV) is: $N_\gamma = 0.10$ photons. If instead of an electron, the charged particle is a pion with same energy, the average number of photons produced is: 0.0065. In this case, the number of photons produced by the pion is negligible if we compare with the electron. Measuring this transition radiation we can separate electrons from for particles in the region 1 to 200 GeV/ c^2 .

Even for electrons, the amount of radiation emitted by a single interface is not enough to be measured. In order to enhance the production of photons, several layers of foils assembled closely together are used. In a single foil, the formation zone of the radiation is the distance needed for the generated photon and the charged particle to decouple and is of the order of the photon wavelength. This is an important parameter because if the foil thickness is much smaller than the formation zone, the interference between the radiation in each surface will suppress the transition radiation. In case the thickness of the foil is of the order of the formation zone, the interference is constructive, giving a final photon production for N foils of the order of N times the photons produced by a single foil.

As we have seen, transition radiation photons are mainly collinear to the incident electrons. These photons have energies in the range of the X-rays (1-20 keV) and they will penetrate into the drift tube producing electron-ion pairs in the gas. This radiation is best absorbed by elements with low lying atomic energy levels and high atomic number, so Xenon gas is the best option. For high energy X-rays, above 20 keV, the photons pass through the detector, reducing the detection efficiency. In case of low energy photons, they will be absorbed in the radiator and the straw materials. In addition to a large probability to absorb the photon in the active gas, it is important to optimize the materials used to build the drift tube and the radiators to minimize the absorption in the energy ranges we are interested. Figure 2.7 presents the absorption length for pure Xenon, the ATLAS TRT mixture (70%Xe, 27%CO₂, 3%O₂), together with the materials to build the TRT straws

(polypropylene and Kapton). As can be seen, the TRT gas is close to the pure Xenon, giving a very good performance for transition radiation absorption.

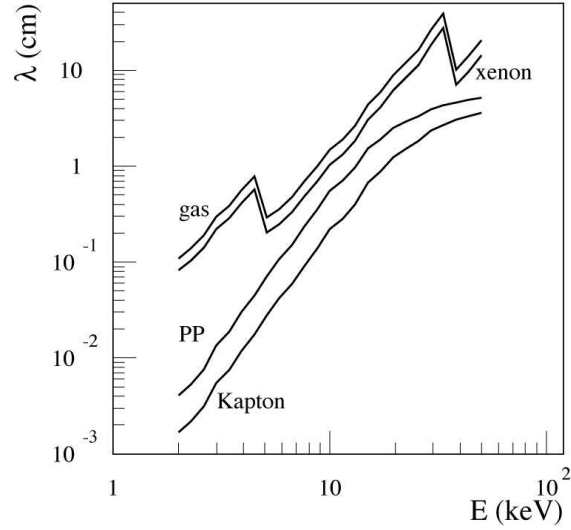


Figure 2.7: Absorption length λ for photons in Xe, the ATLAS TRT gas mixture (70%Xe, 27%CO₂, 3%O₂), polypropylene (PP) and Kapton [20].

The electron-ion pairs originating from transition radiation (n_{TR}), will overlap with the ones produced by the charged particle ionization (n_{ioniz}). To be able to provide electron identification capabilities, the ratio n_{TR}/n_{ioniz} has to be maximized in the detector design. Special attention has to be paid to the tail of the Landau distribution for ionization, which can be confused with transition radiation.

2.2 Detailed picture of the ATLAS TRT

The Transition Radiation Tracker is built of 294304 drift tubes of 2 mm of radius. Different straw lengths and orientations are used for the central (barrel) and the forward (end-caps) regions. As has been shown in previous sections, drift tubes detectors provide good features for tracking and particle identification. This technology was chosen among others because of its intrinsic radiation hardness, the high rate at which can be operated and the relatively low cost compared to other tracking technologies over large volumes. This design is optimized in order to get the best performance [26] [2]:

- Continuous tracking covering $|\eta| < 2.0$ for particles with $p_T > 0.5$ GeV: between 30-40 spatial measurements in $R - \phi$ for charged particles. It is very important for momentum resolution at high momentum due to the large track length measured. With the TRT, the total are measured is up to 1m in the transverse plane.
- Electron identification: transition radiation allows to separate electrons from charged hadrons for electrons with momentum larger than 5 GeV.
- Pattern recognition and level-2 capabilities in combination with Pixel and SCT.
- Low material budget: below 10 % X_0 at any η .

But also, the TRT has to be operated under the LHC environment, so very tight conditions for safety and operation have to be fulfilled:

- Very high occupancy: up to 30 %.
- Very high counting rate: up to 20 MHz/straw.
- Short bunch crossing interval: 25 ns.
- High radiation environment: ~ 10 MRad accumulated per straw in 10 years and $\sim 2 \cdot 10^{14}$ n/cm² year.
- Thermally and chemically stable.
- Fast and chemically passive straw gas to avoid aging effects.
- Very precise and robust mechanical structure.

Some of the requirements are mutually exclusive, so the TRT design was optimized to get the best compromise between them.

In Figure 2.8, the great importance of the TRT for the momentum measurement of charged particles can be seen. The plot shows the uncertainty in the momentum measurement for tracks using the whole Inner Detector and tracks using only Pixel and SCT information. The uncertainty is obtained from splitting the measured tracks, refitting each segment and comparing the momentum of both segments. The improvement obtained adding the TRT information is especially significant for high momentum particles ($p_T > 20$ GeV).

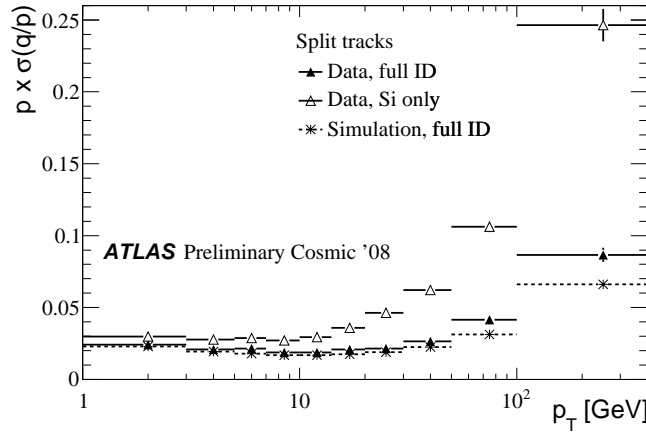


Figure 2.8: Uncertainty of the measured momentum for cosmic rays. Tracks reconstructed using only SCT and Pixel and using full Inner Detector information are shown [28].

For electron identification capabilities, the TRT read-out electronics has a dual threshold discriminator, one for tracking or low threshold (LT) and a second one designed to detect large energy depositions due to the transition radiation absorption, known as high threshold (HT). In Figure 2.9 (left) the high-threshold turn-on curve for the central region is shown. This curve shows the probability to get a high threshold hit depending on the velocity (γ factor) of the detected particle. The turn-on starts at $\gamma \sim 10^3$, this corresponds to a pion momentum of ~ 100 GeV. At $\gamma \sim 10^4$ the plateau is reached, corresponding to electrons of ~ 6 GeV. In Figure 2.9 (right) the fraction of HT hits divided by the total number of hits associated to the particle track is presented for electrons and pions. Making use of this ratio in combination with the electromagnetic calorimeter information, a clear separation between electron and heavier particles is obtained.

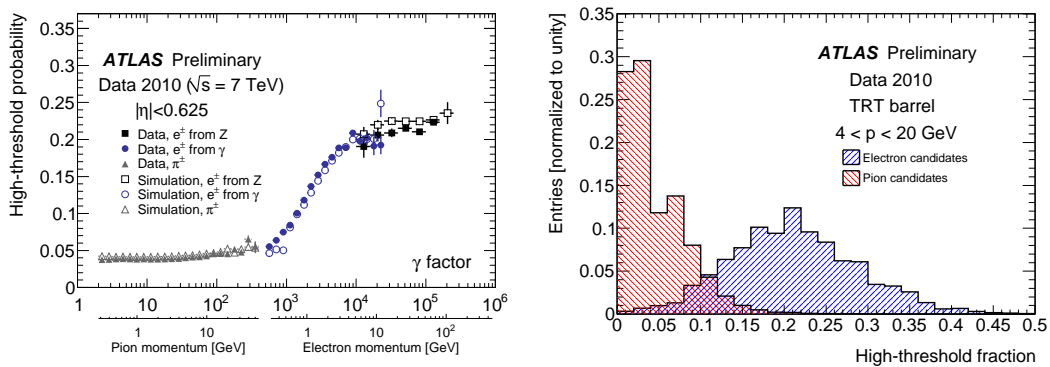


Figure 2.9: The left side plot shows the probability of a TRT high-threshold (HT) hit as a function of the Lorentz factor γ in the central region $|\eta| < 0.625$. The corresponding γ factor for pion and electron momentum is shown. The right side plot shows the HT fraction hit for electron and pion candidates in the barrel region [29].

In this section, the design and construction of the TRT straw, the geometry and electronics are briefly revisited. For more details, extensive documentation is available: [26], [27], [30], [31], [32], [33], [34], [35], [20], [36], [37] and [38].

2.2.1 The TRT straw tube

The design of the TRT Straw tube is made to ensure an efficient and safe operation in a high radiation environment. Drift tubes with a radius of 2mm were chosen. With this size, a great compromise between hit efficiency, due to the number of clusters produced, and short bunch crossing resolution, thanks to the fast electron drift, is obtained. In addition, they have a good mechanical and operational stability.

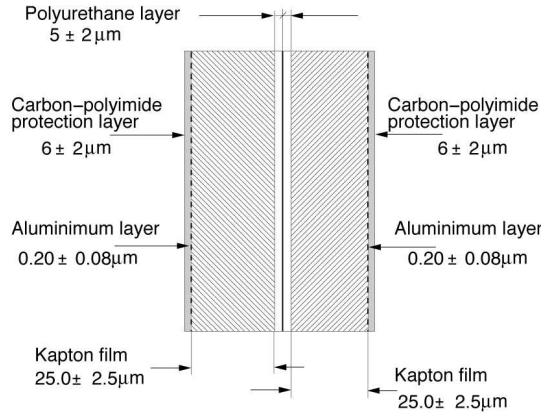


Figure 2.10: Section of the TRT straw tube wall.

The straw drift tubes walls are made of two layer of a Kapton multilayer material [30]. A section of the drift tube wall is shown in Figure 2.10. For each layer, in a $25 \mu\text{m}$ thick Kapton 100VN film, an aluminum layer of $0.2 \mu\text{m}$ was deposited on one side. The aluminum layer is protected by $6 \mu\text{m}$ of carbon-polyamide. On the other side of the Kapton film, $5 \mu\text{m}$ of polyurethane is used as heat-activated adhesive. In Figure 2.11 the manufacturing process is presented. Two tapes of the Kapton multilayer were wound on a precision mandrel at $\sim 260 \text{ }^\circ\text{C}$.

The straw wall works as cathode and its resistance has to be kept as low as possible. With the aluminum layer, the final straw wall resistance is below the TRT specification: $300 \Omega/\text{m}$. The two aluminum layers in each straw are connected together to a high voltage ($\sim 1.5\text{-}1.6 \text{ kV}$) power supply.

Carbon fiber bundles are used to reinforce the straw tube improving greatly the final mechanical properties. Four fibers are attached to the straw at 90 degrees to each other. The final straw has a weight of 1.5 g/m and an expansion coefficient 2 orders of magnitude lower than before the reinforcement.

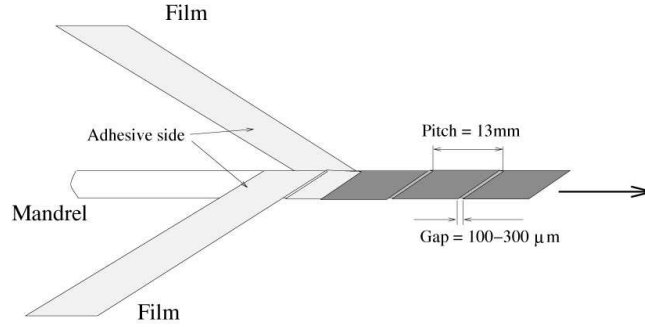


Figure 2.11: Manufacturing process for the TRT straw. Two multilayer films are wound on a precision mandrel.

The anode is done with a $31 \mu\text{m}$ diameter gold-plated tungsten wire and is connected to ground. This small radius was chosen to maximize the gain and at the same time support the required tension. The thickness of the gold layer is between $0.6 - 0.7 \mu\text{m}$. Tolerances to the diameter wire and ellipticity are better than 1 % and 2 % respectively to ensure uniform gas gain. The measured resistivity of the wire is $60 \Omega/\text{m}$ with a signal attenuation length of $\sim 4 \text{ m}$ and a signal propagation time of $\sim 4 \text{ ns/m}$. In total, around 450 km of wire were produced [34].

2.2.2 Gas mixture

The choice of the detection gas is ruled by its X-ray absorption, key to electron identification. Xenon, as shown in Figure 2.7 has an excellent absorption for photon energies in range $\sim 10\text{-}30 \text{ keV}$. The final gas used is a mixture of 70% Xenon (Xe), 27% carbon dioxide (CO_2) and 3% of oxygen (O_2).

In the mixture, the CO_2 gas is working as *quench* gas, absorbing the UV photons produced during the avalanche and confining spatially the avalanche. This is essential to stabilize the amplification process and avoid damage in the straws. In addition, this gas provides a constant drift velocity, low diffusion coefficient and a low deflection of electrons in magnetic field. The studies [30] revealed that the UV photo absorption of CO_2 is not enough to absorb all the photons produced in the avalanche, so a third component is added: oxygen (O_2). A minimum of 2% is needed to provide a safe operation. The O_2 itself does not absorb UV photons, the stabilization is done by the ozone O_3 produced in the avalanches.

The straw wall works as a cathode, for this reason it is connected to a high voltage, between -1.5 to -1.6 kV. In Figure 2.12, the gain for the TRT gas depending on the HV applied is shown. In nominal conditions, the HV voltage is set to 1530 V, obtaining a gain of $2.5 \cdot 10^4$. Thanks to the O_2 , the gas stability is very good, giving a tolerance to straw wire offset up to 0.3 mm. In addition, a large safe margin for the straw operation is ensured.

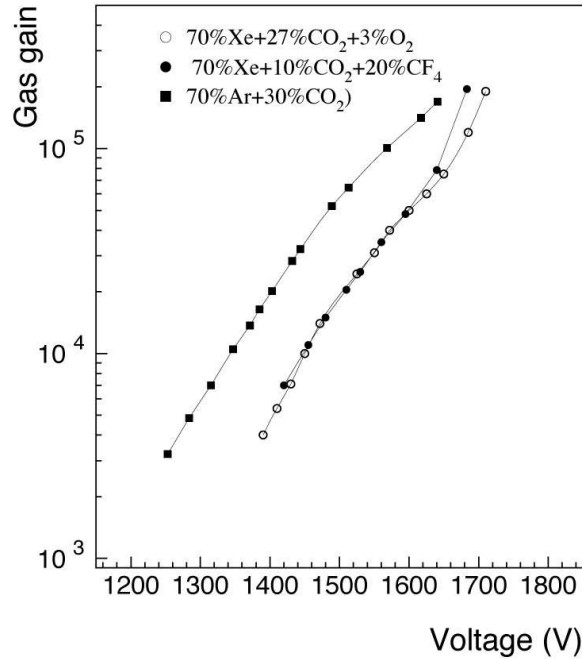


Figure 2.12: Gas gain as a function of different high voltage for different gas mixtures, including in open circles the default TRT mixture and the mixtures used for commissioning as open squares [30].

The Xenon gas is very costly, so during the detector assembly, acceptance test and initial commissioning before the collision data-taking started, another gas mixture was used. This mixture was 70% Argon and 30% carbon dioxide. For Argon, the transition radiation absorption is very low, and is not possible to use this mixture for electron identification. The gain for Argon based gas is presented in Figure 2.12 together with the nominal Xenon gas. An operation HV of 1450 V is used to get a gain of $2.5 \cdot 10^4$. In this gas, the drift velocity is larger than in the Xenon mixture. This, combined with a lower number of ionization clusters per straw, returns a lower spatial resolution.

For completeness, in the original design of the TRT, the gas to use was: $Xe + CF_4 + CO_2$ [26]. The aging studies performed during the R&D of the detector revealed that CF_4 under a high radiation environment can produce fluorine active species that attach and damage some of the straw materials. For this reason this mixture was abandoned. When this problem was realized, the TRT electronics were largely produced, so the new gas mixture was adjusted and validated to get perfect compatibility with the front-end electronics.

The gas mixture has to be kept in the right proportions to ensure the detector performance is not altered. Several processes can affect the gas composition, such as diffusion of the CO_2 envelope through the straw wall, or leak of Xenon. Changes in the gas composition can affect the drift velocity with a direct influence to the spatial resolution. In the same way, leakage of Xenon in the radiators will absorb the transition radiation photons before reaching the drift tube. A complex close-loop gas system is used to exchange every hour

the gas from the whole TRT and purify it. The CO_2 concentration is kept within $\pm 0.5\%$ and the O_2 within $\pm 0.1\%$ of the nominal value. The N_2 level is kept below 0.6% . During operation, a system of membranes is used to purify the gas. When the gas is recuperated, it is frozen and the N_2 and O_2 gases are removed. In addition, a gas stabilization system adjusts the potential between each straw wall and its wire to compensate the variation of the gas gain produced by changes in gas pressure and temperature.

2.2.3 Barrel and end-caps

The TRT surrounds the SCT and Pixel detectors and is embedded in a 2T solenoid. With a total size of 6.2m in length and 2m of diameter, the TRT consists of three parts: a barrel [31] and two end-caps [32]. The barrel covers $|\eta| < 1$ and is made of 52544 straws oriented parallel to the beam axis. In each end-cap there are 122880 straws radially aligned with respect to the beam pipe covering $0.8 < |\eta| < 2.0$. With this geometry, charged particles with $p_T > 0.5$ GeV and $|\eta| < 2.0$ cross about 30-40 TRT straws which makes a great contribution to the final momentum measurement.

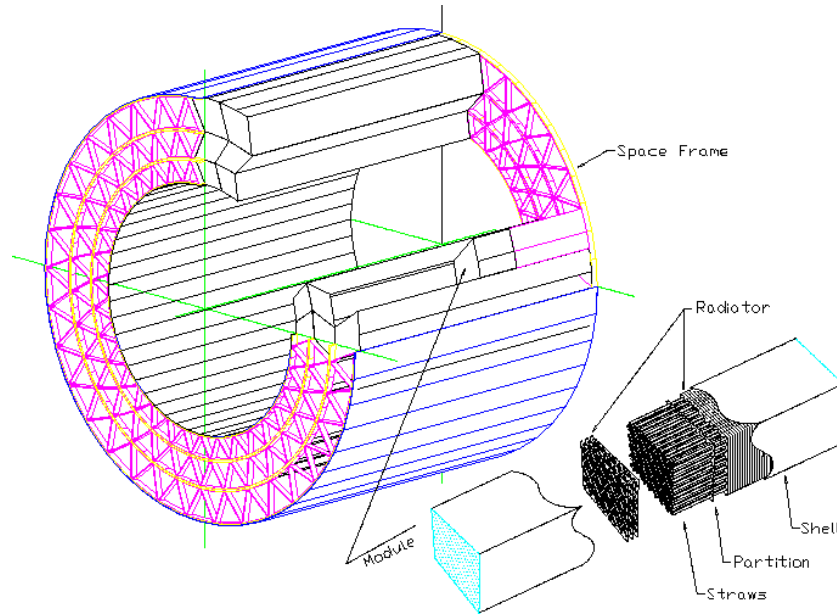


Figure 2.13: Barrel layout showing the support structure and the three cylindrical layers of modules. A detailed view of a module is also shown [31].

The barrel straws are 144 cm in length. The arrangement of the straws has been optimized to minimize the amount of dead tracking area for high momentum particles, maximizing the number of points measured. The barrel consists of 32 axial elements called phi sectors or stacks. Each of these sectors is made of three modules (type 1, 2 and 3) that are identical for all the phi sectors, see Figure 2.13. Each of the modules is a prism that consists on an array of drift tubes embedded in transition radiation material and housed in a carbon-fiber reinforced composite shell. This shell dissipates part of the heat generated

in the straws and provides mechanical rigidity for the system. The straws in the array in each module are parallel to the beam axis with an average distance between straw centers of 6.6 mm. Inside each module, the straws are ordered in layers depending on their distance to the beam pipe.

The inner modules, type 1, have inner radius of 0.56m and outer of 0.70m. Each of these modules contains 329 straws arranged in 19 layers. Type 2 modules, situated in the middle region, have an outer radius of 0.86 m holding 520 straws distributed in 24 layers. Finally, each of the outer modules has 30 layers with 793 straws in total. In Figure 2.14 the dimensions and the straw arrangement for a phi sector is shown. The active gas flow is 110 cc/min for type 1 modules, 170 cc/min for type 2 and 240 cc/min the type 3. These flows make possible one volume of gas change per hour.

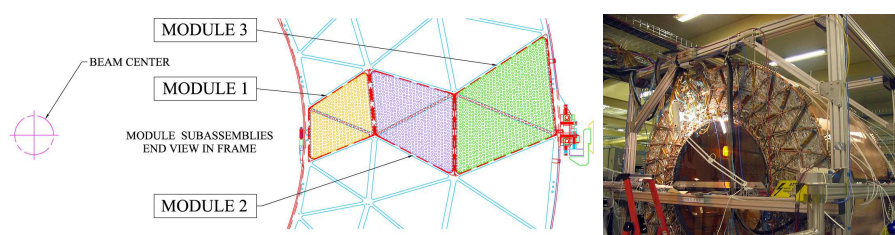


Figure 2.14: The three types of modules for each TRT Barrel phi sector are shown in different colors. The TRT is made of 32 phi stacks, as the one displayed on the left side. The plot is scaled to respect the barrel proportions. On the right side, a photo of the TRT after the final assembly is displayed [39].

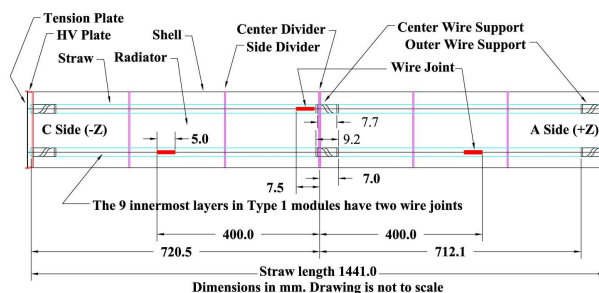


Figure 2.15: Barrel module layout. The straw components and the wire joint positions are shown for a wire with a single joint (up) and for the so-called short straws (down), where the central region is not sensitive [31].

The sense wire is split in the middle by an insulating glass joint and equipped with independent read-out at both ends. This is done to reduce the occupancy rate at the design luminosity. For the nine layers of straws closer to the beam pipe in the module 1, where occupancy is larger, the straws are divided in three, with the middle section not read out. These straws with shorter active region are usually referred to as *short straws*. Details on the electrical split for short and default straws are shown in Figure 2.13. Due to the electrical split, the TRT barrel is not sensitive in the central region: $|z| < 7.7$ mm.

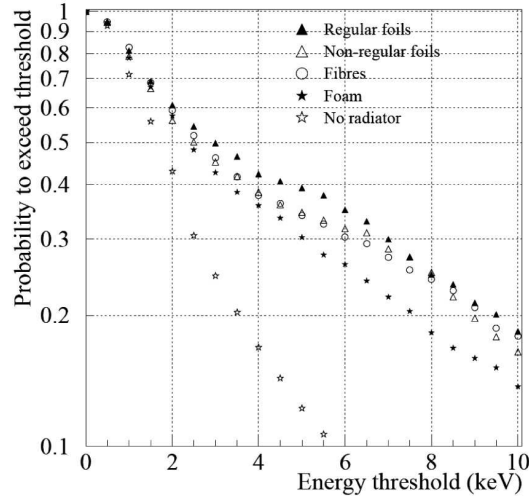


Figure 2.16: Straw probability to measure and energy deposition larger than a given threshold for different radiator types. The TRT end-caps use non-regular foils while the TRT barrel, due to its modular geometry, uses fibers. Both materials have performance close to the ideal material, the regular foils [26].

The transition radiator material, which completely surrounds the straws inside each module, consists of polypropylene-polyethylene fiber matting about 3mm thick. The performance of this material is presented in Figure 2.16 and it is very similar to regular foils. Regular foils have the best transition radiation performance, but due to the barrel geometry, they cannot be used. Regular foils will not fill all the space between straws, leading to loss of produced photons. The absorption length for 5 keV photons, the lowest transition radiation that TRT is measuring, is about 17 mm in the radiator material.

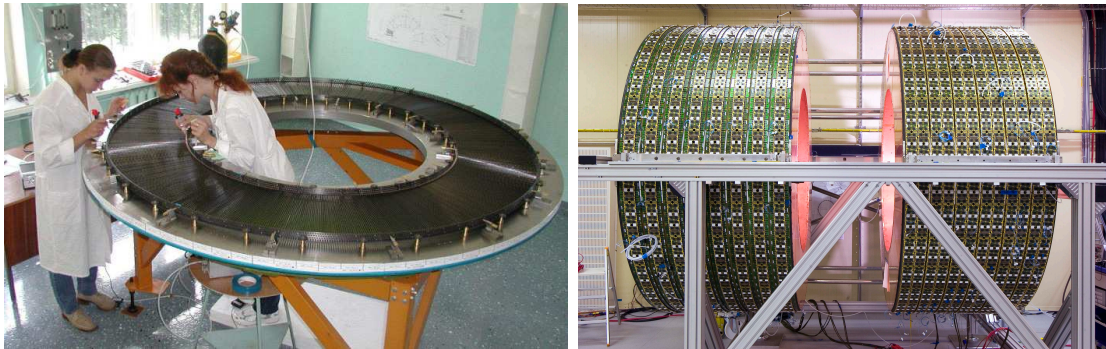


Figure 2.17: End-cap wheel assembly at production site (left). The B wheels and the A wheels ready for final the final assembly of one end-cap (right) [39].

Each of the two end-caps is made of 122880 straws 39 cm in length. The straws form a uniform array in the azimuthal plane perpendicular to the beam, with 768 straws equally spaced. In total, each end-cap has 160 planes (layers) of straws. For the first 96 layers, in

the range $84.8 < |z| < 171.0$ cm, the distance between straws is 8 mm. For the following 64 planes, for $171.0 < |z| < 271.0$ cm, the distance between planes is increased to 15 mm.

Eight planes of straws make an independent module, that is referred to as wheel due to its cylindrical shape with axial straws placed as spokes (Figure 2.17). There are two kinds of wheels; type A for distance between planes of 8mm and type B wheels for distance 15mm. In total, each end-cap is made of 12 A wheels and 8 B wheels (Figure 2.17). In Figure 2.18 a cross-section of an eight-plane wheel is presented. Two four-plane wheels, containing four planes of radial straws, are assembled back to back to produce an eight-plane wheel.

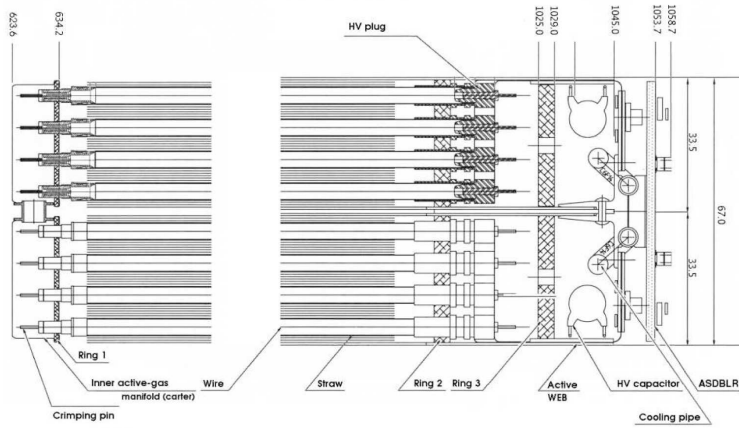


Figure 2.18: Layout for an end-cap wheel. The x-axis corresponds to the distance to the beam and the y-axis is the distance along the beam. Different elements are shown as the straw and wire dimension, such as the high voltage supply, the front-end electronics (ASDBLR) and the radiator material between straws [32].

The TRT end-cap radiators are made of alternating layers of polypropylene film of $\sim 15 \mu\text{m}$ thickness and sheets of a spacer fabric $\sim 250 \mu\text{m}$ thick. The spacer is a synthetic net made of polyamide fibers. The radiators are placed in the gaps between adjacent straw planes and the number of layers for each varies between 7 and 34, depending on the wheel, and straw plane gap position. The foils are not stretched to keep them planar and the spacing has not been precisely controlled to minimize the material and its complexity. In Figure 2.16 the performance of this non-regular foil radiators is presented. The performance is close to the ideal one, the regular foils, and is very similar to the barrel radiators: fibers. Electrons with momentum 40 GeV produce about 11 transition radiation photons at $|\eta| \sim 1.7$ and 5 for $|\eta| \sim 2.0$.

2.2.4 Electronics

The straw analog signal is processed by the front-end electronics [33] and then transmitted to the back-end electronics as illustrated in Figure 2.19. The front-end electronics, designed to be high-speed and low noise, is made of two different circuits: Amplifier Shaper Discriminator BaseLine Restorer (ASDBLR) and Drift Time Measuring Read Out Chip

(DTMROC). They are sampling the analog signal created in the wire and producing the digital time measurement that is sent to off-detector electronics for processing. The back-end electronics is in charge of gathering in a Readout Driver (ROD) the data from many channels, compressing, formatting and sending them to the Readout Buffer.

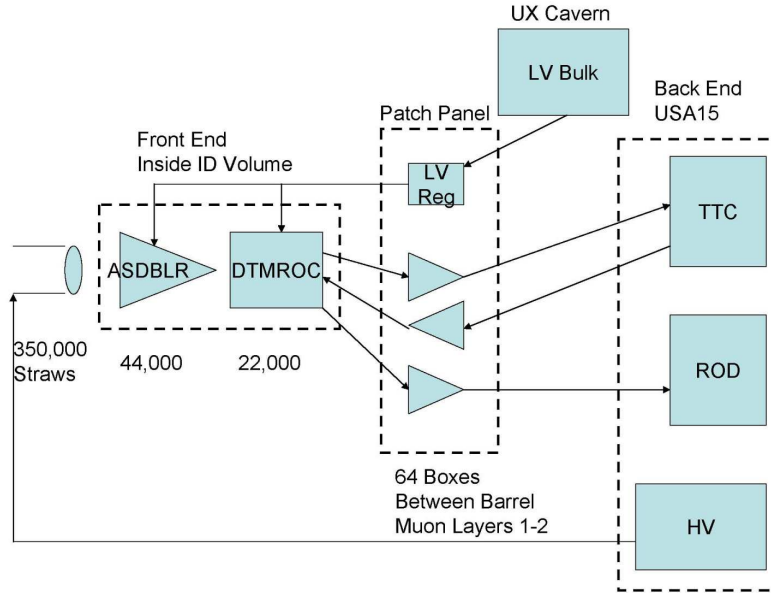


Figure 2.19: Schematic diagram of the TRT front-end electronics, back-end electronics, TTC and High-Voltage (HV) [33].

The ASDBLR is a full-custom, analogue, bipolar ASIC (Application Specific Integrated Circuit) fabricated in a 6.17×7.78 mm silicon substrate using a BiCMOS DMILL radiation-hard process. This ASIC provides the complete analog signal processing chain (see Figure 2.21) for eight straws. The signal is first amplified with a low noise amplifier. Then, the signal is shaped, removing the long tail induced by slow ion drift allowing a high rate operation. The peaking time of the shaper is 7.5 ns and its width is 20 ns. These parameters were optimized to get the best compromise among signal-noise ratio, position resolution and double-pulse resolution [38]. Part of the signal produced in the wire propagates towards the front-end electronic, but the remaining fraction of the signal travels in the opposite direction until it is reflected at the end of the wire and is collected in the front-end electronics. Both parts of the signal are separated from each other by as much as 6 ns.

Finally, two thresholds are applied: a low threshold (LT) at 200-300 eV is used to detect electron avalanches produced by charged particles and provide tracking capabilities. A precise time measurement is needed to know the arrival time of the first electrons reaching the wire. These electrons are produced at the closest approach of the particle to the wire

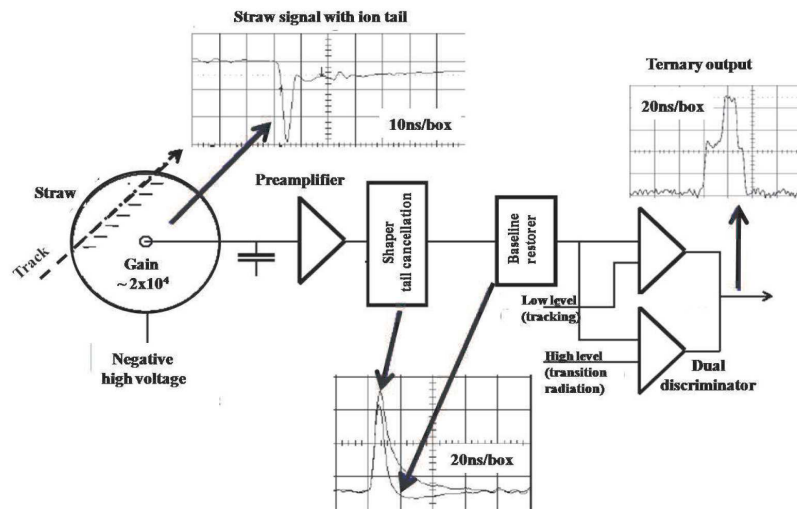


Figure 2.20: Schematic diagram of the TRT front-end ASDLBR electronics. The amplification, shaping, ion tail removal, the baseline restoration and the dual-threshold discrimination are presented together with the ternary output [33].

and the time measurement is directly related to the drift radius used for tracking. A second threshold, known as high threshold (HT), at 6-8 keV detects transition radiation photons produced by electrons. The output of the ASDBLR is a three-level differential current signal that is delivered to its companion chip: the DTMROC.

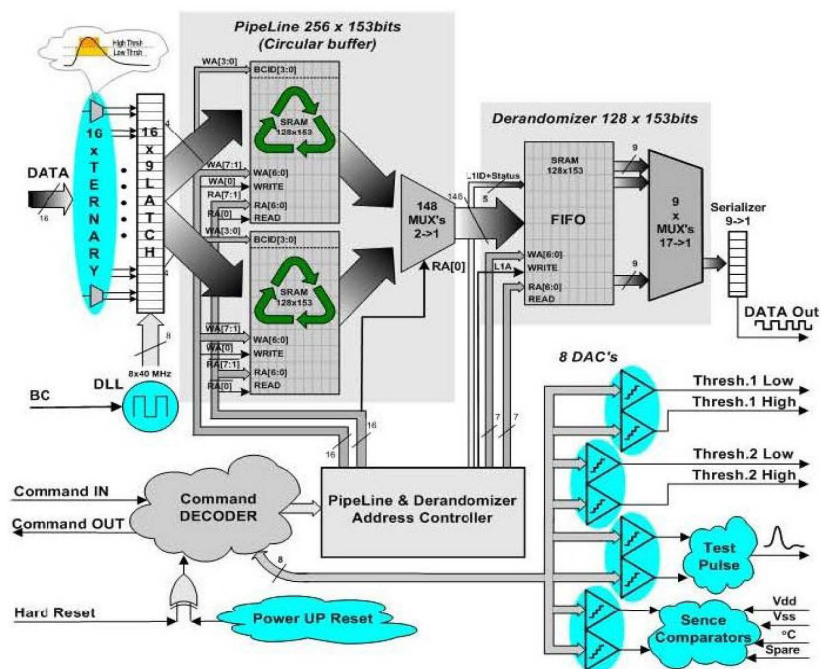


Figure 2.21: Schematic diagram of DTMROC electronics [33].

The DTMROC is a 16-channel ASIC fabricated with DSM technology, a CMOS method which is intrinsically radiation-hard. Each DTMROC controls and processes the time measurement for two ASDBLR returning a digitalized result of the straw measurement (Figure 2.20). It measures the timing information in bins of width 3.125 ns for the low-threshold to get a good position resolution. In total, 8 time bins are used for each bunch crossing (25ns). This information is stored in a pipeline that can store up to $6 \mu\text{s}$ (128 bunch crossings). In case a level-1 trigger signal is accepted, the timing information is extracted from the pipeline for the corresponding bunch crossing and together with the two next bunch crossings. In total, 75 ns are read-out, assuring enough time for the electrons to drift. The data are extracted in 24 bits for tracking, where each bit is a 3.15 ns time bin, and 3 bits are for high threshold information. This information is shipped to the back-end electronics and used in events for Level-2 trigger and in further processing. The DTMROC is also dealing with the communication with the rest of the detector through the TTC lines (Timing, Trigger and Control). Finally, it is giving support to the ASDBLR chips. It is setting the discriminator thresholds, that need to be calibrated to assure a low noise rates. Also, it includes a test pulse generator with programmable timing and amplitude to calibrate and test the ASDBLR.

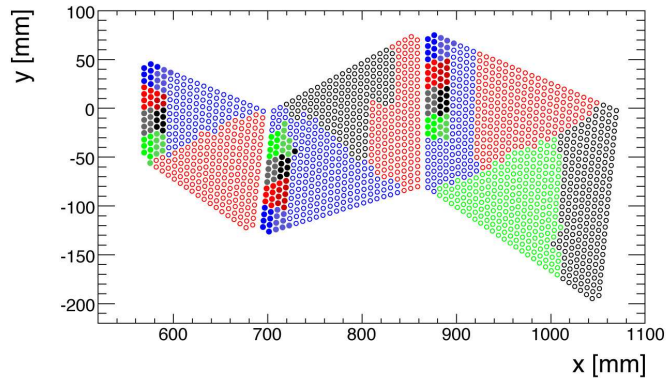


Figure 2.22: Position of straws for one barrel phi sector. Same color open circles are for straws that belong to the same board (TTC line). In solid circles, the straws on four consecutive chips are shown [40].

In the TRT jargon, and as later used in this thesis, the expression *chip* [40] refers to a front-end board containing two ASDBLR and one DTMROC, reading out in total 16 straws. The DTMROC communicates with the rest of the TRT and ATLAS through the TTC lines. Elements under the same TTC line share the same timing and trigger controller, but differences between different TTC lines are expected. There are 9 TTC lines per phi sector in the barrel and 20 per phi stack in the barrel. An example of the straws associated to the same board for one barrel phi sector is presented in Figure 2.22 Each of this TTC lines is called logical board or more often just *board*. For timing calibration, time delays will have variations between different boards but are expected to be similar within groups of straws attached to the same TTC line.

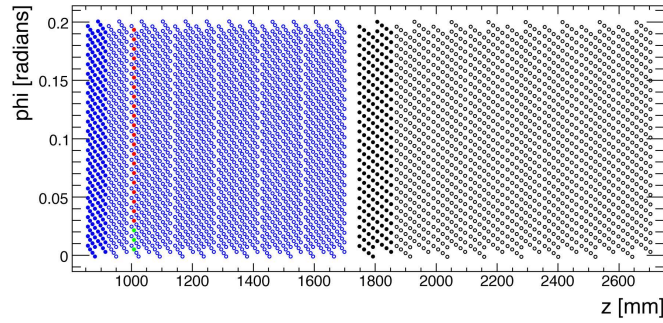


Figure 2.23: Position of straws for one end-cap phi sector. Two wheels are shown, for $z < 1750$ mm a type A wheel in blue and for $z > 1750$ a type B wheel in black. Straws on the first TTC line (board) for each wheel type are shown in solid circles [40].

Each straw needs a high voltage (HV) power supply (Figure 2.19). The TRT HV system delivers between 1.4 and 2.0 kV to each straw with a commercial multichannel HV power supply. Each of the channels delivers power to up to 192 straws. Wires in contact with the cathode can damage the straw wall. Also continuous discharges of the drift tube can damage the aluminum of the cathode, and in some cases produce a hole in the wall. To avoid this, straws not passing the stringent quality test for the drift tube production, such as wire offset below 0.3 mm, are not connected to the HV supply. In addition, to prevent the loss of great detector fraction for failure of a single straw, groups of eight straws are protected with a programmable fuse at the level of the detector.

2.2.5 Cooling

At high counting rates, the straws and their front-end chips need to be cooled down. Per straw, at peak luminosity, the total heat produced due to the energy deposited and the electron transport in the wire is 10-20 mW. The detector performance is sensitive to the temperature changes, so this heat needs to be removed to preserve the temperature in the detector. In addition, the temperature gradient along a straw should not exceed 10° . For this, the TRT straws are kept at 20° using CO_2 . The front-end chips are cooled down with C_6F_{14} to $16^\circ C$. In total, 4160 W need to be dissipated for the straws and 42240 W for the electronics.

The SCT, which is placed in the inside of the TRT, is cooled down to $-7^\circ C$ using nitrogen. The contamination of the drift gas with nitrogen has a significant influence in the drift velocity [34], for this reason, the nitrogen concentration has to be kept below 1%. If the radiators get contaminated by Xenon, the transition radiation photons will be absorbed before reaching the straw. To avoid both effects, the CO_2 used for cooling is also performing ventilation for the straws, keeping the Xenon fraction below 0.1% and the nitrogen below 1%.

Chapter 3

Calibration of the ATLAS Transition Radiation Tracker

As was discussed in the previous chapter, in order to get the best resolution and the best momentum reconstruction in the TRT, a good calibration is needed. The aim of this calibration is to estimate the distance of closest approach of the charged particle to each wire in the TRT. This distance is also called drift circle. Mainly two parameters are needed: the first one is the correction to the time measurement taking into account different propagation effects, known as T_0 . This parameter allows to get the drift time of the electrons produced in the cluster created at the closest approach to the wire. The second parameter is the relation between drift time and drift distance. This parameter is the drift velocity, more often called r - t relation.

The calibration process is an iterative method based on refitting the tracks modifying the T_0 and the r - t relation, until the best performance is obtained. For this reason, in the first section a brief introduction will be given to tracking and hit reconstruction, together with the figures to evaluate the quality of track fit to the measurement. In ATLAS, every run taken has to be calibrated within 24h, and the details about the procedure, the database system and the infrastructure to fulfill this requirement will be explained. The principles for calibration of T_0 and r - t relation will be detailed in the next section. A brief comment on the different methods applied during the data taking will be given. Once the calibration is explained, the results obtained for 2009 cosmic runs will be commented. The proton-proton results for 2010 and 2011 will come after, with few insights into heavy ions collisions performance. These results have been reported in [3]. The last section will be about optimization of the error definition for the drift circles, important for the track fitter algorithm to obtain the best track fits.

Other important property to understand the detector and to obtain the best tracking performance is the alignment, with respect to the SCT and Pixel, and also with respect to the different TRT elements. Large efforts have been done in this area since 2009, first with cosmic rays, then with proton-proton collisions. With cosmic data, a good alignment for the barrel was achieved. Collision data allowed to refine the barrel alignment and also to correct the end-caps. Currently, the whole TRT has been aligned to straw level and several systematic studies have been done. These corrections give significant

improvement in momentum resolution, especially in the end-caps. Documentation about the TRT alignment can be found in: [41], [42] and it is not further discussed in this thesis.

3.1 Tracking with the TRT

3.1.1 Introduction to tracking

In the ATLAS coordinate system, the z direction points anti-clock wise along the LHC accelerator ring. The x direction points to the centre of the accelerator and the y direction points upwards. The origin of coordinates is in the center of ATLAS, where the average interaction point is. The parametrization of a charged particle track is done using five parameters ($z_0, d_0, \theta, \phi, q/p$) at a reference point known as *perigee*. This point is defined as the closest approach of the track to the z axis. The z_0 is the distance to the origin of coordinates in the z direction, often called the longitudinal impact parameter. The transverse impact parameter, d_0 , is distance in the x - y plane to the beam axis. This parameter is signed, defined to be positive when the direction of the track is clockwise with respect to the origin. The polar angle is defined by the parameter θ and it is the angle with the z -axis. ϕ is the angle in the x - y plane, also called the azimuthal angle. q/p is the track curvature related with the momentum of the particle. This last parameter is set to 0 when a magnetic field is not applied. In Figure 3.1 an example of the different track parameters is shown.

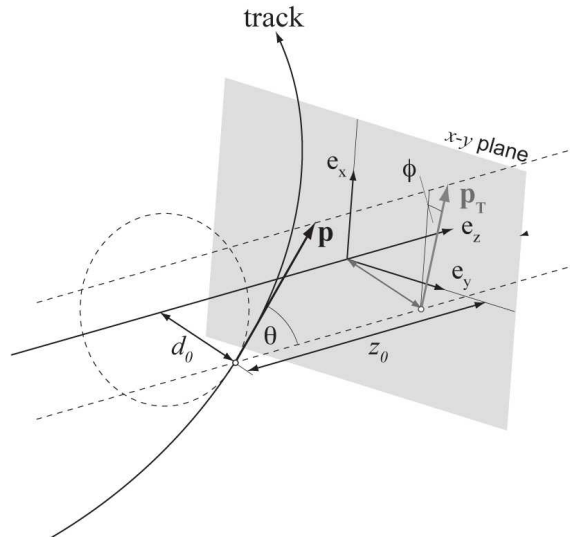


Figure 3.1: Track parameterization in the ATLAS Coordinate system [44].

For the Inner Detector, two main sequences for tracking are available: inside-to-outside and backtracking [43]. In the case of inside-to-outside, the track finding starts from seeds in

the inner layer of the pixel detector and candidate tracks are propagated to outer detection layers. This propagation is done also to the SCT layers and finally to the TRT straws. The backtracking starts looking for track segments in the TRT, that later are propagated to the SCT and Pixel.

The first step before applying tracking sequence itself is to translate the detector readout information to a position measurement and an error matrix. In the case of Pixel and SCT, neighbor hits are joined into clusters. The three dimension *spacepoint* positions of the final clusters are computed together with their errors [45]. For the TRT, the measured time is converted to drift radius with an error, details are given in Section 3.1.2. In this step, the alignment corrections are applied, modifying the final hit positions.

The ATLAS detector has different track fitters, which can be applied to the two used sequences. The most used algorithms are:

- Global χ^2 : The track fit is done minimizing a global χ^2 defined as:

$$\chi^2 = \frac{h_i - t_i}{\sigma_i} \quad (3.1)$$

Where h_i is the measurement position, t_i is the position predicted by the fitted track, and σ_i is the error of the measurement. This is a very robust fitting technique, where the minimization is performed by solving a set of linear equations through a matrix inversion [46].

- Kalman Filter: It is a progressive method that combines pattern recognition and track fitter. Starting from a seed, it propagates the measurement to the next detector plane. Hits close to the prediction are found and included in the new prediction. The weighted average of both estimations is done (filtered). The new prediction is added to the track and it is propagated to the next plane. This is repeated until the track candidate has crossed all detector planes. In this way, Kalman filter combines forward filtering with rejection of hits not compatible with the predictions [47].

In order to find tracks originating from the primary interaction point and also to obtain the tracks that allow to get the coordinates of the primary vertex, the inside-to-outside sequence is used. This starts by finding seeds in the Pixel and the SCT using combination of three dimensional space points. A *road* around the seed is done and all the clusters falling inside this road are collected. A track fit is performed and due to the large amount of track candidates, they are ranked by the ambiguity solver tool that assigns a score to each track depending on the number of hits and the quality of the fit as χ^2 divided by number of degrees of freedom. The tracks with best score are kept and extrapolated to the TRT. A road is created along the extrapolated track and if the TRT drift circles are inside the road, the hits are attached to the track. Finally, the extended tracks are fitted by the track fitter and a score is computed. If this new score is larger than the one produced by the ambiguity solver, the track is kept and replaces the old track. In case the score is lower, the extended track is removed. The minimum transverse momentum requirement is set to 100 MeV, but only tracks with transverse momentum over 500 MeV reach the TRT before bending back. Also, as this sequence is optimized for reconstructing tracks

produced in the primary vertex, a total of seven silicon hits are accepted with an impact parameter $|d_0| < 10$ mm.

The tracking is designed to correct for material interactions, such as for example multiple scattering. The material interaction is described in layers of scattering planes thickness of which represents the amount of material. The tracks are allowed to kink in these layers. There is one scattering plane for each Pixel and SCT layer. In the TRT, in total three scattering planes are modeled.

Tracks produced at secondary decay vertices, such as K_s^0 decays and photon decays to electron-positron pairs (photon conversions), may not have enough hits in the silicon layers to be found in the inside-to-outside sequence. In order to recover these kind of processes, the backtracking sequence was developed. Segments are found in the TRT applying a transformation of the TRT straw centers in projection planes ($r - \phi$ for barrel and $z - \phi$ for end-caps) into a parameter space of the initial azimuthal angle ϕ_0 and the inverse of the momentum q/p . In this new space, each single hit corresponds to a line. For hits that belong to the same track segment, all the lines in the new space cross in the same point, so the global track segment search is reduced to find the local maximum in a two-dimensional histogram. Once these segments are created, the drift time information is added and the segments are processed using a Kalman filter. Finally, the segments are propagated to the SCT and the Pixel detector, producing the final tracks.

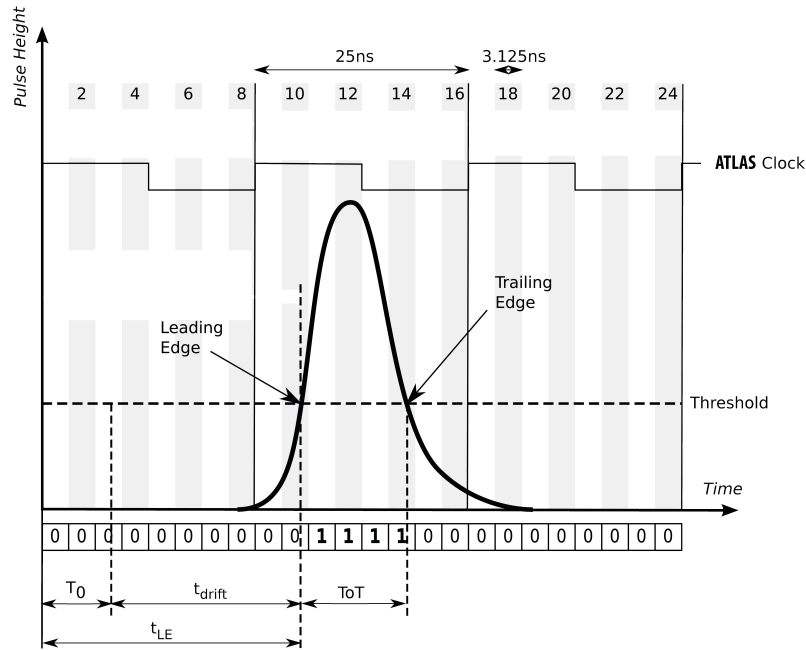


Figure 3.2: Example of a Low Threshold hit, showing the final bit pattern returned by the DTMROC after reading out 3 bunch crossings and how it is related to the Leading Edge t_{LE} , the Trailing Edge t_{TE} , the Time-over-Threshold t_{ToT} and the drift time t_{drift} .

3.1.2 The TRT Hits

The TRT readout returns 24 bits for the drift time information of three bunch crossings (75ns), as shown in Figure 3.2. The first transition from 0 to 1 is known as the Leading Edge (t_{LE}). This transition is related to the arrival time of the electrons produced in the cluster of closest approach to the wire. The transition for 1 to 0, known as the Trailing Edge (t_{TE}), is produced by electrons drifting from clusters produced far away from the wire, close to the straw wall ($\sim 2\text{mm}$). In principle, the Trailing Edge time is expected to be the same for all hits in the straw, independently of the minimum distance to the wire of the particle. However, due to the stochastic nature of the energy loss in the gas together the long tail produced by the ion drift, the distribution is wide with long tails. An example of Leading and Trailing Edge distributions is shown in Figure 3.3. The difference between Trailing and Leading Edge is the Time-over-Threshold ($t_{ToT} = t_{TE} - t_{LE}$). This parameter is related to the ionization power ($\frac{dE}{dx}$) of the charged particle in the gas and has been successfully used to separate electrons from heavier particles [48]. Hits with first bit equal to 1 are rejected to prevent the use of hits produced in previous bunch crossings. This bit information can be converted to time multiplying by the time bin width, 3.125 ns. In addition, three extra bits are available, containing the high threshold information.

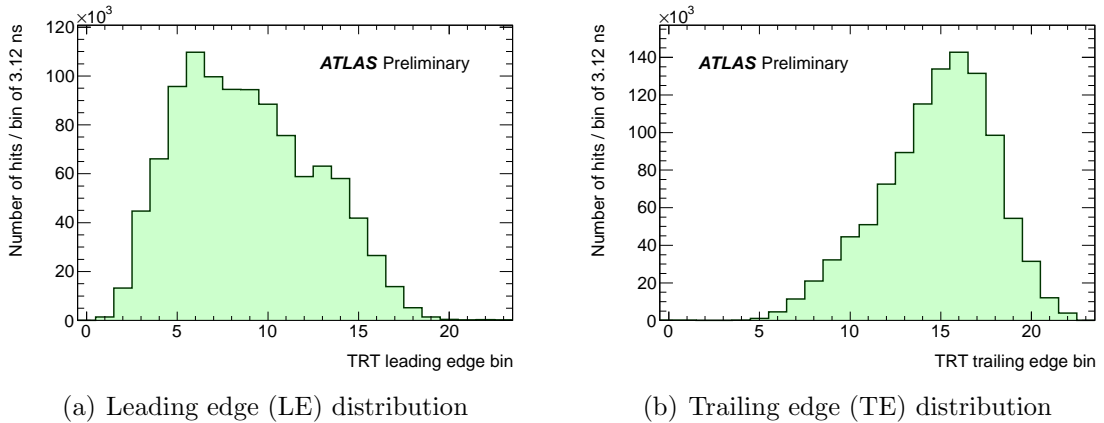


Figure 3.3: Leading Edge (3.3(a)) and Trailing Edge (3.3(b)) distribution for proton-proton collisions. Each bin in the x-axis corresponds to 3.125 ns.

To get the first electron drift time (t), several systematic effects have to be subtracted from the Leading Edge time:

$$t = t_{LE} - (t_{collision} + t_{ToF} + t_{SP}) \quad (3.2)$$

Where $t_{collision}$ is the time at which the proton-proton collision took place relative to the LHC clock, taken into account the TRT read-out window. The time-of-flight (t_{ToF}) is the time that the charged particle takes to travel from the interaction point to the straw. The signal propagation time (t_{SP}) is the time that the pulse takes to travel in the wire to the front-end electronics. The signal propagates in both directions of the wire, one reaching

directly the read out, while the other is reflected at the other end, arriving later to the read-out. The read-out is not able to distinguish both signals, so they are merged. Within small regions of the detector, all these timing corrections do not differ much, so they are taken into account in a single T_0 constant for each straw:

$$t = t_{LE} - T_0 \quad (3.3)$$

The calibration of the T_0 is detailed in later sections. Once the drift time is known (t), it can be translated to the drift radius (r) used in the track fitter, making use of the so called r - t relation ($r(t)$):

$$r = r(t) \quad (3.4)$$

The r - t relation is determined from data and fitted to a third degree polynomial. This, and its calibration, are described in later sections.

Other important parameters required by the track fitter are the drift circle uncertainties (δr_{hit}). This value is important to compute the χ^2 of the track. The uncertainty of the drift radius, due to the discrete number of clusters produced and the motion and amplification of the electrons, will depend on the drift radius. For large drift radius, the distance between clusters has low influence compared to the total drift length, while for particles traveling close to the wire, the distance between clusters increases significantly the uncertainty [35]. In Section 3.5, a method developed to optimize it is described.

The hits described up to now are known as *precision hits*, however, a second class of hits, the *tube hits*, are also used by the track fitter. For the tube hits, the timing information is not used, so the drift radius is assigned to 0 mm with an expected uncertainty of $\delta r_{hit} = d/\sqrt{12}$, where d is the wire diameter. This uncertainty is the standard deviation of a flat probability distribution for a hit produced by a track within a $d = 4$ mm diameter straw. The tube hits are used in the first stage of the tracking, when the pattern recognition is used to find hits that belong to a track. Once they are found, the hits are converted to precision hits and refitted. Due to the noise, the properties of the electron production and the drifting, possible mis-calibration and mis-alignments, some of the hits do not belong to the track or may have wrong timing measurement. For this reason, the track fitter is allowed to convert precision to tube hits and vice-versa in each iteration. The criterion for the conversion is the distance between the fitted track and the drift radius. If it is larger than 2.5 times the drift circle uncertainty, the hit is converted to tube hit. It is important to keep all the hits in the track, but making sure that they do not over-constrain the track, reducing the quality of the fit. At the end of the tracking process, around 88 % of the hits on track are precision measurements.

The track fitter, to prevent ambiguities in the final track, assigns a sign to the drift radius r . The sign is defined similarly as for the d_0 : positive when the direction of the track is clockwise with respect to the origin, otherwise negative. This drift radius sign can be updated during the tracking iterations to improve the final fit quality.

3.1.3 Figures of merit

The ATLAS Inner Detector tracking system has been designed to optimize the momentum and impact parameters (z_0 and d_0) resolution of tracks produced by charged particles. The

motion of a particle moving in a homogenous magnetic field can be described by an helix, in which the radius of curvature is related to the momentum in the transverse plane to the magnetic field by:

$$\rho = \frac{p_T}{0.3B} \quad (3.5)$$

where ρ is the radius of curvature, B is the magnetic field and p_T is the transverse momentum of the charged particle. The momentum resolution can be related to the detector properties by [18] [49]:

$$\frac{\delta p}{p^2} = \frac{\sigma}{0.3BL^2} \sqrt{4C_N} \quad (3.6)$$

where σ is the spatial resolution of the detector, L is the length of the trajectory measured and C_N is given by:

$$C_N = \frac{180N^3}{(N-1)(N+1)(N+2)(N+3)} \quad (3.7)$$

where N is the number of hits on track.

As we can see in Equation 3.6, while the magnetic field, the maximum number of hits in the track and the length of the track measured are fixed by the detector design, the detector resolution depends on how good the calibration and the alignment are. For this reason, the goal of the calibration is to get the best detector spatial resolution and this will be reflected in the final momentum resolution. Also, when the quality of the calibration and the alignment is improved, the number of precision hits included in the track increases.

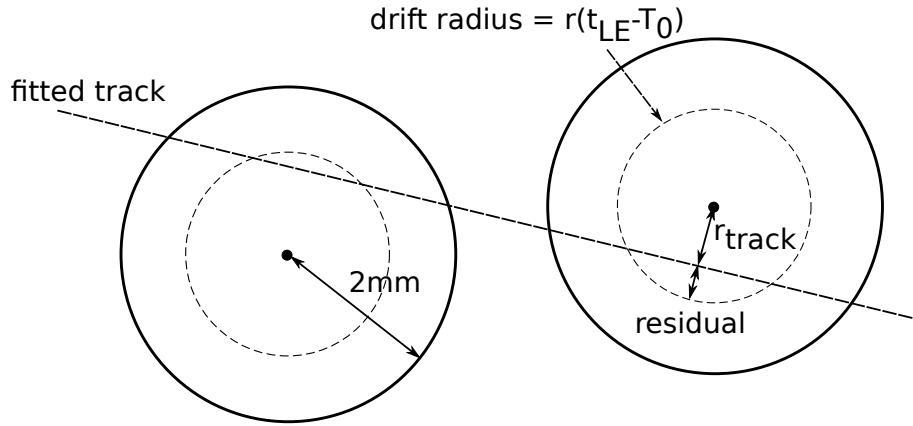


Figure 3.4: Two straws (solid circles) and their drift circles (dashed circles) together with the track fitted to them are shown. The distance of the track to the wire is also shown (r_{track}) and the residual, $r - r_{track}$.

After the tracking is done, the distance between the track and the center of the straw can be obtained. This is known as track-to-wire distance (r_{track}). This radius can be converted to the track drift time (t_{track}) using the inverse of the $r-t$ relation:

$$t_{track} = r^{-1}(r_{track}) \quad (3.8)$$

Making use of this track information and comparing with the hit information, three figures of merit are built to study the detector performance:

- Position residual, often referred to just as residual. It is defined as:

$$\Delta r = r - r_{track} \quad (3.9)$$

An example of this distribution for barrel straws can be seen in Figure 3.4. The width of this distribution is the detector resolution. The mean of the distribution has to be centered at 0 mm because the residual is expected to be symmetric due to the sign of the drift radius. This symmetry makes the position residual mean not sensitive to miscalibration, but it is sensitive to misalignments. The final hit position residual is not a perfect gaussian, due in part to the presence of tube hits. For this reason, the evaluation of the resolution is done fitting the residual distribution to a Gaussian distribution in the range $\pm 1.5 \cdot \sigma_r$ where σ_r is the width returned by the fit. This fit has to be done iteratively. The final position resolution is σ_r , which is sensitive to both misalignments and miscalibrations, and is the variable to be minimized by the calibration procedure.

- Time residual; it is defined as:

$$\Delta t = t - t_{track} = t_{LE} - t_0 - t_{track} \quad (3.10)$$

This distribution is very asymmetric, due to cluster production and electron drift properties in gases. Similarly as for the spatial residual, it is fitted by a gaussian in range $\pm 1.0 \cdot \sigma_t$. The mean of the fitted gaussian (μ_t) is directly related with the quality of the detector timing. In order to minimize the spatial residual, the time residual mean has to be close to 0. Similarly, the time residual width (σ_t) is also related with the r - t relation and final resolution.

- Absolute position residual; defined as:

$$\Delta|r| = |r_{track}| - |r| \quad (3.11)$$

The absolute values are used to remove the symmetry produced by the sign assignment of the radius making it sensitive to miscalibration. The peak of this distribution is also fitted to a gaussian in the range $\pm 1.0 \cdot \sigma_{|r|}$. If the mean ($\mu_{|r|}$) is different from 0 mm, it reflects a systematic offset between the drift radius and the track distance to wire that can be produced by wrong r - t or T_0 calibration.

These three variables are studied in detail depending on different variables, such as drift time for r - t calibration or for different TRT regions, such as barrel and end-caps.

For performing the evaluation of the different residuals, the *unbias* method is used. In this method the hit for which we want to evaluate the residual is removed from the track and the track is refitted without using the information of this hit. This *unbias* residual is larger than the *bias* residual, where the hit information is taken into account, but it is more robust against alignment or calibration issues. A comparison between both methods, for the different figures of merit is shown in Figure 3.5. All the residuals quoted in this work are based on *unbias* estimation if no comment is given.

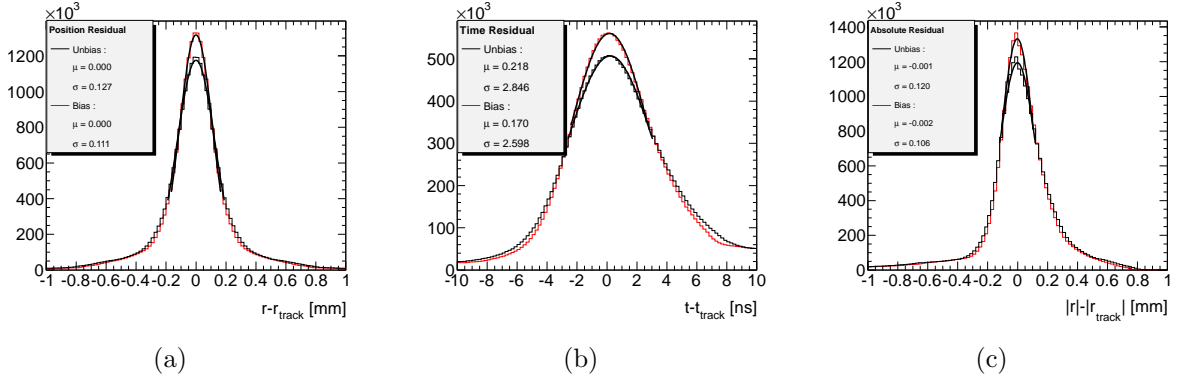


Figure 3.5: Example of position residual (3.5(a)), time residual (3.5(b)) and absolute position residual (3.5(c)) for unbiased (black) and bias (red) calculation. The distributions are fitted to a Gaussian distribution and the mean (μ) and width (σ) are shown for the different distributions. These figures correspond to proton-proton collisions data collected during spring 2011.

3.2 Calibration principles

The main goal of the TRT calibration is to provide the best estimate for the track to wire distance for each measured leading edge. To get this, an iterative method has been developed. Starting from the initial conditions, which are in principle the best knowledge of the detector at the time, the tracks are reconstructed, and the different residuals are evaluated in different detector regions. If these distributions are not optimal, or a decrease in the performance is observed, a new set of T_0 constants and $r-t$ relations are computed using the methods explained later in this section. This new calibration is used to perform again the full reconstruction, and the performance of the new constants is evaluated in terms of residuals. These steps are repeated until no change in the calibration constants is observed, leading to the best resolution of the TRT. The studies performed in Monte Carlo, collision and cosmic data show that the method presented here converges in less than 10 iterations even starting from completely wrong T_0 values and $r-t$ relations. For every day calibration, just one or two iterations are enough to correct for the small changes between runs.

3.2.1 T_0 calibration

As we have seen, the T_0 constants are needed to get the electron drift time, removing the different timing effects due to clock propagation, signal traveling in wires, electronic delays and the time of flight of the particle. The time residuals defined in Equation 3.10 are computed for different detector elements with same T_0 constants and fitted with a Gaussian distribution of mean μ and width σ . Making use of this mean, the T_0 calibration constants are updated according to:

$$T_0^i = T_0^{i-1} + \mu^i - \tilde{\mu} \quad (3.12)$$

Index i is the iteration number and $\tilde{\mu}$ is an offset applied to compensate p_T dependence and other effects. Details on how the offsets are computed are presented in [3]. For proton-proton collisions, the same offset is used for the whole TRT and it is set to 0.5 ns. More details are given later in this chapter. This value is optimized to provide the best position residual for tracks with p_T over 2 GeV while in the calibration, tracks over 1 GeV are used.

3.2.2 r-t calibration

The r - t relation is defined as a third degree polynomial with boundaries for large and short drift times, which relates the drift time measurement t to the drift radius r :

$$r(t) = \left\{ \begin{array}{ll} 0; & f(t) < 0mm \\ f(t); & 0 < f(t) < 2mm \\ 2; & f(t) > 2mm \end{array} \right\} \quad (3.13)$$

where

$$f(t) = a_0 + a_1t + a_2t^2 + a_3t^3 \quad (3.14)$$

This polynomial description is chosen as a simple function that describes well the dependence, with only four parameters to be calibrated. Yet other possible parameterizations have been studied, but they do not produce better performance. Other parameterizations based on the electron drift properties are currently under study, but these methods will not be described here.

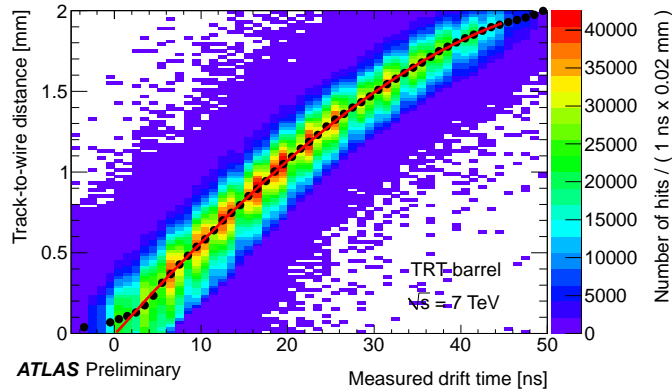


Figure 3.6: r - t relation for the TRT barrel. The points show the peak position of the fit to the track to wire distance distributions in slices of measured drift time (binning in t). The line shows a third degree polynomial fitted to the points. This line corresponds to $f(t)$ in Equation 3.14 and it is used to determine the drift distance depending on the measured time.

The finite number of primary ionization clusters produced in the track path inside the straw, together with the magnetic field and the diffusion effects, makes the path distance for the drift of the closest primary electrons longer than the distance of closest approach between the charged particle and the wire. The drift radius r has to be the best estimate of the track to wire distance r_{track} for a given drift time t .

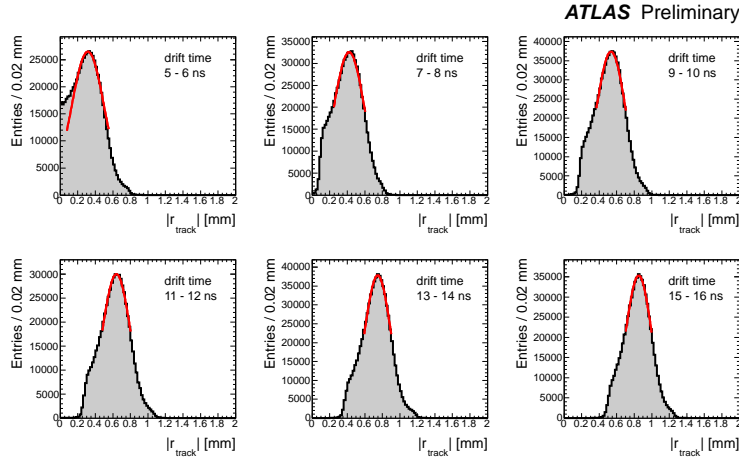


Figure 3.7: The track to wire distances distributions for a selected number of measured drift times for barrel hits are shown. The red lines correspond to the Gaussian fit performed to extract the mean.

For the r - t calibration, the expected agreement between the drift radius r and the track to wire distance r_{track} obtained by the track fitter is used. The track to wire distances are accumulated for different drift times as shown in the two-dimensional histogram in Figure 3.6. In the figure, the x-axis corresponds to different time bins 1 ns wide, while the y-axis is the absolute value of r_{track} of 20 μm width. The absolute value is used to remove the sign dependence, because r - t relation does not depend on it and no difference is expected between positive and negative drift radius. As can be seen, the r - t has an intrinsic width, due the detector finite resolution. To obtain the r - t relation describing the most probable track to wire distance, the two-dimensional histogram is sliced in drift time bins, in the procedure called t-slicing. The peak of the distribution in each slice is fitted to a Gaussian distribution as shown in Figure 3.7. The means of the fitted functions are extracted and their dependence with respect to the different time bins is provided in Figure 3.6 as black circles. Finally, these points are fitted by the third degree polynomial, which describe the new r - t relation as shown in Equation 3.14. This fit is given in the figure by the red smooth line. We can see how the third degree polynomial describes very well the drift distances for almost all the measured drift times, however, for low time values ($t \sim 0$ ns), the r - t relation cannot describe the means of the time bin slices because, as the absolute track to wire distance is used, the means are always positive.

There is an interplay between a global shift of the T_0 constants and shift of the r - t relation along the time axis that can turn the calibration unstable. The polynomial from Equation 3.14 can be re-written to make this dependence explicit:

$$f(t) = a'_1(t - a'_0) + a'_2(t - a'_0)^2 + a'_3(t - a'_0)^3 \quad (3.15)$$

The shape for this parameterization is the same as Equation 3.14. We can see how the offsets in the T_0 constants will lead to a change in the a'_0 parameter. This makes calibration to apply twice the same timing correction when doing r - t and T_0 calibration at the same

time, increasing the number of iterations needed before converging. In order to solve this ambiguity, one point of the r - t relation is fixed.

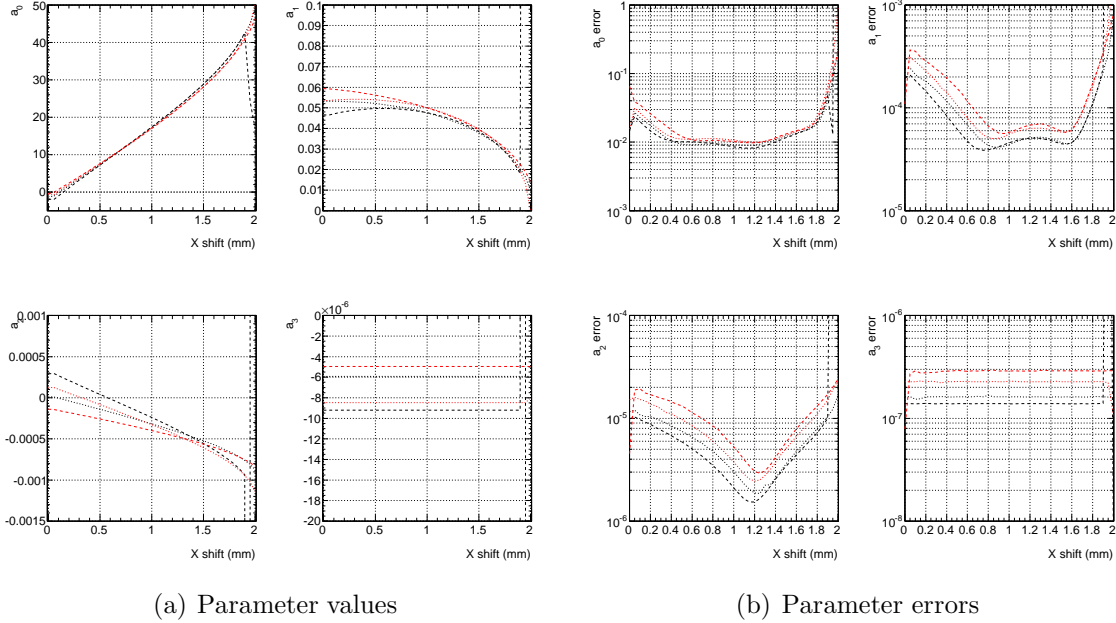


Figure 3.8: The parameters for the r - t fit depending on the X value to be fixed are shown in Figure 3.8(a). In Figure 3.8(b), the errors of these parameters returned by the fit are presented.

Making use of this other parameterization:

$$f(t) = a'_1(t - a'_0) + a'_2(t - a'_0)^2 + a'_3(t - a'_0)^3 + X \quad (3.16)$$

where X is the track to wire distance point to be fixed, the quality of the fit can be studied for different X values. The value of a'_0 corresponds to the drift time at which the drift radius is equal to X . The evolution of these parameters and their errors depending on the X point to keep fixed can be found in Figures 3.8(a) and 3.8(b) respectively. For large values of track to wire distance, the number of events is lower and the r - t relation is truncated, so larger errors for the parameters are obtained. In the case of drift radius close to the wire, the fit quality is poor, due to the absolute value of the track to wire distance used, so the uncertainty in the parameters is larger. The middle region of the straw ($r \sim 1$ mm) returns the lowest errors, thanks to the good quality of the fit.

In addition to the parameter errors, the correlations between the different parameters are presented in Figure 3.9. Large correlations are seen, which makes it difficult to choose the X point to fix. A good compromise between correlations, uncertainties and clarity for implementation is given by drift radius fixed at 1 mm. The final choice is to keep fixed $f(t = 18 \text{ ns}) = 1 \text{ mm}$, which gives for magnetic field on runs: $f(t = 0) \sim 0$.

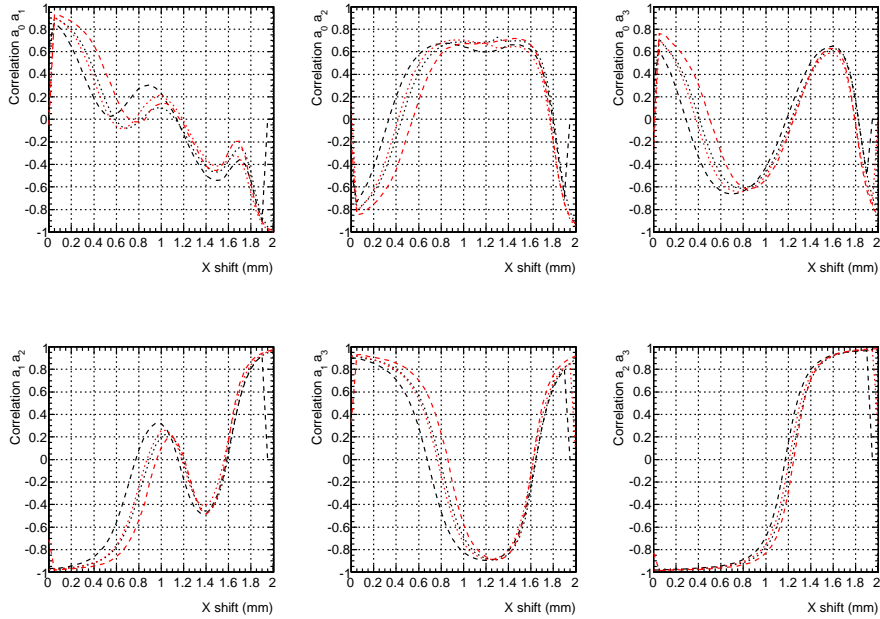


Figure 3.9: Correlation of the r - t parameters in Equation 3.16 depending on the X point to keep fixed.

The method explained until now is the current and up to date r - t calibration used by the TRT. This method is the result of several developments during the 2010-2011 data taking. For completeness, some details on the previous method will be given, mainly used for cosmic rays data taken before Spring 2010. Before this date, the r - t relation was not fixed in a point, thus the T_0 and r - t calibration could not be performed simultaneously needing more iterations before convergence.

In addition, during the initial commissioning, instead of using the current t-slicing, the slicing was done in track to wire distances (r slicing). For each track to wire bin in Figure 3.6, the drift time distribution was fitted to a Gaussian and the peak was extracted. This slicing was used because the drift time distributions are more gaussian-like and they do not have the issues seen for low (~ 0 mm) and high (~ 2 mm) drift distances. However, the reconstruction performance was shown to be degraded by this slicing method.

The use of the t-slicing is preferred by the track fitter because this provides the best estimate of a track to wire distance for a given drift time, while the r binning provides the best drift time estimate for a given drift distance. This was confirmed by the TRT resolution, which improves by $\sim 7 \mu\text{m}$ in the barrel and $\sim 10 \mu\text{m}$ in the end-caps when using the t-slicing instead of the r -slicing. For this reason the t-slicing was decided to be the default calibration method.

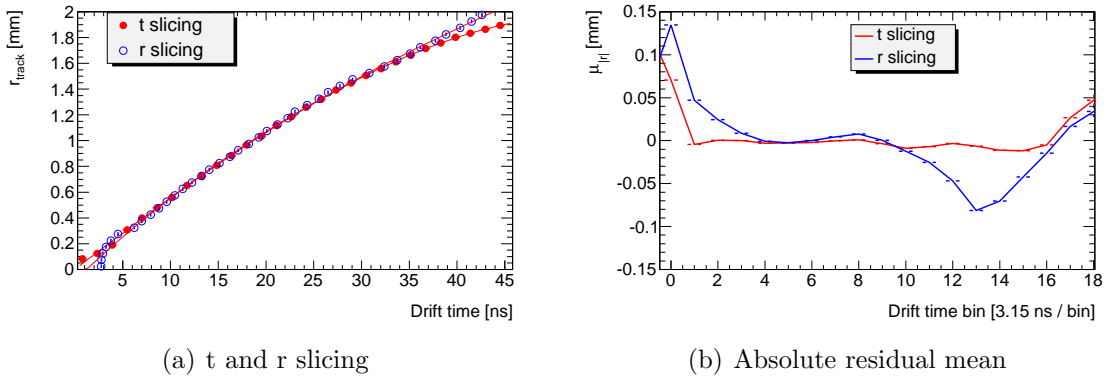


Figure 3.10: The same data has been calibrated using the t and the r slicing. The final r - t relations are presented on the left side, while the distribution of mean absolute residual for different drift time bins is shown on the right side.

3.2.3 Granularity of the calibration

To get a good quality in the r - t relation calibration, a minimum number of 10.000 hits are needed. In the case of the T_0 calibration, the time residual has to have at least 500 hits to get a proper fit. The barrel has in total 105088 readout channels, while each end-cap has 122880. Assuming 30 hits in each reconstructed track, around 6 M tracks with p_T larger than 500 GeV are needed to fully calibrate the TRT. This is a very conservative number because a complete isotropy for the produced tracks is assumed. This amount of tracks is too large to be reached for cosmic data. and for collision data it requires large computing power. For this reason, the TRT calibration can be performed at different detector granularities.

The possible calibration levels, ordered in decreasing number of straws are:

1. Whole TRT: At this level, information for r - t and T_0 are accumulated together for all straws.
2. Subdetector: The barrel is divided in two, side A for straws with the read-out electronics at $z > 0$ mm, and side C for straws at $z < 0$ mm. Similar definition is used for the side A and C end-caps.
3. Layer or wheel: Each side of the barrel is divided into 3 layers, depending on the distance to the beam axis. The end-caps are divided into 14 wheels.
4. ϕ Sector: Each end-cap and each barrel side are divided into 32 sectors.
5. Board: For each ϕ sector in the barrel there are 9 boards or TTC lines. In each end-cap ϕ sector there are 9 boards.
6. Chip: Corresponds to every DTMROC in the TRT, each of them connected typically to 16 straws.

7. Straw: This is the smallest unit, where residual and time residual are stored for each single straw.

These levels are defined following the mechanical structure and electronic signal propagation of the TRT.

The r - t relation is performed at subdetector level. As has been shown, the magnetic field orientation and strength with respect to the electron drift direction are very different between barrel and end-caps. With just four r - t relations, the TRT is fully described with a good accuracy due to the homogeneity of the gas and the relatively low variation of field strength. Results for lower granularity calibration will be shown later.

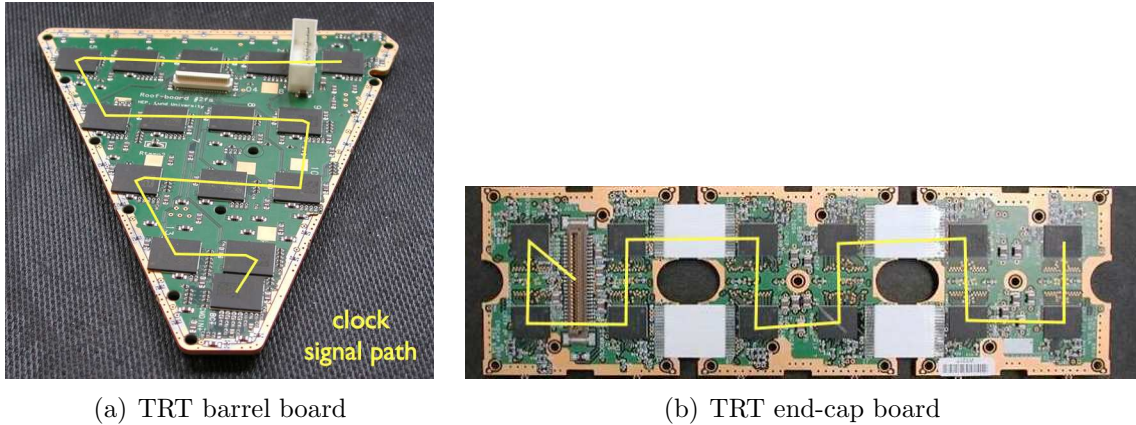


Figure 3.11: Figures showing boards forming a TTC group for a barrel element with 15 DTMROCs (3.11(a)) and end-cap board with 12 DTMROCs (3.11(b)). The line illustrates the clock propagation within the TTC group from one DTMROC to the next.

The T_0 calibration for collisions is done at chip level because all the straws belonging to the same DTMROC are expected to have the same time delays. In each board, the ATLAS clock signal is sent sequentially to all chips, thus reaching them with an increasing delay. An example on how the clock signal propagates for the different DTMROCs is shown in Figure 3.11. This produces a systematic variation of the T_0 values in the range ± 3 ns which can be used when the amount of data is not enough to calibrate at chip level. This systematic shifts have been extensively used for cosmic data. The differences between chips in the same board are not expected to change, for this reason, the calibration is designed to preserve the systematic differences included in the T_0 constants in use. In case of the number of hits at chip level are not enough to perform the calibration, the time residual of the upper level with enough statistics is used to correct the T_0 of the chip. This allows to correct global timing changes without distorting the T_0 differences between elements.

3.2.4 24h Calibration ATLAS policy

The T_0 constants and the r - t relations are stored in the so-called ATLAS Conditions Database. This is implemented in an ORACLE server [53] that allows to store the TRT

calibration constants, among several other conditions, at straw by straw level. The Conditions Database is needed for data reconstruction and it is replicated in several sites around the world. In order to save storage space, the T_0 constants are stored with a resolution of 0.25 ns. This value is small enough to not influence the final resolution. The $r-t$ can be stored also at straw level, and only the four parameters of the polynomial are stored with *float* precision. Just for historical reasons, the drift velocity can be also stored as a set of points and the values between points are linearly interpolated. This method uses more space on disk and memory, and has not shown better performance to justify its use.

Each ATLAS subdetector has to provide the best conditions for each run just 24/36^I hours after the data taking is over [51] [54]. At full luminosity, calibration of the whole run is not feasible within these time limits due to CPU limitations. The approach used is to select samples of events accepted by different triggers for physic processes of interest, and store them in the so-called Express Stream (ES) [52]. The selection rate is fixed to be ~ 10 Hz. Once the run data-taking is finished, the Express Stream is available for monitoring and calibration. The data in this stream have to be fully calibrated within the designated time and in case changes in the T_0 constants or the $r-t$ relations are observed, the new constants have to be uploaded to the Database. After that, the reconstruction of all the events in all the streams is launched, assuming the best knowledge is included in the Conditions Database.

The TRT Calibration requires extensive computing power to perform full reconstruction of the Express Stream in the different iterations. In the early stage, 64 CPUs were dedicated for TRT Calibration. These computers are now used for the performance studies and calibration improvements, while the calibration is automatically run at Tier0 (Computing facility at CERN)^{II}. This system allows to submit the calibration to the Tier0 without human intervention as soon as the run is finished, reporting the results in the Calibration Web Display [55]. This web tool was developed to monitor the calibration. and in case a change in T_0 or $r-t$ constants is observed, perform the upload to the Conditions Database.

3.3 Cosmic Results

In 2007, the installation of the end-caps was done, completing the TRT installation. Since then the Inner Detector achieved few cosmic milestones, until in 2009 the Combined Cosmic Runs started. These runs were very useful to prepare the different systems towards proton-proton collisions, for operation, alignment and calibration. In this section the calibration performed during 2008-2009 using cosmic rays is detailed.

During this time, in order to enhance the number of accepted events in the TRT, a specialized Level 1 was developed and started to be deployed at the end of 2008. This trigger shows a rate of 8.6 Hz on Inner Detector tracks with a track purity around 98 % [56], values that improve the rate and the purity of all previously L1 cosmic triggers used. The TRT trigger is also called *TRT cosmic trigger* or *fast OR* trigger.

^IThe maximum time has been different between different run periods.

^{II}The latest implementation was done by Anthony Hawking (Lund University).

The TRT L1 trigger counts the number of High Threshold (HT) hits and applies a fast hardware logic to select events with a certain number of selected hits in close-by regions. For the trigger setting, the High Threshold is set at lower value than the default collision threshold, such that the normal hits not produced by electrons also exceed the threshold. For this reason it is not possible to use the TRT for particle identification if the level 1 trigger capabilities are used. The HT is still larger than the Low Threshold, and the noise is largely suppressed.

Most of the cosmic rays arriving to the ATLAS detector are coming downwards. This property makes it possible to reconstruct the tracks in the barrel with good precision, projecting the tracks in the $x - y$ plane. However, for the end-caps, due to the radial arrangement of the straws and the projection in the $z - \phi$ plane, the number of hits on a cosmic track is much lower than for the barrel. This increases the timing uncertainty, which makes such tracks useless from the point of view of calibration. For this reason, this section is focused on barrel calibration. In order to get data with good quality, the selected events for calibration must have at least one track with 40 or more hits on track.

3.3.1 Event phase

In proton-proton collisions, the initial time or collision time at which the primary particles are produced is well known for all events and is given by the LHC clock. In cosmic events, the particles can come at any time, so the arrival time of the particles to the detector is unknown. A variable known as event phase T_{TRT} [57] is computed for each event to measure the time at which the cosmic ray passes through the detector with respect to the readout window. This new time correction is the event start time, and the drift time for cosmic rays is given as:

$$t = t_{LE} - T_0 - T_{TRT} \quad (3.17)$$

This starting time can be computed from the measured hits. First, the pattern recognition is applied getting hits associated to tracks. Each track is fitted to the hits without using the timing information, just the center of the wire and large hit uncertainty as done in the case of tube hits. Once the track is fitted, the drift time of the hits on track is computed and the average time residual for all the hits is computed, providing the event phase:

$$T_{TRT} = \langle t_{LE} - T_0 - T_{DT} \rangle_{track} \quad (3.18)$$

where T_{DT} is the drift time of the closest approach of the track to the wire provided by the track fitter making use of the $r-t$ relation. The last step of the tracking is to use the computed event phase to obtain the drift time from 3.17 and refit the track with the corrected drift circles.

From Equation 3.18 it is possible to see that a global shift of the T_0 values will be compensated by an opposite shift in the event phase. In order to avoid this effect, possible problems in calibration and make sure the constants converge, the event phase is computed as:

$$T_{TRT} = \langle t_{LE} - T_0 - T_{DT} + A \rangle_{track} \quad (3.19)$$

where A is a constant given by:

$$A = \langle T_0 \rangle_{barrel} - 20\text{ns} \quad (3.20)$$

here $\langle T_0 \rangle_{barrel}$ is the average T_0 of all straws in the barrel region.

In case multiple tracks are reconstructed, the track with larger number of hits is used to compute the event phase. In events with more than one track, most of the times the tracks are produced in the same cosmic shower, having a common starting time. The probability to have two or more independent cosmic rays in the same time window (75 ns) is negligible compared to the trigger rate (~ 10 Hz).

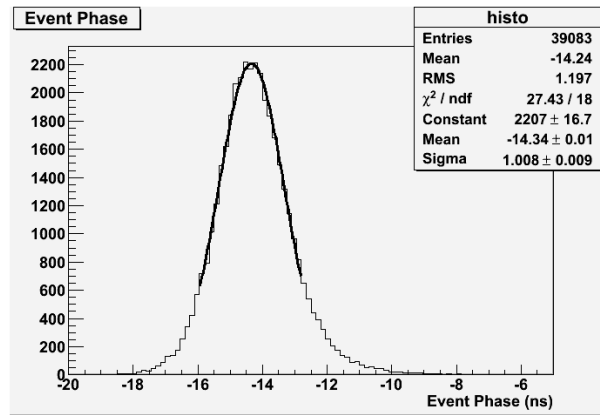


Figure 3.12: Event phase distribution measured in Monte Carlo cosmic rays. The distribution is fitted with a Gaussian function.

Several studies have been performed to analyze the event phase performance. In the Monte Carlo simulations, the same event phase is used for all the events. In Figure 3.12, the event phase distribution for a simulated sample of cosmic muons is shown. The distribution is fitted to a gaussian function giving a width of 1.01 ± 0.01 ns. In data, the event phase resolution is estimated by splitting tracks along the horizontal plane and computing the event phase for the two segments separately. Comparing the event phase for the top and bottom segments and fitting the distribution to a gaussian function, the event phase resolution for data is found to be: 0.97 ± 0.01 ns [57]. Doing a rough approximation for the average drift velocity of electrons moving in Xenon of $50 \mu\text{m}/\text{ns}$, the event phase resolution increases the resolution by $\sim 50 \mu\text{m}$, which have to be added in quadrature to the design resolution.

3.3.2 T_0 calibration

In cosmic runs, due to the relatively low statistics available, the calibration is performed at board (TTC line) level and chip corrections are applied later on. In Figure 3.13 the board T_0 values are shown. The figures show the board coordinate in the $x - y$ plane and their

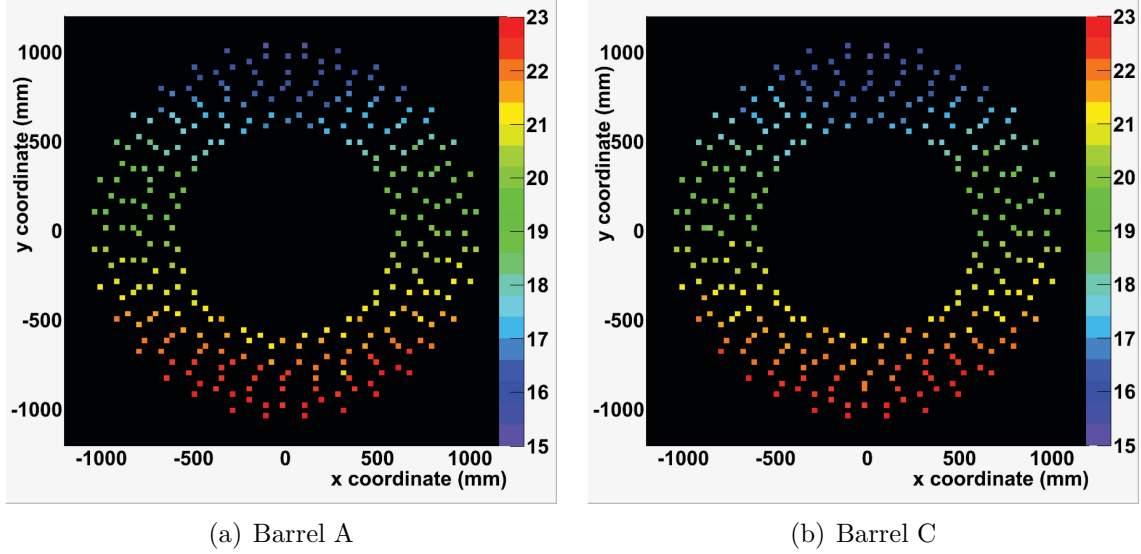


Figure 3.13: Board T_0 values shown at the board position projected in the x – y plane (transverse to beam pipe) for Barrel A: (3.13(a)) and Barrel C (3.13(b)).

T_0 constants for barrel A and C separately. The x and y axes are the standard ATLAS coordinates.

Assuming a particle traveling at the speed of light, a cosmic muon takes ~ 6.7 ns to cross from top to down the TRT, which is around two meters in diameter. In addition to the different electronic delays, this time of flight effect is the dominant correction to be taken into account by the T_0 values. As presented in Figure 3.13, the maximum difference between T_0 constants in the lower and upper region is around 8 ns, compensating the expected time of flight. Those T_0 constants are not optimal for tracks with other geometries, such as muons coming upwards, but the number of such events has been found to be negligible, so no special treatment for such cosmic rays is applied.

Chip corrections

With the deployment of the Level 1 Fast-OR trigger, the rate of collected events increased greatly. The amount of accumulated cosmic events allowed to calibrate the TRT at chip level. However, not for all runs the number of events was enough. For this reason, a detailed study of the timing correction needed for each chip inside a board was done. These systematic timing delays within boards are known as chip corrections. When the number of events in the run does not allow to calibrate at chip level, the calibration is done at board level and the chip corrections are applied to the board constants.

The chip correction has been measured using the hardware fine delay scans [58] and the dependence has been shown to be the same for all the boards of the same kind in different ϕ sectors. The T_0 constants have been calibrated at chip level and the chip corrections after doing the average over all ϕ sectors are presented in Figure 3.14. In this figure, the hardware fine delay scans are also included. The same dependence is found between both

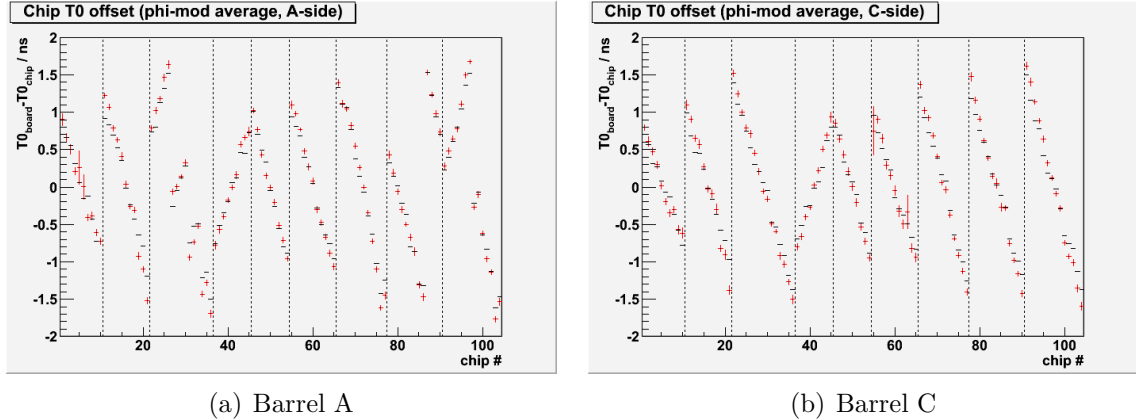


Figure 3.14: Comparison of chip fine delays measurements [58] in black and T_0 offline calibration constants in red for Barrel A: (3.14(a)) and Barrel C (3.14(b)). The dashed lines separate different boards. Same dependence for both methods is found.

methods with small systematic difference between them. The correction obtained by the T_0 calibration is used as default chip correction and it has been monitored during different cosmic run periods without significant changes.

During operation, the T_0 values were very stable. Since 2009, the calibration has been performed on a 24 hours basis. There were few reasons to perform an update of the constants used for reconstruction, such as the change of some hardware due to electronic problems, the change in the electronic delays or the switch between field on and off.

3.3.3 Barrel r - t calibration

During the data taking of 2008 and 2009, the r - t relation calibration was performed using the so-called r -binning explained in Section 3.2.2. The r - t relations for the two TRT gas mixtures, Xenon and Argon based, and for solenoid on and off, are shown in Figure 3.15. The larger collecting time is for the Xenon mixture with field on (Figure 3.15(a)). If the solenoid field is off, the drift of the electrons follows almost a straight line, taking less time compared to field on case (Figure 3.15(b)).

As it was discussed in earlier sections, due to the large cost of the Xenon mixture, during 2008-2009 commissioning an Argon gas mixture was used. In the Figure 3.15(c), the r - t relation for field on is shown. The Argon mixture is faster than the Xenon one and this leads to a different performance. The r - t relation for field off the Argon gas is presented in Figure 3.15(d).

The T_0 constants do not change for the different gas mixtures. For the cosmic calibration the r - t relation was not fixed at $r = 1$ mm, but this is compensated by the use of the event phase which fixes the average of all the T_0 values for the barrel. For the field on, this average was set to $\langle T_0 \rangle = 19.2 \pm 0.1$ ns while for field off was $\langle T_0 \rangle = 19.5 \pm 0.1$ ns. This difference is produced by the bending of the tracks together with the slightly wrong description of the treatment used for the r - t relation.

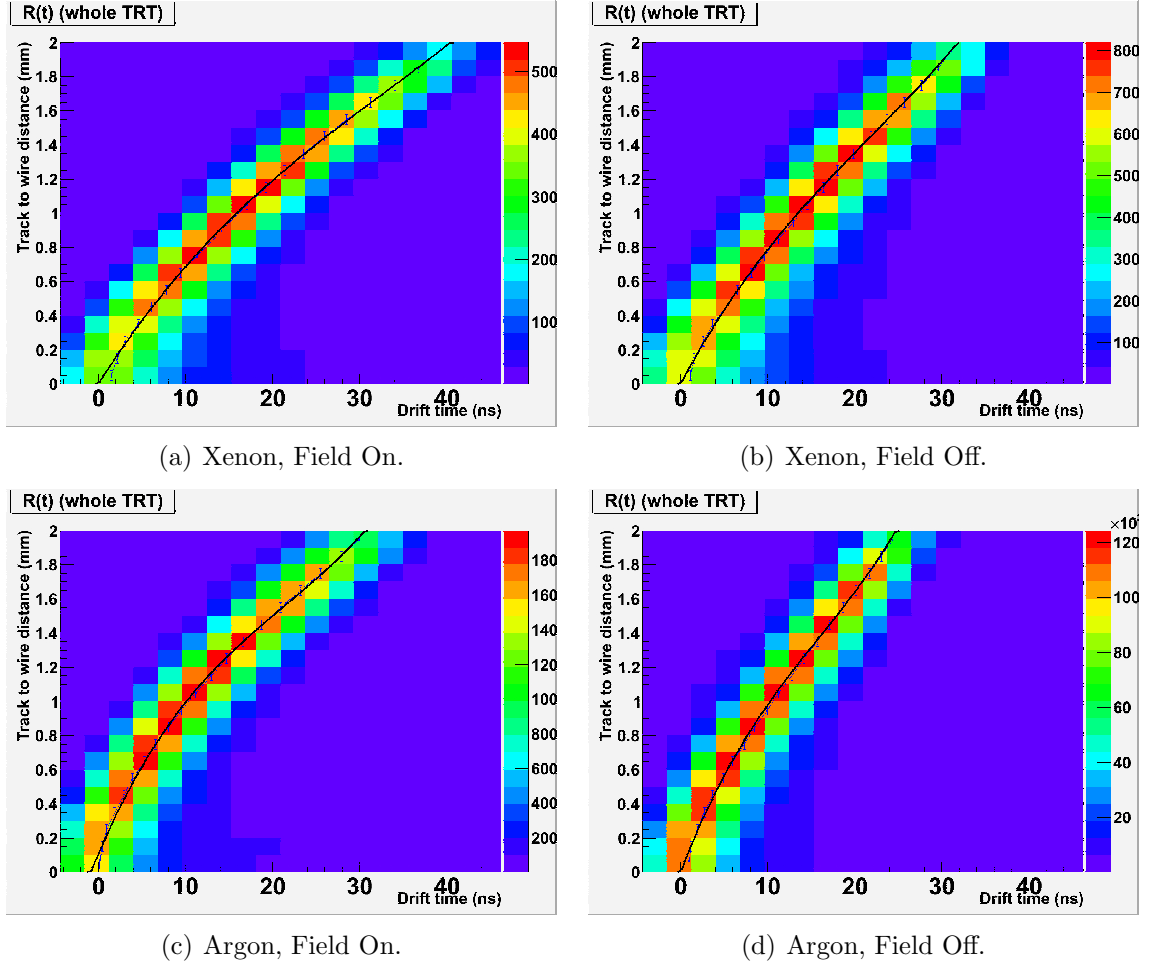


Figure 3.15: TRT $R(t)$ calibration done for whole barrel for Xenon field on: (3.15(a)), Xenon field off (3.15(b)), for Argon field on (3.15(c)) and Argon field off (3.15(d)). These calibrations were performed using the r-binning instead of the t-binning.

3.3.4 Barrel performance

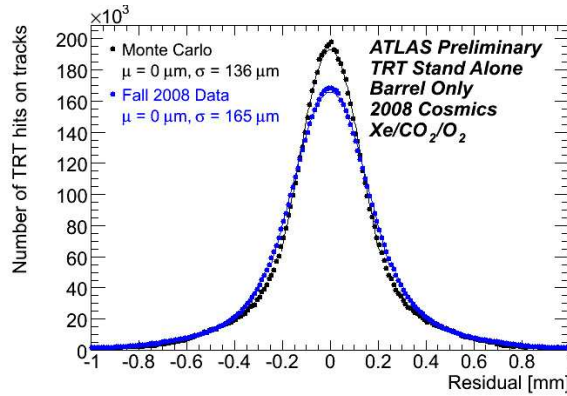
The final goal of the calibration is to get the best position residual out of the data. The different gas mixtures and field settings return different resolutions. In the Table 3.1 a comparison between Xenon and Argon with and without magnetic field is presented. As expected, the best performance is obtained for Xenon mixture with field on. as the drift velocity is slower, the resolution gets improved. The worst resolution is obtained for Argon without magnetic field. In addition to the inability to absorb transition radiation photons, the poor position residual makes the Argon mixture unusable for proton-proton collisions.

The resolution obtained with Xenon mixture is $165 \mu\text{m}$, as can be seen in Figure 3.16. In this figure the cosmic Monte Carlo simulation for Xenon is also presented, which after calibration, returns $136 \mu\text{m}$. The data performance is worse than for Monte Carlo. Possible reasons are alignment issues, also fine tuning of the calibration algorithm were

Table 3.1: Resolution obtained for different gas mixtures and field settings for cosmic ray data.

Gas Mixture	Field On	Field Off
<i>Xe</i>	165 μm	180 μm
<i>Ar</i>	175 μm	195 μm

not yet performed and the event phase which includes an extra uncertainty of 1 ns. It is important to note that the tracking and detector geometry is not optimized for cosmic rays, which makes it difficult to reach the collisions performance.

**Figure 3.16:** Resolution for cosmic data taken with Xenon mixture and field on. Data and Monte Carlo are included for comparison.

The Low Threshold and the High Voltage are different for Xenon and Argon gas mixtures operation. During the 2009 cosmic runs, the LT average was set to 131 DAC counts in the barrel for Argon based gas. For Xenon gas, the LT was set to 121 DAC in the barrel. For the end-caps, for both gas mixtures the threshold was set to 117 DAC. Few runs were taken using larger gain for Argon mixture. The High Voltage was set to 1550 V instead of the default 1530 V used in standard operation. Also the Low Thresholds for the barrel were raised to 180 DAC. This setup improved the position residual by 10 μm . The r - t relation produces slightly larger drifting times than the default conditions. Naively one would think that an increase in the High Voltage must lead to shorter drift times. This effect can be produced by the larger time needed by the signal to cross the threshold. The r - t difference is not large enough to explain the residual improvement. The better performance is due to the raise of the thresholds, which reduces the noise accepted, but also reduces the efficiency of the TRT. As the ionization of a charged particle in a gas depends on its momentum, particles with low momentum are less likely to be detected when increasing the LT.

3.4 Calibration with collision data

On 23 November 2009, the first proton-proton collisions at the center-of-mass energy of 900 GeV were recorded at the LHC. In this section an overview of the calibration and performance results for proton-proton collisions obtained since then are reported, including the up to date calibration results.

In proton-proton collisions, the events to be calibrated must be recorded with all Inner Detector subsystems fully operational. The event is also required to have at least one reconstructed vertex with three or more tracks to avoid backgrounds not produced in the collision, such as beam halo or cosmic events. The tracks used for calibration are reconstructed as Inner Detector combined tracks and are required to have a minimum transverse momentum of 1 GeV, at least six hits produced in the silicon detectors (SCT and Pixel) and 20 TRT hits. To assure tracks are produced in the collision, a loose requirement on the track impact parameter is applied: $|d_0| < 30$ mm.

The data is collected by the Express Stream, which has a rate around 10 Hz, making 40.000 events available per hour of data-taking. In the calibration, the data are reconstructed using the same settings, conditions database and ATLAS software release as the centrally reconstructed ATLAS data. In three hours of data-taking, about two million of tracks are reconstructed for calibration, producing several thousands of hits in each DTMROC. All DTMROCs with more than 500 hits are calibrated, so the amount of hits collected in three hours is large enough for an accurate T_0 calibration. From the point of view of the r - t calibration, the calibration is done for each barrel and end-cap side separately in case 50.000 hits are available, which happens most of the time.

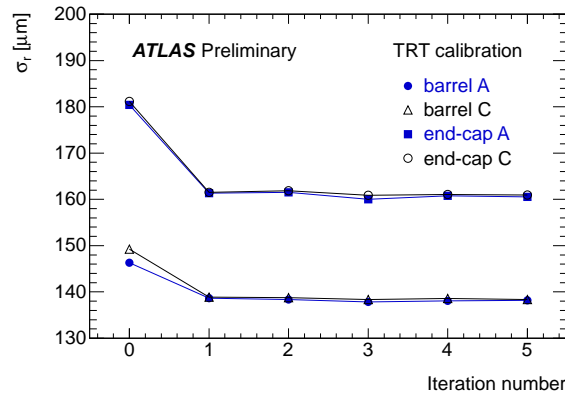


Figure 3.17: Improvement in the position residual width distributions for different TRT detector parts with the calibration iteration number. Iteration 0 refers to the performance obtained with the latest calibration before the run was taken. This calibration was set to be the right r - t relations and the T_0 values for all the straws set to 9.75 ns.

As it was explained, the TRT offline calibration method is an iterative algorithm. To validate the calibration, the position residual is evaluated for each iteration. The method is expected to converge to the optimal calibration constants, after which the resolution

will remain constant. In the 24h calibration, the first iteration is run making use of the latest constants in the database, which are our best detector knowledge before the run was taken. In case a degradation in the performance is observed, more iterations are run until best performance is achieved.

As a test of the calibration method, the Figure 3.17 shows the change of the position residual width with iteration number. In this test, the $r-t$ and T_0 calibration were done using as starting conditions the same T_0 value for all the straws, 9.75 ns, value which is obtained as the average T_0 after calibrating the run, and the $r-t$ relations obtained from the run calibration. As can be observed, after just one iteration, the calibration method is able to correct for the different T_0 granularity, with a fast and stable convergence. Studies starting from fully uncalibrated detector has been done, showing convergence in less than 7 iterations. Large changes in the T_0 values are not observed, except in case of hardware replacements. Similarly, the $r-t$ relation is very stable in time, so most of the changes in the detector can be compensated by just one or two iterations.

3.4.1 $r-t$ calibration

The $r-t$ calibration is expected to be different between barrel and end-caps due to the different orientation of the straws with respect to the magnetic field. During the cosmic runs. the calibration for the barrel was performed, however, the nature of the cosmic rays did not allow to calibrate the end-caps. In early December 2009, thanks to the first proton-proton collision with magnetic field on, the end-caps were calibrated for the first time. In Figure 3.19 the fits for barrel and end-caps are shown together with the barrel $r-t$ relation obtained from the cosmic data. In the barrels, the results obtained for collision and cosmic data are in a good agreement. For the end-caps, the drift time for a given drift radius is shorter than for the barrel, so the drift velocity is larger for end-caps than for barrel. This is because the different orientation of the straws with respect to the z axis and the different magnetic field orientation respect the straw wire for barrel and end-caps. The first proton-proton $r-t$ calibrations were done using the r binning, which now is not used for 7 TeV runs.

Currently, the standard calibration procedure involves the $r-t$ fitted in time bins (t -binning) for every run in the four TRT regions: barrel A, barrel C, end-cap A and end-cap C. Figure 3.19(b) shows the $r-t$ relation for barrel A and end-cap A calibrated in a 2010 October run. The differences between the different TRT regions are shown in Figure 3.19(b). Similarly to the 900 GeV calibration, a systematic difference between barrel and end-caps is observed, indicating to faster drift velocities in the end-caps. The sides A and C of the TRT are symmetric, and the systematic difference observed between them is below 10 μm .

Variation of the $r-t$ relation with detector position

The use of just four $r-t$ relations has shown to describe the TRT well. However, the $r-t$ relation is directly related with the magnetic field strength and orientation. The Inner Detector is embedded inside a solenoid providing 2T field parallel to the beam pipe. In the

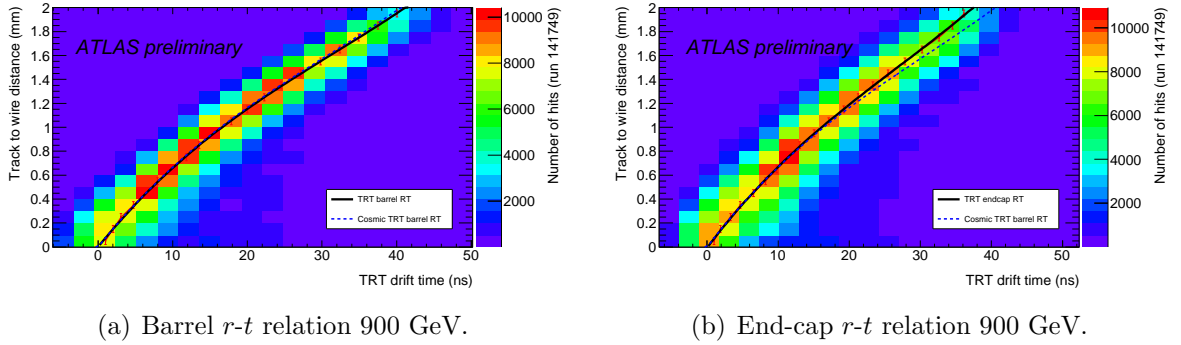


Figure 3.18: TRT r - t calibration done for proton-proton collision at 900 GeV with magnetic field, for the whole barrel (3.18(a)) and end-caps (3.18(b)). These calibrations were performed using the r-binning instead of the t-binning.

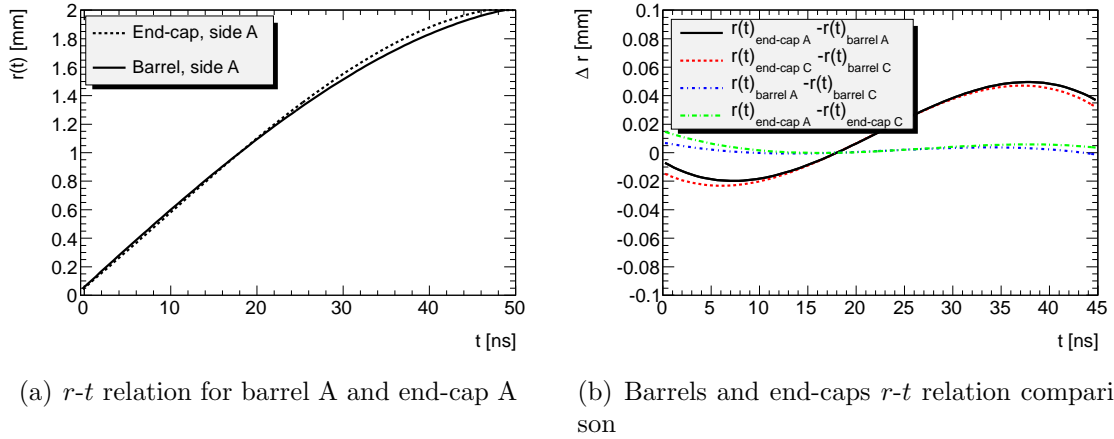


Figure 3.19: TRT r - t calibration comparison for barrel A and end-cap A (3.19(a)) and the difference between all the regions (3.19(b)). These calibrations were performed using the latest r - t calibration method.

central region ($z \sim 0$), the field is very uniform, but getting away from the central region, differences are expected to show up. For this reason, a study at different r - t granularities has been done.

The r - t calibration was done at layer level for barrel and wheel level for end-caps. The differences between the calibration obtained at layer or wheel levels and the r - t at the barrel or end-cap level are shown in Figure 3.20. The systematic differences in the barrel layers are smaller than $20 \mu\text{m}$. In the end-cap, the differences are up to $50 \mu\text{m}$, with systematic changes between central wheels (0) and outer wheels (12).

The electron radial drift velocity is the first derivative of the r - t relation: $\frac{\partial r}{\partial t}$. This derivative allows to look more in detail to the wheel/layer r - t calibration. In Figure 3.21

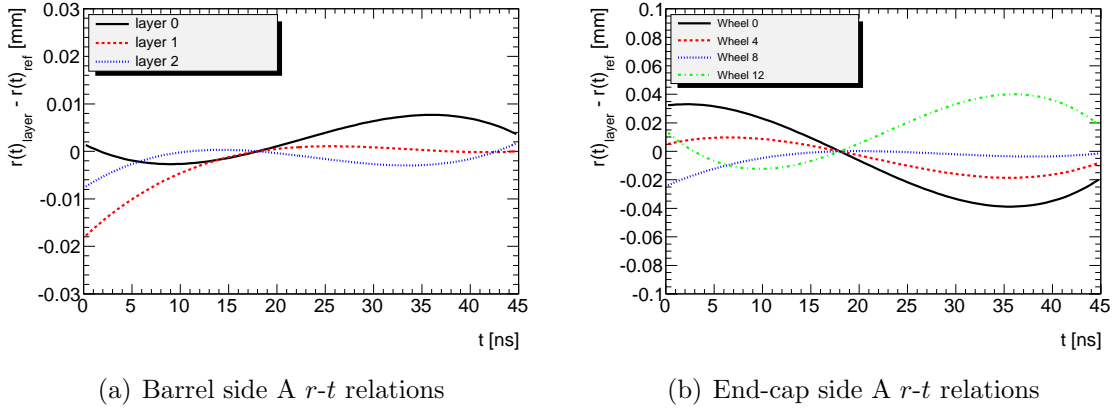


Figure 3.20: r - t relation differences between layer level calibration and the average r - t relation for the barrel side A 3.20(a) for the end-cap side A 3.20(b).

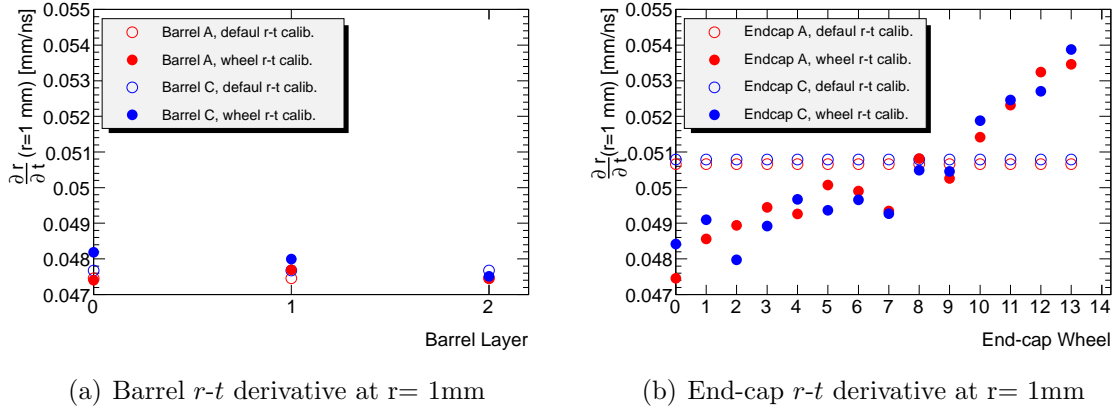


Figure 3.21: r - t derivative ($\frac{\partial r}{\partial t}$) at $r = 1$ mm for barrels 3.21(a) and end-caps 3.21(b). The filled circles correspond to r - t calibration at wheel/layer level and the empty circles correspond to barrel/end-cap calibration used as a reference.

the r - t relation derivative evaluated at $r = 1$ mm is shown for the different barrel layers and end-cap wheels. In addition, as a reference, the results for only barrel side and end-cap side calibration are presented. The evaluation at $r=1$ mm was chosen because this point is well defined, avoiding problems obtained for low and large drift radius, which are less stable in calibration. For the barrels, the radial drift velocity is almost constant, without clear dependence. In the case of the end-caps, a clear dependence is observed. The radial drift velocity becomes faster for outer wheels. This result is expected, because the magnetic field strength reduces when z increases, so the electron path is straighter, arriving earlier to the wire.

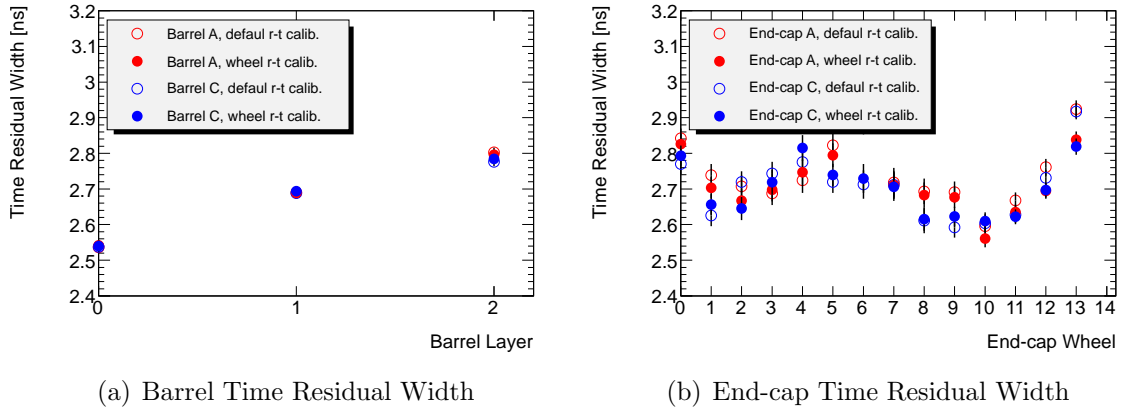


Figure 3.22: Time residual width for barrels 3.22(a) and end-caps 3.22(b). The filled circles correspond to r - t calibration at wheel/layer level and the empty circles correspond to barrel/end-cap calibration used as a reference.

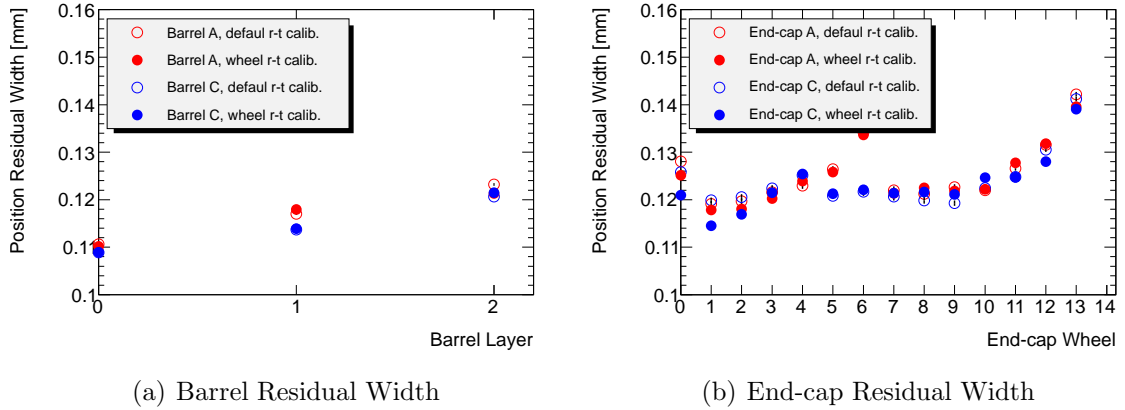


Figure 3.23: Position residual width for barrels 3.23(a) and end-caps 3.23(b). The filled circles correspond to r - t calibration at wheel/layer level and the empty circles correspond to barrel/end-cap calibration used as a reference.

Figures 3.22 and 3.23 show the position residual widths for the different layers and wheels for the default calibration and the low granularity r - t calibration. For the barrel, where the r - t dependence with the wheels is very low, the changes in terms of resolution are negligible. In the end-caps, the wheel r - t calibration improves the width of the time residual for all the wheels, but the improvement is more important for the outer and inner wheels, where the change with respect to the average drift velocity is larger. In terms of spatial resolution, the wheel r - t calibration gets $\sim 3 \mu\text{m}$ improvement for the outer and inner wheels with respect to the whole end-cap calibration. The global improvement for

the TRT is just around $0.5 \mu\text{m}$.

The average region-dependent r - t relation was used during the 2010-2011 data-taking instead of the layer r - t relation due to relative small improvement observed in terms of position resolution. Also, the use of the layer calibration requires a more careful evaluation of the calibration results before deciding to update the database, and in case of low statistics, the calibration can be unstable. The average ionization that depends on the track incidence angle with respect to the straw can affect the r - t relation and contribute to observed changes. Larger improvements for the layer-dependent r - t calibration are observed if the so-called Time-over-threshold correction is applied. This correction, which is not yet documented, compensates the drift time dependence on the ToT, which is a way to measure the average ionization. The layer r - t calibration is one of the improvements considered for the 2012 calibration.

3.4.2 T_0 calibration

The T_0 calibration is based on the time residual distribution at different granularity levels. The number of hits and the width of this time residual determine the statistical error of the calibration. This dependence is well described by the function: p_0/\sqrt{N} , where N is the number of the hits in the time residual distribution and the parameter p_0 has been measured to be 7.5 ns [3]. To obtain the final T_0 values with an accuracy of 0.3 ns, close to the database resolution, at least 500 hits are needed. This time accuracy is equivalent to $1 \mu\text{m}$ spatial residual, close enough to the best TRT performance.

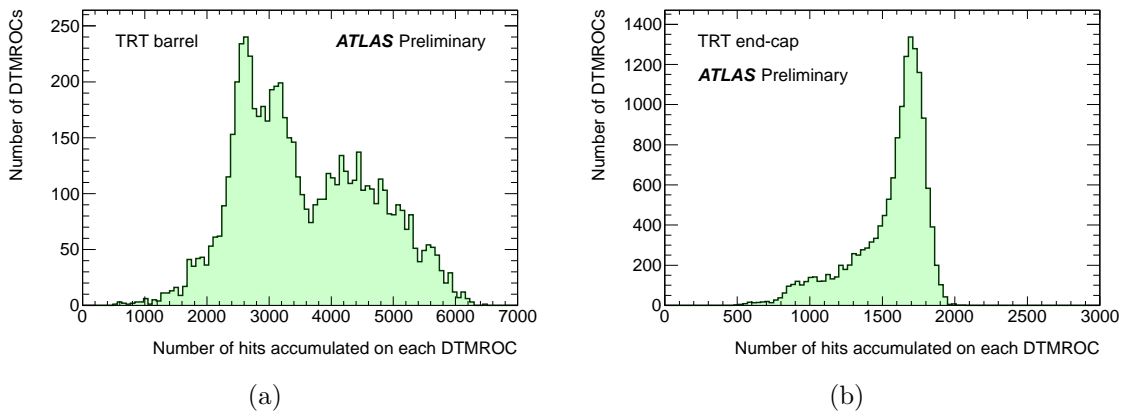


Figure 3.24: Number of hits accumulated on each DTMROC for barrel: (3.24(a)) and end-caps (3.24(b)).

The T_0 calibration, due to the large amount of tracks available in collision data, can be performed most of the times at the DTMROC level. An example of the number of hits per DTMROC for a three hours run that took place in October 2010 is shown in Figure 3.24. As can be seen, the majority of the elements are over 500 hits, which allows an accurate calibration of them.

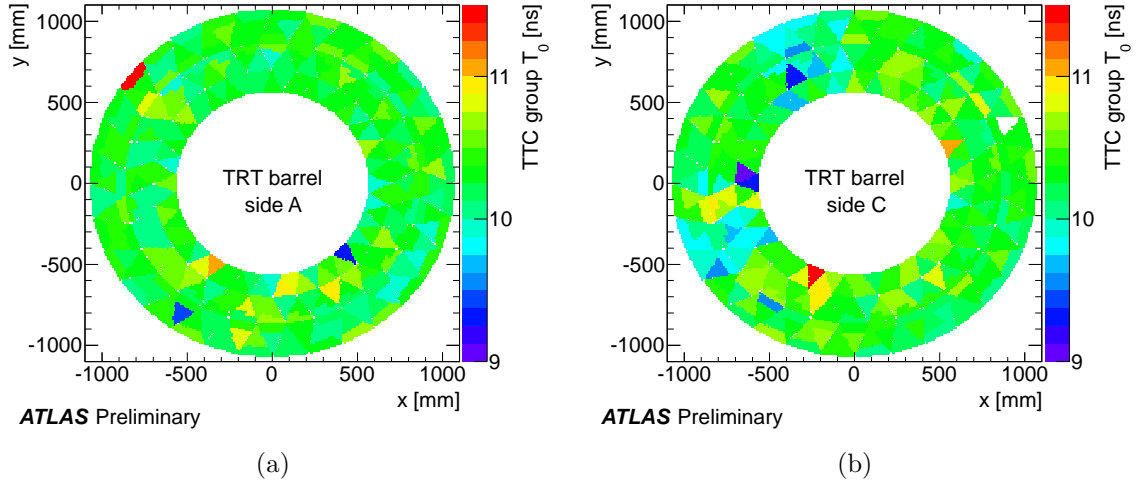


Figure 3.25: T_0 constants averaged over TTC group as a function of the position in the TRT detector for barrel A: (3.25(a)) and barrel C (3.25(b)).

The T_0 constants determined at TTC group level (board level) are shown in Figure 3.29 as a function of the position in the barrels. As discussed, one of the timing corrections included on the T_0 values is the time of flight. Since the barrel extends from 560 mm to 1080 mm in the radial direction, and assuming particles travel at the speed of light, a minimum systematic difference of 1.65 ns will be expected between the inner and outer TTC lines. However, this is not the case, because the TTC lines hardware delays are adjusted to compensate for this effect, giving a very uniform T_0 distribution.

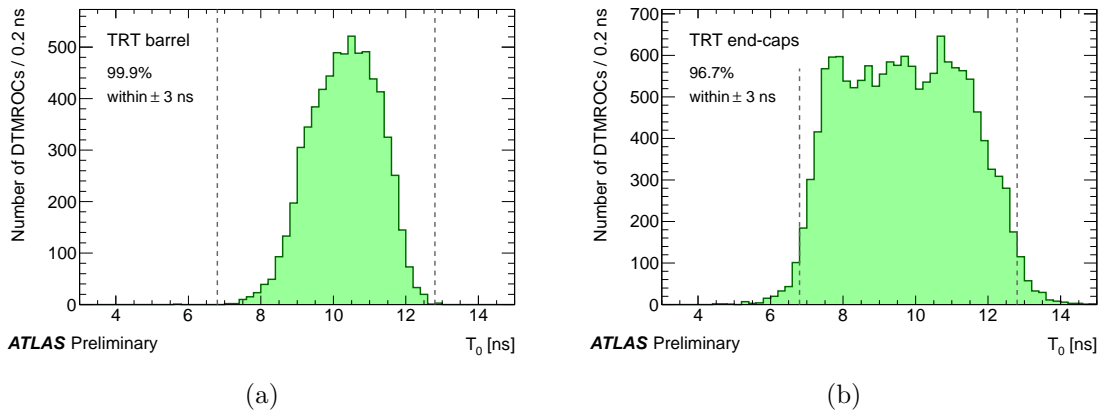


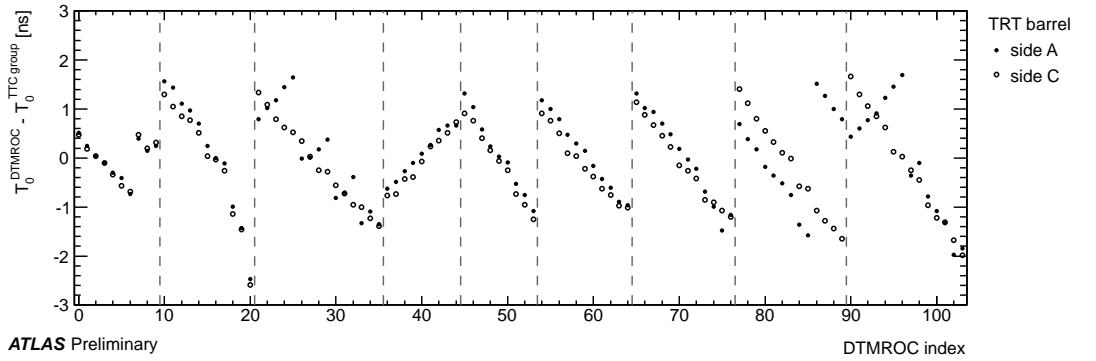
Figure 3.26: Distribution of T_0 constants at DTMROC level for barrel (3.26(a)) and end-caps (3.26(b)).

The T_0 constants for each DTMROC are shown in Figure 3.26. It is important that these T_0 distributions are not very spread, because this indicates that a fraction of the detector is read-out too early or too late. In case some parts of the detector are out of

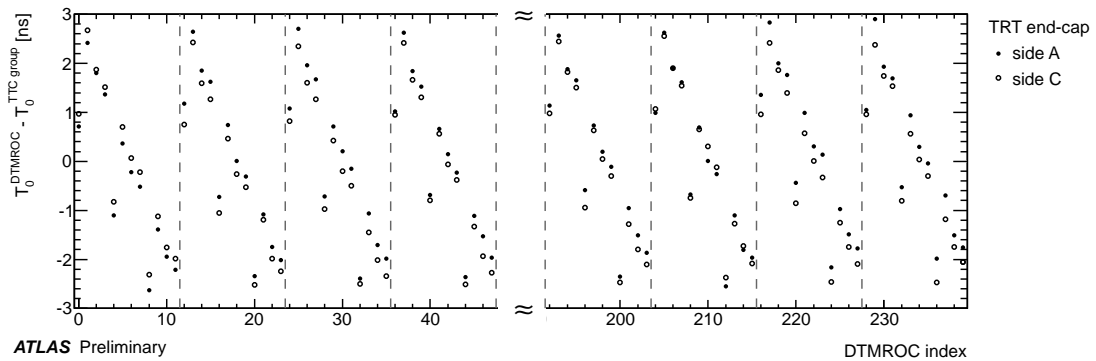
time, an adjustment in the TTC line hardware delay will be needed to assure the full signal is contained in the 75 ns read-out window. The distributions show that almost 100% of the barrel DTMROCs T_0 values and 96.7 % of the end-cap DTMROC T_0 values are within 6 ns. This is in good agreement with the T_0 uniformity observed at TTC line level.

Chip corrections

The chip corrections, defined as the DTMROC T_0 variations for the different TTC lines averaged over ϕ sectors, have been largely used for barrel T_0 calibration during the cosmic data-taking. In Figure 3.27 the differences for the T_0 values at DTMROC with respect to the TTC line T_0 are shown averaged over all ϕ sectors. In addition to the barrels, which follow the same dependence as observed in cosmic data, the end-caps are also presented. The fine delay time scans are not shown because the accuracy obtained with collision data is much better due to the large statistics available. The differences in terms of shape between sides A and C are due to the different DTMROC index order for both sides.



(a) Barrel board



(b) End-cap board

Figure 3.27: T_0 constants variation within TTC groups for barrel 3.27(a) and end-caps 3.27(b). Dashed lines separate different TTC lines.

For the barrel, the maximum T_0 variation within TTC line is 4 ns, while for end-caps it is up to 6 ns. The pattern observed is related with the clock signal propagation in the

TTC line. If for DTMROC the clock signal arrives first, the read-out window starts earlier and the signal starts later, so the T_0 constant is larger. The chip corrections cannot be compensated by the hardware delays because they modify the whole TTC line; for this reason, the spread observed in Figure 3.26 cannot be further corrected.

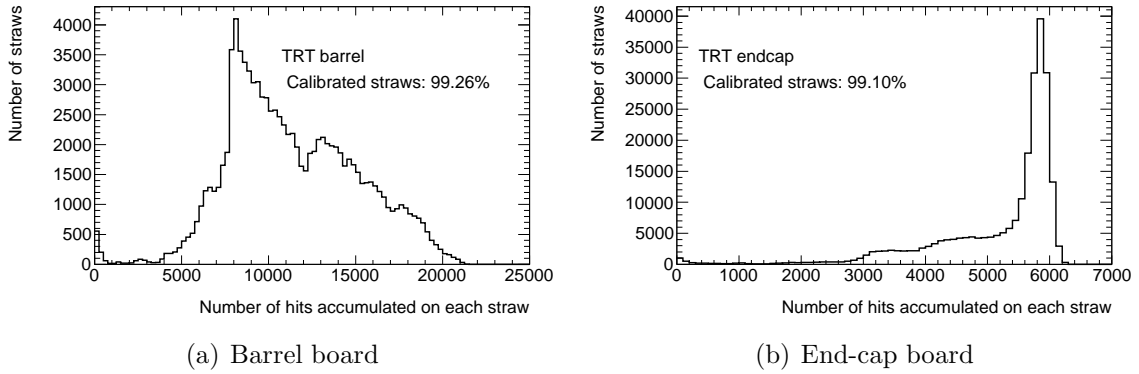


Figure 3.28: Number of hits accumulated at the straw level for barrel 3.28(a) and end-caps 3.28(b).

Straw-by-straw systematic effects

In the standard calibration, the timing for the 16 straws read-out by the same DTMROC is assumed to be the same. However, possible systematic effects are due to different signal propagation and electronic processing of the signal between straws in the same DTMROC. To check this, a run with $7 \cdot 10^6$ events recorded was used to evaluate the T_0 values at straw level. In total, more than 2×10^9 hits were used for this study. Figure 3.28 shows the distributions for the number of hits accumulated on each straw for barrel and end-caps. Similarly to the standard calibration, each straw is calibrated if the number of hits is larger than 500 hits. With the large sample used, 99% of the straws are calibrated with an average time resolution of 50 ps in the barrel straws and 90 ps in the end-cap straws.

The results obtained by the straw-by-straw calibration are compared to the DTMROC calibration of the same run. Distributions showing these differences are shown in Figure 3.29 for barrel and end-caps separately. The RMS of the distributions is larger than the expected statistical resolution, which indicates that systematic effects exist despite the fact they have not been taken into account by the standard calibration method.

In order to check for systematic differences for straws within DTMROCs, the T_0 differences between the straw level and the DTMROC T_0 are shown in Figure 3.30 averaged for all end-cap ϕ sectors. Two TTC lines are shown for type A wheels and one for type B wheels. The 12 DTMROC arrangement for each TTC line is shown in Figure 3.11(b). The four by four groups attached to the same DTMROC are displayed in Figure 3.30. A clear pattern is observed for straws in same relative position in the different DTMROCs, and for different TTC lines. The end-cap straws are connected to the front-end through

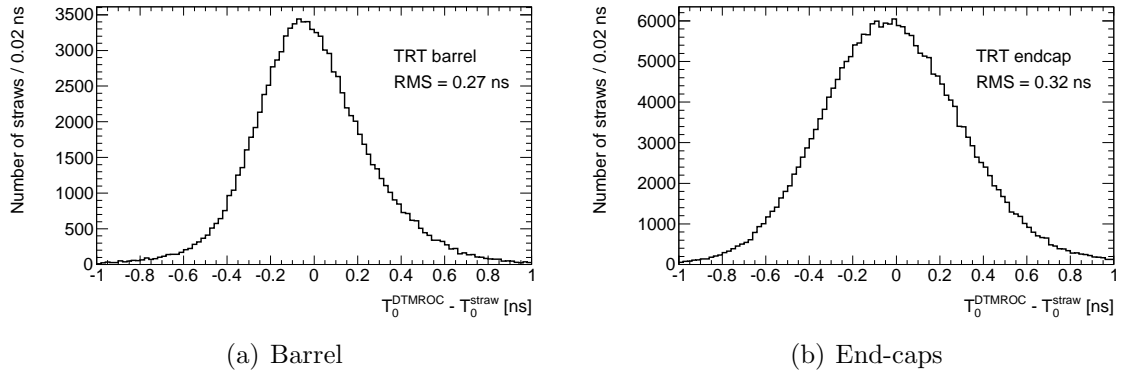


Figure 3.29: Differences between straw-level T_0 calibration and the DTMROC calibration for barrel 3.29(a) and end-caps 3.29(b).

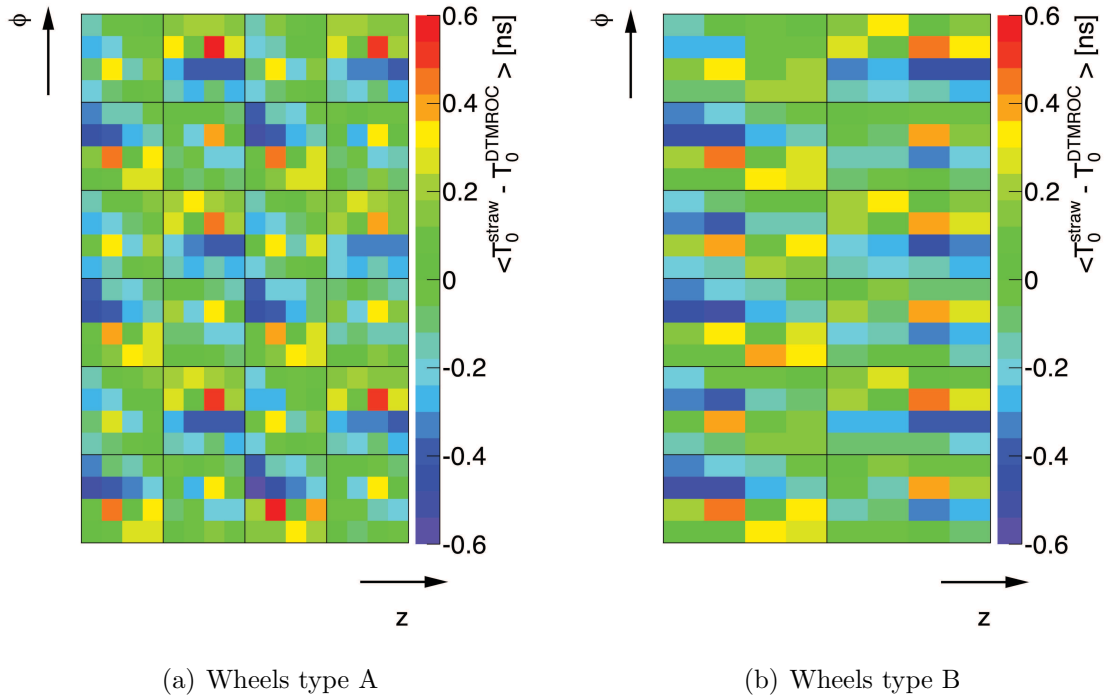


Figure 3.30: Difference between straw level T_0 calibration and DTMROC level calibration for a selected end-cap region for wheels type A 3.30(a) and wheels type B 3.30(b). The differences are averaged over all ϕ sectors. The black lines separate straws that are read-out by different DTMROC chips.

the so-called web connectors, as the one shown in Figure 3.31. Each of them connects 32 straws to two DTMROCs. The T_0 pattern is repeated for each web connector. Different effects can contribute to the observed variations at the order of 0.1ns, such as signal length

propagation in the connector and time of flight differences. The largest variations measured are about ± 0.5 ns, which can indicate small time delays in the DTMROC electronic processing.

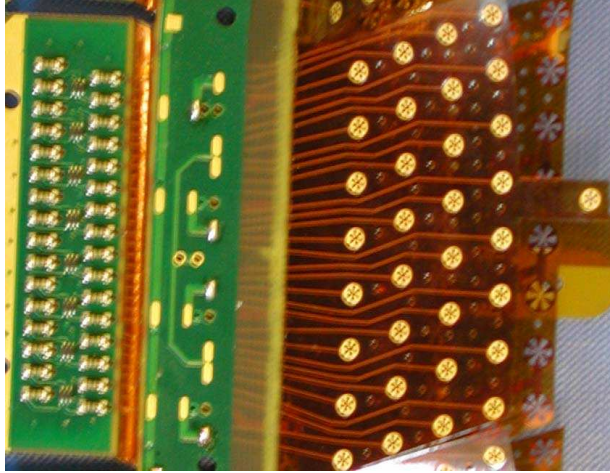


Figure 3.31: Web element used to connect 32 straws to two DTMROCs in the end-caps.

The width of the position residual distribution using the straw-by-straw T_0 correction improves by about $0.3 \mu\text{m}$ in the barrel and $0.7 \mu\text{m}$ for the end-caps. The required statistics to perform straw-by-straw calibration and the amount of computing time needed to do event reconstruction is too large to calibrate at this level on the 24h basis. For 2012 calibration, the calibration at DTMROC level and the application of the straw-by-straw T_0 corrections presented here will be considered.

Global timing effects

In previous sections the influence of lower granularity calibration has been studied. The effects measured are shown to be very stable in time, with differences between runs being within statistical uncertainty, which means no need to update the database. The most frequent reason for constants update was the global shift of all T_0 constants.

The signal time for all the ATLAS subdetectors is synchronized to the LHC Clock, which is transmitted through an optic fiber. This clock has shown to drift slowly from run to run, producing a global T_0 shift that needs to be compensated. Figure 3.32 shows the average T_0 change for the barrel side A from run to run during the 2010 data-taking period. For reference, the TRT measurement was compared to the beam pick-up based timing system (BPTX) [60]. A very good agreement between both methods was found, which indicates that the global T_0 shift is not due to internal the internal TRT reasons. Other systems, such as Liquid Argon detector, have shown the same dependence, which is related to the LHC Clock shift. Since June 2010, the delay of the LHC Clock can be adjusted in steps of 0.5 ns to compensate for this drift, which reduces the need to update the TRT calibration constants.

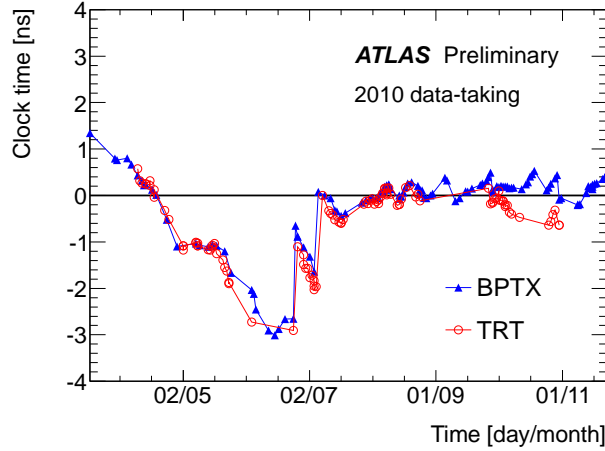


Figure 3.32: Average value of the T_0 constants for the barrel side A during 2010 data-taking period. The measurement of LHC beam 1 time with the BPTX is shown for comparison. The difference between the TRT and the BPTX measurement at the end of 2010 could be explained by an increase of the N_2 concentration in the gas mixture.

3.4.3 Calibration of simulated data

The different physics processes needed for an accurate description of the TRT detector, such as ionization of the gas molecules, cluster creation, drift and amplification of the electrons, signal propagation along the straw wires and signal shaping by the read-out electronics, are modeled by Monte Carlo simulation [35]. The PAI (Photo Absorption and Ionization) model is used to describe the ionization produced for charged particles going through the TRT straws. The model computes a list of clusters and their energy created which depends on particle charge and momentum. This model creates a set of ionization clusters produced by the charged particle and computes the energy loss in each cluster. The number of clusters and the energy loss by the particle depends on the momentum, mass and electric charge of the particle. The energy of the clusters is converted to the number of electrons produced assuming an average ionization energy of 25.3 eV [59]. The gas reabsorbs some of the electrons produced. This is modeled using the Garfield model predictions. The remaining electrons are amplified in an avalanche when approaching the straw wire. The gain is simulated by applying an individual gain factor to each electron in the cluster. To obtain signal time, a drift time for each electron in the cluster is assigned. These times are based on Garfield simulations, which depend on the magnetic field perpendicular to the direction of motion of the electrons. Two relations are simulated, one for the maximum field (2T) and one for zero field. For TRT regions with different field strengths, an interpolation between the two relations is performed. The final signal collected in the straw after amplification is divided in two parts, one is sent directly to the front-end electronics and the other half is reflected on the other side of the straw. The signal propagates at $3/4 c$ and its attenuation in the wire is also simulated. Finally, the signal reaching to the electronics is shaped and discriminated against a threshold. The final tune of these thresholds and of the different simulation parameters was done using

the 2004 test-beam data. The final T_0 constants and r - t relations used for reconstruction of the Monte Carlo samples need to be determined in the same way as it is done for the data.

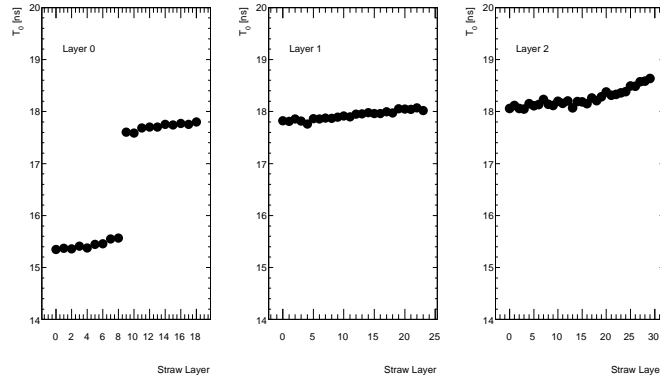


Figure 3.33: T_0 values for Monte Carlo for the three barrel layers separately as a function of the straw layer. Straw layer index in barrel is proportional to the straw distance to the beam axis.

As explained before, in the TRT simulation, the detector granularities are not included. The effect of the time of flight is corrected by shifting the time of the simulated signal. The time for a particle which travels at the speed of light from the interaction point to the end of the straw, where the corresponding electronics front-end board is located, is subtracted from the signal time. The remaining time of flight and signal propagation effects are corrected by the T_0 constants obtained in calibration. For T_0 calibration of Monte Carlo samples, the straws are grouped according to the straw layer index, which is equivalent to the distance to the interaction point. Figure 3.33 shows the barrel T_0 constants obtained for the three barrel layers as a function of the straw layer. The short straws correspond to straws in the layer 0 with straw layer index below 9. The thresholds in Monte Carlo depend on the straw length because of the correlation between noise level and straw capacitance, which is proportional to the wire length. Lower thresholds are used in the simulation of the short straws, which lead to smaller T_0 with respect to the rest of the barrel straws.

In Figure 3.34 the r - t relation in Monte Carlo is compared to the one observed in data for barrels and end-caps separately. In addition, the r - t relation for maximum magnetic field obtained with Garfield and used for the TRT simulation is also shown. For the barrel side A, the calibrated r - t relation for Monte Carlo and the r - t relation used in the simulation are in good agreement, specially for drift times larger than 15 ns. In the low drift time region, the calibrated r - t relation predicts shorter drift radius than the simulation. The simulation r - t relation is used to compute the drift time of the clusters to the wire. For this reason, the drift distance of the electrons to the wire is larger than the closest approach of the track to wire. The r - t calibration corrects for this effect, returning lower drift distances

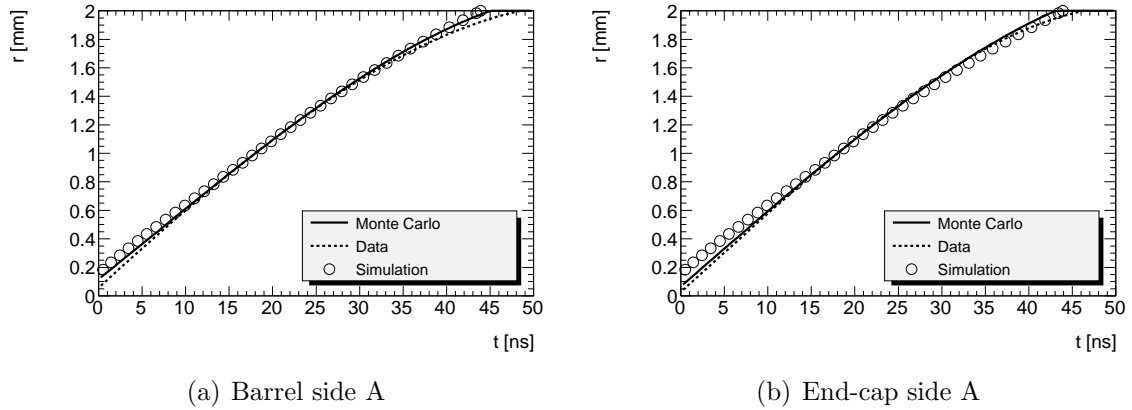


Figure 3.34: r - t relation for 7 TeV data and Monte Carlo. The r - t relation used by simulation is shown as the open circles for comparison with the calibrated r - t relation.

than the simulation r - t . This effect is negligible once getting away from the straw center, improving the agreement between both r - t relations. In the end-caps, the magnetic field is not maximal so the calibrated r - t for Monte Carlo is faster than the simulation r - t relation for maximum field.

The data and Monte Carlo r - t relations are in good agreement in the drift time range $10 \text{ ns} \leq t \leq 35 \text{ ns}$, but in Monte Carlo the slope close to the straw wall and close to the straw axis is lower than in data. A drift velocity of about $47 \mu\text{m}/\text{ns}$ in Monte Carlo is measured close to the straw wire, while for the data the drift velocity is about $60 \mu\text{m}/\text{ns}$. These differences can be produced by a wrong r - t simulation used, but the modeling of the primary ionization, the electron absorption and the signal gain, may also contribute. The differences are not large enough to make a significant change in the performance between data and Monte Carlo. The systematic differences between the calibrated r - t relation for data and Monte Carlo in the barrel are the same for the end-cap, which validates the simulation description depending on the magnetic field.

3.4.4 TRT performance

In the TRT, the measurement of the tracking performance is based on the width of the position residual distributions. The distributions for global position resolution for data and Monte Carlo for barrel short straws, barrel long straws and end-caps are shown in Figure 3.35. The sample on these plots differs slightly from the tracks selected for calibration, applying a transverse momentum cut of 2 GeV and impact parameter cuts: $|z_0| < 300 \text{ mm}$ and $|d_0| < 300 \text{ mm}$. The resolution measured in data is compared also to Pythia dijet Monte Carlo simulation [75].

The short straws have significantly lower occupancy because the central part of the straw is not sensitive, and they show a resolution of $108 \mu\text{m}$. A very good agreement is found between Monte Carlo and data. For the long straws in the barrel, the resolution

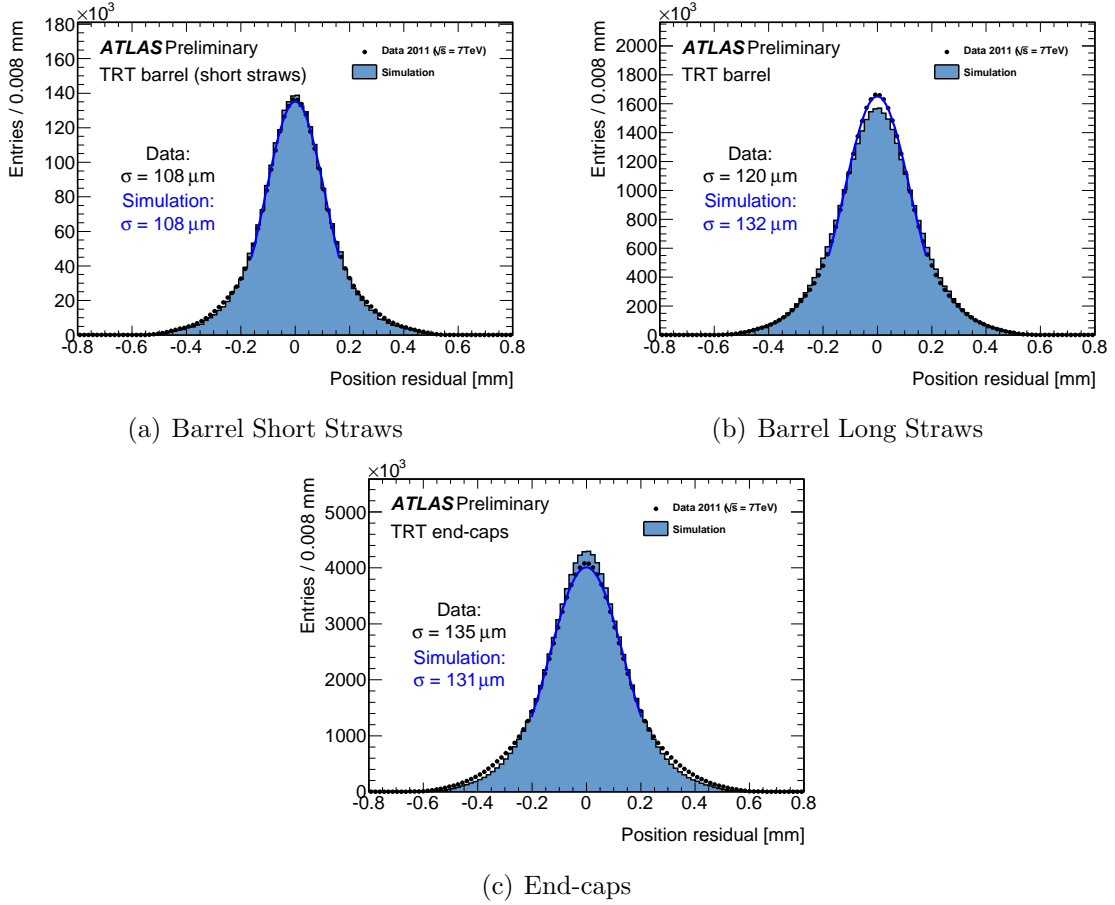


Figure 3.35: TRT hit position resolution measured in data and compared to Monte Carlo for barrel short straws (3.35(a)), barrel long straws (3.35(b)) and end-caps (3.35(c)). Selected tracks have $p_T > 2 \text{ GeV}$, $|d_0| < 10 \text{ mm}$ and $|z_0| < 300 \text{ mm}$ [4].

measured in data is $120 \mu\text{m}$, while in Monte Carlo it is $132 \mu\text{m}$. This simulation overestimation indicates that a further tune of the Monte Carlo, specially the threshold levels, may be needed for the barrel. In the end-cap regions, data shows a resolution of $135 \mu\text{m}$ and the simulation $131 \mu\text{m}$. The simulation is done with a perfectly aligned TRT geometry. The disagreement between data and Monte Carlo in the end-caps indicates that some small mis-alignments are still present in data. Globally, the current TRT performance is better than the design resolution.

A detailed view of the TRT resolution for data averaged for each DTMROC in barrel side C and end-cap side C is presented in Figure 3.36. The selection of tracks used for these plots is identical to the one used for TRT Calibration, with $p_T > 1 \text{ GeV}$ and $|d_0| < 20 \text{ mm}$. For the barrel, the position of each DTMROC is represented in the $x - y$ plane. The inner DTMROCs, closer to the beam pipe, where the short straws are placed, show the best performance. The good performance of the short straws is due to higher effective threshold, smaller time difference between the signal directly propagated in the wire to

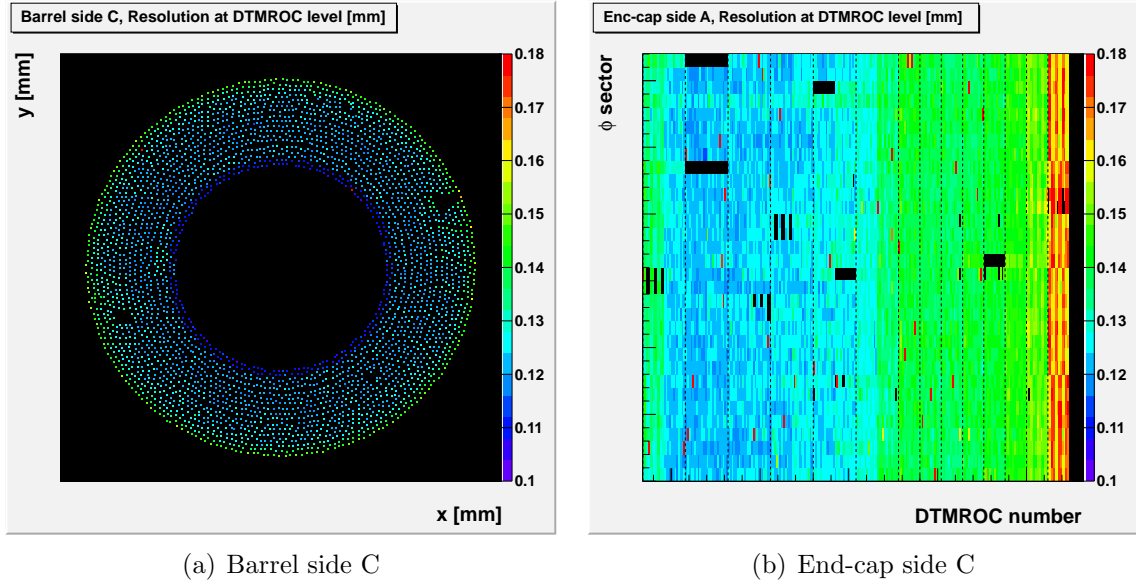


Figure 3.36: TRT hit position resolution averaged by DTMROC for Barrel C depending on the $x - y$ position of the DTMROC (3.36(a)) and end-cap C depending on the DTMROC index number, which is proportional to z coordinate (3.36(b)). Selected tracks are the same as used by TRT Calibration, having $p_T > 1$ GeV and $|d_0| < 20$ mm. Black regions in the end-cap indicate DTMROC not working. Dashed lines separate different end-cap wheels.

the DTMROC and the signal reflected in the electrical split, a lower material traversed by the track and shorter extrapolation distance from the SCT. In the barrel, the resolution degrades for DTMROCs getting away from the interaction point due to larger amount of material crossed, which increases the multiple scattering.

Similar effects are observed in the end-caps. In Figure 3.36(b), the DTMROC positions are represented by their index number, which is proportional to the z coordinate and the ϕ sector. The performance over different ϕ sectors is the same as it is expected from the detector geometry. Large dependence is observed with the DTMROC number. For the first wheel, closer to the interaction point, the tracks have hits in both barrel and end-cap, which reduces the total number of hits on track. In this transition region, the front-end electronics of the barrels are located, which increases the material budget and the multiple scattering, degrading the resolution. Once moving toward large z , the tracks are completely confined in the end-caps, improving the residual. The straw distance in type A wheels is shorter than for type B wheels, for this reason a clear increase of the residual width is observed when moving to type B wheels. At the edge of the end-caps, which corresponds to $\eta \sim 2$, the material budget increases and the number of hits on track is also reduced, increasing the resolution width.

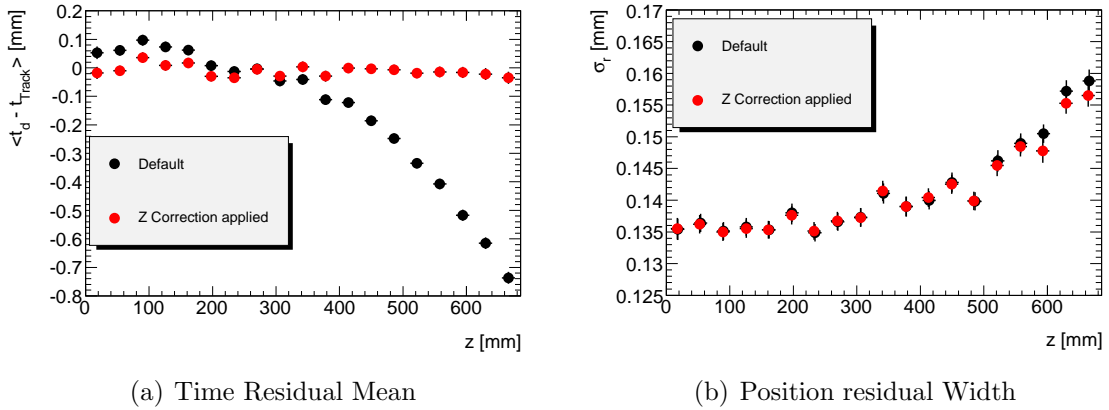


Figure 3.37: Time residual mean (3.37(a)) and position residual (3.37(b)) as a function of z for the barrel straws. The default track reconstruction is shown as black dots and the red dots correspond to a modification of the track reconstruction to compensate for the drift time shift depending on z .

Dependence on z coordinate in barrel

The T_0 values are calibrated at DTMROC level and no extra timing corrections are applied depending on the z hit position for the barrel or $x - y$ coordinate in the end-caps. In the way the T_0 values are computed, they are optimal, meaning by optimal an exact 0 ns time residual shift, for the average η distribution in the straw. The mean of this η distribution can be translated to a z coordinate for the barrel and $x - y$ coordinate in the end-caps. However, out of these points, time residuals offsets appear, motivated by the change in the time of flight of the particle and the signal propagation in the wire. The pulse amplitude is attenuated while signal travels in the straw wire. This, and the superposition of the signal directly sent to the read-out chip with the reflection from the end of the wire opposite to the read-out electronics, modifies the final amplitude collected by the electronics. The amplitude and width of the final pulse depends on the point where the particle crossed the straw. Larger signals exceed the threshold sooner, producing shorter drift times. Those effects are smaller in the short straws, producing an outstanding performance.

To test these effects and check for possible corrections, the time residual and the position residual were studied depending on the z coordinate in the barrel straws. The result is shown in Figure 3.37. A clear dependence is observed for the time residual mean, which decreases from about 0.1 ns when close to $z = 0$ mm to about -0.7 ns at the straw end. The position residual also increases when moving towards the edges of the straws, where the time residual is more shifted.

A timing correction was implemented in the track fitter to compensate for the time residual offset observed. An initial track fit to the default hits is done, and once the track is known, the z coordinate in the straw can be extrapolated. Using a simple parameterization, a second degree polynomial fitted to the data time residual, a time correction depending

on z was applied to the reconstructed hits. The track was refitted to those hits, which were corrected for the z time change. The result after applying this correction is also shown in Figure 3.37. The time residual mean dependence is fully corrected. On the other hand, the influence on the position residual is very low, mainly noticeable for $|z| > 500$ mm, where the time correction is larger. As expected, a timing correction of the order of 1 ns is not correcting the large dependence observed in the position residual. This indicates that the resolution is dominated by other parameters instead of the timing, such as signal amplitude and multiple scattering. Another reason is that the signal reflection, which contributes to produce wider pulses, produces larger uncertainty in the time measurement. Similar dependence has been observed in the Monte Carlo.

The implementation of this correction in the official ATLAS software release is not obvious because several changes in the reconstruction algorithms are needed to obtain the z coordinate and recalculate the TRT drift circles. As has been shown, the impact on the final resolution is negligible. For this reason, this correction will not be applied in the short term.

Dependence with drift time

The TRT detector is a gas based detector, which makes the resolution to be dependent on the drift distance. The drift distance is directly related to the drift time by the r - t relation. In the Figures 3.38(a) and 3.38(b), the residual width is shown as a function of the drift time for barrel A and end-cap A. Data and Monte Carlo are shown. The Monte Carlo distributions are shifted about two time bins to the right relative to the data due to different timing properties used in simulation. For short drift times, corresponding to particles getting close to the straw wire, the discrete production of clusters during the ionization of the charge particle in the gas has a larger impact on the final resolution than for electrons produced at large drift radius. Also, close to the wire, the stochastic processes of electron drift and amplification increase the timing uncertainties. This is clear in the residual width plots, where the residual decreases when the drift time increases. Same effect is observed in data and in Monte Carlo and between barrel and end-caps. In data, the resolution measured in data for end-cap is worse than for the barrels, as shown in previous sections. For very short drift times, the residual width improves again. This is assumed to be a feature produced by the track fitter for hits going very close to the wire, actually crossing the wire. The number of hits with drift time lower than 4 ns for data is very low.

Apart from the residual width measurement, the track fitter associates an error of the fitted track in the hit position. The distributions of the track error radius are shown in Figures 3.38(c), 3.38(d) for barrel and end-cap. There is no dependence on the drift time, which shows that all the drift time dependence for the resolution is handled by the TRT hit errors. In Figures 3.38(e), 3.38(f) the number of precision hits divided by the total number of hits as a function of the drift time is shown. This ratio indicates the quality of the fit to the hits, showing that more than 90 % of the hits are treated as precision hits, using their timing information in the fit. A small dependence is shown on the drift time, very similar for data and Monte Carlo and also between barrel and end-cap.

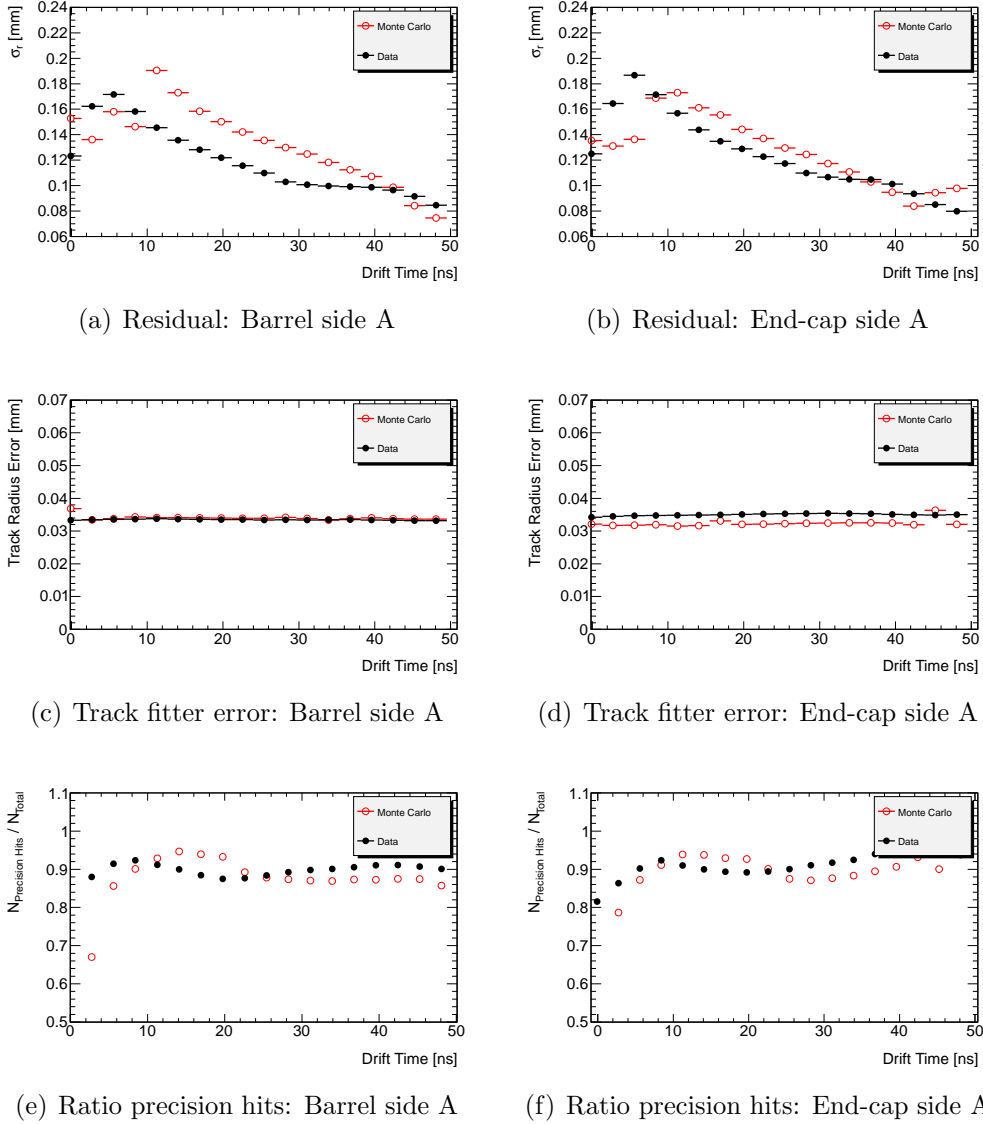


Figure 3.38: Position residual, track fit error and ratio of precision hits over total number of hits as a function of the hit drift time for barrel side A and end-cap side A.

Dependence on the particle momentum

The scattering of particles in the detector material decreases the detector performance. The multiple scattering decreases when the momentum of the particle increases and an improvement of the residual width is expected. In Figure 3.39, the residual width and the time residual width are presented as a function of the particle transverse momentum for barrel and end-cap. A large improvement is observed once the p_T increases due to the multiple scattering reduction and the increase of the ionization. The Monte Carlo describes the same dependence as the data, with a remarkably good agreement for the barrel time

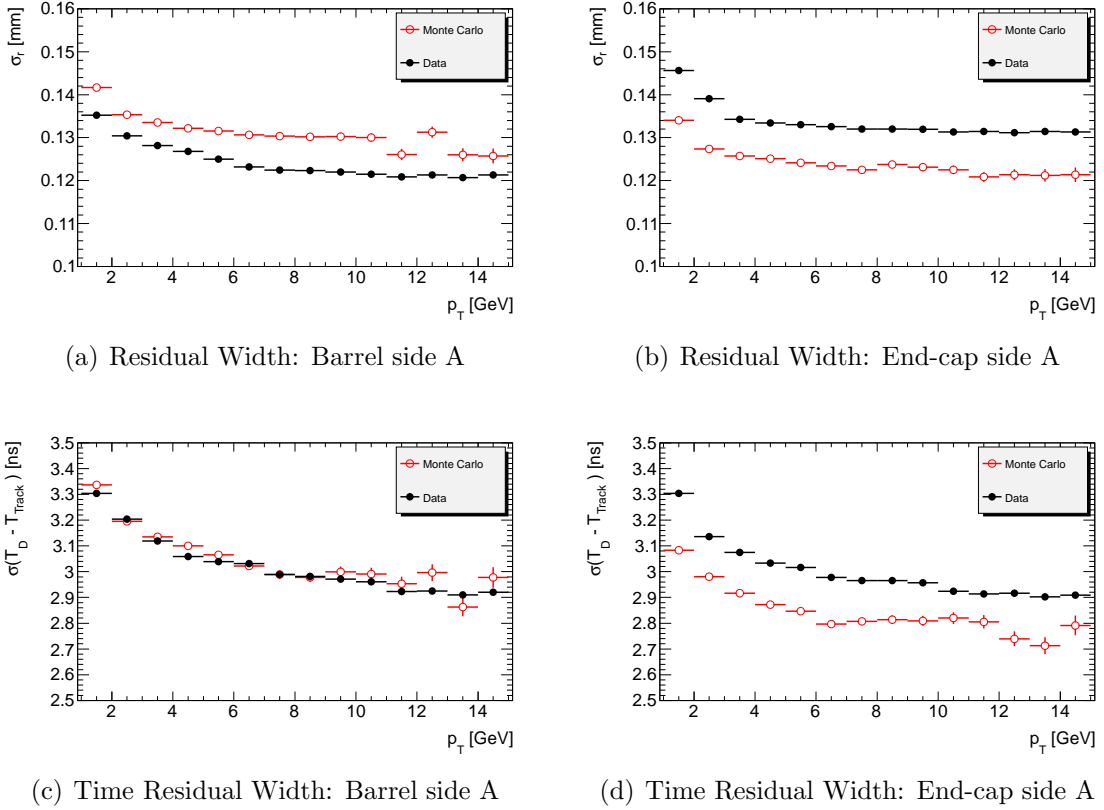
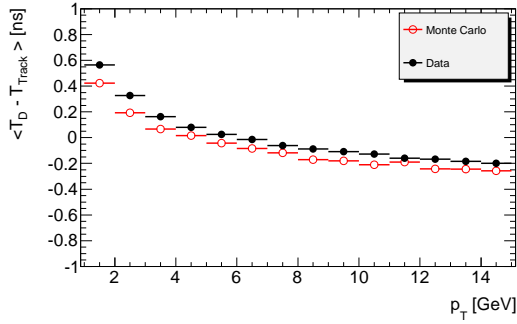


Figure 3.39: Position residual width and time residual width for data and Monte Carlo as function of the particle transverse momentum separately for barrel A and end-cap A.

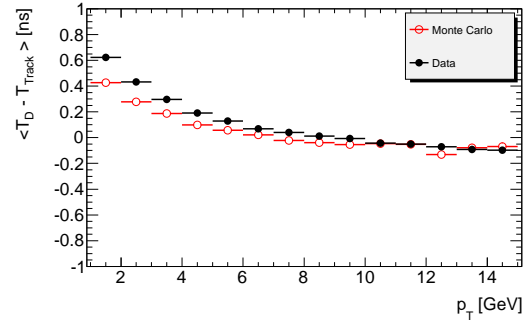
residual width. The barrel short straws for tracks with p_T over 15 GeV have shown to have a resolution of just $102 \mu\text{m}$ [4], far below the $130 \mu\text{m}$ design resolution. The larger p_T selection also reduces the residual degradation observed in earlier sections once getting further from the interaction point.

The T_0 values are expected to correct for the time of flight of the particles. If the particle momentum increases, the time of flight will be reduced leading to shorter measured drift times. Also, the larger momentum increases the ionization, which is reflected in the creation of larger signals. Larger signal crosses earlier the electronic threshold, producing also shorter measured drift times. The dependence of the time residual mean on the track momentum is presented in Figures 3.40(a) and 3.40(a). In the barrel, the time residual mean for low momentum particles is about 0.6 ns while for p_T around 14 GeV it is -0.2 ns. Similar values are observed for the end-cap, and same dependence is obtained in Monte Carlo.

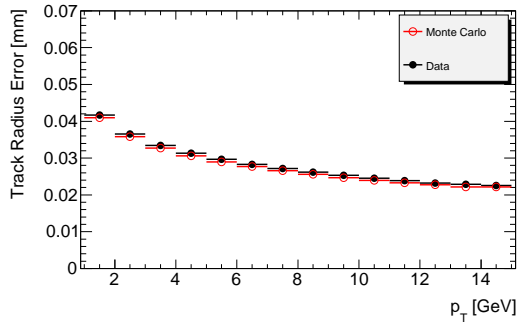
Time corrections have been applied depending on the particle momentum. However, the timing correction applied is negligible compared to the effect of the multiple scattering. For this reason, a global shift is applied in the T_0 values as shown in 3.2.1 by $\tilde{\mu}$. This



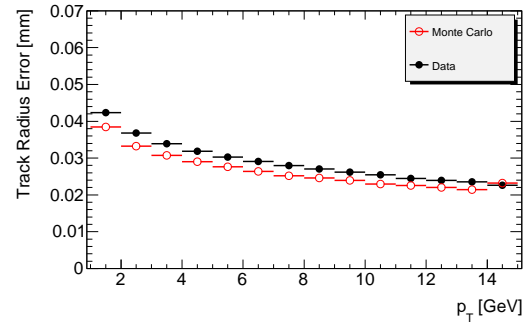
(a) Time Residual Mean: Barrel side A



(b) Time Residual Mean: End-cap side A



(c) Track fitter error: Barrel side A



(d) Track fitter error: End-cap side A

Figure 3.40: Time residual mean and track fitter error for data and Monte Carlo as a function of the particle transverse momentum, separately for barrel A and end-cap A.

shift is optimized to improve the performance of particles with p_T over 2 GeV, while the calibration uses tracks with $p_T > 1$ GeV.

The track fitter is designed to take into account the possible multiple scattering of the track. For this reason, the error assigned to the track in the hit position must reflect it. In Figures 3.40(c) and 3.40(d), the track fitter error for barrel A and end-cap A are shown as a function of transverse momentum. A large decrease is observed, which is in good agreement with the Monte Carlo distributions.

3.4.5 Heavy Ions calibration

The TRT is also important to measure large momentum particles in heavy ions runs. A dedicated track reconstruction setup has been prepared for such busy environments. The calibration framework settings are the same as in the proton-proton collisions, but with a limitation in the detector occupancy. For very central heavy ions collisions, TRT occupancies larger than 90 % can be reached. The track quality fit in such busy events is not good, and the amount of CPU time needed for pattern recognition is very large, making impossible to calibrate the runs within 24h. For these reasons, events with TRT

hits in more than 50% of the straws are rejected. This cut has been tested and the final influence observed is small global T_0 shifts. The T_0 and r - t relations obtained for heavy ions are compatible with proton-proton results and for this reason no more details are shown here.

3.5 TRT hit error definition

The track fitter, in order to get an optimal fit, requires an accurate estimation of the measurement error (δr_{hit}). In Figure 3.38 we can see how the nature of the TRT makes this error estimation very dependent on the drift time. In order to validate the errors, the pull of each hit can be calculated as:

$$Pull = \frac{\Delta r}{\delta r} \quad (3.21)$$

where Δr is the position residual of the hit defined as $\Delta r = r - r_{track}$. δr corresponds to the hit error and for unbiased evaluation of the residual it is defined as: $\delta r = \sqrt{\delta r_{hit}^2 + \delta r_{track}^2}$. δr_{hit} depends on the hit drift time, and δr_{track} is the error associated to the track. If the different errors associated to the hits and the track are correct, the width of the pull distribution must be equal to 1. For the TRT, the tube hits are removed from the pull evaluation and the final distribution is fitted to a Gaussian in the range ± 2.5 . This range was chosen because precision hits are converted to tube hits if the hit residual is larger than 2.5 times the hit error. In case the pull width is larger than 1, the hit error and the track error are underestimated, while if the pull width is below 1, the errors are overestimated. If the pull mean is different from 0, it indicates a systematic mis-alignment or incorrect r - t calibration.

The hit errors used by the TRT during the cosmic runs and in early 2010 were derived during the 2004 test beam. A detailed evaluation of the residual pull widths as a function of the drift time has shown that these errors were wrong. In Figure 3.41(a) the pull widths obtained as a function of drift time are shown. A large overestimation of the errors was used. One of the effects of this overestimation is presented in Figure 3.41(d), where the track to wire distance for precision hits is presented. The wrong error assignment biased the track fitter, giving wrong track estimations. In order to fix the error definition, an iterative calibration method was developed and the residual pulls are now checked on a 24h basis.

The pull for each time bin i is computed as:

$$Pull^i = \frac{\Delta r}{\sqrt{\delta r_{hit}^i{}^2 + \delta r_{track}^2}} \quad (3.22)$$

where δr_{hit}^i is the hit error for the time bin i used in reconstruction. The hit error of the time bin is updated as:

$$\delta r_{hit}^i{}' = \delta r_{hit}^i \times \sigma(Pull^i) \quad (3.23)$$

in which $\sigma(Pull^i)$ is the width of a gaussian distribution fitted to the pull distribution.

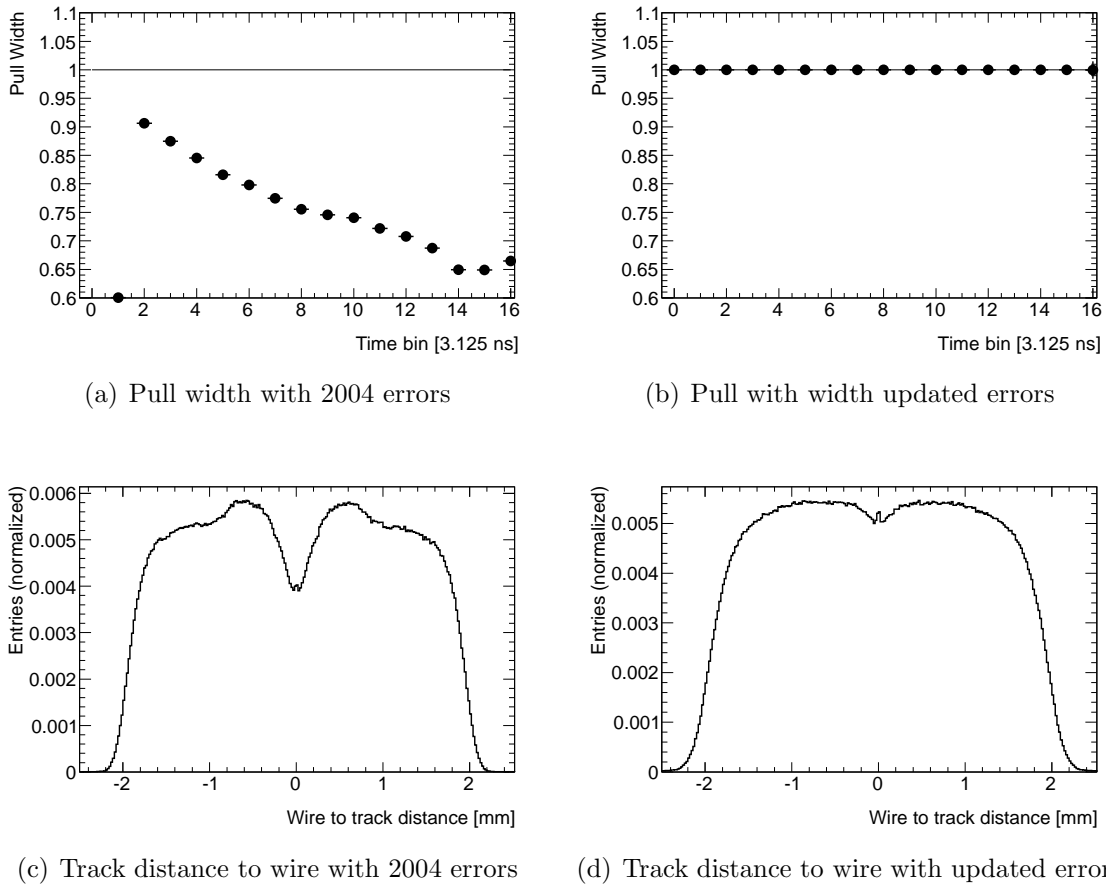


Figure 3.41: Pull width as a function of drift time bin for TRT hit errors computed in 2004 (3.41(a)) and after calibration is applied (3.41(b)). The track to wire distance is also shown before the calibration is applied (3.41(c)) and after (3.41(d)).

In three iterations, the pulls computed with the 2004 error from Figure 3.41(a) are corrected, returning pull widths exactly equal to 1 as shown in Figure 3.41(b). Also the track to wire distance is corrected, as presented in Figure 3.41(d). Other effects observed is the increase of precision hits per track.

The use of a wrong error definition leads to a final position residual which does not reflect the real detector resolution. If the errors are underestimated, the position residual will decrease, but this will not mean that the resolution is better. Also the number of hits will decrease and number of tube hits will increase, producing a worsening of the tracking efficiency.

In the Figure 3.42, the 2004 test beam errors are shown. Same distribution was used for barrel and end-caps adding $50 \mu\text{m}$ in quadrature for the end-caps. Also, the first error estimation using the error optimization algorithm done in May 2010 is shown. Barrel and end-cap have very different errors because by that time, the end-cap mis-alignments were

very large. By October 2010, after further developments in the TRT calibration and with a great improvement of the barrel and especially end-caps alignment, a new version of error was computed. In this new version, barrel and end-cap errors are much similar, but the end-cap errors definitions are larger due to the remaining mis-alignments.

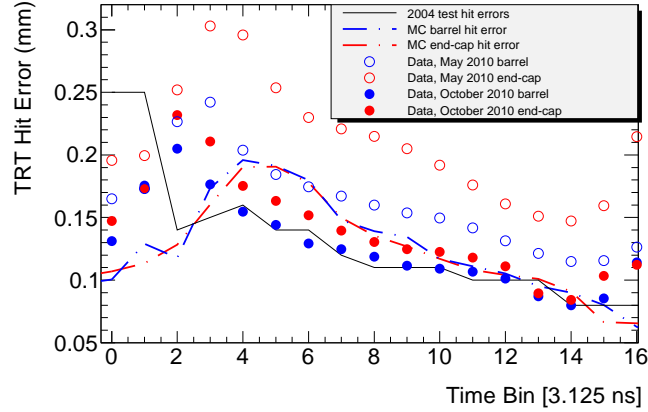


Figure 3.42: TRT hit error definitions computed in May and October 2010, compared to the 2004 test beam estimation.

3.6 Conclusion and outlook

In this chapter, the current TRT calibration method has been presented together with its performance. The calibration method is currently computing the best T_0 values and r - t relations for each run in order to get the best detector timing and therefore the best position residual and the best momentum reconstruction. My contribution is developing the algorithm. The work done in the last years in the TRT has allowed to get a resolution that nowadays is better than the designed one. The quality of the TRT timing allows to detect changes below 0.1 ns in LHC Clock signal, which is far beyond the expectations.

The error optimization has been a fundamental development to guarantee a good quality fit. Also the correct hit errors have been essential for a realistic resolution evaluation. Currently, two sets of errors are used, one for barrel and one for end-caps. In the future, in order to improve detector description, a lower granularity has to be used.

Additional corrections have been studied in order to minimize the different systematic effects observed. However, the size of these corrections is small enough to have a very low influence in the final resolution. The combination of all the corrections will be tested in the future, but very few μm improvement is expected. The main improvement to be done in the short term is the r - t relation at the layer and wheel level.

Chapter 4

Multiparticle correlations in proton-proton collisions

In order to find a needle in a haystack we not only need to know what a needle is, but also the properties of hay.

T. Sjöstrand, at Particle Physics Phenomenology course.

The ATLAS detector is designed and optimized to measure a wide range of high energy processes. The search of the Higgs boson, measurements of top quark properties, bottom quark physics and the search of Supersymmetry rely on a very low production rate. In the Figure 1.1 some of these processes cross-sections are shown together with the total proton-proton collision cross section. Differences of up to 8 orders of magnitude are expected between the processes of interest and the total cross-section. This implies a large amount of background events which need to be understood in order to discriminate against the signal processes. For this reason, the Quantum Chromodynamics (QCD), which is responsible for the large total cross-section in proton-proton collisions, needs to be studied in detail and the Monte Carlo generators have to describe it accurately. The study of QCD is very important because some processes, especially the ones at low energy, are not fully understood, and we need to analyze them and validate the used models. These models are implemented in the Monte Carlo generators that have multiple parameters, which are tuned to describe the data.

Particularly interesting is the description of the correlations between the particles produced in the proton-proton collisions. This chapter and the next one are devoted to the study of different properties related to the multiparticle correlations. This chapter is focused on the theory, models and methods description, while the next chapter is dedicated to presenting the results obtained in ATLAS with 2010 data.

In the next section, a brief review of Quantum Chromodynamics is given. The application of QCD to describe the multiparticle production is explained after that with some remarks about the most used Monte Carlo generators for *minimum bias* events in ATLAS. The measurement of the charged particle production in ATLAS and its properties is one of the earlier measurements done during 2010 at 900 GeV and 7 TeV. The charged particle distributions contain information about the particle correlations, which can be explored

using the factorial moments, cumulants and their ratios, the high order moments, so the theory behind these concepts is presented. Finally, an introduction to normalized factorial moments and the concept of intermittency in high energy collisions is discussed.

4.1 Quantum Chromodynamics

The protons are made of quarks that interact by exchanging gluons. The theory of the strong interactions, which explains the interaction between quarks and gluons, is known as Quantum Chromodynamics (QCD) [61]. QCD is a SU(3) non-abelian gauge theory of color charge. The quarks carry color charge and are represented as *triplets*: $\psi_q = (\psi_q^r, \psi_q^g, \psi_q^b)$, where r, g, b denote the color quantum numbers. The QCD group is represented as a set of unitary 3×3 matrices of determinant 1 called the adjoint representation. There are 9 linearly independent unitary matrices, one of which has determinant -1, so in total there are 8 independent directions in the adjoint color space. This means that there are 8 force carrying bosons, the gluons. One important feature is that the gauge bosons carry color charge, so they can interact with quarks and with each other (gluon self-interaction).

The QCD Lagrangian is given by:

$$\mathcal{L}_{QCD} = \sum_q \bar{\psi}_q^i ((i\gamma^\mu)(D_\mu)_{ij} - \delta_{ij}m_q)\psi_{qj} - \frac{1}{4}F_{\mu\nu}^a F^{a\mu\nu} \quad (4.1)$$

Where the sum runs over the number of quark flavors, 6 in the SM. ψ_{qj} denotes the 4-component Dirac spinors describing quarks of color j and flavor q . γ^μ is a Dirac matrix with μ being a Lorentz vector index, m_q are the quarks masses and D_μ is the covariant derivative in QCD:

$$(D_\mu)_{ij} = \delta_{ij}\partial_\mu - ig_s t_{ij}^a A_\mu^a \quad (4.2)$$

Here A_μ^a is the bosonic gluon field with color index a with 8 possible values, one for each degree of freedom of the gluon field and t_{ij}^a are the generators of the SU(3) group. g_s is the strong coupling which will be discussed later in detail. $F_{\mu\nu}^a$ is the gluon field strength for a gluon with color index a , given by:

$$F_{\mu\nu}^a = \partial_\mu A_\nu^a - \partial_\nu A_\mu^a - g_s f_{abc} A_\mu^b A_\nu^c \quad (4.3)$$

where f_{abc} are the structure constants of the SU(3) symmetry group. The subscripts a, b, c take values between 1 and 8. The last term in Equation 4.3, arising from the non-abelian nature of QCD, is responsible for the gluon self-interaction. From the Lagrangian, we can see that the fundamental parameters of QCD are the quark masses (m_q) and the strong coupling constant g_s , more often used as $\alpha_s = g_s^2/4\pi$.

Quantum Chromodynamics has two important and unique properties:

- Asymptotic freedom [63]: The running coupling constant becomes weak at high energies, which is equivalent to short distances, so quarks and gluons interaction probability is very low.

- **Color confinement:** The force between two quarks increases when they are separated and an infinite amount of energy is needed to separate them. For this reason, quarks are bound in quark groups known as hadrons, which are colorless objects. Two types of hadrons exist: mesons, made of one quark and one antiquark, and baryons made, of three quarks or three antiquarks. The confinement is the reason why it is not possible to observe free quarks or gluons propagating over macroscopic distances. If two interacting quarks are separated, the energy increases, such that new interacting particles are created and new colorless hadrons are formed.

These two properties are related to the strong coupling constant, often called *running coupling constant*, which runs logarithmically with the momentum scale (Q):

$$Q^2 \frac{\partial \alpha_s}{\partial Q^2} = \frac{\partial \alpha_s}{\partial \ln Q^2} = \beta(\alpha_s) = -(b_0 \alpha_s^2 + b_1 \alpha_s^3 + \dots) \quad (4.4)$$

with:

$$b_0 = \frac{33 - 2n_f}{12\pi} \quad (4.5)$$

$$b_1 = \frac{153 - 19n_f}{24\pi^2} \quad (4.6)$$

which are known as the 1-loop and 2-loop coefficients. n_f corresponds to the number of quark flavors, which depends on the momentum scale (Q : $m_q < Q$). This is a consequence of the renormalization method used in perturbative QCD to remove ultraviolet divergences. The predictions for the observables are expressed in terms of the renormalized coupling $\alpha_s(\mu_R)$, where μ_R is the unphysical renormalization scale. When the theory is applied to a different scale Q , the coupling constant adjusts to the new scale following the Renormalization Group Equation (RGE), which is the Eq. 4.4. This equation allows to measure the coupling strength at one scale and calculate it at any other scale in the perturbative regime.

At leading order an exact solution of 4.4 is given by:

$$\alpha_s(Q) = \frac{1}{b_0 \ln(Q^2/\Lambda_{QCD}^2)} \quad (4.7)$$

The integration constant Λ is referred to as the scale of QCD. This parameter denotes when perturbation theory is not applicable any more.

The value of the strong coupling constant has been measured in several experiments. The latest world average evaluated at the scale corresponding to the Z boson mass ($Q^2 = M_Z^2$, with $M_Z = 91.2$ GeV) in 2009 is [62]:

$$\alpha_s(M_Z) = 0.1185 \pm 0.0007$$

while the QCD scale is:

$$\Lambda_{\overline{MS}} = (213 \pm 9) \text{ MeV}$$

These values are based on measurements that use Next-to-next-to leading order (NNLO) QCD perturbation theory. The final value of the QCD scale depends on the renormalization scheme used.

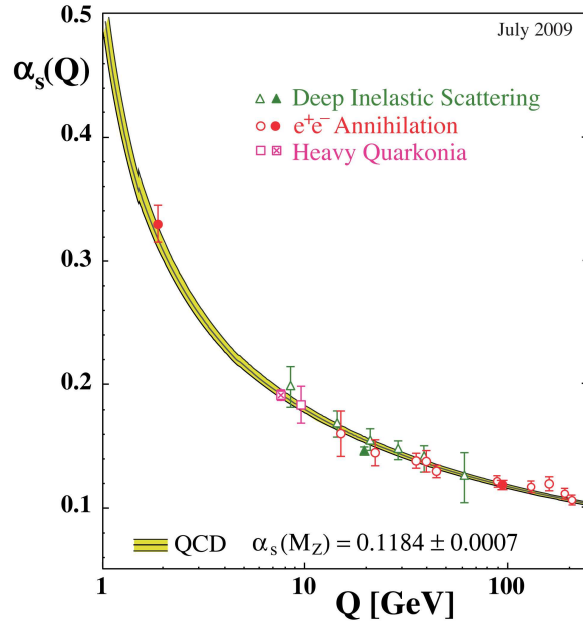


Figure 4.1: Summary of the measurements of α_s as a function of the respective energy scale Q . The band is the best fit QCD prediction [62].

In Figure 4.1, the measurements for the strong coupling at different Q are shown. In addition, the best QCD evolution fit to the data is presented, which shows strong evidence for the correct prediction by QCD of the scale dependence of the strong coupling. The QCD coupling decreases with energy, giving origin to the asymptotic freedom. This weak interaction at large energies allows to apply perturbative theory for QCD, with a fast convergence for high energy processes, with a coupling constant around 0.1 in the 100 GeV-TeV range. Perturbative QCD (pQCD) is the main tool to calculate cross-sections and kinematic distributions in high-energy collider physics. Towards smaller energies, the coupling diverges rapidly for energies below 1 GeV and for the QCD scale (~ 200 MeV) the coupling nominally becomes infinite^I. so the perturbative techniques cannot be applied any more. In this regime, phenomenological models fitted to data are used.

4.2 Multiparticle production in proton-proton collisions

For the multiparticle production in proton-proton collisions, several different physics processes contribute to the observed activity. Depending on the final state, the components can be separated in elastic and inelastic. Moreover, the inelastic interaction can be divided into single (sd), double (dd) and non-diffractive (nd) physics. Based on this description,

^IThe strong coupling running parameterization is only valid as a perturbative result, so QCD is not exhibiting a divergence for $Q \rightarrow \Lambda$.

the final total cross-section for proton-proton collisions can be written as:

$$\sigma_{tot} = \sigma_{el} + \sigma_{inel} = \sigma_{el} + \sigma_{nd} + \sigma_{sd} + \sigma_{dd} \quad (4.8)$$

For elastic processes, the only exchanged quantity between the initial protons is momentum, and no excitation of the initial protons is produced, having in the final state only two protons. The inelastic scattering covers all the other possibilities where new particles are produced. For diffraction, only momentum is exchanged between the protons, but one or both gets excited. In the single (double) diffractive topologies, the final state looks like the decay of an excitation of one (two) of the initial protons. In these cases, in the interaction between the protons there is no color exchange, and particles are produced dominantly in the forward directions with a gap at low rapidity. In non-diffractive events, the constituents of the protons, the partons, interact involving a color flux between them. This is characterized by a large production of particles mainly in the central rapidity region, containing no gap. A schematic view of the different processes is shown in Figure 4.2.

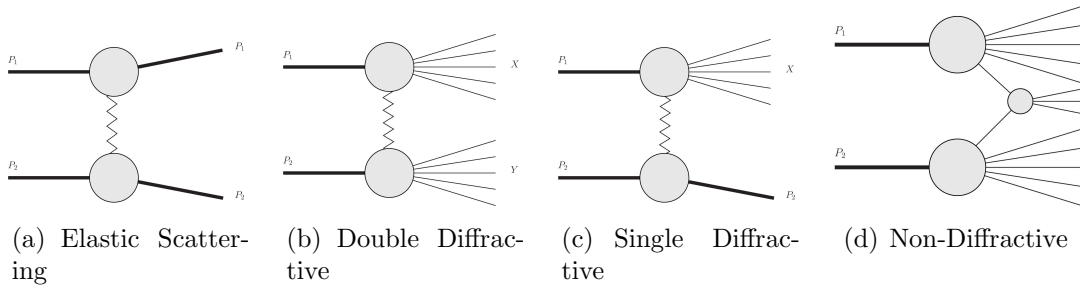


Figure 4.2: Schematic representation of the different possible processes for proton-proton collisions. In the Single and Double Diffractive events, a colorless object (a Pomeron) is exchanged between the two protons while in Non-Diffractive events a color flux it is possible.

Experimentally, the term minimum bias (MB) is used to designate event selection with the lowest possible trigger bias. The final definition depends on the detector and the trigger system used, but as an approximation it can be considered as the inelastic component of the particle production, so this section is focused on this component. The largest contribution to the inelastic cross-section is due to the non-diffractive events, followed by double and single diffractive respectively.

The diffractive processes are not fully understood yet, so different approaches exist to model them. The most used method involves the Regge theory in which the interaction between protons is described by the exchange of a colorless and flavorless particle known as Pomeron. This model, together with the application of the optical theorem [64] allows to compute the total and the elastic cross-sections [66] in reasonably good agreement with data [65]. One common parameterization of the total cross-section for proton-proton colliders is:

$$\sigma_{tot} = X^{pp} s^\epsilon + Y^{pp} s^{-\eta} \quad (4.9)$$

where $X^{pp} \approx 21.7$, $Y^{pp} \approx 56.1$, $\epsilon \approx 0.0808$ and $\eta \approx 0.4525$ are parameters fitted to the data. The relation with the elastic cross-section is given by:

$$\sigma_{elas} = \frac{\sigma_{tot}^2}{16\pi B_{elas}} \quad (4.10)$$

Here B_{elas} is the elastic slope which has to be measured in data.

In the non-diffractive events, the interactions are between the constituents of the protons, the partons. The hadrons consist of a number of valence quarks (uud for the proton) and an infinite number of gluons and light quarks known as the *sea*. Each parton carries only a fraction x of the total hadron four-momentum and the probability to find a parton a , inside a beam of hadrons P carrying a fraction x of the total momentum is described by the Parton Distribution Functions (PDFs): $f_{a,P}(x_a, Q^2)$. The PDFs depend on the scale of the process (Q) and this dependence is often described by the DGLAP (Dokshitzer–Gribov–Lipatov–Altarelli–Parisi) evolution equations [67]. However, the dependence on x and the value at a certain reference Q_0 needs to be measured in data. For a given perturbative order and a renormalization scheme used, the PDFs are universal, so they can be measured in one experiment, such as deep inelastic scattering experiments, and be used in other, such as hadron colliders. Nowadays different groups provide the PDFs used in the Monte Carlo generators based on latest measurements. Among the most used ones are CTEQ [68] and MSTW [69]. In Figure 4.3(a) the CTEQ PDFs are shown for up and down quarks and gluons inside a proton at $Q^2 = 10000$.

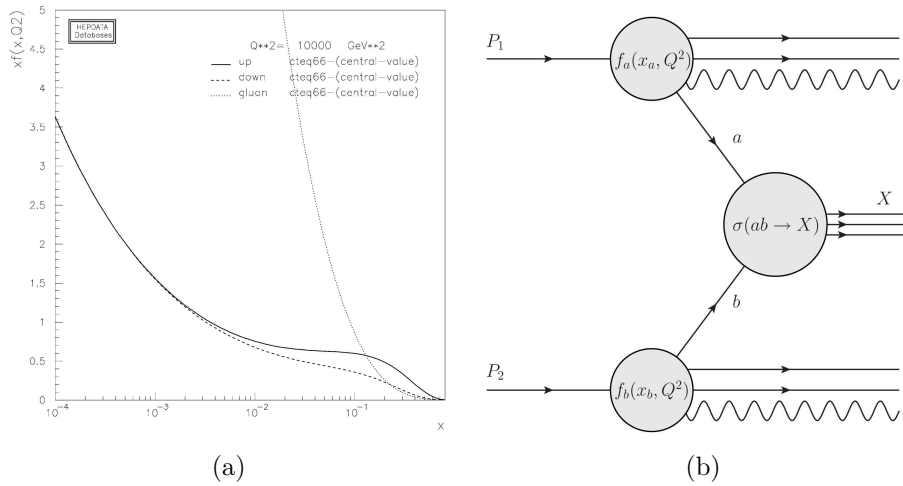


Figure 4.3: In Figure 4.3(a) the CTEQ PDFs [68] for up and down quarks and gluons for protons at $Q^2 = 10000 \text{ GeV}^2$ are shown. The Figure 4.3(b) shows the schematic view of a proton-proton scattering.

The cross-section for a given non-diffractive process ($pp \rightarrow X$) can be written as the sum over all possible initial partons a, b of the factorized product of the partonic cross-sections

($\hat{\sigma}_{ab \rightarrow X}$) and the PDFs for each parton:

$$\sigma_{pp \rightarrow X} = \sum_{a,b} \int dx_a dx_b f_{a,P_1}(x_a, Q^2) f_{b,P_2}(x_b, Q^2) \hat{\sigma}_{ab \rightarrow X} \quad (4.11)$$

A diagram of a non diffractive process is shown in Figure 4.3(b). The total non-diffractive cross-section is given by the sum over all possible final states X :

$$\sigma_{nd} = \sum_X \sigma_{pp \rightarrow X} = \sum_X \sum_{a,b} \int dx_a dx_b f_{a,P_1}(x_a, Q^2) f_{b,P_2}(x_b, Q^2) \hat{\sigma}_{ab \rightarrow X} \quad (4.12)$$

Some corrections need to be applied. Particularly important is the multiple parton interaction, in which in a single proton-proton collision more than a single parton-parton interaction occurs. This will be discussed later in the Monte Carlo section. The prediction done up to now is done at parton level, however, in the detector only hadrons and leptons are measured. In the next sections the parton showers and the final hadronization, which contribute to the final particles are explained.

4.2.1 Parton showers

In the previous section, only initial and final partons have been taken into account. However, the quarks and the gluons involved in the interaction carry color charge, so the partons can radiate soft and collinear gluons ($q \rightarrow qg$, $g \rightarrow gg$) and gluons also can emit quark-antiquark pairs ($g \rightarrow q\bar{q}$), which is known as parton branching. The outgoing partons after the radiation can undergo branching as well, producing the so-called parton showers. Depending whether the emissions took place before the hard scattering or after, the processes are known as *initial* or *final state radiation*.

The low momentum involved in the processes makes the low order perturbative QCD failing to describe the parton showers, and high order calculations get too complicated for practical use. The usual approach is to give an approximate perturbative treatment to all orders based on the DGLAP evolution equation [70].

4.2.2 Hadronization

In QCD, the confinement means that quarks and gluons cannot propagate freely over macroscopic distance. When two quarks become separated, at some point it is more energetically favorable to spontaneously create a new quark-antiquark than to keep the two quarks connected. The quarks and gluons produced in the parton showers and in the scattering need to be combined to produce colorless objects, and this process is known as hadronization. This is a low energy process and cannot be explained using perturbative QCD. This is one of the less understood processes in the whole QCD domain, but phenomenological models are able to describe it in good agreement with data. Hadronization is assumed to be universal, so models describing the electron-positron data are expected to describe well the hadron collisions. The Lund string model [71] and the cluster model [72] are among the most popular ones.

In the Lund model, a color flux tube, string, is stretched between the quark and the antiquark. This model is based on the assumption of the linear color confinement. When the quark and the antiquark move apart along the string, they lose kinematic energy that is converted into potential energy stored in the string spanned between them. The quark-antiquark fluctuations inside the string field can make the transition and become real particles absorbing energy from the initial string. The creation of the quark-antiquark makes the string to split in two new strings and this process continues ongoing until only ordinary hadrons remain. In this framework, more complicated topologies are included, in which gluons are represented as transverse kinks in the color strings. In addition, the baryon production is possible by allowing strings to break also by the production of diquarks-antidiquarks, which are loosely bound states of two quarks or two antiquarks. This model describes very well the data and is the most used nowadays. It was originally implemented in Jetset and currently is part of Pythia [75].

Some of the particles produced after the hadronization are unstable. Before arriving to the detector, these particles decay and only stable particles are detected. For this reason, the different branching ratios and decay modes for the produced hadrons have to be taken into account for the final state description.

4.2.3 Monte Carlo generators

In collider physics, to compare theory with the measured data, Monte Carlo (MC) generators are used to simulate events following the expected theory. As we have seen, the particle production in proton-proton collisions is a combination of many different processes. Some of them can be accurately described using pQCD, however, others are not fully understood yet and cannot be explained using the fundamental principles of the Standard Model. For such processes, the use of phenomenological models, which parameters are adjusted (*tuned*) to describe experimental data, is unavoidable. Detailed up-to-date information on the different techniques implemented by some of the most used MC generators is presented in [73].

The different model choices together with the tune of the parameters for the different generators to the current data, reduces the predictive power of the Monte Carlo generator for minimum bias at new energies. As an example, the cross-sections for inelastic processes predicted at 900 GeV and 7 TeV by Pythia [75] and Phojet [76] generators are shown in Table 4.1. For these predictions, both generators were tuned to UA5 and Tevatron data [27]. Phojet predicts a total inelastic cross-section around 5-10 % larger than Pythia and a slightly different splitting between the diffractive and non-diffractive components. Similar effect is seen for the number of particles produced in the central region, which is shown in Figure 4.4. Due to the different predictions for different generators and multiple tunes for several observables, the measurement of these distributions and their properties in data at the new energies is fundamental to improve the Monte Carlo description. In the following, some remarks about the Pythia and Phojet generators are given. These generators are used later in this thesis to study the multiparticle correlations. A very detailed comparison between Pythia and Phojet for minimum bias predictions is given in [74].

Process	900GeV [mb]	7 TeV [mb]
Pythia		
σ_{nd}	34.4	48.5
σ_{sd}	11.7	13.7
σ_{dd}	6.4	9.3
σ_{inel}	52.5	71.5
Phojet		
σ_{nd}	39.9	61.6
σ_{sd}	10.5	10.7
σ_{dd}	3.5	3.9
σ_{cd}	1.1	1.3
σ_{inel}	55.0	77.4

Table 4.1: Cross-section for the inelastic components for $\sqrt{s} = 900$ GeV and 7 TeV as predicted by Pythia and Phojet [27].

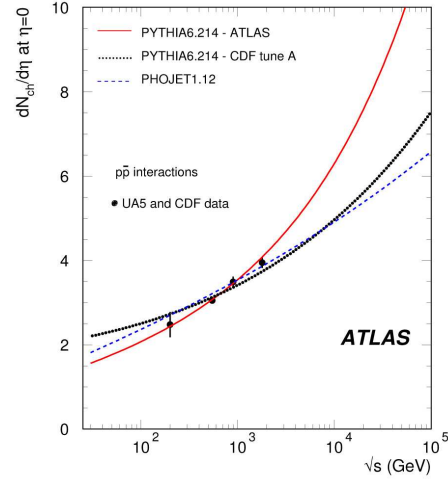


Figure 4.4: Central charged particle density for non-single diffractive inelastic events as a function of energy [27].

Pythia

In Figure 4.5, an overview of the main mechanisms simulated in Pythia for a hard scattering and their interplay is shown. The hard interaction between the partons of the protons is computed with a matrix element (ME) at leading order, where several $2 \rightarrow 1$, $2 \rightarrow 2$ and $2 \rightarrow 3$ processes are implemented. These processes cross-sections are convoluted with the Parton Density Functions (PDF). Pythia makes use of several PDFs, such as CTEQ and MRST at LO and NLO and allows also the use of external libraries. The initial state and final state radiation (ISR and FSR) of the partons are included using parton showers ordered by transverse momentum^{II}.

Pythia includes the possibility of having multiple partonic interactions occurring in a single hadron-hadron collision. One of the reason to include the Multiple Partonic Interaction (MPI) is because at low transverse momentum transfers, which are dominated by t-channel gluon exchange, the differential QCD partonic cross-sections behaves as:

$$d\hat{\sigma}_{2 \rightarrow 2} \propto \frac{dp_t^2}{p_t^4} \quad (4.13)$$

The integrated cross-section for a given lower transverse momentum cutoff exceeds the total proton-proton cross-section for cutoff values (4-5 GeV) well above the QCD scale (~ 0.2 GeV). This cross-section is calculated by parton interaction, however the protons include several partons, which can interact, producing more than one interaction. If an

^{II}Pythia release 6 allows to choose the parton showering order in transverse momentum or virtuality while since release 8, only p_t dependence is available

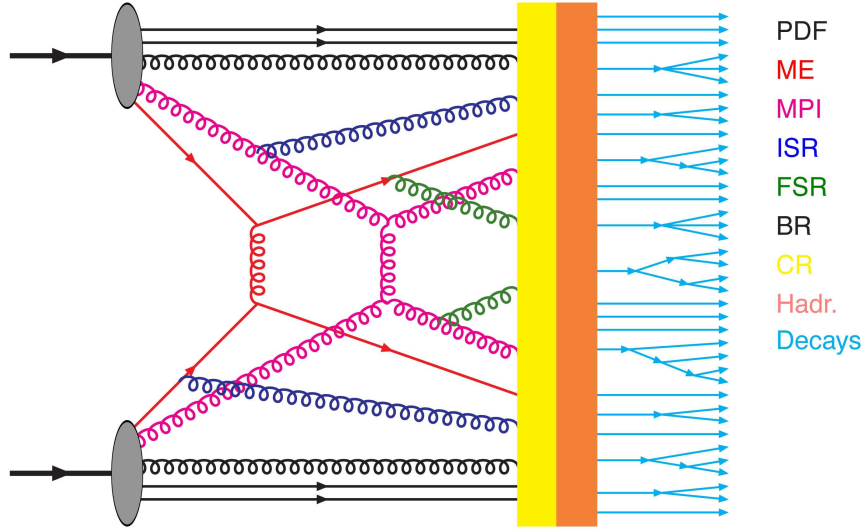


Figure 4.5: Schematic representation of a proton-proton event. Several processes are included such as Parton Density Functions (PDF), Matrix Element (ME), Initial and Final State Radiation (ISR and FSR), Beam Remnant (BR), Color Reconnection (CR), Hadronization and Decays. T. Sjöstrand, at Particle Physics Phenomenology course.

event contains two parton-parton interactions, it will count twice for $\sigma_{2\rightarrow 2}$, but only once for σ_{tot} . Assuming that the interactions are independent, the number of interactions per event is distributed according to a Poissonian distribution:

$$P_n = \langle n \rangle^n \frac{\exp(-\langle n \rangle)}{n!} \quad (4.14)$$

where $\langle n \rangle$ is the average number of collisions per interaction. The MPI together with color screening fix the partonic cross-section divergence at low momentum. The amount of multiple interactions depends on the matter distribution of the hadrons and the overlap between them when colliding. Pythia can use different shapes, among which the double Gaussian matter distribution is the most popular. One of the results of the MPI is an increase of the final state activity, which produces an enlargement of the total particles produced.

The MPI is not fixing completely the divergences at low momentum. To compute the differential cross-section, Pythia adds a regularization factor to the differential cross-section which looks like:

$$\frac{\alpha_s(p_t^2 + p_t, min^2)}{\alpha_s(p_t^2)} \frac{p_t^4}{(p_t^2 + p_t, min^2)^2} \quad (4.15)$$

Where p_t^{min} is an unknown parameter, which regulates the smooth transition between soft and hard QCD. This correction is based on the principle of color screening, in which partons are unable to resolve each other at low momentum. The wavelength for the exchanged particle in the interaction can be approximated as $1/p_t$, so for low momentum it becomes larger than the typical color-anticolor separation distance. In this case, the particle couples

to an average color charge which vanishes when $p_t \rightarrow 0$, hence leading to suppressed interactions.

After the scattering and the parton showering, a number of leftover partons are found in the proton beam remnants (BR), which carry momentum, flavor numbers and are color connected with the scattered partons. These partons are integrated with the rest of quarks and gluons by a process known as Color Reconnection (CR). In this process, there is a certain probability for partons produced at different steps to interarrange in a way that reduces the total color string length. It has been observed that in order to describe the average momentum of pp collisions, some amount of color reconnection is needed. This process has a significant impact on the final amount of particles produced and their transverse momenta, so its tune has to be done carefully. After the color reconnection is done, the partons are hadronized using the Lund string model. In the last step, unstable hadrons and leptons are decayed.

Up to now the generic chain for an event production in Pythia has been presented. For the simulation of non-diffractive events, Pythia uses all hard QCD processes with their expected cross-sections combined with low p_T events. Then the whole machinery for multiparton interactions, parton showers and hadronization is applied.

The diffraction is handled using the Pomeron as mediator, in which the Pomeron is treated as a multiple gluon state with the quantum numbers of the vacuum. In single diffractive events, one proton emits a Pomeron reducing the proton momentum. The Pomeron interacts with the other proton to produce a system of particles. The Pomeron-hadron collision can be handled as a normal hadron-hadron non-diffractive event, making use of MPI, ISR, FSR, CR and hadronization. Double diffractive collisions are treated similarly, with two Pomeron-proton interactions.

A very general overview of Pythia has been presented; of course the Monte Carlo generator field is much more complex, but I only want to give a general overview of the different effects simulated which can influence the final particle production and their correlations. In addition, few Pythia tunes are available, the used ones in this work will be described in the next chapter.

Phojet

Phojet provides an alternative approach to Pythia to model the charged particles production in hadrons. The main feature of Phojet is the use of the Dual Parton Model (DPM) to describe the soft interactions, while hard interactions are calculated using pQCD. Phojet can be considered as a two-component model with a transition between the soft and hard regions at a given p_t^{min} . The DPM is a non-perturbative approach, which uses topological expansions of QCD providing a complete phenomenological description of soft processes in hadron collisions. The mechanism of Pomeron exchange is the core of the Dual Parton Model. To preserve the total cross-section at low momentum interactions, in which the soft cross-section is larger than the total one, Phojet includes multiple Pomeron exchanges (soft interactions). For increasing center of mass energy, the hard cross-section increases significantly, and multiple hard parton scatterings are implemented to compensate for this effect.

The parton showering can be included using the leading-log approximation. Phojet is interfaced to Pythia to simulate the final hadronization. Another interesting feature of Phojet is the reduced number of parameters to be tuned with respect to Pythia.

4.3 The charged particle multiplicity distribution and its correlations

The charged particle distribution is defined as:

$$P_n = \frac{\sigma_n}{\sigma_{inel}} \quad (4.16)$$

where σ_n is the cross-section of a n-particle production processes. The charged particle distribution is one of the most fundamental observables in any high-energy collision processes and has been measured and studied in detail at different energies and colliders. For recent reviews on charged particle multiplicities from a theoretical and experimental results, the reader is referred to [79] and [77].

For independent emission of single particles, the expected multiplicity must follow a Poissonian distribution. The deviation from this shape reveals correlations in the particle production. These correlations are the signatures of the mechanisms involved from PDFs to the final hadronization and decay processes, which produce the final-state particles.

The shape and the correlations of the charged particle multiplicity distribution can be measured using the normalized factorial moments defined as [77]:

$$F_q = \frac{\langle n(n-1)\dots(n-q+1) \rangle}{\langle n \rangle^q} = \frac{\sum_{n=1}^{\infty} n(n-1)\dots(n-q+1)P_n}{\left(\sum_{n=1}^{\infty} nP_n\right)^q} \quad (4.17)$$

The factorial moment of order q corresponds to the integral over all the q -particle density and reflects all the correlations in particle production. For a Poissonian distribution, all the factorial moments are equal to 1, other values imply the existence of correlations in the particle production. For correlated production, the factorial moments are larger than the unity while for anti-correlated production the F_q are smaller than one. By definition the factorial moments are always positive.

To access the genuine particle correlations for q -particles production, the normalized cumulant moments are used. They are defined by:

$$K_q = F_q - \sum_{a=1}^{q-1} \frac{(q-1)!}{a!(q-a-q)!} K_{q-a} F_a \quad (4.18)$$

The cumulants of rank- q represent genuine q -particle correlations not reducible to the product of lower order correlation. For independent particle production, defined by Poisson distribution, the K_q are equal to 0. Positive values of the cumulants indicate a correlation in the particle production while negative values represent anti-correlation.

One very powerful tool to study the charged particle multiplicity is the use of high order moments H_q . The F_q and the $|K_q|$ increase with the order q , so it is very useful to define the ratio H_q

$$H_q = \frac{K_q}{F_q} = 1 - \frac{\sum_{a=1}^{q-1} \frac{(q-1)!}{a!(q-a-q)!} K_{q-a} F_a}{F_q} \quad (4.19)$$

These H_q moments reflect the genuine q -particle correlation integral relative to the density integrals. It gives the genuine q particle correlation with respect to the whole spectrum of correlations for q or less particles. $|K_q|$ and F_q increase with order q when correlations exist, while H_q have the advantage of being of the same order of magnitude which makes easier to represent and study it than the factorial moments and cumulants

4.3.1 Analytical QCD prediction

The H_q have been calculated for the soft gluon multiplicity distribution at different orders of perturbative QCD [78]:

- DLLA: In the Double Leading Logarithmic Approximation H_q decreases asymptotically to 0 as q^{-2}
- MLLA: In the Modified Leading Logarithmic Approximation H_q has a minimum at $q \sim 5$ and then rises asymptotically to 0.
- NLLA : In the Next-to-Leading Logarithmic Approximation H_q has a positive minimum at $q \sim 5$ and then increases to a positive constant value.
- NNLLA: In the Next-to-next-to-Leading Logarithmic Approximation H_q has a minimum at $q \sim 5$ and for large q values, it shows quasi-oscillations around 0.

The main difference between the different orders is how the energy and momentum conservation is implemented, where NNLLA gives the most accurate treatment. These dependences are shown in Figure 4.6.

The same behavior is expected for the multiplicity distribution when the Local Parton Hadron Duality^{III} (LPHD) hypothesis is assumed. For this reason, when quasi-oscillations are observed in data, they are often understood as a confirmation of the LPHD and high-order QCD.

4.3.2 Phenomenological descriptions

In the past, the Negative Binomial Distributions (NBD) has been used with certain success to describe the charged particle distribution. The NBD is defined by:

$$P^{NBD}(n, p, k) = \frac{\Gamma(n+k)}{\Gamma(n+1)\Gamma(k)} (1-p)^n p^k \quad (4.20)$$

^{III}This assumes that calculated distributions at parton level describe the hadron observables up to some constant factor.

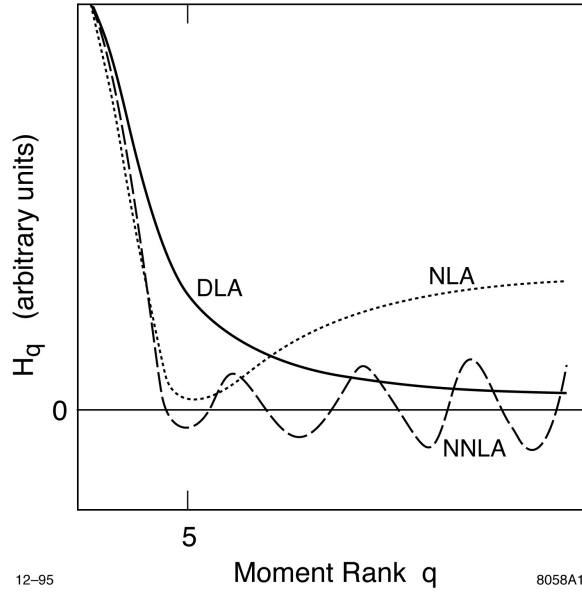


Figure 4.6: Qualitative behavior of H_q for various perturbative QCD approximations [78].

It gives the probability for n failures and $k - 1$ successes in any order before k 'th success in a Bernoulli experiment with a success probability p . The distribution converges to a Poisson distribution if $k_{-1} \rightarrow 0$. The mean of the distribution $\langle n \rangle$ is related to p by:

$$\frac{1}{p} = 1 + \frac{\langle n \rangle}{k} \quad (4.21)$$

Using this property, the common form used to describe the charged particle multiplicity using NBD is:

$$P_{\langle n \rangle, k}^{NBD}(n) = \frac{\Gamma(n+k)}{\Gamma(n+1)\Gamma(k)} \frac{1}{(1 + \frac{\langle n \rangle}{k})^k} \left(\frac{\frac{\langle n \rangle}{k}}{1 + \frac{\langle n \rangle}{k}} \right)^n \quad (4.22)$$

The negative binomial distributions have been used to describe the experimental multiplicity distributions in a wide variety of processes and over a large energy range. The NBD describes qualitatively the distribution of charged particles in almost all inelastic, high energy processes, however the physical origin for charged-particle distributions to follow NBD has not been fully understood. The NBD shape of the multiplicity distribution can be deduced using the *clan* model [80]. In this model, a particle can emit additional particles by decay or fragmentation, producing a cascade. The particles produced by the same ancestor are contained in a clan, and the ancestors are produced independently following a Poisson distribution. Assuming that the probability to produce a certain numbers of particles in the cluster is proportional to the number of particles already produced, it is possible to shown that P_n follows a NBD [77].

The NBD distribution does not describe the shape of the charged particle multiplicity at very large energy as the LHC ones. It was shown by the UA5 [81], with proton-antiproton

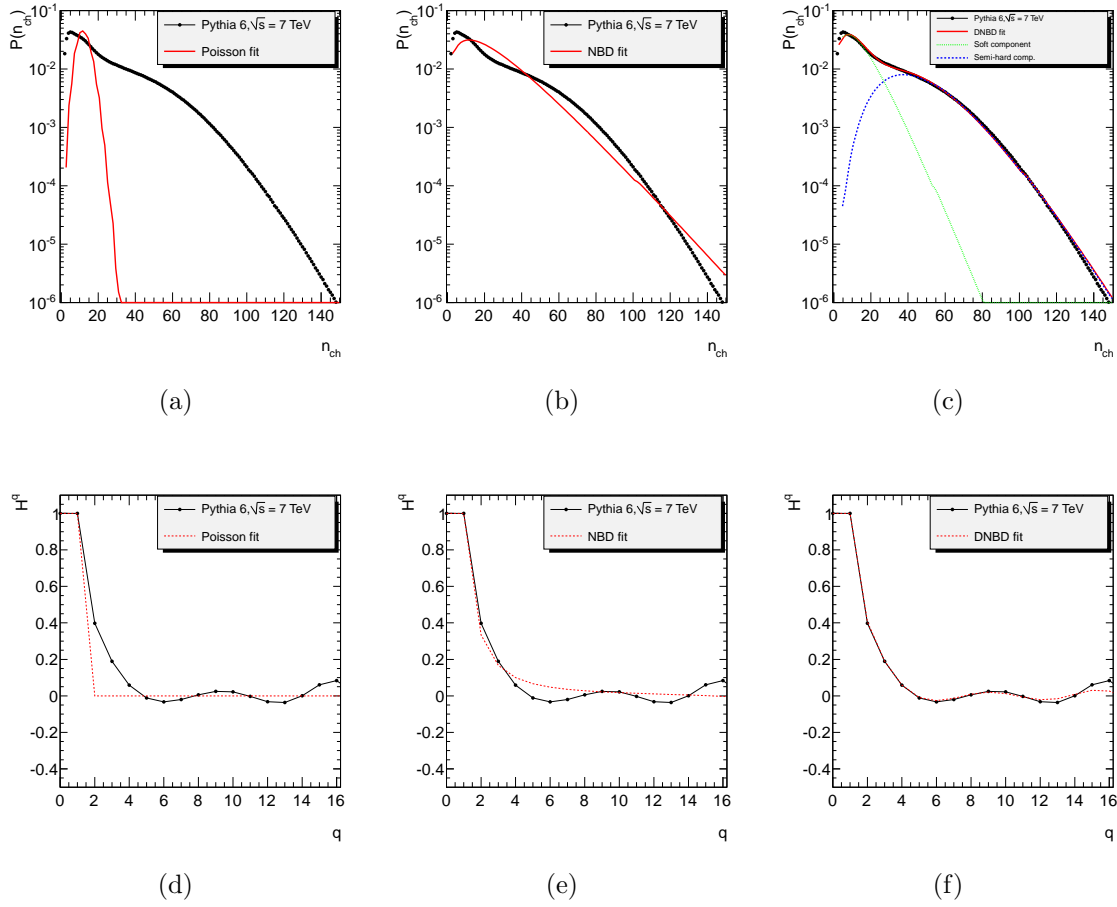


Figure 4.7: The figures in the top row show the charged particle multiplicity generated with Pythia 6 for $\sqrt{s} = 7$ TeV and its fit to different parameterizations. Figure 4.7(a) corresponds to a Poissonian distribution, in Figure 4.7(b) the NBD is used and in Figure 4.7(c) two negative binomial distributions are used and the components of each NBD are shown. The bottom figures correspond to the high order moments for the MC distribution and the different parameterizations: Figure 4.7(d) corresponds to the Poissonian distribution, in Figure 4.7(e) the NBD is displayed and in Figure 4.7(f) the double negative binomial distributions is included.

collisions at 540 GeV, that at large energies the multiplicity distribution can be fitted by two negative binomial distributions. A systematic investigation [82] has shown that these two distributions can be understood as two components: soft and semi-hard. In this interpretation, the semi-hard component corresponds to events with minijets^{IV} while in the soft part minijets are not present. In this approach, the Double Negative Binomial Distribution (DNBD) is given by:

$$P^{DNBD}(n) = \alpha_{soft} \times P_{\langle n \rangle_{soft}, k_{soft}}^{NBD}(n) + (1 - \alpha_{soft}) \times P_{\langle n \rangle_{semi-hard}, k_{semi-hard}}^{NBD}(n) \quad (4.23)$$

where α_{soft} corresponds to the fraction of soft events over the total. In this approach,

^{IV}In UA5 experiment a minijet was a group of particles with total transverse energy larger than 5 GeV.

two kinds of events are taken into account but an event cannot contain soft and semi-hard components at the same time.

The Figure 4.7 illustrates the different phenomenological descriptions for $\sqrt{s} = 7$ TeV. Pythia 6 has been used to simulate the inelastic particle production. Assuming a completely independent particle production, the multiplicity distribution has been fitted to a Poisson distribution in Figure 4.7(a). The quality of the fit is really bad, which demonstrates large correlations in the particle production. In the Figure 4.7(b) together with the MC distribution, its fit to a NBD is shown. The NBD is not able to describe properly the multiplicity distribution due to the shoulder appearing at $n_{ch} \sim 30$. This is fixed using the DNBD, which gives a remarkable fit quality in the whole spectrum. At large n_{ch} the tail of the DNBD overestimates slightly the Monte Carlo distribution.

The high order cumulants for the Pythia 6 simulation and the different parameterizations to the multiplicity distributions are shown in Figures 4.7(d), 4.7(e) and 4.7(f) for Poisson, negative binomial and double negative binomial distributions respectively. Pythia predicts a clear pseudo-oscillation in qualitative agreement with analytical QCD predictions. This Monte Carlo generator uses a LO matrix method to compute the parton-parton scattering, however the quasi-oscillations are expected for analytic calculations at higher orders in QCD. The generators include an exact energy momentum conservation, which explains why oscillations are observed. The Poisson distribution, as it does not contain correlations, is exactly 0 for $q > 1$. The NBD decreases to 0, with no oscillations, with a poor fit quality. On the other hand, the DNBD describes very well the moments up to q 12, showing the same oscillations as Pythia. The disagreement at large order is the result of the DNBD overestimation on the tail of multiplicity distributions. Thanks to the good description by the DNBD of the charged multiplicity, we use this distribution in the next chapter to study different systematic effects for the high order cumulants, such as truncation effects.

4.4 Normalized factorial moments and intermittency

The study of the multiplicity distribution involves limited dynamical information based on charge and momentum conservation. For homogenous distributions, the average multiplicity decreases while the considered volume decreases and the statistical fluctuations increase. The study of the evolution of the multiplicity distribution with decreasing phase-space can provide information on the dynamics of the underlying interaction.

Normalized factorial moments (NFMs) measure the size of particle-density fluctuations above their mean. By distributing a given distribution into different numbers of bins and analyzing the dependence of the NFMs on the bin size, one can distinguish genuine dynamical effects from purely statistical fluctuations [83]. The method of NFMs provides an elegant way to analyze multiparticle correlations and identify intermittent behavior, which can reveal the underlying soft multihadron dynamics. NFMs have been studied extensively in a variety of interactions, such as e^+e^- , $p\bar{p}$, hp , lp , and heavy-ion collisions.

The NFM of order q is defined by,

$$F_q(M) = \frac{1}{M} \sum_{m=1}^M \frac{\langle n_m^{[q]} \rangle}{\langle n_m \rangle^q} \quad (4.24)$$

where the chevrons denote an average over events; M is the number of bins into which the η space is divided; the index $m = 1, 2, \dots, M$ runs over the bins; n_m is the charged-particle multiplicity in the m th bin; and $n_m^{[q]} = n_m(n_m - 1) \cdots (n_m - q + 1)$ is the q th-order (unnormalized) factorial moment of n_m .

The most important feature of the factorial moments is that they are not contaminated by statistical noise. When the original multi-cell multiplicity distribution is convoluted with a Poisson distribution, which represents statistical fluctuations, it is possible to demonstrate that normalized moments for the original distribution and the NFMs for the distribution including statistical noise are equivalent. The detailed explanation can be found in [86]. It is important to note that for a NFM of order q , the contribution to the numerator only takes into account events with $n_M \leq q$, acting as a filter for spikes. In case the particles are produced independently in η , the factorial moments are constant for all M . If the particles are produced according to a Poissonian distribution, $F_q(M) = 1$.

The method of NFMs consists in analyzing the dependence of F_q on M . If multiplicity fluctuations are caused purely by Poisson noise, the F_q are independent of M . Any dependence on M is a sign of dynamical correlations. Intermittency (i.e., self-similar behavior) can be recognized as a power-law rise of F_q with M :

$$F_q(M) \propto \left(\frac{\Delta\eta}{M}\right)^{-\phi_q} \quad (4.25)$$

where $\Delta\eta$ is the phase space covered and ϕ_q is a positive constant known as *intermittency index*. If F_q rises with M up to a certain value, the value of M at which they stabilize is a measure of the correlation length [83].

There are two possible definitions for the experimental factorial moments.

- Horizontal factorial moments, defined as:

$$F_q(M) = \frac{1}{M} \sum_{m=1}^M \frac{\langle n_m^{[q]} \rangle}{\langle \bar{n}_m \rangle^q} \quad (4.26)$$

where $\langle \bar{n}_m \rangle = \bar{N}/M$, with \bar{N} the average multiplicity for full phase space. In this case the normalization is not local and the horizontal factorial moments are sensitive to the shape of the single particle density.

- The so-called vertical factorial moments are given by:

$$F_q(M) = \frac{1}{M} \sum_{m=1}^M \frac{\langle n_m^{[q]} \rangle}{\langle n_m \rangle^q} \quad (4.27)$$

The normalization is done locally, for this reason they are sensitive to multiplicity fluctuation in each bin, being independent on the form of the space of phase distribution.

Both definitions are equivalent for $M = 1$. In the rest of this thesis, the NFMs refers to the vertical factorial moments definition.

4.5 Summary

In this chapter an introduction to QCD has been presented. Some regimes of QCD cannot be described using pQCD and models are needed. These models are implemented in Monte Carlo generators, which are basic tools to understand the data measured in the experiments. However, differences are expected between generators, and for this reason a brief overview of the two generators used to describe the particle production in ATLAS has been given.

It has been shown that in addition to the models, within generators several parameters can be tuned to describe with large accuracy the experimental data. For this reason the understanding of the correlations in the charged particle production is important to assure a good description of the QCD.

How to measure information about the particle correlation from the charged multiplicity has been presented. In addition, the method of factorial moments to measure intermittency has been introduced. The next chapter is focused on the application of these methods in 2010 ATLAS data.

Chapter 5

High Order Moments and Factorial Moments in ATLAS

In this chapter the measurement of multi-particle correlation in ATLAS is presented. The data used corresponds to the early 2010 data-taking, where the pile-up was very reduced. In the Figure 5.1 the total luminosity versus week is shown, but only a fraction of these data is used in these analyses.

The analyses described here follow the ATLAS Minimum Bias recommendations presented in [88], where the multiplicity distributions for Minimum Bias data were measured. For the high order moments, some modifications over the standard method are included, specially for the correction from reconstructed hadrons to particle level, because the high

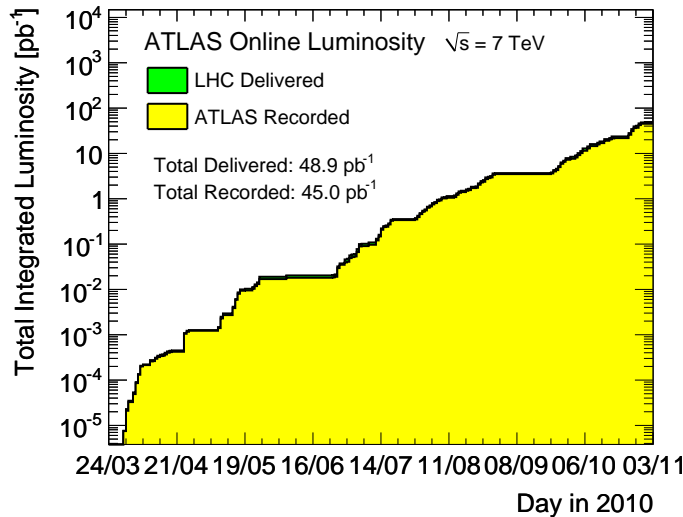


Figure 5.1: Cumulative luminosity versus week delivered to, and recorded by ATLAS during stable beams and for $\sqrt{s} = 7$ TeV. The luminosity is determined from counting rates measured by the luminosity detectors [95].

multiplicity tail has to be accurately described. In the measurement of the factorial moments, the same selection criteria are applied, but the corrections are applied by a bin-by-bin technique.

This chapter starts by describing the event selection. In the Section 5.2, the different Monte Carlo generators and their tunes are described. The next section is focused on high order moments, with description of how to measure the charged particle multiplicity and its uncertainties, systematic effects for high order moments, and finally the measurement of H_q at $\sqrt{s} = 7$ TeV and $\sqrt{s} = 900$ GeV are shown. In Section 5.4 the attempt to measure the factorial moments in ATLAS is presented. Only results at reconstructed level are displayed and a discussion on possible methods to measure them at particle level is given. The chapter finishes with conclusions and outlook for the multiparticle correlations in ATLAS.

5.1 Event selection

The analysis presented here is based on the same data sample as that of [88] and uses the same event and track selection criteria. Each event is required:

- to have been recorded during a period of stable beam, with all Inner-Detector sub-systems at nominal conditions;
- to have well-defined beam spot values;
- to have passed the Level-1 Minimum Bias Trigger Scintillator (MBTS) single-arm trigger;
- to have a reconstructed primary vertex, and no additional vertices with four or more tracks in the same bunch crossing to remove events with more than one interaction per bunch crossing;
- to have at least two good quality tracks, as defined below.

The tracks are reconstructed using the inside-outside algorithm, in which candidates require a minimum of Silicon hits and then they are extrapolated to include the TRT measurements. This process is done in two steps, the first one uses the standard tracking settings, while the second step is run on hits not used in the first step with wider road extrapolation and looser requirement in the number of Silicon hits. This second step assures a good reconstruction of tracks with low momentum ($p_T < 200$ MeV), which bend before reaching the inner layer of the SemiConductor Tracker (SCT). A good track is defined as one that satisfies:

- $p_T > 100$ MeV,
- $|\eta| < 2.5$,
- a hit in the first layer of the Pixel detector if the track is crossing a sensitive area in this first layer,

- at least one hit in any of the three layers of the Pixel detector,
- at least 2, 4, or 6 hits in the SCT if $p_T > 100$ MeV, $p_T > 200$ MeV, or $p_T > 300$ MeV, respectively,
- transverse and longitudinal impact parameters with respect to the event primary vertex of $|d_0| < 1.5$ mm and $|z_0 \cdot \sin(\theta)| < 1.5$ mm, respectively,
- a χ^2 probability > 0.01 if $p_T > 10$ GeV. This cut is applied to remove mis-measured tracks due to misalignment or nuclear interactions at relatively high momentum.

The vertexing algorithm needs at least two tracks with $p_T > 100$ MeV, for this reason, only events with two good tracks are accepted.

In addition to the good track definition, which leads to the number of reconstructed tracks in the event (n_{sel}), a second definition known as preselected tracks (n_{sel}^{BS}) is used to parametrize the trigger and the vertex efficiency reconstruction. For preselected tracks, the existence of primary vertex is not needed and the impact parameter cuts with respect to the primary vertex are replaced with a cut on the transverse impact parameter relative to the beam spot: $|d_0^{BS}| < 1.8$ mm.

The total recorded luminosity for the data sample is approximately $7 \mu\text{b}^{-1}$ at $\sqrt{s} = 900$ GeV and $190 \mu\text{b}^{-1}$ at $\sqrt{s} = 7$ TeV. 357,523 events are selected and 4,532,663 tracks at $\sqrt{s} = 900$ GeV, and 10,066,072 events and 209,809,432 tracks at $\sqrt{s} = 7$ TeV.

The fraction of cosmic ray background is estimated to be smaller than $\sim 10^{-6}$. At the instantaneous luminosity used for the data-taking and with the pile-up removal selection, the probability to have more than one interaction in the same bunch crossing is estimated to be of the order of 0.1 %. The number of beam backgrounds expected is less than the 0.1 % of the selected events. These three sources of background are considered negligible for our analyses [88].

5.2 Monte Carlo samples

For corrections and systematic-error studies, Monte Carlo samples were generated with the ATLAS MC09 [87] tune of Pythia^I. This tune employs the MRST LO* parton density functions (PDFs) [69] and the p_T -ordered parton shower. The parameters were derived by tuning to underlying event and minimum-bias data from Tevatron at 630 GeV and 1.8 TeV. This is the reference tune used to determine detector acceptances and efficiencies and to correct data.

For the purpose of comparing the present measurement to different phenomenological models describing minimum-bias events, in addition to the MC09 Pythia tune, Monte Carlo samples were produced with the Perugia0 [89] and the DW [90] tunes of Pythia, and with Phojet^{II}. For the Perugia0 tune, which uses CTEQ 5L PDFs, the soft-QCD part is tuned using minimum bias data from the Tevatron and CERN $p\bar{p}$ colliders. The DW tune

^IPythia 6.4.21

^{II}Phojet 1.12

uses virtuality-ordered (mass) parton showers and the CTEQ5L PDFs. It was derived to describe the CDF Run II Drell-Yan and underlying event data.

The non-diffractive, single-diffractive, double diffractive contributions in the generated samples were mixed according to the generator cross-sections to fully describe the inelastic scattering. All the events were processed through the ATLAS detector simulation, based on Geant4 [121]. The reconstructed Monte Carlo events and tracks are processed using the same analysis chain as data, satisfying the same criteria as data tracks and events.

To measure the distributions predicted by Monte Carlo, each generated event is required to have at least one good generated track. A good generated track has a non-zero charge, a lifetime $\tau > 0.3 \cdot 10^{-10}$ s and it is produced in the primary vertex or in the subsequent decays of unstable particles. Finally, generated particles are required to have the same kinematical cuts as reconstructed tracks: $p_T > 100$ MeV and $|\eta| < 2.5$.

The standard non-diffractive sample which is fundamental to produce the high multiplicity tail, was not enough populated. Two additional MC09 Pythia samples for the non-diffractive contribution were used for generated charged particles for $n_{ch} > 80$ and $n_{ch} > 120$. These samples were merged with the MC09 default contributions according to their cross-section, removing the possible overlap between samples. The use of these samples allows us to get a good description on the high multiplicity tail for 7 TeV data.

Additionally, just for comparison at generator level, the predictions of Pythia 8^{III}, tuned to latest LHC data and using CTEQ 6L1 PDFs are presented [91]. This sample was not passed through the whole analysis chain, just the events with stable generated particles inside the detector acceptance were used.

5.3 High order moments

For the measurement of the high order moments, the charged particle multiplicity is needed. To obtain it, the same method as done in [87] is applied. The reconstructed distribution is corrected taking into account the trigger and vertex reconstruction efficiencies, which were measured by the ATLAS Minimum Bias working group. The obtained distribution is unfolded to correct for detector effects. The final high order moments are obtained using this fully corrected distribution.

5.3.1 Correction procedure for the charge multiplicity distribution

The trigger and the vertex efficiencies are shown in Figure 5.2 as a function of the number of preselected tracks (n_{sel}^{BS}). The effect of events lost due to these efficiencies is corrected using an event-by-event weight:

$$\omega_{ev}(n_{sel}^{BS}) = \frac{1}{\epsilon_{trig}(n_{sel}^{BS})} \cdot \frac{1}{\epsilon_{vtx}(n_{sel}^{BS})} \quad (5.1)$$

^{III}Pythia 8.160

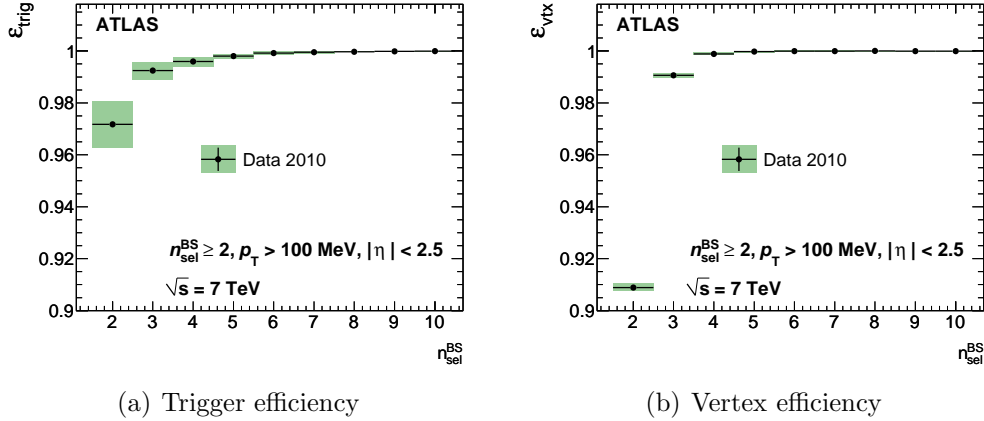


Figure 5.2: Trigger efficiency (a) and vertex efficiency (b) with respect to the event selection as a function of reconstructed tracks before the vertex requirement, n_{sel}^{BS} [88].

where $\epsilon_{trig}(n_{sel}^{BS})$ and $\epsilon_{vtx}(n_{sel}^{BS})$ are the trigger and vertex efficiencies respectively. This weight is applied to all the measured events.

The distribution obtained after using the event-by-event weight corrects the total number of events selected (N_{sel}) with n_{sel} particles. However, to obtain the number of events (N_{ch}) with n_{ch} primary charged particles, other detector effects, such as track reconstruction inefficiencies and additional tracks from secondary decays of long-lived particles, need to be taken into account. A bin-by-bin correction cannot be applied due to the bin migration, in which one event with n_{ch} primary particles can be reconstructed with different values of n_{sel} . The standard technique to correct for such effects is the unfolding method. The unfolding can be expressed by:

$$\mathbf{N}_{sel} = M(n_{sel}|n_{ch})\mathbf{N}_{ch} \quad (5.2)$$

here, \mathbf{N}_{sel} is the reconstructed charged particle multiplicity after the trigger and vertex corrections are applied. The \mathbf{N}_{ch} is the primary charged particle multiplicity: the true multiplicity distribution. The matrix $M(n_{sel}|n_{ch})$, known as the migration or smearing matrix, expresses the probability that a given track multiplicity with n_{ch} primary particles is reconstructed with n_{sel} charged particles:

$$M(n_{sel}|n_{ch}) = P(n_{sel}|n_{ch}) = \frac{N(n_{sel}, n_{ch})}{\sum_{n_{sel}} N(n_{sel}, n_{ch})} \quad (5.3)$$

This matrix takes into account the bin migration and it is obtained from Monte Carlo samples.

The Equation 5.2 can be inverted to obtain the expected true distribution from the measured data:

$$\mathbf{N}_{ch} = R(n_{ch}|n_{sel})\mathbf{N}_{sel} \quad (5.4)$$

where $R(n_{ch}|n_{sel})$ is given by:

$$R(n_{ch}|n_{sel}) = P(n_{ch}|n_{sel}) \quad (5.5)$$

It is important to note that if $R(n_{ch}|n_{sel})$ is defined in the same manner as $M(n_{sel}|n_{ch})$:

$$R(n_{ch}|n_{sel}) = \frac{N(n_{ch}, n_{sel})^T}{\sum_{n_{ch}} N(n_{ch}, n_{sel})^T} \quad (5.6)$$

it is not in general the same as $M(n_{sel}|n_{ch})^{-1}$ due to the different normalization of the matrices. The normalization of the M matrix is independent of the true multiplicity, while the normalization of R defined as Equation 5.6 depends on it. For this reason, the matrix R may bias the final result to the distribution used to compute the smearing matrix. Also, the direct inversion of $M(n_{sel}|n_{ch})$ is not possible most of the times because the matrix can be singular. In the cases where the matrix can be inverted, the result obtained produces large oscillations due to statistical fluctuations, and a regularization term needs to be introduced. For these reasons, in this analysis, we apply a Bayesian unfolding developed by DAgostini [92].

The Bayesian unfolding is an iterative method based on the Bayes' theorem, which allows to relate $P(n_{ch}|n_{sel})$ and $P(n_{sel}|n_{ch})$ by:

$$P(n_{ch}|n_{sel}) \cdot P(n_{sel}) = P(n_{sel}|n_{ch}) \cdot P(n_{ch}) \quad (5.7)$$

where $P(n_{ch})$ is known as the prior or initial probability and in our case it is unknown. Using the properties of conditional probability, we can write:

$$P(n_{sel}) = \sum_{n'_{ch}} P(n_{sel}|n'_{ch}) \cdot P(n'_{ch}) \quad (5.8)$$

Applying this into 5.7, $P(n_{ch}|n_{sel})$ is given by:

$$P(n_{ch}|n_{sel}) = \frac{P(n_{sel}|n_{ch}) \cdot P(n_{ch})}{\sum_{n'_{ch}} P(n_{sel}|n'_{ch}) \cdot P(n'_{ch})} \quad (5.9)$$

in which the only unknown parameter is the initial probability, but it can be obtained with an iterative method.

In the first iteration, the initial probability $P(n_{ch})^0$ is set to best knowledge, in our case we use the true distribution produced with Pythia MC09. The expected distribution is given by: $\hat{N}_{ch}^0 = P(n_{ch})^0 \sum_{sel} N_{sel}$. Using Equations 5.4 and 5.9, the unfolded distribution, $\mathbf{N}_{ch}^{(0)}$, is computed. A χ^2 comparison is done between the expected distribution (\hat{N}_{ch}^0) and the unfolded one ($N_{ch}^{(0)}$). Depending on the value of the χ^2 , more iterations are performed using as prior the unfolded distribution of the previous iteration: $P(n_{ch})^{(1)} = N_{ch}^{(0)} / \sum_{ch} N_{ch}^{(0)}$. This is repeated until the measured χ^2 value is small enough. In this analysis, after four iterations, the unfolded distributions are not changed, so the results shown later are produced after four iterations.

In Figure 5.3, the migration matrix populated with the Pythia MC09 7 TeV sample is presented. This matrix includes the standard single, double diffractive and non-diffractive samples and also the non-diffractive samples with $n_{ch} > 80$ and $n_{ch} > 120$ which assures a good description of the high multiplicity tail for data. This is the matrix used in this analysis to unfold the data distribution.

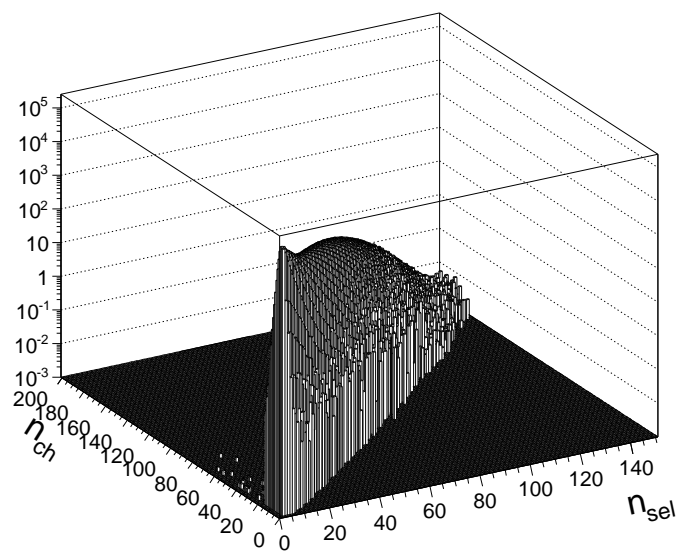


Figure 5.3: Migration matrix $M_{ch,sel}$ containing the probability of selected tracks n_{sel} is produced by n_{ch} generated charged particles.

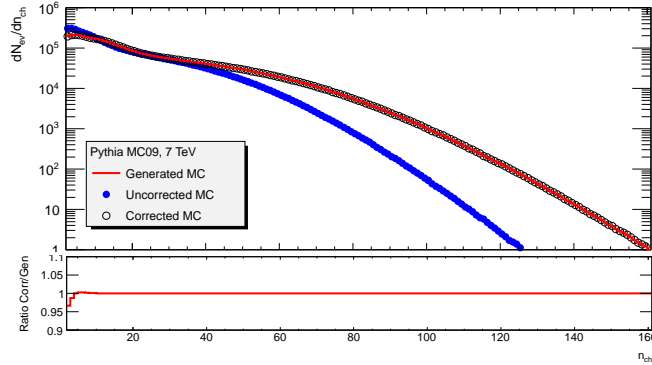


Figure 5.4: Closure test for the multiplicity distribution for Pythia MC09 7 TeV sample. The uncorrected distribution corresponds to the reconstructed charged particles (n_{sel}). The corrected distribution includes all the corrections explained in the text.

An additional correction term is included to the number of events as a function of n_{ch} to account for the events that were not selected due to track reconstruction inefficiencies:

$$\omega_{ev,lost}(n_{chl}) = \frac{1}{1 - (1 - \epsilon_{trk})^{n_{ch}}} \quad (5.10)$$

Where ϵ is the mean effective track reconstruction and it has been measured to be $(67.2\% \pm 0.5\%)$ and $(66.9\% \pm 0.4\%)$ for 7 TeV and 900 GeV analyses [88]. This term correct for events migrating out of the selected kinematical range ($n_{ch} > 2$), which the migration matrix does not account for.

The analysis chain to produce the charged particle distributions was validated with Monte Carlo. In the Figure 5.4 the closure test for MC09 Pythia 7 TeV is shown. The full correction chain is applied to the uncorrected distribution (reconstructed distribution of n_{sel}) returning the corrected distribution as a function of n_{ch} . This distribution is compared to the true (generator level) one and a very good agreement is found, which confirms the good performance of the method. Small discrepancies are found in the low multiplicity region where the efficiency correction shows to be $\sim 3\%$ below the true distribution. This discrepancy is compatible with the uncertainty evaluation, which is described in next section.

Uncertainty evaluation

For uncertainty evaluation of the charged multiplicity distribution, the same method as used in [88] is applied. The statistical and systematic uncertainties for the trigger and vertex efficiencies are taken into account. This is done modifying the events weight, computing the modified reconstructed distributions and propagating it though the unfolding procedure.

The largest systematic uncertainties corresponds to track reconstruction efficiency uncertainty and the different p_T spectrum between MC and data. In the Figure 5.5 the track

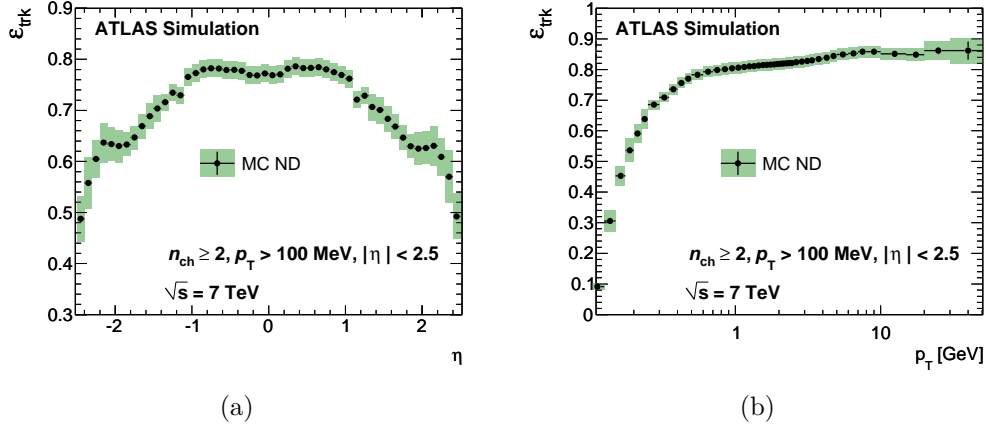


Figure 5.5: Track reconstruction efficiency as a function of p_{T} (5.5(a)) and η (5.5(b)) for $\sqrt{s} = 7$ TeV [88].

reconstruction efficiency and its uncertainties is presented as a function of η and p_{T} . For very low momentum the tracking efficiency drops due to the material interaction and the large curvature radius of the track, which produces very few hits in the Silicon detectors. To estimate the uncertainty due to the tracking efficiency uncertainty, starting from number of selected tracks of each event (n_{sel}), tracks are randomly removed from the distribution according to the efficiency uncertainty for each track in the event. The new distribution is unfolded, corrected and compared to the nominal charged particle multiplicity.

The track efficiency depends strongly on the transverse momentum. The p_{T} spectrum disagreement between data and the Monte Carlo sample used to populate the migration matrix is the other main source of uncertainty. The average track reconstruction efficiency as a function of p_{T} is compared between MC and data. The differences between these efficiencies are treated in the same way as the track efficiency uncertainty.

The uncertainties measured for 7 TeV data vary between 2% for low n_{ch} and 40% for high multiplicities for the p_{T} systematic uncertainties and between 3% and 25% for the tracking uncertainties.

5.3.2 Charged particle multiplicity

The fully corrected charged particle multiplicity for data at $\sqrt{s} = 7$ TeV and $\sqrt{s} = 900$ GeV are shown in Figure 5.6. The data is compared to the different Monte Carlo estimations, such as MC09, DW, Perugia0 tunes of Pythia 6 and Phojet. It is important to remark that the data distributions presented here are fully compatible with the published ATLAS result [88] and only a finer binning is employed.

For 900 GeV, all Pythia 6 predictions provide lower multiplicities than the corrected data. In this case, similar tail as for data is observed. For 7 TeV, all the Pythia 6 and Phojet estimations return lower multiplicities than the data. The Pythia 8 has been tuned to the ATLAS and ALICE 900 GeV and 7 TeV data. This tune was produced by the

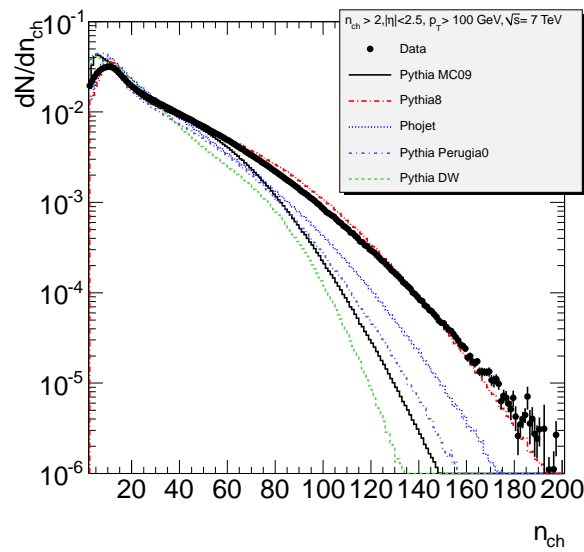
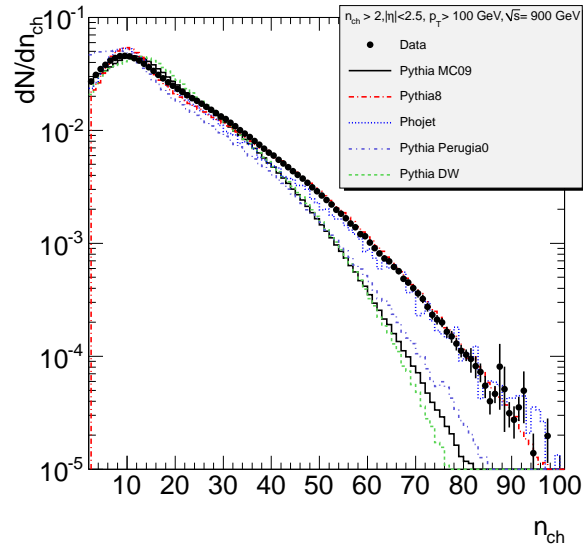


Figure 5.6: Corrected charged particle multiplicity distributions for data and true distributions for MC for $\sqrt{s} = 7$ TeV (a) and 900 GeV (b).

Pythia group, starting from pre-LHC tunes and reducing the cross-section for diffraction and modifying the multiple interaction parameters in order to describe 900 GeV and 7 TeV data. For this, the agreement found between Pythia 8 and the measured charged multiplicity is the best.

Fits to phenomenological models

In this section, the corrected distributions for data have been fitted to two possible phenomenological description: a negative binomial distribution (NBD) and a double negative binomial distribution (DNBD), which were introduced in Section 4.3.2, Equations 4.22 and 4.23.

The fit was performed using the MINUIT package [123]. The convergence for NBD is fast, however in the DNBD case, several local minimums are found. The fit was performed 20000 times for each center-mass-energy, using as initial conditions random parameters. The set of parameters providing the lowest χ^2 over degree of freedom are used as central values. To evaluate the uncertainty on the fit, instead of using the MINUIT estimation, which treats the uncertainties as uncorrelated, a set of toy Monte Carlo tests were run. In these tests, the reconstructed charge multiplicity was modified following the systematic uncertainties and the new distribution was propagated through the unfolding process. Finally, the new corrected distribution was fitted using as initial condition of the function the values that minimize the original charged multiplicity.

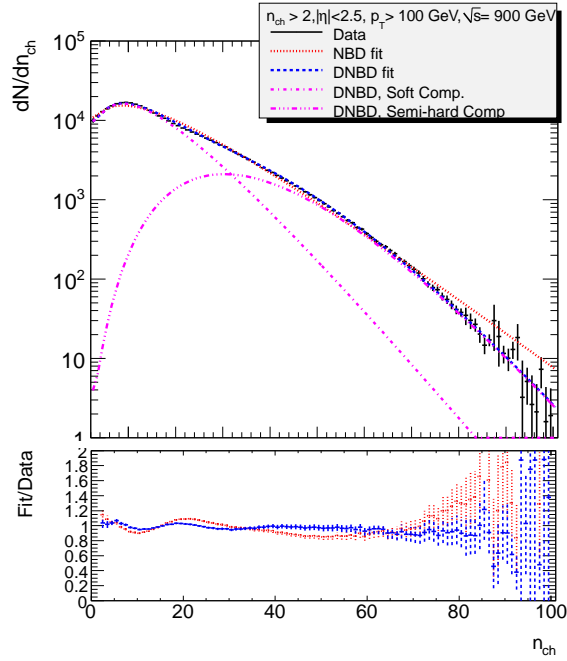
In the Figure 5.7, the result of the fits for 900 and 7 TeV are shown. The NBD and DNBD fits are presented, and also the soft and semi-hard components of the DNBD are displayed. The NBD is not describing well the data, which is very interesting because at lower center-of-mass energy, all the data measured has been successfully described by this distribution. This is another evidence that the KNO scaling is violated at large energies.

In the case of the DNBD, the description for 900 GeV is very good, but for $n_{ch} > 150$ at 7 TeV, the distribution overestimates the data. A significant effort has been done to describe the tail, however this is the best possible fit obtained. This is assumed to be because at this range of energy, a third component is needed.

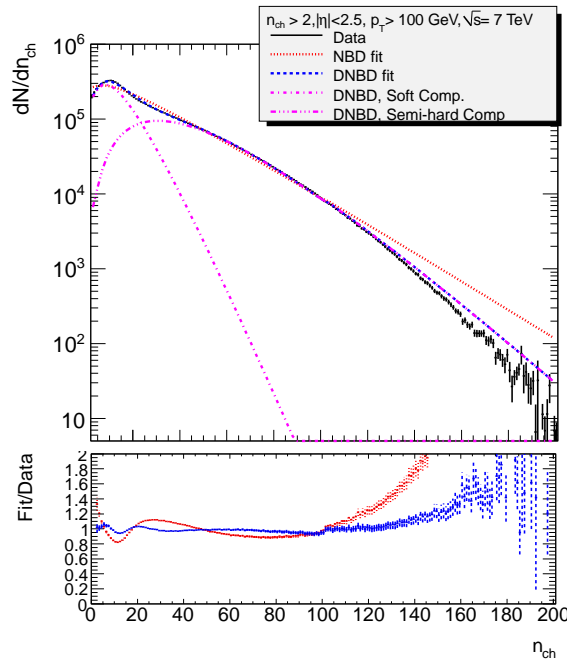
Table 5.1: Parameters fit to a NBD distribution for corrected data at 7 TeV and 900 GeV.

\sqrt{s}	k	$\langle n \rangle$
900 GeV	1.93 ± 0.04	17.09 ± 0.08
7 TeV	1.341 ± 0.006	27.4 ± 0.1

The fit parameters for NBD and DNBD are presented in Tables 5.1 and 5.2, respectively. For the DNBD, one can see how the fraction of soft component decreases when the center-of-mass energy increases. The soft component parameters are very similar 900 GeV and 7 TeV, while larger and wider contribution for the semi-hard component is measured for 7 TeV than for 900 GeV.



(a)



(b)

Figure 5.7: Data on charged particle multiplicity corrected to particle level and the fits to the NBD and DNBD models for $\sqrt{s} = 7$ TeV (a) and $\sqrt{s} = 900$ GeV (b). For the DNBD fit, the soft and semi-hard components are also shown.

Table 5.2: Parameters fit to a DNBD distribution for corrected data at 7 TeV and 900 GeV.

\sqrt{s}	α_{soft}	k_{soft}	$\langle n \rangle_{soft}$	$k_{semi-hard}$	$\langle n \rangle_{semi-hard}$
900 GeV	0.82 ± 0.04	2.6 ± 0.1	13.4 ± 0.5	7.9 ± 0.9	34 ± 1
7 TeV	0.54 ± 0.02	2.4 ± 0.1	13.2 ± 0.4	3.6 ± 0.2	45 ± 1

5.3.3 Statistical uncertainties for high order moments

Assuming that the errors in the bins of the charged multiplicity distribution P_n are uncorrelated, the final errors can be calculated from the partial derivatives and the uncertainty of the charge multiplicity. The total uncertainty for factorial moments, cumulants and high order moments is given by:

$$\Delta X_q^2 = \sum_{n,n'} \left(\frac{\partial X_q}{\partial P_n} \right) \left(\frac{\partial X_q}{\partial P_{n'}} \right) (\Delta P_n) (\Delta P_{n'}) \quad (5.11)$$

where X_q can be the factorial moments (F_q), the cumulants (K_q) or the high order moments (H_q) and ΔP_n is the uncertainty of the multiplicity distribution.

In the case of the factorial moment, the derivative at order q is given by:

$$\frac{\partial F_q}{\partial P_n} = \frac{n(n-1)\dots(n-q+1)}{\langle n \rangle^q} - \frac{F_q q n}{\langle n \rangle} \quad (5.12)$$

In a similar way, the uncertainty for the cumulants can be obtained iteratively with:

$$\frac{\partial K_q}{\partial P_n} = \frac{\partial F_q}{\partial P_n} - \sum_{a=1}^{q-1} \frac{(q-1)!}{a!(q-a-q)!} \left(\frac{\partial K_{q-a}}{\partial P_n} F_a + K_{q-a} \frac{\partial F_a}{\partial P_n} \right) \quad (5.13)$$

Finally, once the factorial moments and cumulants uncertainties are known, the high order cumulant derivatives are given by:

$$\frac{\partial H_q}{\partial P_n} = -H_q \left(\frac{1}{K_q} \frac{\partial K_q}{\partial P_n} - \frac{1}{F_q} \frac{\partial F_q}{\partial P_n} \right) \quad (5.14)$$

This method is used to compute the uncertainties for high order moments from charged particle multiplicity distribution in which unfolding has not been applied.

For data corrected at particle level, a large number of multiplicity distribution are generated from the originally reconstructed one by allowing random variation of the multiplicities within the systematic and statistic uncertainties. The new reconstructed distribution is unfolded and the H_q is computed. The uncertainty is then extracted from the distribution of the generated H_q . For a large number of tests, both methods are in good agreement.

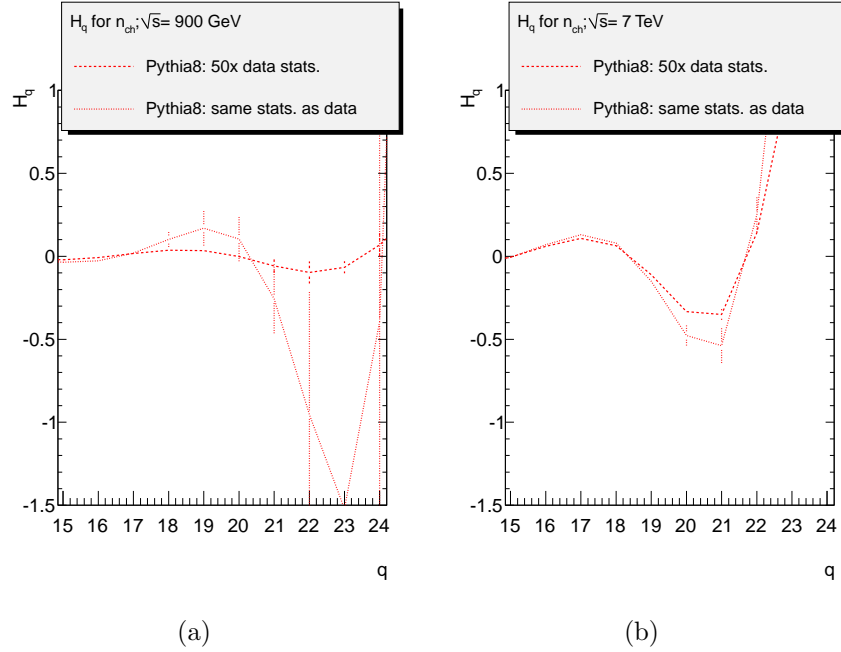


Figure 5.8: High order moments with $q > 15$ for Pythia 8 samples for $\sqrt{s} = 900$ GeV (a) $\sqrt{s} = 7$ TeV (b). At each energy, two samples were produced: one with same statistics as data and another with 50 times the data events.

5.3.4 Systematic effects for high order moments

In this section, the effect on the truncation of the charged multiplicity and its effect on the high order moments is studied. Due to the finite data sample, the measured multiplicity will be always truncated at large multiplicities. In the past it has been seen that this truncation can affect the final moments.

In this analysis, in addition to truncation at large values, the minimum number of charged particles accepted is 2. The missing information for 1 particle has not influence on the H_q . As the high order moments measure accurately mainly the multiplicity tail, truncation up to $n_{ch} < 5$ presents an influence in the moments that is negligible.

For the truncation at large multiplicities, different tests have been done to evaluate the effect of the total statistics, the influence of the large uncertainty for the tail of the multiplicity distribution and the possible merge of bins to reduce the total uncertainty. These tests were done using the DNBBD fits for data and Pythia 8 simulations.

The Figure 5.8 shows the H_q for order larger than 15, produced by Pythia 8 samples for 7 TeV and 900 GeV. At each energy, two samples were produced, one with the same number of events as measured in data, and one with 50 times more events. The effect of the increasing in statistics is especially important for 900 GeV, where the number of measured events is much lower than for 7 TeV. When the statistics decreases, the fluctuations at large q get amplified as well as the uncertainties. Similar effect is observed for 7 TeV.

The same tests over Pythia 8 samples are shown for $q < 16$ in Figure 5.8. In this

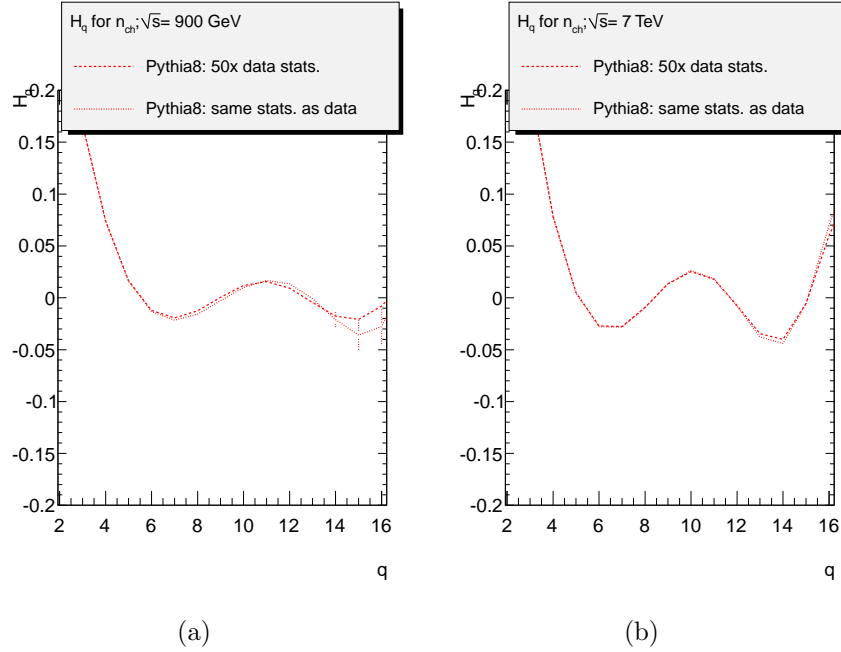


Figure 5.9: High order moments with $q < 16$ for Pythia 8 samples for $\sqrt{s} = 900$ GeV (a) $\sqrt{s} = 7$ TeV (b). At each energy, two samples were produced: one with same statistics as data and another with 50 times the data events.

range, the influence of the tail statistical fluctuations is very low and well defined by the uncertainty estimation. These tests have been performed also using DNBD distributions to produce random multiplicity samples and comparing the H_q between the exact DNBD and the samples produced with different statistics. Similar results have been obtained.

The influence of the large uncertainty in the multiplicity has been also studied. The truncation at lower values, to remove such parts of the tail, reduces the moments uncertainties for large q order, however if the truncation is done at very low values, the whole spectrum can be distorted. The rebinning of the multiplicity tail has a similar influence. A moderate merge of bins in the tail (below 10 bins merged together) has a good impact on the moments uncertainty, but if several bins are merged together, the whole high order moment spectrum is changed.

In conclusion, with the measured and corrected multiplicity distribution, a good description of the high order moments can be achieved for $q < 16$ without removing parts of the tail, so the data results only this range is shown.

5.3.5 High order moments at reconstructed level

Before looking to the full moments obtained for fully corrected distributions, the moments measured at reconstructed level for data and MC are shown in Figure 5.10. All the MC samples show the quasi-oscillatory behavior, and so does the data. The position of the first minimum differs between MC generators and between data. In data the first minimum is

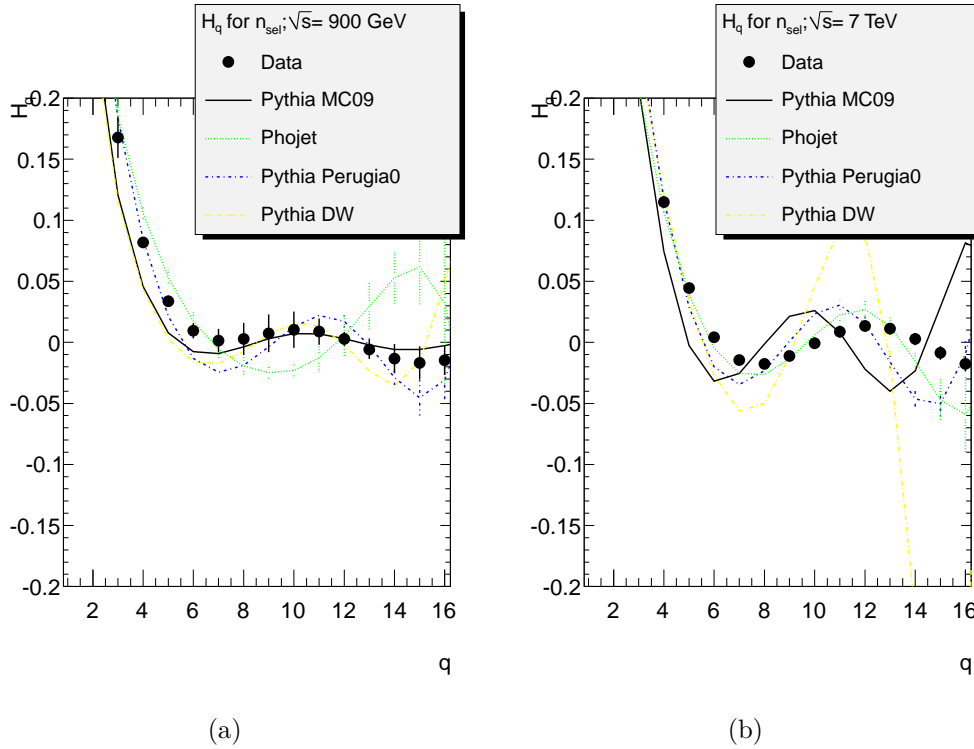


Figure 5.10: High order moments at reconstructed level for data and several Monte Carlo samples for $\sqrt{s} = 900$ GeV (a) $\sqrt{s} = 7$ TeV (b).

found at $q = 7$ at $\sqrt{s} = 900$ GeV and at $q = 8$ at $\sqrt{s} = 7$ TeV. All the Pythia 6 tunes have the first minimum at $q = 7$ at 900 GeV, in agreement with the data. However Phojet, at this energy, has the first minimum at $q = 9$ and much larger amplitude.

At 7 TeV, Perugia and DW tunes have the first minimum at $q = 7$. MC09 first minimum is at $q = 6$ and Phojet is in agreement with data, with first minimum at $q = 8$. The amplitude of the oscillations are in qualitative agreement for all MC generators except the DW tune.

5.3.6 High order moments at particle level

The high order moments, after applying the correction at generator level, are shown in Figure 5.11. In addition to previous MC generators, the Pythia 8 prediction is shown. This prediction used 50 times the statistics measured in data.

At $\sqrt{s} = 900$ GeV, the first minimum is at $q = 7$, as in the reconstructed case, but in this case, the amplitude of the oscillations is larger. The Pythia 8 sample has its first minimum at $q = 7$ and the amplitude of the oscillations is in agreement with data, however the period is a bit shorter. The DW tune has the first minimum at $q = 6$, and the amplitude and period of the oscillation is similar to Pythia 8. MC09 has smaller amplitude oscillations as the data and the first minimum is at $q = 6$. For Perugia tune, the amplitude of the

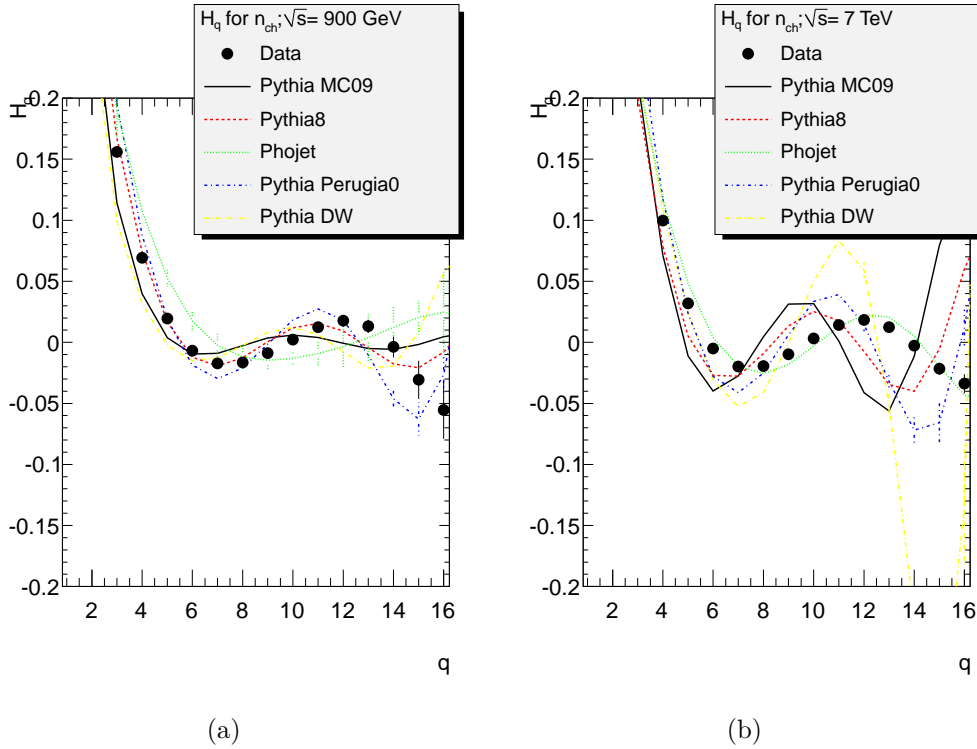


Figure 5.11: High order moments at reconstructed level for data and several Monte Carlo samples for $\sqrt{s} = 900$ GeV (a) $\sqrt{s} = 7$ TeV (b).

oscillation is larger than for data with a first minimum at $q = 7$. Finally, the largest disagreement is found for Phojet, which first minimum is at $q = 9$, and the amplitude period is larger than for data, however the statistics of the data sample used causes quite large uncertainties. As expected, due to the good description of the data multiplicity tail, the best agreement is found for Pythia 8, however the disagreement observed at $q > 8$, may indicate that further fine tuning will be needed.

The results at $\sqrt{s} = 7$ TeV shows the first minimum for data at $q = 7$. The DW and the Perugia tunes have the first minimum also at $q = 7$, however the amplitudes of the oscillations for DW tune are much larger than for data. MC09 has the first minimum at $q = 6$, and oscillations with slightly larger amplitude and shorter period than data. For Pythia 8, the first minimum is at $q = 7$, as in data, with an amplitude very similar also to the data. The Phojet sample, at this energy, shows a remarkable agreement with data, even when this generator underestimates the contribution of the tail for charged particle multiplicity.

5.3.7 Interpretation

As has been shown, none of the current Monte Carlo generators describes accurately the H_q at both energy ranges. However, all of them describe qualitatively the quasy-oscillation

predicted by QCD under LPHD for high order perturbation theory. Different amplitudes and positions of the first minimum have been observed between generators and data. It is important to note, that none of the used generators are implemented at NNLLA order, as the quasi-oscillation predictions is done. They use an exact implementation to take care of the energy-momentum conservation, which is expected to be the responsible of H_q behavior [86].

The results shown here are in agreement with the study done by I.M Dremin for the CMS multiplicity distributions [93]. Also, the oscillatory behavior has been measured in a range of experiments from proton-antiproton to electron-positron colliders. It is very striking to see how this oscillatory behavior is common to all collision processes.

The traditional interpretation of the H_q oscillations implies that the large positive values for low q corresponds to strong correlation between particles produced from resonances, the positive values after the first minimum imply the production of clusters of particles at the given multiplicity scale (q). This implies the existence of clusters or minijets [77]. The negative values around the first minimum suggest anti-correlations between resonances and particles inside these clusters. At larger range, a complicated mixture of attractive and repulsive forces inside higher multiplicity groups leads to more oscillations [86]. It is interesting that these features are rather universal in nature.

5.4 Study of normalized factorial moments in η bins

Here a preliminary study of Normalized Factorial Moments in ATLAS is presented. The NFMs are measured in η with a maximum number of bins of $M = 100$ in the range $|\eta| < 2.5$. The same data sample with same event and track selection is used as for the high order moments study. The corrections applied in the high order moments analysis cannot be applied in this case because of the event-by-event measurement nature of this analysis.

5.4.1 Statistical uncertainties

Statistical errors are calculated using the method described in [94]. This estimation is based on uncertainty propagation. As a cross-check, the data sample was divided into subsamples of 3000 events each. The NFMs were calculated for each sample and the statistical uncertainty was estimated from the RMS of the distribution of subsamples of NFMs divided by the square-root of the number of subsamples. These two independent methods yield consistent values for the statistical uncertainty evaluation of the NFMs, and due to computational simplicity, in the next sections the analytical evaluation is used.

5.4.2 Systematic uncertainties

A number of possible sources of systematic error have been studied. These are described below.

Measurement accuracy

To ensure the accuracy of the measured NFMs, it is important that the measurement resolution in η is smaller than the size of the smallest bin. In this analysis, the latter value is 0.05. The tracking resolution was measured in MC. The reconstructed tracks were matched to generated ones using a cone algorithm in $\eta - \phi$. In this algorithm the angular distance between the reconstructed and generated particle is computed as: $\Delta R^2 = (\eta_{rec} - \eta_{gen})^2 + (\phi_{rec} - \phi_{gen})^2$, where *rec* variables corresponds to reconstructed track parameters, while *gen* variables belong to generated particles. All the possible combinations between reconstructed and generated particles are tested, and only pairs with lowest ΔR are kept.

In the Figure 5.12, the difference between the measured and the generated pseudorapidity ($\Delta\eta$) for the MC09 7 TeV sample is presented. In this figure, in addition to global resolution for all tracks, the resolution for low and large momentum particles is also included. The total resolution measured is $\Delta\eta \sim 0.01$, well below our requirements, 0.05. The effect of the tails is also very small, with 4 orders of magnitude less tracks in $\Delta\eta = 0.05$ than in $|\Delta\eta| < 0.0005$. For relatively high momentum particles, with $p_T > 1.0$ GeV, the resolution improves greatly to $\Delta\eta \sim 0.004$, however, for low momentum particles ($p_T < 0.4$ GeV), the resolution gets worse: $\Delta\eta \sim 0.015$. In this region, the rate of tracks in the tail of the distribution increases to about 3 orders of magnitude between $\Delta\eta = 0.05$ and $|\Delta\eta| < 0.0005$.

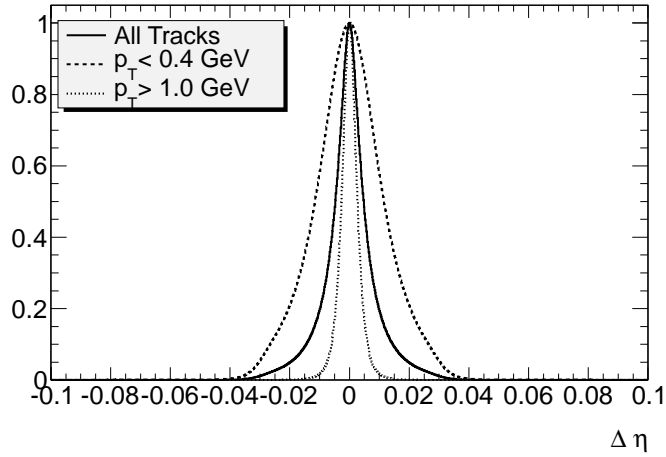


Figure 5.12: Track error for η for MC09 at $\sqrt{s} = 7$ TeV.

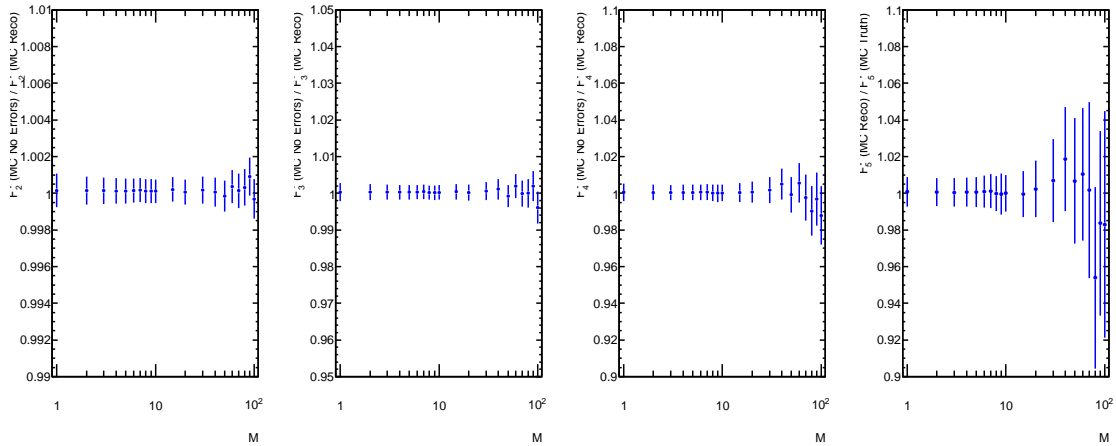


Figure 5.13: Ratio of NFMs for a reconstructed MC09 sample $\sqrt{s} = 7$ TeV using for η the true value obtained by truth matching divided by the NFMs using the reconstructed information. Errors are statistical.

Very similar resolution is expected in data. To check it, the errors returned by the track fitter for MC and data were compared. Data have slightly larger track fitter errors than MC, as it is expected, but uncertainties of the same order are assumed between them.

To test the influence on the resolution in the NFMs, in a Monte Carlo sample, the measured value of η was replaced with its true value, obtained by the matching algorithm. The effect of using the true value of the measurement is shown in Figure 5.13. The ratio

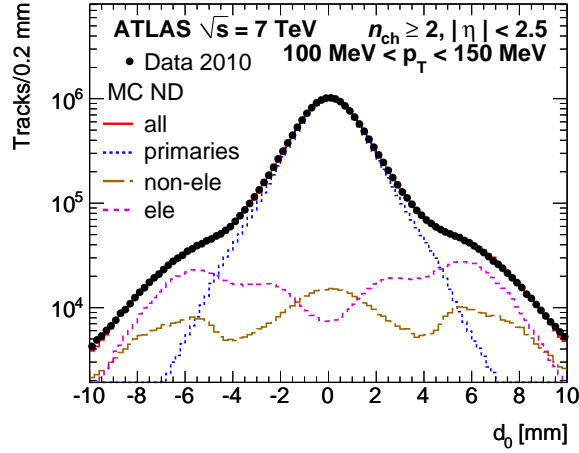


Figure 5.14: Transverse impact parameter, d_0 , distribution at $\sqrt{s} = 7$ TeV for primary and non-primary particles for $100 < p_T < 150$ GeV [88].

between the NFMs obtained with the true η and the reconstructed one is shown for MC09 7 TeV sample. As can be seen, the effect of the resolution is negligible and compatible with the statistical uncertainty of the sample.

Related with the resolution effect, there is a possibility to double-count tracks or reconstruct as a single track two or more nearby-charged tracks. The first effect is expected to bias the NFMs upwards, while the second one biases the NFMs downwards. Both effects were checked in MC, using truth matching and checking the number of tracks reconstructed for a given generated tracks and the other way around. Both effects are negligible in the checked samples.

Resonance decays

Since the products of the decay of resonances are necessarily correlated, it is important to understand the possible contamination of the sample by Dalitz decays, photon conversions, and the decays of resonances such as K_S^0 as the main source of any observed correlations. The expected effect on the NFMs of such resonance decays is an increase of their value.

With the selection used, the contamination produced by secondaries has been accurately measured in [88], and in the Figure 5.14 the fraction of secondaries is shown. The p_T range presented in the figure corresponds to the lowest possible range, the one which can be measured in ATLAS, where the largest contamination is expected. For larger momentum, the contamination decreases by more than an order of magnitude.

To estimate the influence of this effect in the NFMs, a study was done, in which reconstructed Monte Carlo tracks were matched to true tracks. The moments were then re-calculated, excluding tracks matched to a true track produced in a secondary vertex, which excludes Dalitz decays, photon conversion and decay from resonances. The results of this test indicate that the presence of secondary particles in the sample biases the measured NFMs upward. This bias increases with M and with q . In all cases, the bias

was found to be smaller than 3%.

Finite size of the data sample

When the average value of $n_m^{[q]}$ is close to or smaller than unity, the measurement of $F_q(M)$ can be distorted as a result of the empty-bin effect [85]. This effect typically manifests itself as a fluctuation at large values of q and M and can bias measured NFMs toward smaller values. To determine whether these measurements are susceptible to the empty-bin effect, the subsample NFM distributions described in Section 5.4.1 have been inspected. These distributions show no significant distortion for $q < 5$ but suggest that the fifth-order moments may be slightly distorted toward smaller values, especially at large M . The effect is slightly more significant at $\sqrt{s} = 900$ GeV than at $\sqrt{s} = 7$ TeV.

5.4.3 Correction procedure

In previous Factorial Moment measurements done at LEP the good agreement between Monte Carlo and data allowed to use a bin-by-bin correction. The same approach has been tried here. To correct the observed NFMs to the particle level, a Monte Carlo samples of approximately 10^7 events at each centre-of-mass energy, generated with the MC09 tune of PYTHIA is used. The raw NFMs are corrected as:

$$F_q(M)^{\text{corr}} = c_q(M) \times F_q(M)^{\text{raw}} . \quad (5.15)$$

The correction factor $c_q(M)$ is given by:

$$c_q(M) = \frac{F_q^{\text{true}}}{F_q^{\text{rec}}} , \quad (5.16)$$

where F_q^{true} is the NFM calculated using generated primary tracks, and F_q^{rec} is the NFM calculated using reconstructed tracks. Statistical uncertainties are propagated assuming no correlations.

The reconstructed level for 900 GeV and 7 TeV for MC09 are shown in Figures 5.15 and 5.18. In addition to the MC09 sample, the DW, Perugia and Phojet samples are also included. This is done in order to check possible generator dependence of the correction factors. The particle level (true level) NFMs for same set of samples are presented in Figures 5.16 and 5.19. The ratio between the true and the reconstructed level that corresponds to the correction factors for all the Monte Carlo samples are shown in Figures 5.17 and 5.20 for 900 GeV and 7 TeV.

As can be seen, the dependence of the correction factors on M is very similar for the different generators at given center-of-mass energy, however the normalization is different for each samples. This dependence needs to be taken into account as a systematic uncertainty, which increases the uncertainty to a minimum of 12% for NFMs of order 2 up to 30% for order 5. This large uncertainty makes the corrected results insensitive to produce useful results; and for this reason, this method cannot be used in the case of ATLAS.

The differences between the MC samples are caused primarily by the different p_T and η distributions, and the tracking efficiency. To correct for these effects, other methods have

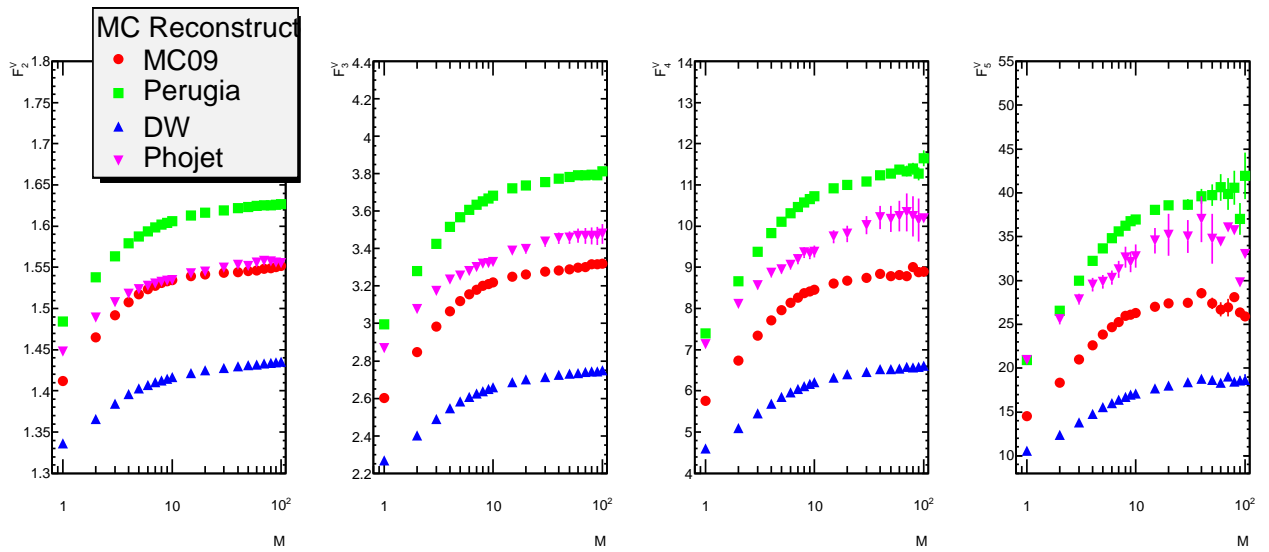


Figure 5.15: Reconstructed NFMs for different Monte Carlo generators at $\sqrt{s} = 900$ GeV. Errors are statistical.

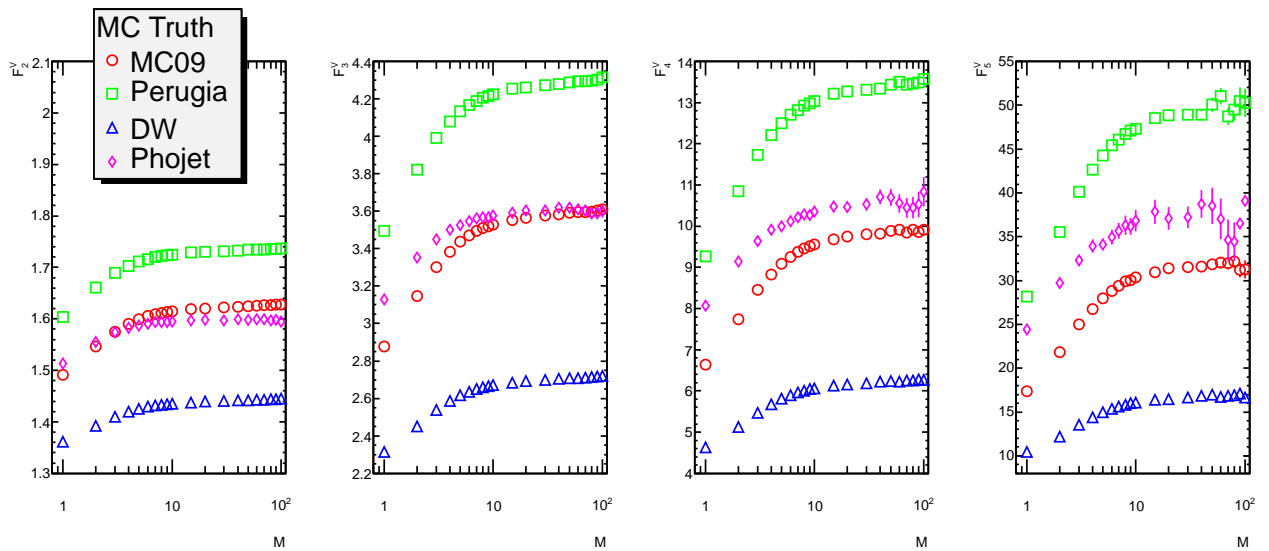


Figure 5.16: True NFMs for different Monte Carlo generators at $\sqrt{s} = 900$ GeV. Errors are statistical.

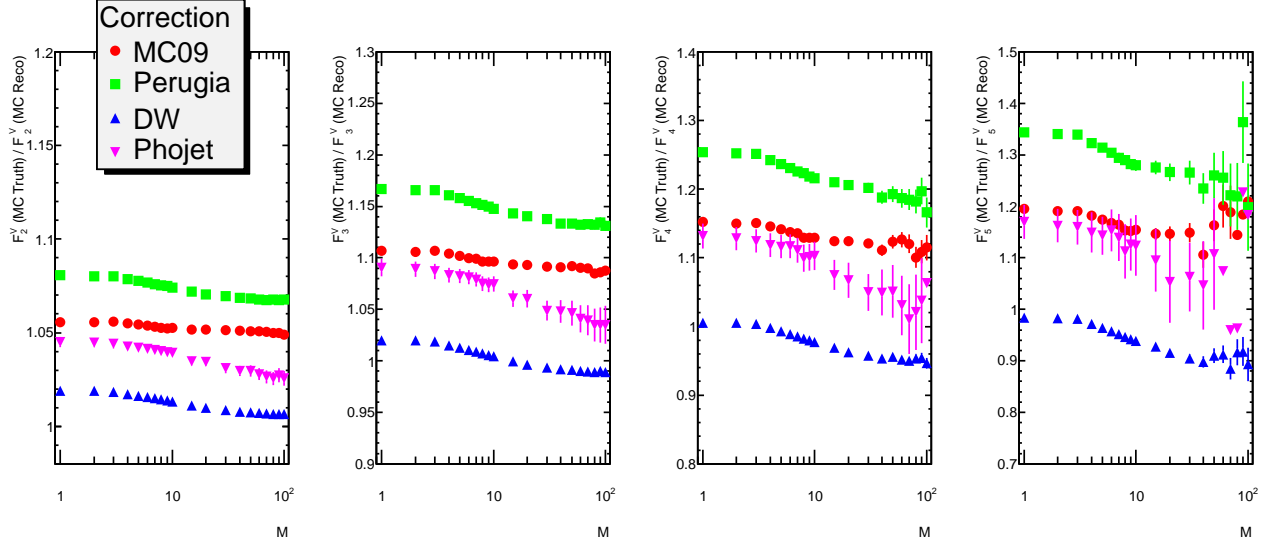


Figure 5.17: NFMs correction factors for different Monte Carlo generators at $\sqrt{s} = 900$ GeV. Errors are statistical.

been tested, such as adding and removing randomly tracks to correct the final distribution to the true level. Methods based on the creation of tracks randomly in each event have shown to distort the final distribution and cannot be applied. All the attempts to create a method to correct to particle level the measured NFMs have been so far unsuccessful, so only results at reconstructed level are presented.

Future applicable method

The Bayesian unfolding showed a good performance for high-order moments. These moments are actually making use of the NFMs for $M = 1$, so in principle, the same correction can be applied to NFMs for $M \neq 1$. The factorial moments can be rewritten in terms of the charged particle multiplicity at bin m , $P_m(n)$:

$$F_q(M) = \frac{1}{M} \sum_{m=1}^M \frac{\langle n_m^{[q]} \rangle}{\langle n_m \rangle^q} = \frac{1}{M} \sum_{m=1}^M \frac{\frac{1}{N} \sum_{i=1}^N n_m^i [q]}{(\frac{1}{N} \sum_{i=1}^N n_m^i)^q} = \frac{1}{M} \sum_{m=1}^M \frac{\sum_{n=1}^{n_{max}} n^{[q]} P_m(n)}{(\sum_{n=1}^{n_{max}} n P_m(n))^q} \quad (5.17)$$

where n_{max} corresponds to the maximum multiplicity measured in the bin m . Using this, in principle, the reconstructed $P_m(n)$ can be corrected and unfolded to $P_m^{corr}(n)$, which can be used in equation 5.17 to obtain the particle level corrected NFMs. One of the possible drawbacks is that this method requires to compute several migration matrices which can make very tedious to keep track of their good quality. The computing of such matrices will require the use of very large MC samples, and very intensive CPU use.

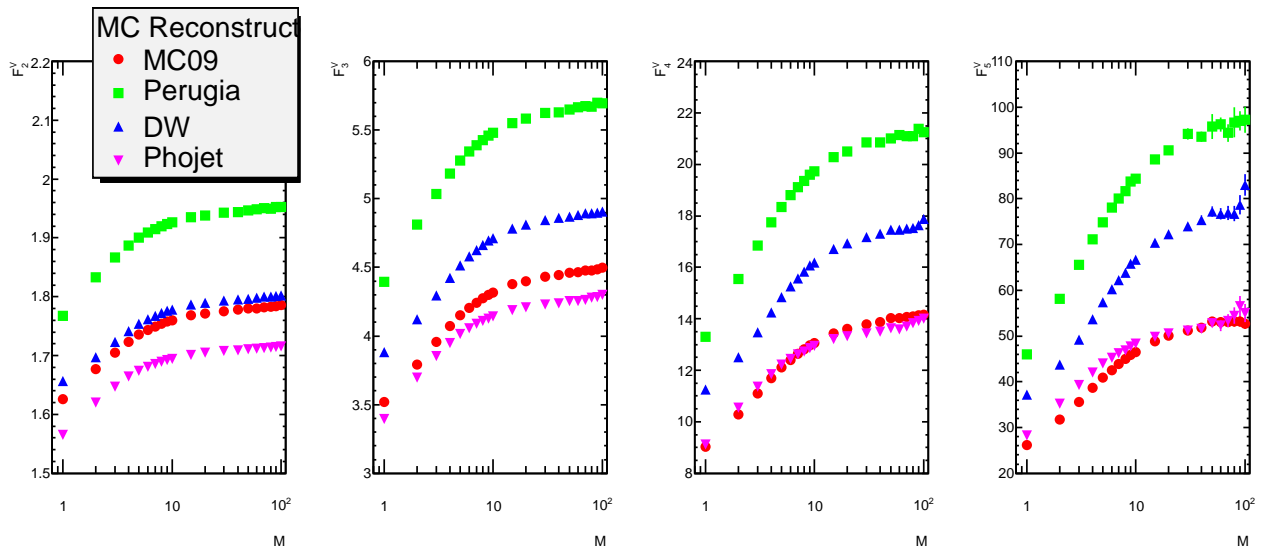


Figure 5.18: Reconstructed NFMs for different Monte Carlo generators at $\sqrt{s} = 7$ TeV. Errors are statistical.

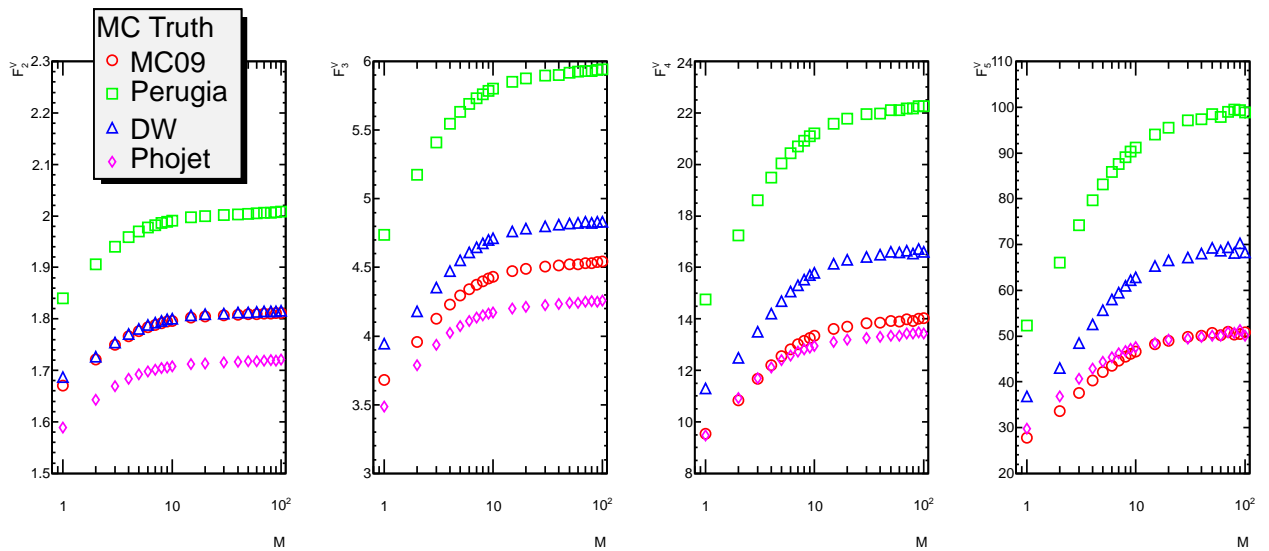


Figure 5.19: True NFMs for different Monte Carlo generators at $\sqrt{s} = 7$ TeV. Errors are statistical.

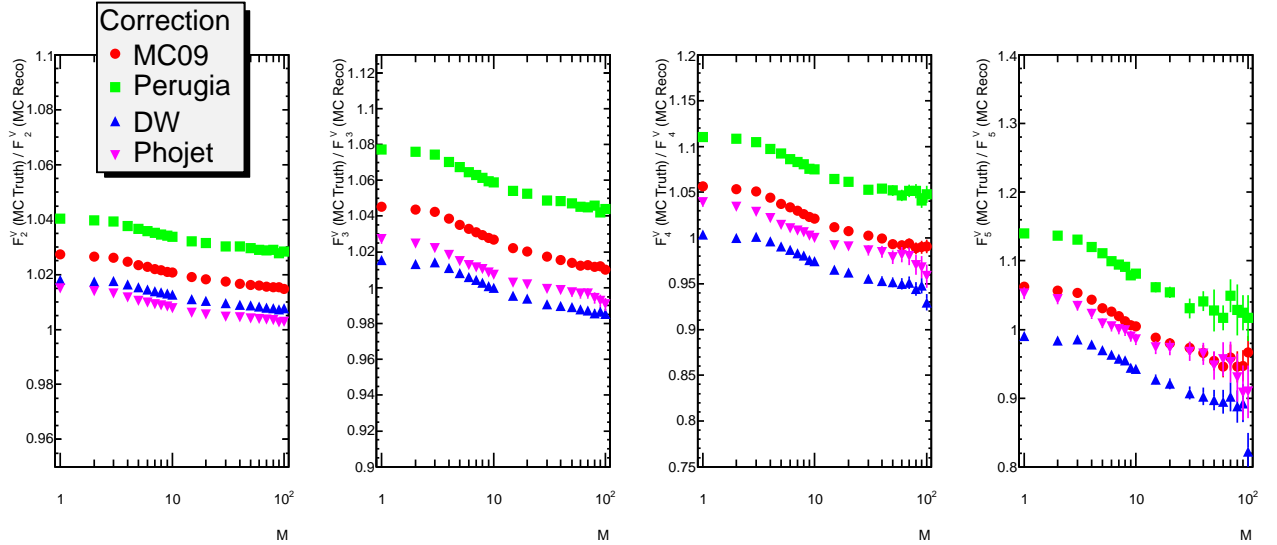


Figure 5.20: NFMs correction factors for different Monte Carlo generators at $\sqrt{s} = 7$ TeV. Errors are statistical.

5.4.4 Results at reconstructed level

Figures 5.21 and 5.22 show the reconstructed factorial moments for data, along with the ones for MC09, Perugia0, and Phojet Monte Carlo samples, at $\sqrt{s} = 900$ GeV and 7 TeV, respectively. At a fixed order q , the measured NFM increases with decreasing bin size, eventually reaching a plateau. At a fixed bin size M , the NFMs increase with increasing order. While all three Monte Carlo samples reproduce these effects qualitatively, none is able to simultaneously predict the size of the observed NFMs and their rate of increase with M and q at both center-of-mass energy.

At both $\sqrt{s} = 900$ GeV, the best agreement is found by Perugia0 and Phojet. MC09 sample underestimates the measured factorial moments and for DW the underestimation is even larger. In the case of 7 TeV, DW sample shows the best agreement in terms of normalization, while Perugia0 tune overestimates the data measurement. At this range energy, Phojet and MC09 underestimate the data.

The current technical impossibility to correct to generator level prevents to make strong conclusions, however it is interesting to see how, depending on the parameter tune, a same MC generator can return different normalization and dependence for the NFMs. On the other hand, it is remarkable the level of accuracy in physics modeling implemented in the MC generators which allows to describe qualitatively the multiparticle correlations.

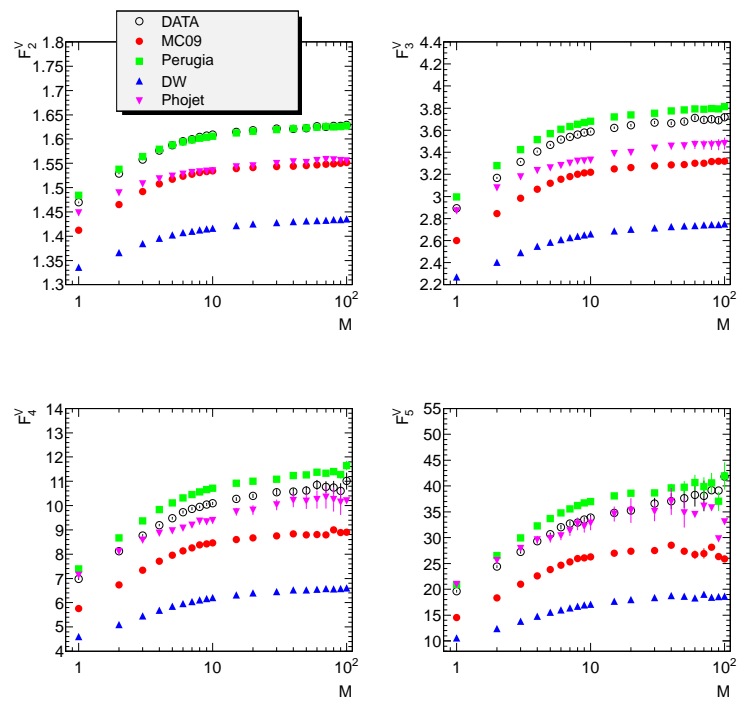


Figure 5.21: Reconstructed NFMs for data and different MC at $\sqrt{s} = 900$ GeV. Errors are statistical.

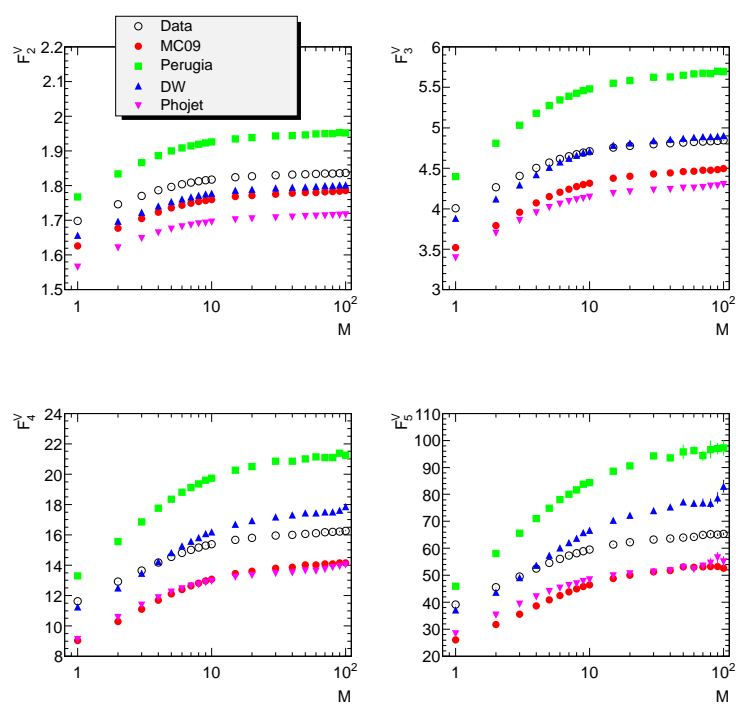


Figure 5.22: Reconstructed NFMs for data and different MC at $\sqrt{s} = 7$ TeV. Errors are statistical.

5.5 Summary and outlook

The first measurement of high order moments in ATLAS has been presented. This measurement is based on a detailed description of the multiplicity tail. The quasi-oscillations predicted by QCD and the LPHD are observed in data. All the Monte Carlo generators qualitatively describe this behavior, but the position of the first minimum and the amplitude of the oscillations vary between generators and tunes.

The attempt trial to measure the NFM's in ATLAS has been also presented. The large dependence on the correction factors and the MC generators makes impossible at this stage to correct to the generator level. A possible model independent method has been described, but has not been yet implemented because it requires large computing resources. The reconstructed level has been compared to the reconstructed MC. None of the generators is able to describe accurately the data NFM's, however similar dependence but different normalization is observed between samples.

Dedicated Minimum Bias runs are expected for 2012. This will allow, with updated detector simulation, better detector understanding and improved Monte Carlo description of data, to redo these analyses.

Chapter 6

Same-sign top and b' searches

In 2011, after few months of technical stop, the LHC started to collect data again. Thanks to the upgrades and the 2010 experience, the delivered luminosity increased substantially. The ATLAS recorded the delivered data with an efficiency larger than 93 %. In Figure 6.1 the total accumulated luminosity delivered and recorded can be seen. Due to this great performance, a new stage began for the LHC experiments: the new physics searches.

Among these new searches, the study of the production of same-sign top quark pairs mediated by new resonances is one of the candidates to explain the forward-backward asymmetry observed at the Tevatron [102]. A hypothetical fourth family of quarks can also produce same-sign top quarks, with important implications for charge-parity non-conservation in B-meson decays [106]. This chapter is focused in the analysis for the search of same-sign top production and the fourth family of quarks [6], making use of

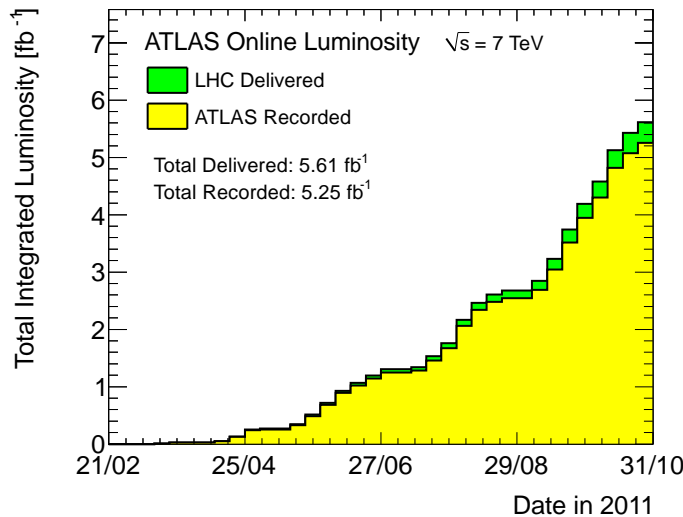


Figure 6.1: Cumulative luminosity versus week delivered to (green), and recorded by ATLAS (yellow) during stable beams and for $\sqrt{s} = 7$ TeV. The luminosity is determined from counting rates measured by the luminosity detectors [95].

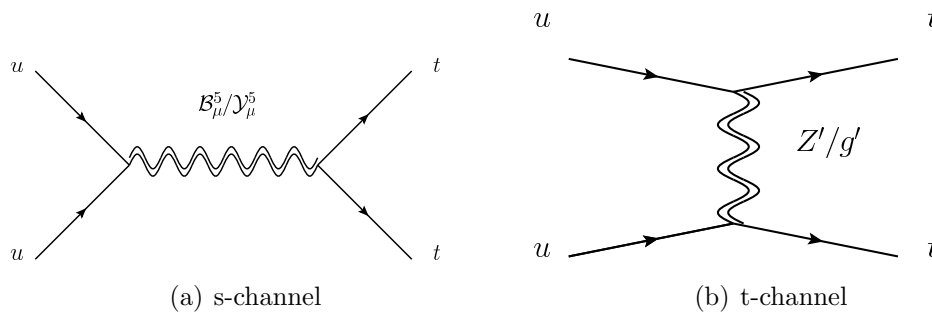


Figure 6.2: Same-sign top pair production for s-channel (left) and t-channel (right).

1 fb^{-1} data accumulated before the summer of 2011.

In the first two sections, the motivation for same-sign top and b' searches is explained. The next section defines how leptons, jets and other objects are reconstructed in ATLAS. The event selection for the analysis is explained in Section 6.4. The main background contributions compatible with the used selection are shown in Section 6.5. One important background that cannot be derived from Monte Carlo is the charge mis-identification of electrons and muons. A detailed description on the methods used to measure it is presented, providing the data-driven estimation used for the final analysis. In the last chapter, the results about the charge flip rates are presented together with the final measurement of the b' mass and the same-sign top cross-section production.

6.1 Same-sign top search

Different Beyond Standard Models (BSM) can generate two top quarks at tree level. For the s-channel, a new resonance is required, as shown in Figure 6.2 left. New particles will be needed and they must be a color triplet or a color sextet with charge $4/3$. The t-channel is mediated by a color singlet (Z') or octet (g') with charge 0. This channel is of great interest because it can give a solution [98] for the Tevatron forward-backward asymmetry observed in D0 [102] and CDF [101], which deviates from the Standard Model (SM) expectations. Independently of the production mechanism, the final state of the process we are interested in is two same-sign leptons, two large momentum jets and missing energy. This final state has a very low background in the Standard Model (SM), for this reason in case same-sign top exists, this is a very clean process to be measured at LHC.

At the LHC, the initial partons that mediate this process are up or charm quarks to produce the top quark, as required by charge conservation. To produce two top quarks at LHC, two up or charm quarks need to be involved. As LHC is a proton collider, the probability for producing two anti-top pairs which require two anti-up or two anti-charm quarks is much smaller, for this reason we will not consider the anti-top pair production. Similarly, up quarks are dominant in protons PDFs, so the leading production mechanism for like-sign top pairs is: $uu \rightarrow tt$.

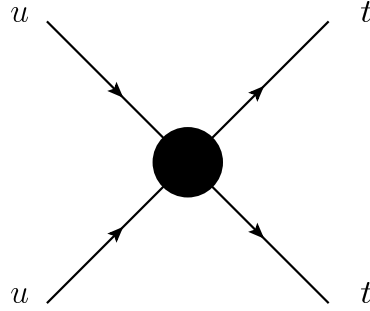


Figure 6.3: Same-sign top pair production effective model, valid for resonance masses much larger than the electroweak symmetry breaking scale.

An effective four-fermion interaction as shown in Figure 6.3 can be built to describe all the modes of $uu \rightarrow tt$ production when the resonance masses are larger than the electroweak symmetry breaking scale ν . There are five independent four-fermion operators contributing to the process $uu \rightarrow tt$ [99]. These operators generate the four-fermion terms, providing the lagrangian terms we are interested in:

$$\begin{aligned} \mathcal{L}_{4F} = & \frac{1}{2} \frac{C_{LL}}{\Lambda^2} (\bar{u}_L \gamma^\mu t_L) (\bar{u}_L \gamma_\mu t_L) + \frac{1}{2} \frac{C_{RR}}{\Lambda^2} (\bar{u}_R \gamma^\mu t_R) (\bar{u}_R \gamma_\mu t_R) \\ & - \frac{1}{2} \frac{C_{LR}}{\Lambda^2} (\bar{u}_L \gamma^\mu t_L) (\bar{u}_R \gamma_\mu t_R) - \frac{1}{2} \frac{C'_{LR}}{\Lambda^2} (\bar{u}_{La} \gamma^\mu t_{Lb}) (\bar{u}_{Rb} \gamma_\mu t_{Ra}) + \text{h.c.}, \end{aligned} \quad (6.1)$$

where the subscripts a, b indicate the color contractions, Λ is the new physics scale and C_{LL} , C_{RR} , C_{RL} and C'_{RL} are the effective operator coefficients.

The total cross section at LHC with 7 TeV is [100]:

$$\sigma(tt) = \frac{16.0}{\Lambda^4} [|C_{LL}|^2 + |C_{RR}|^2] + \frac{2.00}{\Lambda^4} [|C_{LR}|^2 + |C'_{LR}|^2] + \frac{0.96}{\Lambda^4} \text{Re} C_{LR} C'_{LR} \quad \text{pb} \cdot \text{TeV}^4,$$

The subprocess for $\bar{u}\bar{u} \rightarrow \bar{t}\bar{t}$ is around 100 times smaller. The inclusive $uu \rightarrow tt$ cross section is equal to 8 pb for same-sign top quarks with identical helicity states (LL or RR). For opposite helicity states (LR) the inclusive cross-section is 2.4 pb.

Top quark pairs decay to a b quark and a W boson 99 % of the times. In order to get the clearest signature in the detector, only leptonic decays for W bosons are taken into account. The final state for the same-sign top pairs is shown in the Figure 6.4, where the two same-sign leptons, the two jets and the two neutrinos, leading to large missing energy can be seen.

A search for like-sign top pairs has been reported recently by CDF [103]. Agreement with the Standard Model was found, so a 95% CL limit for the effective operator coupling was set:

$$\frac{|C_{RR}|}{\Lambda^2} < 3.7 \text{ TeV}^{-2} \quad (6.2)$$

The CMS collaboration, with LHC 2010 data, also performed a same-sign top search [104]. Similarly as CDF, they compute a 95%CL limit for the cross-section production:

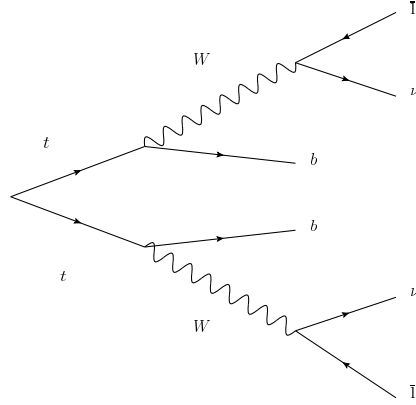


Figure 6.4: Same-sign top pair decay in leptonic channels.

$\sigma_{pp \rightarrow tt} < 17.0$ pb and also for the effective couplings:

$$\frac{|C_{RR}|}{\Lambda^2} < 2.7 \text{ TeV}^{-2} \quad (6.3)$$

It is important to remark that CDF did the analysis with 6.1 fb^{-1} of $p\bar{p}$ data and CMS used only 35 pb^{-1} of pp data. The CMS limit is more stringent than CDF limits. This shows that same-sign top production is favored in proton-proton collisions, production cross-section at LHC is three orders of magnitude larger than for Tevatron, so a very high sensitivity is expected for 2011 data.

6.2 Fourth family of quarks

In the Standard Model, three generations of fermions are accommodated, but a fourth generation is not prohibited. Recent studies show that within the electroweak constraints it is possible to introduce a new generation of fermions [105]. This hypothetical new generation could explain some physics measurements and processes, such as the recent measurement of charge-parity non-conservation in B-meson decays, which shows more than 2σ deviation from the Standard Model and is sensitive to contributions from an extra generation [106]. A four-generation model could provide sources of particle-antiparticle asymmetries large enough to account for the baryon asymmetry of the universe [107]. Also it can accommodate a heavier Higgs boson than the three-generation model [108]. For all these reasons, the search for fourth generation b-like quarks has been also attempted. The final state can have two same-sign leptons, jets and large missing transverse energy that is compatible with the signature for same-sign top search.

In Figure 6.5 the production and decay chain of $b'\bar{b}'$ are shown. The process is:

$$pp \rightarrow b'\bar{b}' + X \rightarrow t + W^- + \bar{t} + W^+ + X \rightarrow b + W^+ + W^- + \bar{b} + W^- + W^+ + X \quad (6.4)$$

It is assumed that b' decays to a top quark with 100% probability. In addition, only leptonic decays for W bosons are shown in the figure. This allows final states with up to

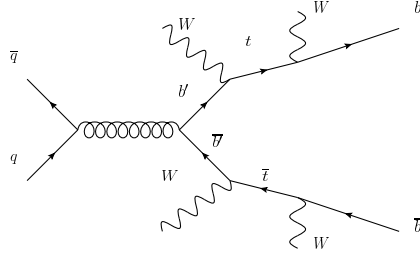


Figure 6.5: Pair production and decay of b' quarks with decays to $WWbWWb$. Events are selected in which one W decays leptonically, either a W from the t or the b'

four leptons, two positive and two negative. Also up to four neutrinos can be produced leading to large missing transverse energy. Two b -quarks are produced in the top decay, so at least two jets are produced in the event. This leads to the signature we are interested in.

Direct searches for fourth family of quarks were performed by CDF [109] and D0 [124] collaborations at Tevatron. In these searches evidence for a fourth generation has not been found. The mass limits obtained for $b'\bar{b}'$ pair production are: $m_{b'} > 338$ GeV in the dilepton plus jets final state. For the single lepton plus jets, the limit is: $m_{b'} > 385$ GeV. The CMS collaboration has also performed a search in the same-sign dilepton plus jets channel [110] with 2011 data. The mass limit obtained is: $m_{b'} > 495$ GeV at 95% confidence level.

It is still possible that events have escaped detection because the relevant branching fractions are smaller than 100 % and (or) the lifetimes are so long that they escaped the acceptance of the analysis cuts. Searches at Tevatron have been performed for long lifetimes fourth family quarks, providing much lower mass limits [111].

6.3 Object definition

- **Electrons:** Electron candidates are reconstructed by matching cluster energy deposits in the electromagnetic calorimeter to tracks in the Inner Detector. Depending on the properties of this matching and the clusters quality, different selections are defined in ATLAS. For this analysis, a stringent selection is used, known as *tight* [96]. The tracks which pass the good quality cuts, such as minimal number of Pixel, SCT and TRT hits and χ^2 , are extrapolated to the electromagnetic calorimeter, and the extrapolation and cluster positions differences must fulfill the following requirements: $|\eta_{trk} - \eta_{cluster}| < 0.01$ and $|\phi_{trk} - \phi_{cluster}| < 0.005$, where the *trk* variables correspond to measurements done with the inner detector tracker, while *cluster* measurements are done in the electromagnetic calorimeter. The energy measured in the calorimeter must be consistent with the momentum measured in the tracker: $0.7 < E/p < 5.0$. This set of cuts makes use of all the particle-identification tools currently available for electrons, so if the electrons are in the acceptance region of the TRT, the number of high threshold hits over the total number of TRT hits must be larger than 0.08 for

the central region and 0.155 for electrons in the end-cap regions. TRT information is very important to reject the dominant background from charged hadrons. Besides, in order to prevent conversions from photons decaying in electron-positron pairs, the electron track must have at least one hit in the silicon layer closest to the interaction point (b-layer).

The final candidates are required to have a transverse energy (E_T) over 25 GeV and $|\eta_{Cluster}| < 2.47$ with an impact parameter $d_0 < 1mm$ ¹. At this electrons energies, the TRT plays an important role for the track reconstruction and a good calibration is fundamental to obtain an excellent momentum resolution. In addition, the information provided by the TRT is used to propagate the track to the electromagnetic calorimeter and to improve the track-cluster matching. Electrons falling in the calorimeter crack regions, the transition between barrel and end-caps at $1.37 < |\eta_{Cluster}| < 1.52$, are also rejected to get the best quality of the measured energy.

To reduce fakes from QCD jets and electrons from heavy flavor decays inside jets, the electrons candidates must be isolated. The transverse energy (E_T^{iso}) deposited in the calorimeter towers in a cone in $\phi - \eta$ space of radius $\Delta R < 0.2$ around the electron is summed. The E_T from the electron is subtracted and the final value is corrected for the uncorrelated energy flow in the event depending on the number of primary vertexes. The final E_T^{iso} isolation is required to be less than 3.5 GeV.

- Muons: Muon candidates [97] are reconstructed by searching for track segments in different layers of the muon chambers. These segments are matched with tracks found in the Inner Detector [16]. Similarly as in the electron case, the long track arm measured in the TRT improves the matching between the Inner Detector tracks and the Muon Spectrometer segments. The final candidates are refitted to use the full track information. The final quality of the muons must be *tight*.

Final candidates need to satisfy $p_T > 20$ GeV and $|\eta| < 2.5$. To reduce the acceptance of fake muons, the muons have to be isolated. Only candidates with corresponding calorimeter isolation energy in a cone of $\Delta R = 0.3$ less than 4 GeV are accepted. We also require a tracking isolation less than 4 GeV in a $\eta - \phi$ cone of $\Delta R = 0.3$.

To prevent the acceptance of cosmic muons, in case there are two muon candidates back to back ($\Delta\phi > 3.1$), both candidates are rejected. The last requirement, to maximize the charge efficiency measurement, both tracks (muon spectrometer and inner detector) must have same-sign.

- Jets: Jets are reconstructed using the anti- k_t algorithm with distance parameter $R = 0.4$. The seeds for the jet algorithm are topological energy clusters in the calorimeter reconstructed at the electromagnetic scale. A Monte Carlo based correction is applied to the jets to restore the hadronic energy scale. This correction is applied on p_t and η .

¹ d_0 is the distance in the transverse plane for the electron closest approach to the primary vertex.

In order to remove out-of-time energy deposits caused by various sources as hardware problems or cosmic muons, a jet quality criteria is applied [112]. The final accepted jets must be $p_T > 20$ GeV and $|\eta| < 2.5$.

- Missing Transverse Energy, E_T^{miss} : Protons colliding at the LHC have equal and opposite momenta. Therefore, the total vector momentum sum in an event should be zero. This assumes a full spatial coverage and also detection of all produced particles in the collision. But low interacting particles, such as neutrinos transverse the detector without leaving trace, and this will produce an imbalance in the sum, which is known as missing transverse energy (E_T^{miss}).

In ATLAS, this imbalance is computed with other reconstructed objects:

$$E_{x,y}^{miss} = E_{x,y}^{electrons} + E_{x,y}^{muons} + E_{x,y}^{jets} + E_{x,y}^{softjets} + E_{x,y}^{cellout} \quad (6.5)$$

where x and y are the coordinates in the transverse plane. $E_{x,y}^{softjets}$ corresponds to the low p_T jets that are included at electromagnetic scale. $E_{x,y}^{cellout}$ is made of the remaining clusters not associated to high p_T objects. The final value used is the module of the x and y components:

$$E_T^{miss} = \sqrt{E_x^{miss^2} + E_y^{miss^2}} \quad (6.6)$$

6.4 Event selection and signal region

The data used for this analysis were collected between March 2011 and July 2011. The total recorded integrated luminosity that passed good data quality requirements for leptonic analysis, such as muon spectrometer and electromagnetic calorimeters fully operative, is $1.035 \pm 0.036 \text{ fb}^{-1}$.

After the objects are reconstructed and selected, some extra requirements are applied to avoid overlap between electrons, muons and jets. If an electron and a jet candidate overlap in a cone $\Delta R < 0.2$ in the $\eta - \phi$ plane, the jet is rejected. In case of electron or muon candidates overlap with a jet in a cone $\Delta R < 0.4$, the electron or muon candidates are not selected but the jet is kept.

We require the first primary vertex reconstructed in the event to have at least 5 tracks. First primary vertex is considered the vertex with largest sum of transverse momentum of the track originated in the vertex.

During the data-taking, on April 30th 2011, a front-end board electronics in the Liquid-Argon calorimeter was lost. For data taken since then until after the board was replaced if a jet with $P_T > 20$ GeV falls in the calorimeter region covered by this board, the event is rejected.

This signal region selection has been derived from a significance optimization for the same-sign top production:

- The final states we are interested in have two top quarks. These quarks decay into b-quarks producing 2 energetic b-jets, for this reason events are requested to have two or more jets with $p_T > 20$ GeV in $|\eta| < 2.5$.

- The top decays to W bosons and b-quarks. To get a clear signature, only leptonic decay of the W boson will be taken into account. These decays will produce neutrinos, leading to a large fraction of transverse energy not measured in the detector, so only events with a transverse missing energy greater than 40 GeV are accepted.
- Two large momentum same-charge leptons are expected for same-sign tops so at least two leptons with same-sign ($e^\pm e^\pm$, $\mu^\pm \mu^\pm$ or $e^\pm \mu^\pm$) are requested. The trigger setting known as *EF_mu18* is used for selecting muon leading events. This trigger reaches the plateau efficiency for muons above 20 GeV. For electrons, the trigger used is called *EF_e20_medium* with plateau efficiency at $E_T > 25$ GeV. Events with more than two leptons are accepted since b' signal events have more than 2 leptons in the final state for ~ 26 % of the events.
- The event energy (H_T), computed as the transverse scalar sum of all accepted leptons and jets in region $|\eta| < 2.5$, has to be larger than 350 GeV.

6.5 Background contribution

Based on Standard Model contributions and also taking into account detector effects, the main backgrounds are:

- Irreducible SM background: SM processes with real same-sign dilepton pairs, including WZ , ZZ , $t\bar{t}W$, $t\bar{t}W + jets$, $t\bar{t}Z$, $t\bar{t}Z + jet$, $t\bar{t}W^+W^-$, $W^+W^+ + 2jets$. Their contribution is small, but they are irreducible backgrounds of this analysis. The estimation is based on Monte Carlo samples normalized to the data luminosity.
- Leptons originated from jets or photons: This is the main contribution for the analysis. These "fake" leptons are jets and photons mis-reconstructed as leptons. The possible mechanisms leading to "fake" electrons are semi-leptonic decays of heavy flavors, decay in flight of a π^\pm or a kaon to a π_0 overlapping with a charged particle and conversion of photons. In the case of muons, the main mechanism is heavy flavor decays. The *matrix method*, a data-driven technique, is applied to measure the fraction of the selected sample that contains events with a fake lepton. Detailed information on the method can be found elsewhere: [6] [113]. A control selection is defined to measure lepton-like jets. For muon-like jets the isolation requirements are dropped and for electrons, in addition to isolation, the quality cut of the track is removed. Two control regions are created, one for "real" leptons making use of the Z resonance, and other for "fake" ones with a single lepton-like jet reconstructed produced far from the primary vertex and low missing E_T . Making use of both control regions and the "fake" like selections, the so-called fake rates (f) are measured depending on the lepton p_T and $|\eta|$ and applied in the analysis signal region.
- Lepton charge mis-identification: leptons can be mis-reconstructed giving events with same-sign leptons from opposite-sign processes: $Z + jets$, $t\bar{t}$ and dibosons. In the next section, the data-driven methods used to measure the charge mis-identification

for electrons and muons will be described in detail. This is my main contribution to the analysis, developing and validating new methods never used before on data that improves the sensitivity of the analysis.

6.6 Charge mis-identification

Processes with two opposite-sign leptons as $t\bar{t}$ may contribute to the same-sign lepton final state if one of the lepton's charge is mis-identified.

To estimate the contribution to the same-sign signature produced by opposite-sign leptons with an electron or muon charge mis-reconstructed, the probability that the lepton charge is reconstructed with the wrong charge (charge flip rate) is measured using data-driven methods. These rates are then applied to weigh events with the signal signature but having opposite-sign leptons. This provides the expected background contribution for the same charge final state which we are interested in.

In this section we present the methods developed and used to estimate the probability of charge mis-identification on Monte Carlo and data for electrons and muons. The methods require physics processes with a large purity of opposite-sign leptons, and with very low same-sign background contaminations. For this reason, the Z resonance is used to get a clear sample of opposite charge leptons to study the same-sign leptons spectrum.

For these studies, in order to enhance the acceptance for Z bosons, the event selection is the same as the general analysis, but modifying the following cuts:

- Leptons do not need to be same-sign.
- Number of jets ≥ 0 .
- $H_T > 0$ GeV.
- $E_T^{miss} > 0$ GeV.

6.6.1 Monte Carlo samples

The study requires large samples of simulated $Z/\gamma^* + \text{jets}$ (Drell-Yan) events. The main samples used are produced with ALPGEN [114]. The parton shower distribution function CTEQ6.6 [115] is used for the matrix element calculation and the parton shower evolution. All events are hadronized with HERWIG [116], using the JIMMY [117] underlying event. The corresponding AUET1 HERWIG and JIMMY tune [118] to the ATLAS data is used. These samples simulate the production of a Z boson and up to 5 jets with $p_T > 20$ GeV and $|\eta| < 2.5$. In addition a sample produced with Sherpa [119] is used for studies of systematic uncertainties.

For evaluating the $t\bar{t}$ contribution, the production and the fully leptonic decay of the W bosons is simulated with MC@NLO [120] generator using a top quark mass of 172.5 GeV and the next-to-leading order parton distribution function CTEQ6.6. The parton shower and the underlying event were simulated using HERWIG and JIMMY generators.

All the MC samples passed through the ATLAS simulation framework [121], which uses a GEANT4 [122] based detector simulation. The samples are reconstructed and passed through the same chain as the data. Few extra corrections are needed to correct the MC to data expectations: the samples are weighted to reproduce the number of interactions per bunch crossing observed in data. Also, the electrons and the muons momentum measurements are smeared to match the MC resolution to data.

6.6.2 Electron charge mis-identification

There are two main sources for charge mis-identification:

- **Hard Bremsstrahlung:** an electron will radiate a high momentum photon that will convert producing an electron-positron pair. This is known as trident electron. In this case, as shown in Figure 6.6, the electron and positron will have the same direction, due to the large momentum of the photon ($p_\gamma \gg 2m_e$). The whole energy of the electron-positron pair will be deposited in the calorimeters, but the charge will be mis-reconstructed in case the clusters are matched to the positron track.
- **Low curvature of the track:** the charge measurement is done with the curvature of the track in the Inner Detector. The detector has a limited resolution, so for high momentum electrons, where the curvature is low, it is possible to get a wrong charge measurement. This effect will be dominant at very high momentum and ruled by the intrinsic resolution of the Inner Detector. For Monte Carlo this effect was studied in detail [16].

Monte Carlo Estimation

In Monte Carlo, the reconstructed electrons can be matched to the generated from the Z decay. Using this, we evaluate the rate of electron charge mis-identification (ϵ_{chg}). A simple cone $\Delta R = \sqrt{\Delta\phi^2 + \Delta\eta^2}$ matching is used. In case of using a very tight cone radius, the charge mis-identification reduces to negligible values but also the efficiency drops. In Figure 6.7 it is shown that, for $\Delta R > 0.05$, the size of the cone has no incidence on the matching performance, so a radius of $\Delta R \leq 0.2$ is used to find reconstructed electrons that correspond to true electrons produced from the Z decay. The matching is done only to primary electrons, the ones produced directly from the Z decay. This prevents matching reconstructed electrons to electrons produced in the conversion of radiated photons from primary electrons to electron-positron pairs or to electrons produced in other secondary processes. In the case of the trident electrons, the reconstructed electrons will be matched to the primary electron if the electrons produced in the conversion are almost collinear to the primary electron.

In Figure 6.7, the charge mis-identification rates are shown in different η bins for Alpgen Z + jets. The central region of the Inner Detector, where the material budget is smaller, as shown in Figure 6.8, and the track resolution has the best performance, the charge mis-identification is very reduced. Once moving to the outer part of the end-caps, the amount

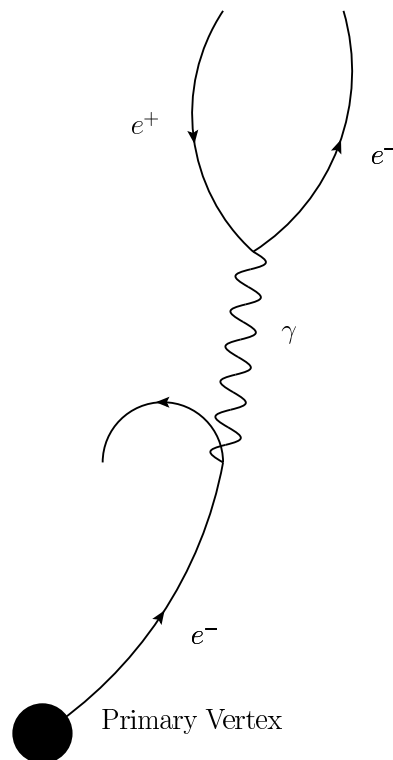


Figure 6.6: Production of *trident electrons*. An electron is produced in the hard proton-proton interaction. Due to material interaction, the electron radiates a large momentum photon. An electron-positron pair is produced from the photon decay. The final energy deposition in the calorimeter can be matched to the either the positron or the electrons. In case the matching is to the positron, this leads to a wrong charge measurement. Same process can happen if the primary particle is a positron.

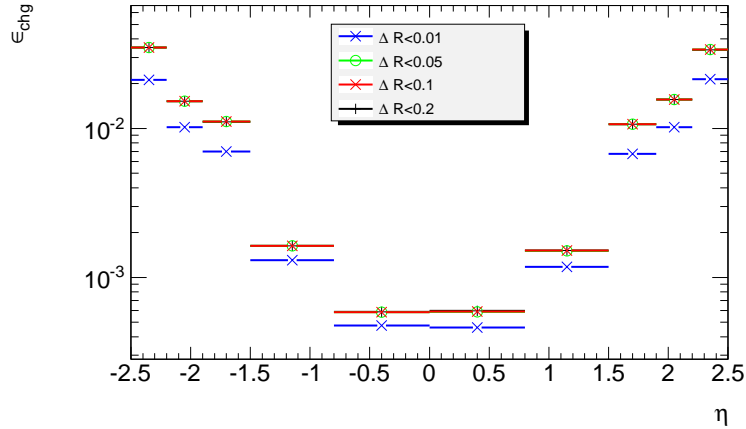


Figure 6.7: Charge mis-identification rate for electrons, based on truth matching with cone algorithm for different radius as a function of η . For ΔR larger than 0.05, the same charge mis-identification is observed. A $Z + \text{jets}$ Monte Carlo sample has been used.

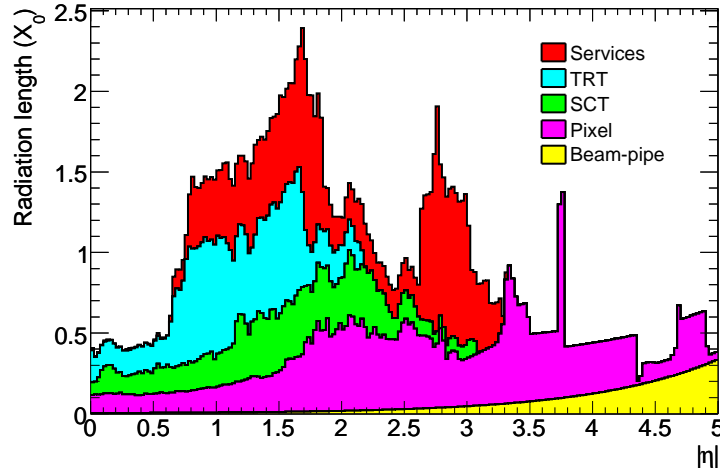


Figure 6.8: Material distribution at the exit of the Inner Detector. Beam pipe, Pixel, SCT, TRT and services contributions are shown as a function of $|\eta|$ [27].

of material the electrons go through increases, raising the fraction of trident electrons and mis-reconstructed electron charge.

The E_T dependence is shown in Figure 6.9. Once the momentum of the electrons increases, the charge mis-identification increases because the curvature decreases and the measurement is more sensitive to the intrinsic resolution of the Inner Detector.

The largest dependence observed is a function of pseudorapidity. A factor larger than 50 is observed between the central region and the outer part of the end-caps for the charge

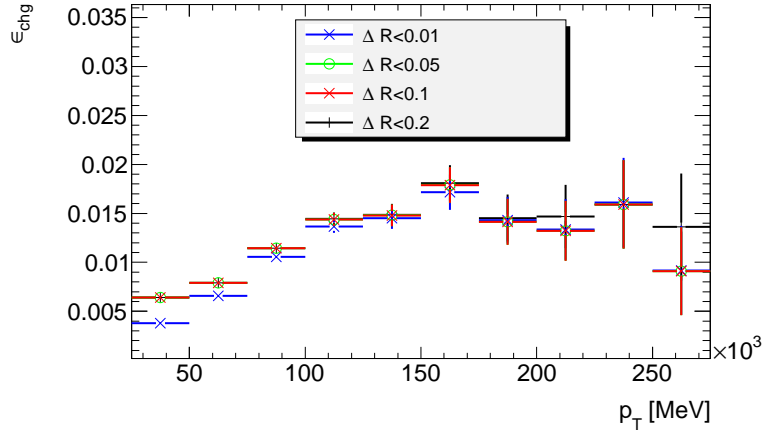


Figure 6.9: Charge mis-identification rate for electrons, based on truth matching with cone algorithm for different radius as a function of p_T . For ΔR larger than 0.05, the same charge mis-identification is observed. A $Z + \text{jets}$ Monte Carlo sample has been used.

mis-identification. For the momentum dependence, just a factor below 3 is seen in MC for high over low momentum electrons for the charge flip rate. For this reason in the next sections several methods to measure the charge flip rate for different η bins will be discussed.

Global Charge Mis-identification

In this section, we derive the charge mis-identification rate by examining the number of same-sign and opposite-sign events in the Z peak mass region in the data and MC. In Figure 6.10, the same-sign and opposite-sign invariant mass distributions for data and Monte Carlo are shown. For the simulations, the smearing factor has been applied to reconstructed electrons in order to fit the MC momentum resolution and energy scale to the data. In the figure, a simulated sample with $Z + \text{jets}$ together with data events are presented. From these Figures, we can see an excellent agreement for the Z resonances between data and MC in terms of resolution (width of the resonance) and energy scale (peak of the resonance). The Z peak for same-sign electrons is shifted to lower mass, both in data and Monte Carlo: this is because electrons in the same-sign case radiate photons and the measured electrons have lower momentum than at the moment of the production in the Z decay, leading to a lower invariant mass. The good agreement of this effect between MC and data is remarkable. In the same way, the resolution for MC and data, i.e. the width of the measured Z resonance, is in very good agreement, validating the detector simulation in this aspect.

The charge mis-identification rate (ϵ_{chg}) is computed as:

$$\epsilon_{chg} = \frac{N_{ss}}{2(N_{os} + N_{ss})}$$

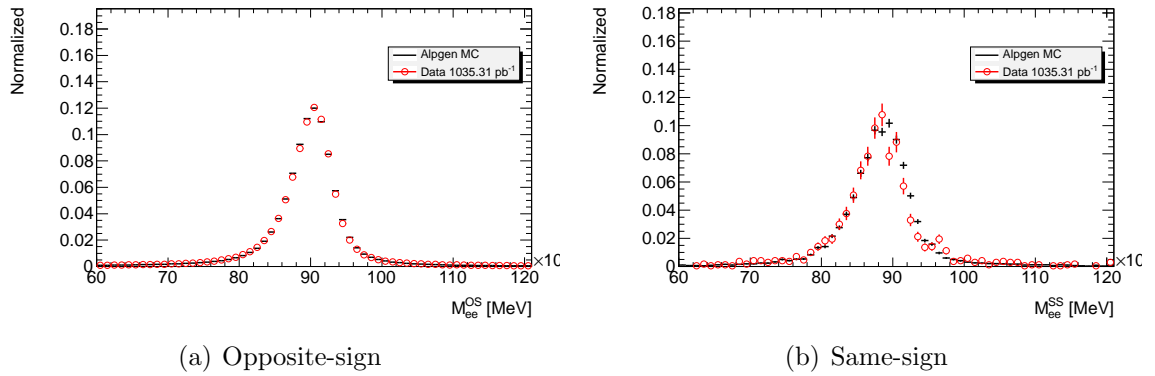


Figure 6.10: Dielectron invariant mass distribution for opposite-sign and same-sign electrons. All distributions are normalized to 1.

where the 2 is because we have two electrons in each probe. The uncertainty is evaluated following the gaussian approximation to the binomial:

$$\Delta\epsilon_{chg} = \sqrt{\frac{\epsilon_e(1 - \epsilon_e)}{N_{os} + N_{ss}}}$$

To obtain the number of electron pairs (dielectrons) in the Z region, the invariant mass M_{ll} of the two electron system is evaluated and a background extraction is performed. Backgrounds are estimated using sideband method described below. A fit to different templates for background and signal has been used to evaluate systematic uncertainties, later in this thesis this method is called profile fit. For the sideband, the default method, the invariant mass distribution is divided in three regions (A, B, C) delimited by 61, 81, 101 and 121 GeV. The number of signal events is evaluated in region B (81-101 GeV), so the background is estimated in the A and C regions and interpolated to the region B. This is similar to a linear background subtraction. The way this is evaluated is:

$$N_B^s = N_B - \frac{N_A + N_C}{2}$$

where $N_{A(B,C)}$ is the number of events in the region A (B,C) and N_B^s is the number of signal events in region B after the background extraction.

For the profile fit, signal is fitted by a Breit-Wigner convoluted with a *Crystal Ball* function [125]. The Crystal Ball function is a gaussian distribution for the core and high invariant mass and a power-law tail for the low invariant mass, describing the energy loss processes and resolution effects. This signal function describes very well the shape of the Z resonance taking into account the resolution of the detector. The background is described by an exponential. It is important to note that electrons used in this analysis are *tight*, getting a very clean sample of dielectron events, so the background contribution is very low, order of 1-2%. For this reason, very low dependence on the background extraction

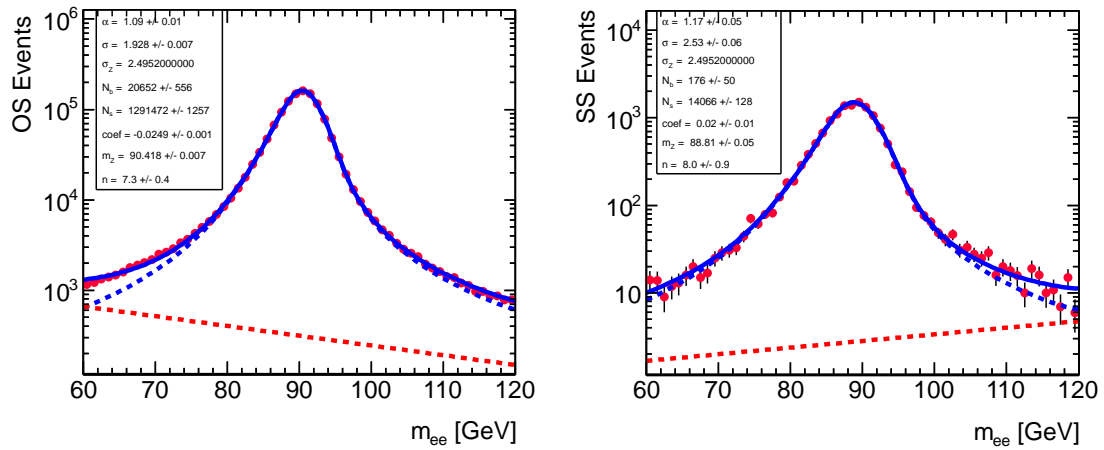


Figure 6.11: Invariant mass distribution of dielectrons with same and opposite-sign for Monte Carlo Z + Jets.

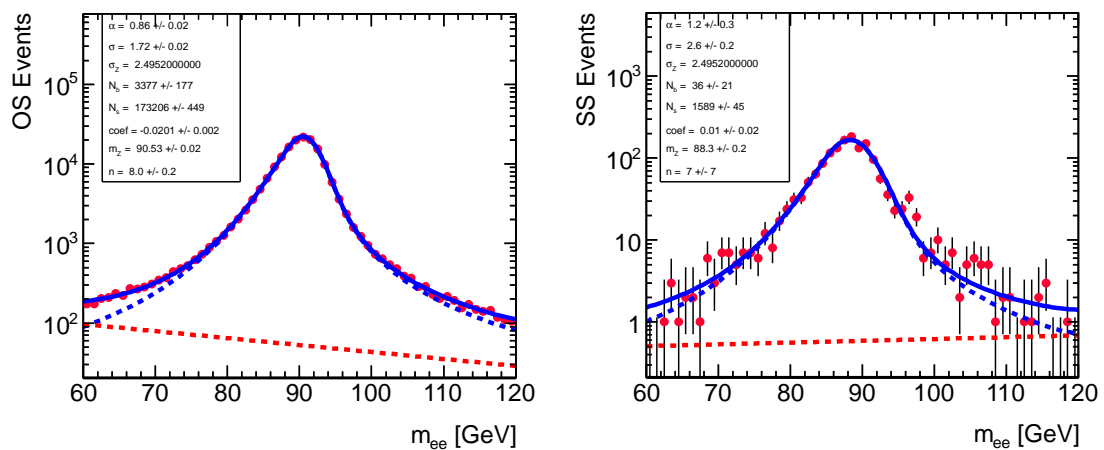


Figure 6.12: Invariant mass distribution of dielectrons with same and opposite-signs for Data, 1035 pb^{-1} .

method is expected. In Figure 6.11, we can see the invariant mass distributions for Monte Carlo and Figure 6.12 shows the same for data together with the profile fit. As expected, the function used describes very fairly the shape of the Z resonance.

In Table 6.1, the global charge mis-identification is shown for data and MC and is also compared with the MC truth based estimation derived in previous section. In this table, we can see how truth matching with a cone radius of 0.2 is in very good agreement with the measurement done in the Z peak for Monte Carlo. Different variations of the background extraction are presented.

Table 6.1: Global electron charge mis-identification for Monte Carlo Z + Jets and data with 1035.3 pb^{-1} . Errors are statistical only.

Method	Data	Monte Carlo
Sideband	0.00438 ± 0.00008	0.00527 ± 0.00003
Sideband Short Range	0.00415 ± 0.00008	0.00515 ± 0.00003
Profile Fit	0.00459 ± 0.00008	0.00541 ± 0.00003
Profile Fit Short Range	0.00450 ± 0.00008	0.00545 ± 0.00009
Profile Fit Linear Bkg	0.00457 ± 0.00008	0.00547 ± 0.00003
Truth Matching $\Delta R < 0.2$	—	0.00541 ± 0.00003

Tag-and-probe method

In this section, I derive the electron charge mis-identification rate in data and Monte Carlo using a tag-and-probe technique technique described below and resolving different bins for pseudorapidity ($|\eta|$). The selected electrons are divided in 2 classes: *tag* with a very low charge mis-identification rate and *probe* with the electron selection that we want to study, that is, the *tight* electrons in this analysis.

In our case, as the electron selection in ATLAS with lowest charge mis-identification is already used, a variation of the tag-and-probe method is used. The tag electrons used are signal electrons in the central region $|\eta| < 0.8$. As shown in Monte Carlo, the charge mis-identification rate in the central region is at least an order of magnitude lower than for electrons in the end-cap regions. Pairs of electrons are selected with at least one of them fulfilling the tag condition and the number of same-sign and opposite-sign events based on the properties (η) of the probe electron are evaluated. The charge mis-identification rate will be obtained using:

$$\delta_e^i = \frac{N_{ss}^i}{(N_{os}^i + N_{ss}^i)}$$

where i corresponds to each bin in η . These values contain the charge mis-identification rate of one tag and one probe electron. In order to get the charge mis-identification rate for each lepton, the tag efficiency has to be extracted. For the first η bin, 2 tag electrons

will be accepted: the final charge mis-identification is therefore given by:

$$\epsilon_{chg}^0 = \frac{\delta_e^0}{2}$$

For the rest of the bins, the tag efficiency has to be computed as:

$$\epsilon_{chg}^i = \delta_e^i - \epsilon_{chg}^0, i \neq 0$$

In order to get the best estimation, even if in the current electron selection the contamination is very low, it needs to be subtracted. The same methods as defined for global charge mis-identification are used: sideband and profile fit to Breit-Wigner convoluted with a Crystal Ball. In Tables 6.2 and 6.3, the results for different pseudorapidity bins are presented for Monte Carlo and data together with a comparison between different methods. Several systematic effects have been studied to understand the tag-and-probe method performances:

1. Default: This is default sidebands method and selection.
2. Sideband short range: Sidebands applied on regions: 69, 83, 97, 111 GeV.
3. Positive/Negative: Only one charge is selected. The charge mis-identification is expected to be lower for positrons than electrons due to tracking properties.
4. Profile Fit: Fit between 60 to 120 GeV.
5. Profile Fit short range: Fit between 70 to 110 GeV.
6. Profile Fit Linear Background (Bkg): Using linear background estimation instead of exponential.
7. Tag Condition: Apply a tighter selection for the tag electrons and E/P between 0.5 and 1.5. The charge identification efficiency is reduced to 1/3 of the original tag condition.
8. $E_T^{miss} < 40$ GeV: Remove all events with large E_T^{miss} to avoid W and other sources of same-sign leptons.
9. Sherpa: For MC, a second generator, Sherpa [119]. was used to validate the dependence.

Those systematic uncertainties are presented in Tables 6.2 and 6.3.

In the ideal case, the tag condition has to be applied without using any kinematic restriction. In our case, with *tight* electrons, it was impossible to find an unbiased selection. The tag condition used, known as central region condition, defines as tag electrons the one in $|\eta| < 0.8$. Both electrons are produced from a resonance, the Z boson decay, so one drawback of this selection, as presented in Figure 6.13, is the bias on the kinematical distribution of probe electron produced for the tag condition. It has been shown in earlier sections that the largest dependence of the charge flip rate is in η . The probe electrons have a lower mean for each η bin. Similar effect is observed for p_T , where the distribution is biased to lower values. With these changes in the η and p_T , and as charge mis-identification decreases when η and p_T decreases, it is expected to get lower values than for MC truth.

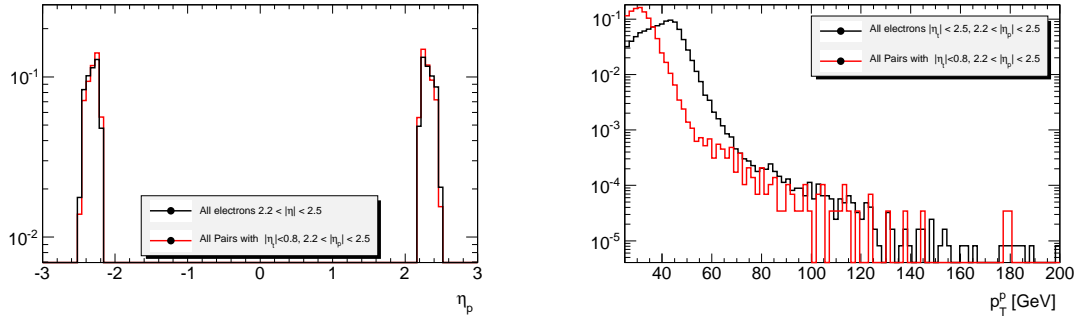
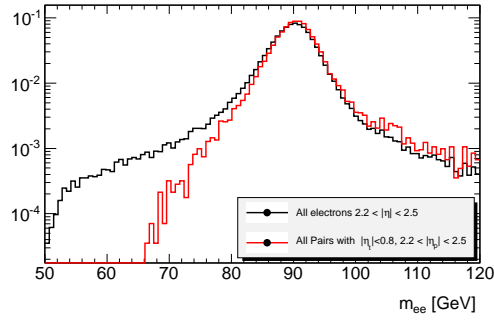
(a) Bias for tag-and-probe selection in η (b) Bias for tag-and-probe selection in p_T (c) Bias for tag-and-probe selection in m_{ee}

Figure 6.13: Distributions comparing kinematical properties of all electrons in $2.2 < |\eta| < 2.5$ (black line) with respect to the probe electrons in region $2.2 < |\eta| < 2.5$ (red line) when the tag electron is in $|\eta| < 0.8$.

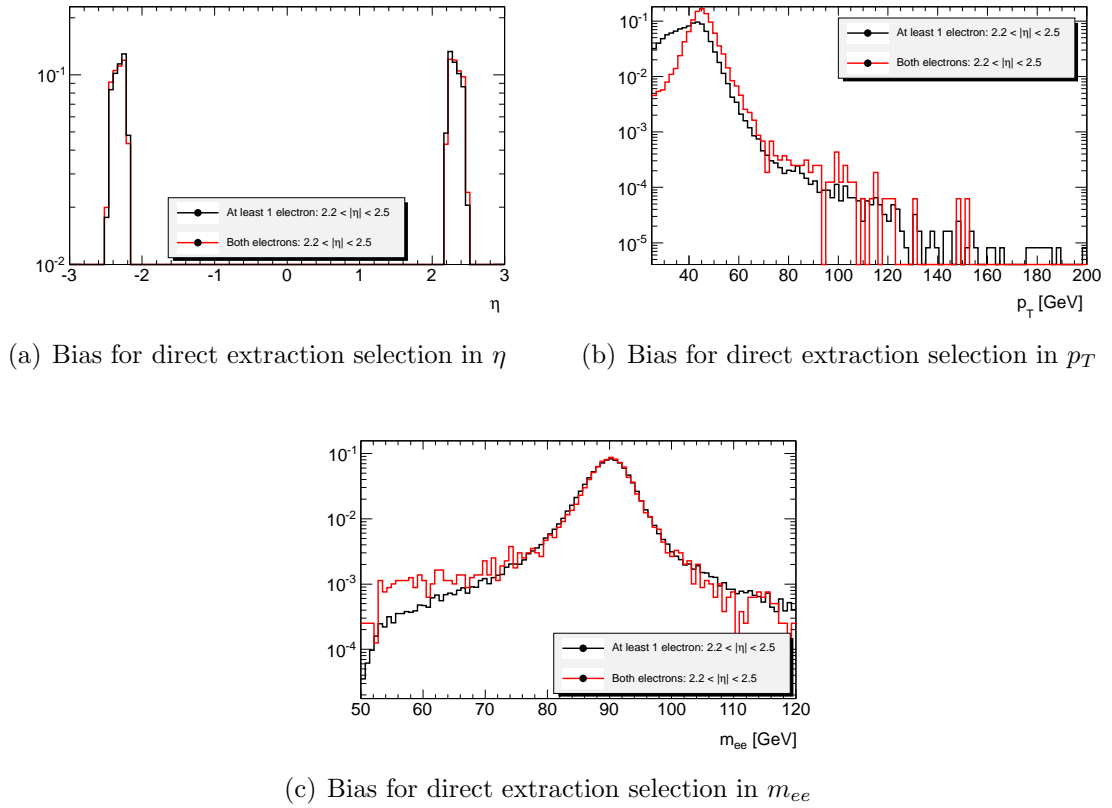


Figure 6.14: Distributions comparing kinematical properties of all electrons in $2.2 < |\eta| < 2.5$ (black line) with respect to the selected electron for direct extraction method (red line). Both electrons for direct extraction must fulfill the condition $2.2 < |\eta| < 2.5$.

Data: Direct extraction

Based on a similar principle as for tag-and-probe method, it is possible to extract directly the charge mis-identification for a given η bin, using a $Z \rightarrow e^+e^-$ event, where both electrons are in the same $|\eta|$ bin. Using this simple approach, the charge mis-identification can be obtained as:

$$\epsilon_i = \frac{N_{ss}^i}{2(N_{os}^i + N_{ss}^i)}$$

Where N_{ss}^i (N_{os}^i) is the number of events with both same-sign (opposite-sign) electrons in same rapidity bin i . In the same way as previous methods, the background has to be extracted, so sidebands and profile fit methods are used.

The results of this simple method are presented in Tables 6.2 and 6.3 for MC and data. Similar as for tag-and-probe, in direct extraction both electrons have to be in the same η bin. This produces a bias in the kinematical properties as can be seen in Figure 6.14. In this case, the average η and p_T values increase, so it is expected to get an overestimation with respect to the MC truth value. Nevertheless, this method can be used to study

systematic uncertainties of the final method.

Data: Likelihood method

The standard tag-and-probe method requires an electron selection for tag condition with a very low charge mis-identification rate. In this analysis, since tight electrons are used, no selection can provide a negligible charge mis-identification compared to tight electrons. As it has been shown, one way to avoid this is to use, as tag, the region with lowest charge mis-identification of the selection (in this case, electrons with $|\eta| < 0.8$). This method provides a good result but, as one electron is forced to be in one kinematical region, it biases the kinematical properties of the probe electron. In addition, this method reduces the statistics of the sample. A similar effect is seen for the direct extraction method. Here another method is presented, using the likelihood to find the charge mis-identification rates, and taking into account electron pairs with all $|\eta|$ combinations.

Assuming that the charge mis-identification rates for different pseudorapidity regions (ϵ_i) are independent, the probability can be expressed through a number of same-sign events (N_{ss}^{ij}) with electrons in η region i and j as a function of the number of events (N^{ij}). This will lead to:

$$N_{ss}^{ij} = N^{ij}(\epsilon_i + \epsilon_j) \quad (6.7)$$

Assuming all same-sign events in the Z mass region are produced by charge mis-identification, N_{ss}^{ij} is described by a Poisson distribution. The same method can be applied for binomial and gaussian distributions, when the statistics is very reduced, or for large number of events respectively. Using Poisson distribution:

$$f(k; \lambda) = \frac{\lambda^k e^{-\lambda}}{k!} \quad (6.8)$$

Here k is the number of occurrence of an event, in this case will be the number of same-sign events for a certain η combination: $k = N_{ss}^{ij}$. λ is equal to the expected number of occurrences during the total events: $\lambda = (\epsilon_i + \epsilon_j)N^{ij}$. Introducing these values in previous equation, the probability for both to produce a charge flip is given by:

$$P(\epsilon_i, \epsilon_j | N_{ss}^{ij}, N^{ij}) = \frac{(N^{ij}(\epsilon_i + \epsilon_j))^{N_{ss}^{ij}} e^{-N^{ij}(\epsilon_i + \epsilon_j)}}{N_{ss}^{ij}!} \quad (6.9)$$

This will be for a given i,j $|\eta|$ combination, but the probability can be evaluated for all $|\eta|$ combinations to obtain the likelihood for all the events:

$$L(\epsilon | N_{ss}, N) = \prod_{i,j} \frac{(N^{ij}(\epsilon_i + \epsilon_j))^{N_{ss}^{ij}} e^{-N^{ij}(\epsilon_i + \epsilon_j)}}{N_{ss}^{ij}!} \quad (6.10)$$

In this likelihood all the information is known but ϵ_i, ϵ_j . A maximization of the likelihood depending on the charge mis-identification can be applied to obtain ϵ_i, ϵ_j . In order to

simplify the numerical calculation, one can use the negative logarithmic of the likelihood:

$$-\ln L(\epsilon|N_{ss}, N) = \sum_{i,j} \ln(N^{ij}(\epsilon_i + \epsilon_j)) N_{ss}^{ij} - N^{ij}(\epsilon_i + \epsilon_j) - \ln(N_{ss}^{ij}!) \quad (6.11)$$

The terms that do not depend on the extracted variable (ϵ) are removed and the final function to minimize is:

$$-\ln L(\epsilon|N_{ss}, N) \propto \sum_{i,j} \ln(N^{ij}(\epsilon_i + \epsilon_j)) N_{ss}^{ij} - N^{ij}(\epsilon_i + \epsilon_j) \quad (6.12)$$

The signal events are selected within the invariant mass region of 81 to 101 GeV and stored in two triangular matrices, with the electrons ordered by η , one for same-sign and one for all events:

$$N = \begin{bmatrix} N^{11} & N^{12} & N^{13} & \dots \\ 0 & N^{22} & N^{23} & \dots \\ 0 & 0 & N^{33} & \dots \\ \vdots & \vdots & \ddots & \dots \\ 0 & 0 & \dots & \ddots \end{bmatrix}, \quad N_{ss} = \begin{bmatrix} N_{ss}^{11} & N_{ss}^{12} & N_{ss}^{13} & \dots \\ 0 & N_{ss}^{22} & N_{ss}^{23} & \dots \\ 0 & 0 & N_{ss}^{33} & \dots \\ \vdots & \vdots & \ddots & \dots \\ 0 & 0 & \dots & \ddots \end{bmatrix}$$

The package MINUIT [123] is used to find the minimum value of the multi-parameter problem and MINOS package is used to estimate the computational error. The charge mis-identification rates are obtained for data and Monte Carlo. The final results are presented in Tables 6.2 and 6.3 together with some variations in the invariant mass region width for systematic uncertainties studies.

As it was shown in earlier sections, the electrons evaluated in tag-and-probe and direct extraction methods contain bias due to the kinematical properties of the probe electron. The likelihood method contains the information of the two previous methods and adds the correlations from all possible electron $|\eta|$ combinations. Looking to the matrices N and N_{ss} , the diagonal terms of the matrices are exactly the same information as used to compute the direct extraction method, both electrons in the same η bin. Similarly, first row of each matrix contains the same information as the one needed for tag-and-probe, one electron in the central region (tag) and the second taking any η value. Selecting only the first row, or the diagonal terms, the likelihood method shows the same performance as tag and probe and direct extraction respectively.

In addition to the information contained in previous methods, likelihood technique also adds all possible η combinations for the electrons produced by the Z boson. This is leading to lower mis-identification rates and as can be observed in the Monte Carlo, where very close results to the MC truth are obtained. In addition, as the likelihood takes all the electron pairs, better use of the current accumulated events is done with this method, allowing to get low statistical errors.

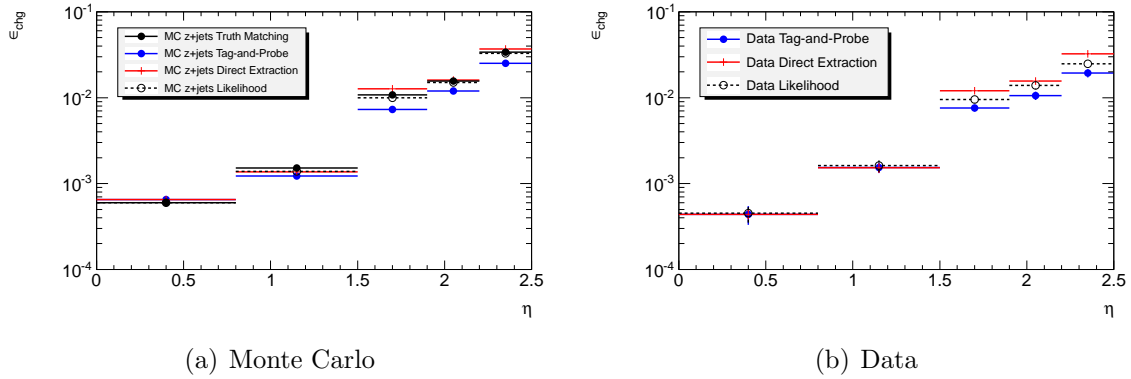


Figure 6.15: Electron charge mis-identification for tag and probe, direct extraction and likelihood for MC $Z + \text{jets}$ and data. 1035 pb^{-1} .

Methods comparison and closure test

The comparison between the three methods is displayed in Figure 6.15 for data and MC. All methods (including truth matching for MC) predict similar charge mis-identification rates when pseudorapidity increases, with some systematic differences between them. The larger charge mis-identification rates for each bin are predicted by the direct extraction method. This is related to the kinematic selection applied. On the other hand, tag-and-probe predicts the lowest charge mis-identification rate. Again, this is related to the fact that the tag electron is forced to be in the central region. The likelihood method takes into account both cases, the likelihood and the direct extraction, and in addition takes into account all other possible η combinations. This leads to a prediction that is in between the other two methods and in the MC case to a very good agreement with truth matching method.

The charge mis-identification rates obtained by the three (four for Monte Carlo) methods described, have been applied to the Z peak regions to validate their performance. All opposite-sign electron pairs are examined; for each pair, a weight $\omega(i, j)$ is calculated:

$$\omega(i, j) = \frac{\epsilon_i + \epsilon_j}{(1 - \epsilon_i)(1 - \epsilon_j)} \quad (6.13)$$

where ϵ_i is the charge flip rate in the η bin i . The denominator is coming from the fact that the closure test will be applied to only the opposite-sign electrons.

The final expected same-sign distribution is obtained from the opposite-sign dielectron invariant mass weighted with $\omega(i, j)$ and a sideband background extraction is performed. For Monte Carlo, the closure test shows an underestimation for the tag-and-probe method of around 20%. On the other hand, for the direct extraction, an overestimation of 10% is observed. Finally, for the likelihood method, the best agreement is found, with an overestimation of only 1.6%. Detailed results are presented for data and Monte Carlo in Table 6.4. Similar differences are found also for data between the three methods. In Figure

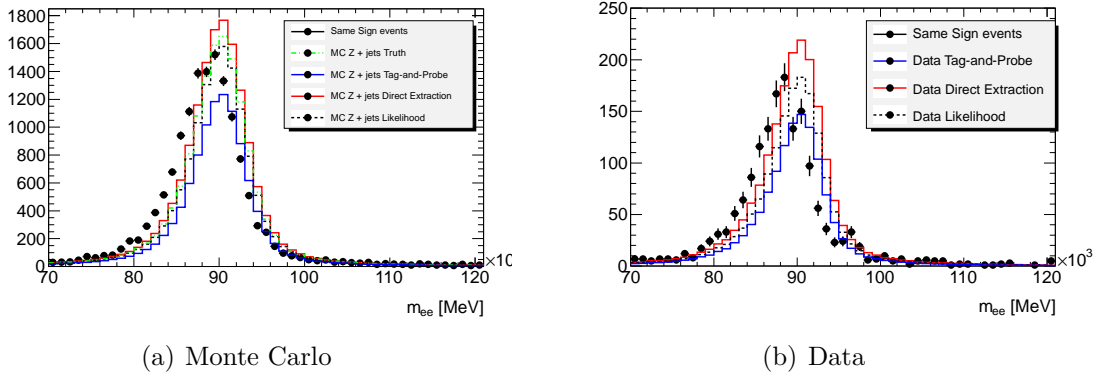


Figure 6.16: Dielectron invariant mass distribution for same-sign and opposite-sign weighted with the corresponding charge mis-identification.

6.16, the invariant mass distributions for same-sign and opposite-sign electrons weighted with $\omega(i, j)$ are shown for data and Monte Carlo. From these figures one can see that the best agreement is obtained for the likelihood method. The Z peaks for same-sign electrons are displaced towards lower invariant mass with respect to opposite-sign weight because a larger momentum fraction has been radiated for the same-sign and for this effect, the closure test has not been corrected for the opposite-sign case.

Dependence on p_T

Due to the large dependence on η , the evaluation of the charge mis-identification rate in data depending only on p_T is not applicable for estimation of the same-sign contribution produced for real opposite-sign events. For just p_T dependence, the three methods presented will be very dependent on the η distribution of the selected samples, in this case the Z boson making the obtained efficiencies useless for evaluation of $t\bar{t}$ same-sign contribution. For this reason, it is much more interesting to evaluate the dependence on η and p_T simultaneously. Figure 6.17 shows the charge mis-identification rate depending on η for three different p_T regions: 20 GeV to 50 GeV, 50 GeV to 75 GeV and over 75 GeV based on truth matching with $\Delta R < 0.2$. Together with Z + jets MC efficiencies, the charge mis-identification rate for leptons produced in the W decays of a $t\bar{t}$ sample is included. Both samples are in good agreement within the statistical uncertainties.

The first attempt to measure the charge mis-identification rate for η and p_T can be seen in Figure 6.18 for MC and data. Likelihood method can be easily extended to measure the charge mis-identification rate depending on 2 parameters, so this method is used as data-driven method for data and MC. The charge mis-identification for η only is included for comparison. Most of the electrons produced in the Z decay have momentum below 50 GeV, for this reason, a good agreement is found for charge mis-identification in 20 GeV $< p_T < 50$ GeV and without taking into account the p_T dependence as the ratio plots show. Once the p_T of the electrons increases, the low number of electrons produced by Z

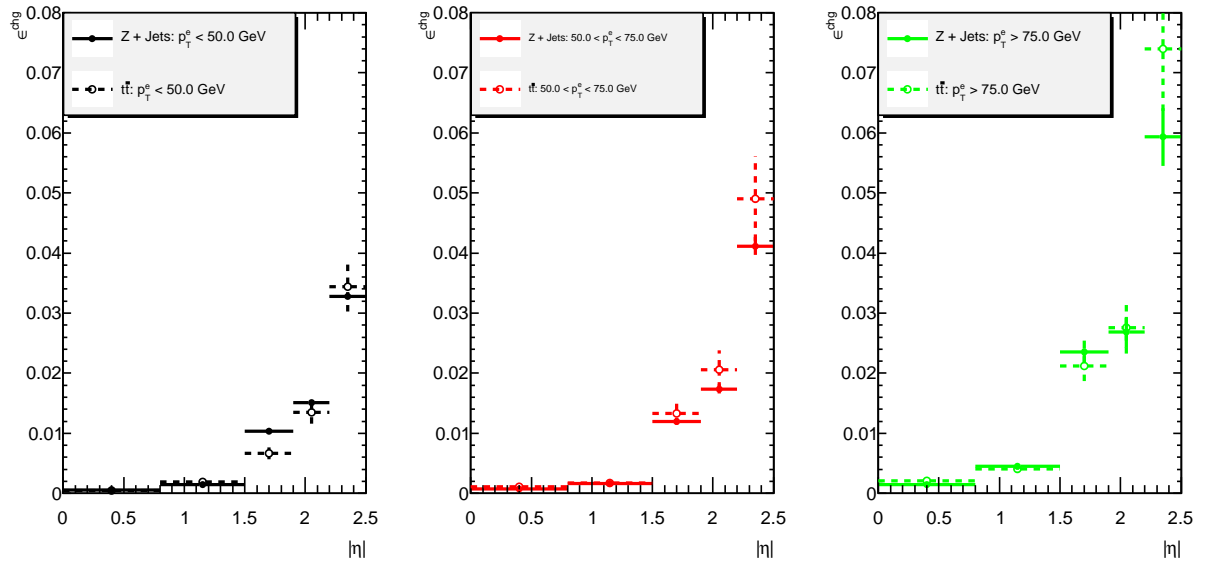


Figure 6.17: Charge mis-identification rate for different p_T bins, left: [25 GeV, 50 GeV], middle: [50 GeV, 75 GeV], right: [75 GeV, -] for MC $t\bar{t}$ and Z + jets. Truth matching method with a $\Delta R < 0.2$ was used to evaluate the charge mis-identification rate. Only statistical errors are included.

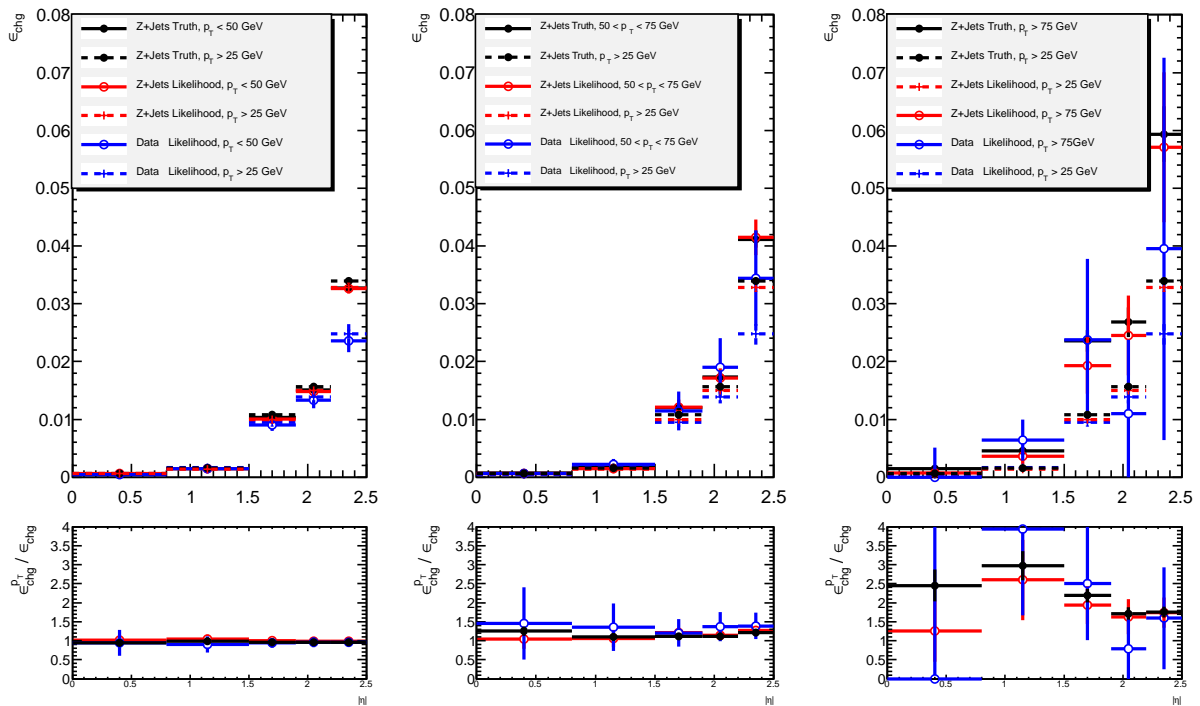


Figure 6.18: Charge mis-identification rate for different p_T bins, left: [25 GeV, 50 GeV], middle: [50 GeV, 75 GeV], right: [75 GeV, -]. Dark solid lines are from $Z \rightarrow ee$ MC using truth information, red lines are from $Z \rightarrow ee$ MC using likelihood method, and blue dash lines are from data.

bosons drops dramatically and for p_T over 75 GeV, the number of electrons lead to very large statistical uncertainties. The detailed numeric values can be found in Tables 6.5 and 6.6 for Monte Carlo Z + jets and data respectively. For completeness, the results for tag-and-probe and direct extraction are shown also for the 2D evaluations. As can be seen, the best use of the current statistics is done for the likelihood, where all the possible η and p_T combinations are taken into account, leading to the lowest statistical uncertainty. For data, an extended sample of 2 fb^{-1} is used to evaluate the charge mis-identification rate. An improvement for the uncertainties the high p_T bins is obtained, but a larger sample will be needed to produce values that can be directly used in same-sign dielectron analysis.

Final values and systematic uncertainties

Three different charge mis-identification estimation data driven methods for electrons have been presented together with a closure test. The likelihood method shows the best performance both in data and Monte Carlo. For this reason, in this analysis, the values from likelihood are used. The statistical uncertainty is the symmetric error provided by MINUIT when minimizing the likelihood. The main contributions to systematic uncertainties come from the differences between the methods: the largest difference between the likelihood value and the other methods is taken as the systematic uncertainty. These differences are clearly dominant for $|\eta| > 1.5$. For the central region, the differences between methods are comparable within the statistical uncertainties: therefore, the differences between background extraction methods are taken into account. The final results are displayed in Table 6.7.

The dominant systematic uncertainty arises from the p_T dependence of charge mis-identification rate. With the current accumulated luminosity and due to the kinematics of the Z boson, the number of high p_T electrons is very low, leading to very large statistical uncertainties for the data driven methods and for this reason the measured values cannot be used. For the final same-sign top analysis, it is assumed no p_T dependence on the rate and we additional 50% and 100% upper systematic fluctuation for $50 < p_T < 75 \text{ GeV}$ and $p_T > 75 \text{ GeV}$ are applied. These values are obtained from computing the average ratio between the charge flip rate only on η bins and the one also including the p_T bins. These 50% and 100% are an overestimation of the measured ratios.

6.6.3 Muon charge mis-identification

The bremsstrahlung cross section depends on the inverse of the particle mass squared and for this reason, bremsstrahlung production is much smaller for muons than for electrons, so this component for the charge mis-identification can be neglected. The other source for the charge mis-identification is the q/p measurement resolution. In the case of the muons, the curvature measurement is a combination of the Inner Detector and also in the Muon Spectrometer (MS) measurements. For the ID measurement, the relatively short track measurement is compensated with a very high spatial resolution that provides a very low charge mis-identification for muons with relatively low p_T . On the other hand, the MS, due to the large track length measured, provides a very low charge flip rate at large

momentum. This leads to a charge mis-identification for muons that is extremely low and negligible.

We validate this in simulation by examining the same-sign and opposite sign invariant mass distributions for Z + jets Monte Carlo, shown in Figure 6.19. In the Monte Carlo, with the statistics used, the number of same-sign pairs is very low. For opposite-sign, in the mass range $81 < M_{\mu\mu} < 101$ GeV, there are 1976687 events. For same-sign, only 2 events are accepted and for this reason it is difficult to see the Z resonance^{II}. From these values a charge flip for muons of $(1.0 \pm 0.7) \cdot 10^{-6}$ is found for Monte Carlo.

In data, as illustrated in Figure 6.20, the same effect is observed. The number of events measured for the opposite-sign peak is 332095, while for same-sign it is just 17. Again, due to the low statistics, it is not possible to appreciate clearly the Z resonance shape. With these results, a muon charge mis-identification of the order of $(5.2 \pm 1.2) \cdot 10^{-5}$ is assigned.

Data returns a larger charge mis-identification than MC. To evaluate the background contamination in data, the charge mis-identification was checked for events with $E_T^{miss} < 40$ GeV: $(3.9 \pm 1.1) \cdot 10^{-5}$ and for events with $E_T^{miss} < 20$ GeV: $(2.7 \pm 0.8) \cdot 10^{-5}$. This shows that the background contamination is not the reason for the discrepancy between data and MC and we can rely on the data estimation. As has been shown, the charge mis-identification for muons is at least two orders of magnitude lower than for electrons, for this reason, the charge flip rate for muon is considered negligible.

The momentum measurement for muons is done in the Inner Detector (ID) and the Muon Spectrometer (MS). The muon selection in this analysis requires both measurements to provide the same-sign measurement. Removing this selection and using events with same-sign or opposite-sign charge in the Z boson invariant mass region, the charge mis-identification rate for every subsystem can be studied. In Figure 6.21(a) events with two opposite charged muons for the ID measurement are selected. For these selected events, the rate of charge mis-identification for the MS measurement depending on the muon transverse momentum is shown. In similar way, selecting muons with opposite charge for the Muon Spectrometer, the charge mis-identification rate for ID can be evaluated; this rate is shown in Figure 6.21(b). The final selected muons in this analysis have same-sign for ID and MS measurements: multiplying the charge flip rates for ID and MS will provide the global charge mis-identification rate. With the current number of Z events available, several regions in p_T cannot be studied: for this reason, in Figure 6.22 the 67% upper limits are presented for data (a) and Monte Carlo (b). For data, the combined charge flip is 10^{-8} for the low p_T region (25-100 GeV) and increases up to 10^{-3} for p_T between 250 to 400 GeV.

^{II}One explanation for not seeing the resonance is that at high momentum the tracks are very straight and the error of the measurement is high, leading to a wrong measurement that will produce an invariant mass far away from the Z resonance. We have checked the momentum resolution in Monte Carlo. This resolution is below 20 % for muons with transverse momentum over 200 GeV, so a clear resonance is expected for larger statistics

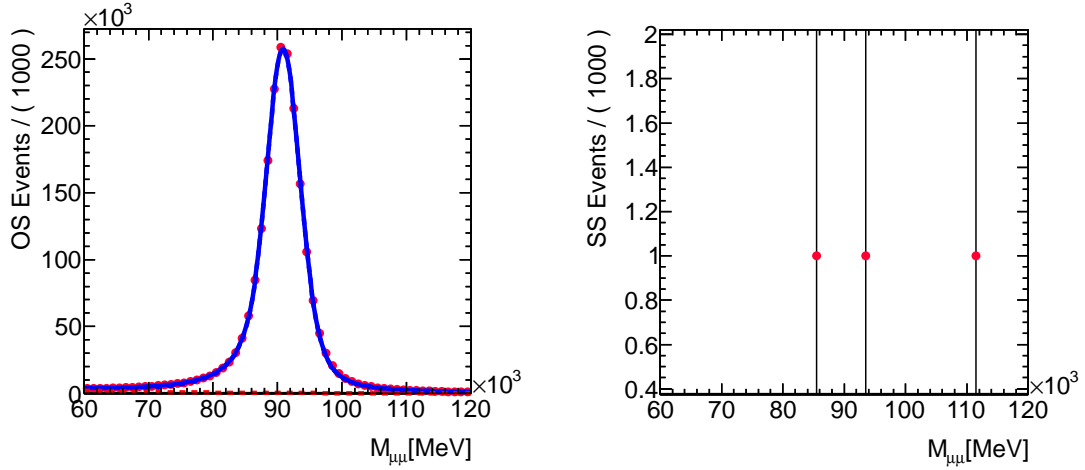


Figure 6.19: Invariant mass distribution of dimuons with opposite (left) and same (right) signs for Monte Carlo Z + Jets.

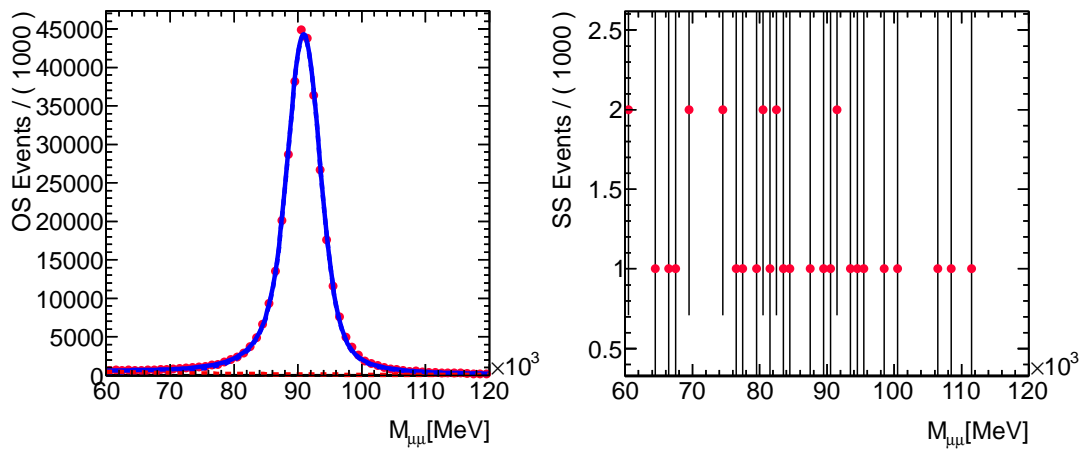
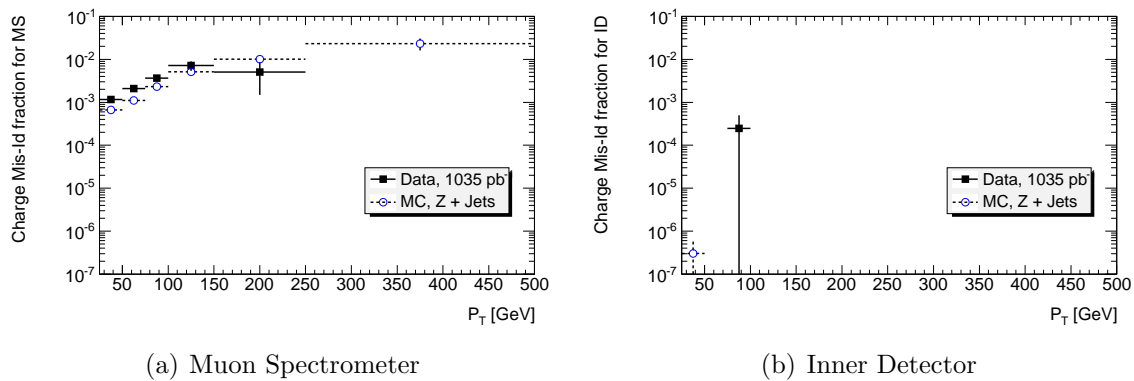
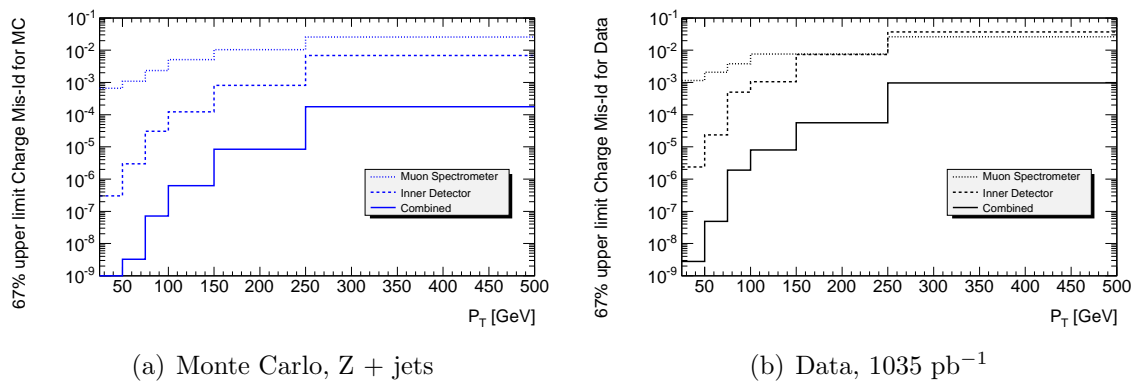


Figure 6.20: Invariant mass distribution of dimuons with opposite (left) and same (right) signs for data, 1035 pb^{-1} .



(a) Muon Spectrometer

(b) Inner Detector

Figure 6.21: Probability of charge flip for the different subsystems.

(a) Monte Carlo, Z + jets

(b) Data, 1035 pb^{-1} **Figure 6.22:** 67 % upper limit of charge flip for data and MC.

6.6.4 Extrapolation for high momentum leptons charge mis-identification

Muons and electrons at very high momentum will behave in the same way, because the hard bremsstrahlung will be reduced and the main reason for charge mis-identification will be the low curvature of the track in the Inner Detector tracker. For muons we can compare the sign of the ID part of the track and the sign of the MS part. The charge mis-identification for the Muon Spectrometer will be very low, and will provide a way to check the properties of the reconstruction in the Inner Detector. In addition, this will lead to a minimal value for the electron charge mis-identification.

The similar behavior for electrons and muons was studied in Monte Carlo [16]. In Figure 6.23, the resolution for the track curvature (ρ), directly related with the charge estimation ($\rho = q/p_T$), is shown for simulated electrons and muons with $p_T = 500$ and 2000 GeV. The shaded areas in the plot show the amount of mis-identified charge leptons reconstructed. The agreement for very large momentum between electrons and muons is very reasonable.

In data, the amount of electrons and muons with very large momentum is reduced. In Figure 6.24 the charge mis-identification based on 67% upper limit for the electrons and for the ID measurement of the muons are presented for data and Monte Carlo. Even at this energy range (25-500 GeV) one can appreciate how dominant the Inner Detector resolution is. At low momentum, due to the bremsstrahlung, the charge mis-identification rate for electrons is larger than for muons. Once p_T increases, the resolution effect becomes dominant and similar order of magnitude for the charge mis-identification is found for muons and electrons.

6.7 Conclusions and outlook

In this chapter, new methods to measure the charge mis-identification data for electrons have been developed for the needs of the same-sign top and b' searches and which can be adapted and used in other same-sign lepton analyses. Among the methods developed, the likelihood method has the best performance, improving the previous method used by the ATLAS collaboration. Furthermore, the first attempt to measure the charge mis-identification rates in η and p_T has been presented. With the accumulated data available for this analysis (1fb^{-1}), for high momentum electrons, the statistics obtained around the Z resonance are very low, so more accumulated luminosity is required to get a more accurate charge mis-identification measurement at this range.

In Figure 6.25 the same-sign leptons control region is presented. This control region is made of events with 2 same-sign leptons and no jets measured. In addition, the H_T and E_T^{miss} cuts have been removed to increase the acceptance of W and Z bosons. In the plots, one can see how a precise knowledge of the charge mis-identification rate is fundamental to get agreement between data and Monte Carlo.

The signal region plots are presented in Figure 6.26. For the same-sign top search, a good agreement between data and the Standard Model is found. 95 % upper limits [126]

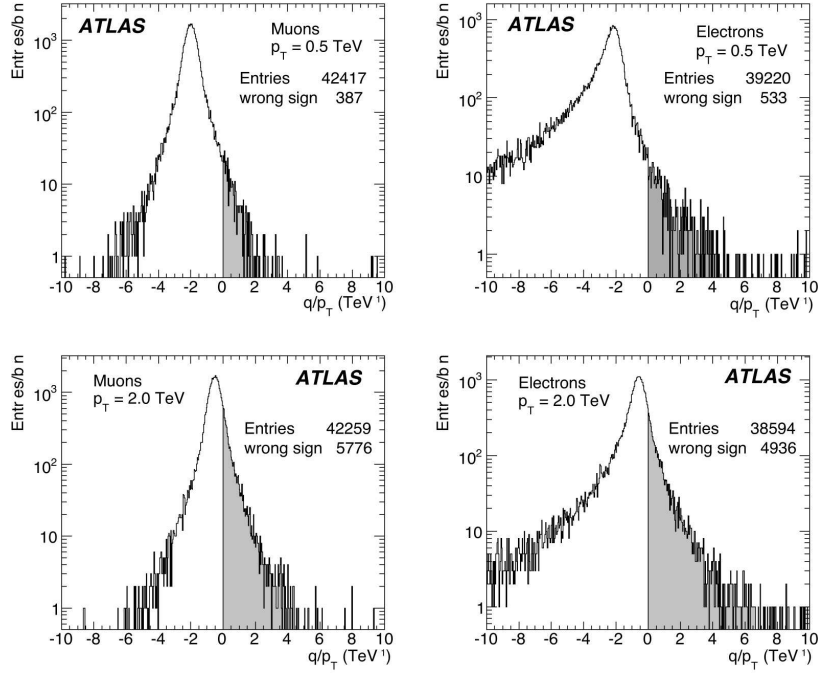


Figure 6.23: Reconstructed inverse transverse momentum multiplied by the charge for high-energy μ^- (left) and e^- (right) for $p_T=0.5$ TeV (top) and $p_T=2$ TeV (bottom). All leptons have $|\eta| < 2.5$. Shaded regions represent tracks with charge incorrectly reconstructed. Study done with Monte Carlo of pure electrons and muons with a given p_T [16].

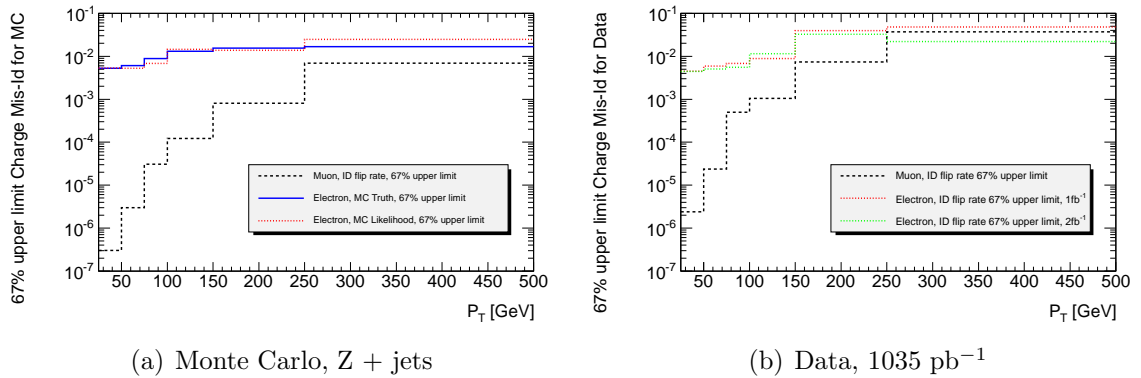


Figure 6.24: 67 % upper limit of charge flip for data and MC. Comparison between electrons and muons for Z samples depending on p_T .

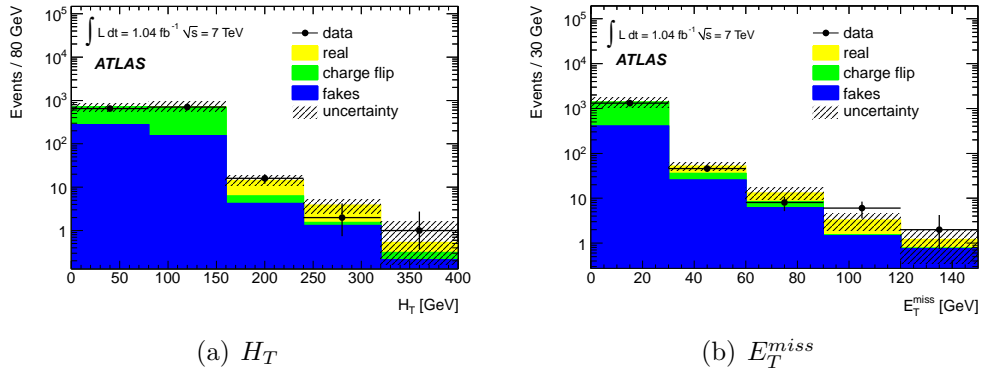


Figure 6.25: Control region plots for same-sign leptons. Selection is modified to only include events with 0 jets, $H_T > 0$ GeV and $E_T^{miss} > 0$ GeV [6].

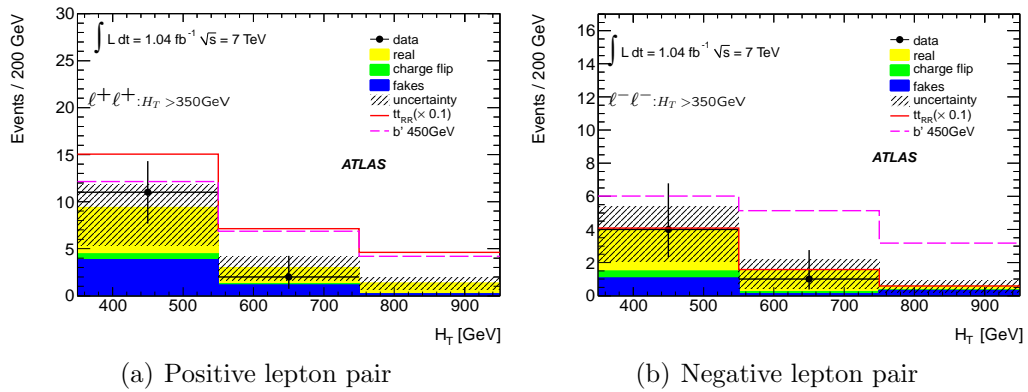


Figure 6.26: Signal region plots for same-sign leptons [6].

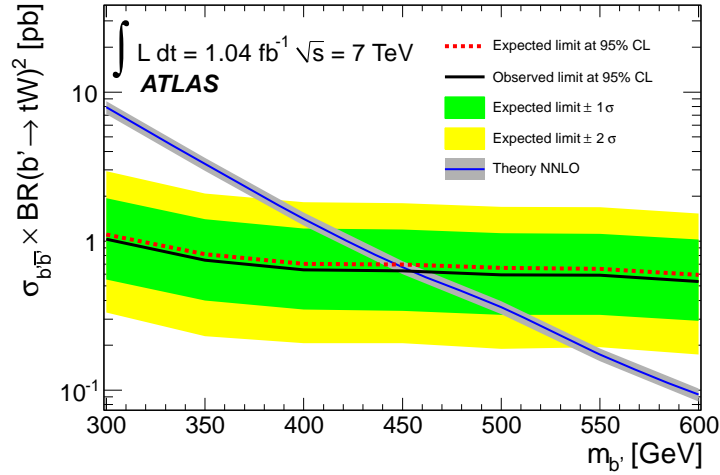


Figure 6.27: 95 % C.L. exclusion limits on cross section times branching ratio for $b'\bar{b}'$ signals [6].

on the cross-section production for same-sign top and its effective couplings have been set and can be seen in Table 6.8. The exchange of a t-channel Z' boson has been proposed as a possible mechanism that could increase the value of the forward-backward asymmetry in $t\bar{t}$ at the Tevatron. For a given mass and coupling of the Z' boson, the $t\bar{t}$ cross-section and the Tevatron forward-backward asymmetry are related. With the current measurement, it is not possible to explain the $t\bar{t}$ asymmetry with minimal Z' models. In models with more than one Z' boson, as they partially cancel their contribution to same-sign top quark production, still possible to explain the Tevatron asymmetry. This analysis will be updated with more luminosity during 2012.

Finally, as for same-sign top, the good agreement with the Standard Model allows to setup lower limits for the b' mass. In Figure 6.1, $m_{b'} < 450$ GeV are excluded at 95% C.L. This is currently the upper limit for a new family of quarks.

The Z boson is considered a *standard candle* for electrons and muons because a clear sample of opposite-sign leptons can be obtained to understand the detector effects and apply them to final analyses. In the nowadays analyses, as in this analysis is done, the Z boson is used but it has the intrinsic problem of the relatively low p_T of the final leptons produced. In order to be able to study high momentum leptons, leptons produced in t decays are good candidates. The good agreement found in this analysis with the Standard Model opens the door to use $t\bar{t}$ as new *candle*. In particular, for the electron channel, it will be of great interest to use $t\bar{t}$ decaying to $e\mu$, where the μ can be used as tag lepton with a charge mis-identification negligible compared to the probe electron. The likelihood method can be used to measure the charge mis-identification rate for ee and $\mu\mu$ but also $e\mu$. In this way the best use of the accepted accumulated statistics will be done, giving the opportunity to cross-check the mis-identification rates for each method and also, start to study muons at large momentum. Similarly as for charge mis-identification studies, the use of $t\bar{t}$ will be of interest for trigger and reconstruction efficiencies.

Table 6.2: Charge flip rates in η bins for Monte Carlo $Z + \text{jets}$. Only statistical uncertainties included.

Method	Systematics	$0 < \eta < 0.8$	$0.8 < \eta < 1.5$	$1.50 < \eta < 1.9$	$1.9 < \eta < 2.2$	$2.2 < \eta < 2.5$
MC truth matching	$\Delta r < 0.2$	0.00061 \pm 0.00002	0.00157 \pm 0.00005	0.01081 \pm 0.00013	0.01557 \pm 0.00018	0.03415 \pm 0.00034
Tag-and-Probe	Default	0.00065 \pm 0.00005	0.00123 \pm 0.00009	0.00730 \pm 0.00029	0.01193 \pm 0.00048	0.02510 \pm 0.00100
Tag-and-Probe	Sideband short range	0.00060 \pm 0.00003	0.00121 \pm 0.00009	0.00720 \pm 0.00031	0.01205 \pm 0.00050	0.02563 \pm 0.00104
Tag-and-Probe	Positive	0.00067 \pm 0.00005	0.00131 \pm 0.00013	0.00840 \pm 0.00045	0.01258 \pm 0.00072	0.02754 \pm 0.00150
Tag-and-Probe	Negative	0.00063 \pm 0.00005	0.00113 \pm 0.00012	0.00641 \pm 0.00039	0.01134 \pm 0.00065	0.02289 \pm 0.00130
Tag-and-Probe	Profile Fit	0.00068 \pm 0.00003	0.00123 \pm 0.00009	0.00804 \pm 0.00030	0.01204 \pm 0.00047	0.02499 \pm 0.00095
Tag-and-Probe	Profile Fit short range	0.00066 \pm 0.00003	0.00125 \pm 0.00009	0.00830 \pm 0.00031	0.01221 \pm 0.00048	0.02511 \pm 0.00096
Tag-and-Probe	Profile Fit Linear Bkg	0.00067 \pm 0.00003	0.00136 \pm 0.00009	0.00818 \pm 0.00030	0.01210 \pm 0.00047	0.02527 \pm 0.00096
Tag-and-Probe	Tag Condition	0.00065 \pm 0.00005	0.00135 \pm 0.00009	0.00729 \pm 0.00031	0.01237 \pm 0.00052	0.02465 \pm 0.00104
Tag-and-Probe	MEP < 40GeV	0.00064 \pm 0.00005	0.00123 \pm 0.00009	0.00742 \pm 0.00030	0.01193 \pm 0.00049	0.02518 \pm 0.00099
Tag-and-Probe	Sherpa	0.00066 \pm 0.00009	0.00142 \pm 0.00016	0.00876 \pm 0.00060	0.01187 \pm 0.00092	0.02459 \pm 0.00194
Direct extraction	Default	0.00065 \pm 0.00003	0.00136 \pm 0.00008	0.01265 \pm 0.00045	0.01603 \pm 0.00058	0.03696 \pm 0.00114
Direct extraction	Sideband short range	0.00060 \pm 0.00003	0.00134 \pm 0.00008	0.01147 \pm 0.00046	0.01607 \pm 0.00061	0.03809 \pm 0.00120
Direct extraction	Profile Fit	0.00070 \pm 0.00003	0.00140 \pm 0.00008	0.01290 \pm 0.00042	0.01619 \pm 0.00055	0.03753 \pm 0.00107
Direct extraction	Profile Fit short range	0.00066 \pm 0.00003	0.00142 \pm 0.00007	0.01350 \pm 0.00045	0.01607 \pm 0.00058	0.03696 \pm 0.00113
Direct extraction	Profile Fit Linear Bkg	0.00067 \pm 0.00003	0.00139 \pm 0.00007	0.01306 \pm 0.00043	0.01604 \pm 0.00056	0.03806 \pm 0.00111
Likelihood	Default	0.00060 \pm 0.00005	0.00139 \pm 0.00010	0.00997 \pm 0.00034	0.01502 \pm 0.00047	0.03285 \pm 0.00082
Likelihood	Range 75-105 GeV	0.00061 \pm 0.00005	0.00140 \pm 0.00010	0.01018 \pm 0.00033	0.01519 \pm 0.00046	0.03286 \pm 0.00080
Likelihood	Range 83-97 GeV	0.00057 \pm 0.00005	0.00131 \pm 0.00010	0.00946 \pm 0.00034	0.01478 \pm 0.00048	0.03276 \pm 0.00084

Table 6.3: Charge flip rates in η bins for data with 1035.3 pb^{-1} . Only statistical uncertainties included.

Method	Systematics	$0 < \eta < 0.8$	$0.8 < \eta < 1.5$	$1.50 < \eta < 1.9$	$1.9 < \eta < 2.2$	$2.2 < \eta < 2.5$
Tag-and-Probe	Default	0.00044 ± 0.00011	0.00154 ± 0.00021	0.00759 ± 0.00073	0.01050 ± 0.00114	0.01935 ± 0.00218
Tag-and-Probe	Sideband short range	0.00043 ± 0.00011	0.00154 ± 0.00022	0.00702 ± 0.00075	0.00991 ± 0.00115	0.01984 ± 0.00227
Tag-and-Probe	Positive	0.00045 ± 0.00015	0.00153 ± 0.00030	0.00796 ± 0.00108	0.01043 ± 0.00162	0.02294 ± 0.00335
Tag-and-Probe	Negative	0.00040 ± 0.00014	0.00155 ± 0.00030	0.00732 ± 0.00101	0.01073 ± 0.00161	0.01579 ± 0.00279
Tag-and-Probe	Profile Fit	0.00047 ± 0.00014	0.00159 ± 0.00021	0.00774 ± 0.00070	0.01100 ± 0.00112	0.01948 ± 0.00210
Tag-and-Probe	Profile Fit short range	0.00043 ± 0.00010	0.00165 ± 0.00021	0.00690 ± 0.00069	0.00967 ± 0.00107	0.01937 ± 0.00213
Tag-and-Probe	Profile Fit Linear Bkg	0.00045 ± 0.00011	0.00135 ± 0.00019	0.00749 ± 0.00069	0.01106 ± 0.00113	0.01969 ± 0.00213
Tag-and-Probe	Tag Condition	0.00045 ± 0.00010	0.00160 ± 0.00022	0.00770 ± 0.00078	0.01077 ± 0.00122	0.01969 ± 0.00234
Tag-and-Probe	MET < 40GeV	0.00043 ± 0.00011	0.00152 ± 0.00022	0.00764 ± 0.00074	0.01051 ± 0.00114	0.01944 ± 0.00219
Direct extraction	Default	0.00044 ± 0.00011	0.00153 ± 0.00019	0.01207 ± 0.00104	0.01563 ± 0.00139	0.03238 ± 0.00260
Direct extraction	Sideband short range	0.00044 ± 0.00011	0.00129 ± 0.00018	0.01120 ± 0.00106	0.01652 ± 0.00148	0.03074 ± 0.00266
Direct extraction	Profile Fit	0.00046 ± 0.00011	0.00150 ± 0.00018	0.01234 ± 0.00094	0.01548 ± 0.00130	0.03163 ± 0.00240
Direct extraction	Profile Fit short range	0.00044 ± 0.00011	0.00153 ± 0.00018	0.01321 ± 0.00103	0.01532 ± 0.00132	0.03188 ± 0.00245
Direct extraction	Profile Fit Linear Bkg	0.00046 ± 0.00011	0.00145 ± 0.00018	0.01214 ± 0.00095	0.01546 ± 0.00056	0.03201 ± 0.00244
Likelihood	Default	0.00045 ± 0.00010	0.00161 ± 0.00024	0.00950 ± 0.00078	0.01386 ± 0.00133	0.02475 ± 0.00176
Likelihood	Range 75-105 GeV	0.00049 ± 0.00010	0.00162 ± 0.00024	0.00969 ± 0.00076	0.01381 ± 0.00106	0.02504 ± 0.00171
Likelihood	Range 83-97 GeV	0.00046 ± 0.00010	0.00154 ± 0.00024	0.00895 ± 0.00080	0.01353 ± 0.00112	0.02413 ± 0.00180

Table 6.4: Closure test results for Monte Carlo Z + Jets and data with 1035 pb^{-1} .

	Method	OS	SS	OS weighted	Error(%)
MC	Truth Matching	$1.16758 \cdot 10^6$	12299	12651.2 ± 224.2	-2.8
MC	Tag-and-Probe	$1.16758 \cdot 10^6$	12299	9418.4 ± 436.0	23.4
MC	Direct extraction	$1.16758 \cdot 10^6$	12299	13599.3 ± 503.5	-10.6
MC	Likelihood	$1.16758 \cdot 10^6$	12299	12105.9 ± 433.5	1.6
Data	Tag-and-Probe	154277	1351.5	1098.8 ± 132.0	18.7
Data	Direct extraction	154277	1351.5	1648.8 ± 159.3	-22.4
Data	Likelihood	154277	1351.5	1370.1 ± 130.4	-1.4

Table 6.5: Charge mis-identification rates in η bins and η and p_T bins for Monte Carlo $Z + \text{jets}$. Only statistical uncertainties included.

Method	Systematics	$0 < \eta < 0.8$	$0.8 < \eta < 1.5$	$1.50 < \eta < 1.9$	$1.9 < \eta < 2.2$	$2.2 < \eta < 2.5$
MC truth matching	Default	0.00061 ± 0.00002	0.00157 ± 0.00005	0.01081 ± 0.00013	0.01557 ± 0.00018	0.03415 ± 0.00034
Tag-and-Probe	Default	0.00065 ± 0.00005	0.00123 ± 0.00009	0.00730 ± 0.00029	0.01193 ± 0.00048	0.02510 ± 0.00100
Direct extraction	Default	0.00065 ± 0.00003	0.00136 ± 0.00008	0.01265 ± 0.00045	0.01603 ± 0.00058	0.03696 ± 0.00114
Likelihood	Default	0.00060 ± 0.00004	0.00139 ± 0.00011	0.00997 ± 0.00034	0.01502 ± 0.00047	0.03285 ± 0.00083
MC truth matching	$P_t < 50$ GeV	0.00057 ± 0.00002	0.00149 ± 0.00005	0.01036 ± 0.00019	0.01511 ± 0.00027	0.03276 ± 0.00050
Tag-and-Probe	$P_t < 50$ GeV	0.00068 ± 0.00006	0.00125 ± 0.00015	0.00787 ± 0.00045	0.01215 ± 0.00073	0.02564 ± 0.00124
Direct extraction	$P_t < 50$ GeV	0.00068 ± 0.00006	0.00153 ± 0.00018	0.01357 ± 0.00106	0.01605 ± 0.00132	0.03747 ± 0.00260
Likelihood	$P_t < 50$ GeV	0.00061 ± 0.00005	0.00145 ± 0.00010	0.01002 ± 0.00037	0.01483 ± 0.00056	0.03260 ± 0.00090
MC truth matching	$50 > P_t > 75$ GeV	0.00075 ± 0.00007	0.00167 ± 0.00013	0.01196 ± 0.00053	0.01736 ± 0.00078	0.04117 ± 0.00153
Tag-and-Probe	$50 > P_t > 75$ GeV	0.00059 ± 0.00018	0.00168 ± 0.00048	0.01471 ± 0.00362	0.02079 ± 0.00731	0.03529 ± 0.02046
Direct extraction	$50 > P_t > 75$ GeV	0.00061 ± 0.00078	0.00141 ± 0.00224	0.01355 ± 0.01174	0.01969 ± 0.01615	0.03292 ± 0.02507
Likelihood	$50 > P_t > 75$ GeV	0.00062 ± 0.00015	0.00146 ± 0.00029	0.01210 ± 0.00125	0.01714 ± 0.00168	0.04151 ± 0.00321
MC truth matching	$P_t > 75$ GeV	0.00147 ± 0.00027	0.00452 ± 0.00065	0.02357 ± 0.00218	0.02683 ± 0.00267	0.05935 ± 0.00558
Tag-and-Probe	$P_t > 75$ GeV	0.00041 ± 0.00056	0.00226 ± 0.00140	0.02154 ± 0.01241	0.03180 ± 0.02919	0.03196 ± 0.06933
Direct extraction	$P_t > 75$ GeV	0.00311 ± 0.00308	0.00237 ± 0.00539	0.02621 ± 0.02934	0.03967 ± 0.05037	0.04107 ± 0.07230
Likelihood	$P_t > 75$ GeV	0.00116 ± 0.00056	0.00388 ± 0.00135	0.02104 ± 0.00435	0.02550 ± 0.00564	0.05790 ± 0.01248

Table 6.6: Charge mis-identification rates in η bins for data and Z +jets. Only statistical uncertainties included. Comparison of P_t bins. If there is not enough events for MINUIT to find the charge efficiency, the symbol — is displayed and the uncertainty corresponds to the lower limit of the charge mis-identification rate.

Method	Systematics	$0 < \eta < 0.8$	$0.8 < \eta < 1.5$	$1.50 < \eta < 1.9$	$1.9 < \eta < 2.2$	$2.2 < \eta < 2.5$
Tag-and-Probe	Default	0.00044 ± 0.00011	0.00154 ± 0.00021	0.00759 ± 0.00073	0.0105 ± 0.00114	0.01935 ± 0.00218
Direct extraction	Default	0.00044 ± 0.00011	0.00153 ± 0.00019	0.01207 ± 0.00104	0.01563 ± 0.00139	0.03238 ± 0.00260
Likelihood	Default	0.00045 ± 0.00012	0.00162 ± 0.00024	0.00950 ± 0.00078	0.01386 ± 0.00110	0.02475 ± 0.00178
Likelihood, 2fb	Default	0.00049 ± 0.00010	0.00147 ± 0.00023	0.00946 ± 0.00073	0.01252 ± 0.00097	0.02285 ± 0.00156
Tag-and-Probe	$P_t < 50$ GeV	0.00050 ± 0.00014	0.00120 ± 0.00038	0.00743 ± 0.00126	0.01083 ± 0.00192	0.01998 ± 0.00342
Direct extraction	$P_t < 50$ GeV	0.00051 ± 0.00015	0.00167 ± 0.00051	0.01288 ± 0.00279	0.01403 ± 0.00355	0.03183 ± 0.00693
Likelihood	$P_t < 50$ GeV	0.00042 ± 0.00012	0.00145 ± 0.00027	0.00897 ± 0.00101	0.01329 ± 0.00134	0.02357 ± 0.00194
Likelihood, wide range	$P_t < 50$ GeV	0.00045 ± 0.00012	0.00147 ± 0.00026	0.00928 ± 0.00100	0.01341 ± 0.00138	0.02399 ± 0.00191
Likelihood, short range	$P_t < 50$ GeV	0.00042 ± 0.00012	0.00133 ± 0.00027	0.00849 ± 0.00103	0.01299 ± 0.00139	0.02302 ± 0.00217
Likelihood, 2fb	$P_t < 50$ GeV	0.00048 ± 0.00010	0.00150 ± 0.00024	0.00924 ± 0.00084	0.01241 ± 0.00114	0.02265 ± 0.00169
Tag-and-Probe	$50 > P_t > 75$ GeV	0.00034 ± 0.00041	0.00230 ± 0.00130	0.01693 ± 0.00933	0.01154 ± 0.01827	— ± 0.03422
Direct extraction	$50 > P_t > 75$ GeV	0.00160 ± 0.00347	— ± 0.00630	—	0.02500 ± 0.04726	— ± 0.06773
Likelihood	$50 > P_t > 75$ GeV	0.00065 ± 0.00040	0.00220 ± 0.00096	0.01144 ± 0.00834	0.01897 ± 0.00504	0.0344 ± 0.00824
Likelihood, wide range	$50 > P_t > 75$ GeV	0.00083 ± 0.00044	0.00220 ± 0.00095	0.01111 ± 0.00821	0.01903 ± 0.00497	0.0334 ± 0.00788
Likelihood, short range	$50 > P_t > 75$ GeV	0.00074 ± 0.00043	0.00236 ± 0.00102	0.01111 ± 0.00841	0.01817 ± 0.00515	0.0341 ± 0.00851
Likelihood, 2fb-1	$50 > P_t > 75$ GeV	0.00050 ± 0.00031	0.00235 ± 0.00080	0.01130 ± 0.00275	0.01599 ± 0.00388	0.0309 ± 0.00653
Tag-and-Probe	$P_t > 75$ GeV	— ± 0.00098	0.01427 ± 0.01250	— ± 0.01817	— ± 0.04908	— ± 0.64066
Direct extraction	$P_t > 75$ GeV	— ± 0.00766	— ± 0.02372	— ± 0.07599	— ± 0.11976	— ± 0.54334
Likelihood	$P_t > 75$ GeV	— ± 0.00506	0.00638 ± 0.00336	0.02378 ± 0.01401	0.01100 ± 0.01274	0.03949 ± 0.03304
Likelihood, wide range	$P_t > 75$ GeV	— ± 0.00162	0.00598 ± 0.00340	0.02235 ± 0.01340	0.01004 ± 0.01190	0.03648 ± 0.03085
Likelihood, short range	$P_t > 75$ GeV	— ± 0.00353	0.00690 ± 0.00387	0.01925 ± 0.01294	0.01194 ± 0.01356	0.02763 ± 0.02833
Likelihood, 2fb-1	$P_t > 75$ GeV	0.00051 ± 0.00099	0.00526 ± 0.00355	0.02334 ± 0.00975	0.01313 ± 0.01128	0.03461 ± 0.02449

Table 6.7: Charge mis-identification: tag-and-probe results in η bins for Monte Carlo and data with 1035 pb^{-1} . Statistical and systematic uncertainties are included.

	MC	Data
$0 < \eta < 0.8$	$0.00061 \pm 0.00005 \pm 0.00005$	$0.00045 \pm 0.00010 \pm 0.00004$
$0.8 < \eta < 1.5$	$0.00157 \pm 0.00010 \pm 0.00016$	$0.00162 \pm 0.00024 \pm 0.00032$
$1.5 < \eta < 1.9$	$0.01081 \pm 0.00034 \pm 0.00267$	$0.00950 \pm 0.00078 \pm 0.00224$
$1.9 < \eta < 2.2$	$0.01557 \pm 0.00047 \pm 0.00205$	$0.01386 \pm 0.00110 \pm 0.00253$
$2.2 < \eta < 2.5$	$0.03415 \pm 0.00083 \pm 0.00593$	$0.02475 \pm 0.00178 \pm 0.00651$

Table 6.8: Expected and observed 95 % upper limits on the effective operator, for each chirality configuration.

Chirality Configuration	Expected Limit, σ	Observed Limit, σ	Observed Limit, C
LL	$\sigma < 1.8 \text{ pb}$	$\sigma < 1.7 \text{ pb}$	$C_{LL}/\Lambda^2 < 0.34 \text{ TeV}^{-2}$
LR	$\sigma < 1.7 \text{ pb}$	$\sigma < 1.7 \text{ pb}$	$C_{LR}/\Lambda^2 < 0.98 \text{ TeV}^{-2}$
RR	$\sigma < 1.7 \text{ pb}$	$\sigma < 1.7 \text{ pb}$	$C_{RR}/\Lambda^2 < 0.34 \text{ TeV}^{-2}$

Chapter 7

Diboson estimation for SUSY analysis

In addition to the models presented in the previous chapter for physics beyond the Standard Model, there are several others. One of the most popular is known as Supersymmetry (SUSY). A detailed up-to-date introduction can be found in [127]. This theory uses a fermionic-bosonic symmetry in which elementary particles of a given spin are related to other particles that differ by half a unit of spin, known as superpartners. At the Large Electron-Positron collider (LEP) several efforts were made to look for such new particles. The Tevatron experiments have also performed extensive SUSY searches. In both accelerators the searches have been negative and they have set limits to the free parameters of the different models. In 2010, with the start of the LHC, CMS and ATLAS started to look for these new particles. In 2011, LHC delivered a large amount of data, and several searches in many different channels for SUSY were performed. One of the most interesting final states is 2 leptons with large missing transverse energy. This chapter is focused on this search and the study of one of the irreducible backgrounds: two weak boson production. The background estimation results described in this chapter together with the final result of the SUSY search are reported in [7].

A brief introduction to SUSY will be given in the first section. It is followed by a short discussion on object reconstruction. The different signal regions will be explained in Section 7.3. A short description on the possible backgrounds for the final states will be given in Section 7.4. One of the few irreducible backgrounds is the diboson contribution. A detailed study of the different diboson productions will be given together with a summary of the latest measurements done at the LHC. Also a detailed evaluation of the MC generator systematic uncertainties will be presented. Finally, the importance of the diboson contribution will be discussed and the general result of the SUSY analysis for $1.04fb^{-1}$ will be presented.

7.1 Supersymmetry, MSSM and mSUGRA

SUSY is one of the best-motivated scenarios for new physics beyond Standard Model at the TeV scale. It offers the possibility of unifying fermionic matter particles with boson force particles. Supersymmetry protects the Higgs mass from acquiring large values as the dominant quantum corrections from standard particles are exactly compensated by the contributions from their superpartners. In addition, supersymmetric theories with R-parity conservation predict that the lightest supersymmetric particle is stable and nearly undetectable. This makes it a good candidate for dark matter.

A natural way to extend the Standard Model is to find additional symmetries. Supersymmetry is a hypothetical new symmetry (Q) which turns a bosonic state into a fermionic state and vice versa:

$$Q|boson\rangle = |fermion\rangle \quad (7.1)$$

$$Q|fermion\rangle = |boson\rangle \quad (7.2)$$

The operator Q that generates such transformations is an anti-commuting spinor because Q is a fermionic operator and must satisfy:

$$\{Q, Q^\dagger\} \sim p^\mu \quad (7.3)$$

$$\{Q^\dagger, Q^\dagger\} = \{Q, Q\} = 0 \quad (7.4)$$

$$[p^\mu, Q^\dagger] = [p^\mu, Q] = 0 \quad (7.5)$$

where p^μ is the four-momentum generator of space-time translations.

The single-particle states of a supersymmetric theory fall into irreducible representation of the SUSY algebra, called supermultiplets. They contain both fermion and boson states, that are known as superpartners of each other. The mass operator P^2 commutes with operator Q and with the space-time operators. From this, it is possible to derive one of the main properties of the supersymmetric models: all particles that are in the same supermultiplet have equal masses and gauge charges. Other important property is that within a supermultiplet, the number of bosonic and fermionic degrees of freedom is the same. From the SM spectrum, it is clear that none of known particles can be supersymmetric partners of each other. This means, that we have to double the number of SM particles, introducing the associated supersymmetric partner for each. With the addition of these new particles, there are also many possible new interactions.

The minimal extension of the Standard Model that realized supersymmetry is known as Minimal Supersymmetric Standard Model (MSSM). In this model, the Higgs boson has a fermionic superpartner, the Higgsino, which mass is radiatively stable, as it is for all fermions. In Supersymmetry the baryon number and the lepton number are not longer conserved and this implies that the proton can decay in 10^{-2} s. In order to assure the

proton stability, MSSM introduces R-parity conservation ¹. Other important effect of the R-parity conservation is that the lightest supersymmetric particle is stable, being a potential candidate for dark matter.

The new superparticles predicted by the MSSM model are:

- Higgsino: They are the superpartners of the Higgs boson. Two complex Higgs doublets are needed to avoid gauge anomaly. They are usually called: $\tilde{h}_u = (\tilde{h}_u^+, \tilde{h}_u^0)$ and $\tilde{h}_d = (\tilde{h}_d^-, \tilde{h}_d^0)$.
- Gauginos: The vector bosons of the Standard Model reside in gauge supermultiplets. Their fermionic superpartners are called generally gauginos. They are fermions and they can be divided in different categories, depending on the SM partner. The gluinos are fermionic partners of the gluon. They are Majorana fermions so they are their own antiparticles and they cannot mix with any other particles. The gravitino is the superpartner of the graviton. Wino and bino are the superpartners of electroweak gauge bosons. The mixtures of wino and bino, corresponding to the superpartners of Z boson and photon, are called zino and photino.
- Squarks: They are the scalar superpartners of the quarks and there is one version for each Standard Model quark.
- Sleptons: They are the scalar partners of the Standard Model leptons.
- Neutralinos: They are the four eigenstates produced from the combination of neutral higgsinos and the neutral gauginos. The higgsinos and the electroweak gauginos mix with each other because of the effect of the electroweak symmetry breaking. The neutralinos are labeled as: $\chi_1^0, \chi_2^0, \chi_3^0$ and χ_4^0 . The χ_1^0 is usually assumed to be the lightest stable supersymmetric particle if R-parity is conserved and there is no lighter gravitino.
- Charginos: They are the two eigenstates produced from the combination of charged higgsinos and the charged gauginos. Charginos are usually labeled as: χ_1^\pm and χ_2^\pm .

In the MSSM there are 33 distinct masses corresponding to undiscovered particles, including the gravitino (superpartner of the graviton). In addition, taking into account all the unknown parameters, MSSM has 134 parameters.

As data from LEP and Tevatron have shown that, SUSY is a broken symmetry, because the masses of the SM objects and their superpartners are different. A large theoretical effort has been made to understand the mechanism for supersymmetry breaking. Several different mechanisms have been suggested for the MSSM model. One of the most popular mechanisms is known as Gravity-Mediated Supersymmetry Breaking. In these models, the supersymmetry breaking is done through gravitational interactions.

¹R-parity is a multiplicative quantum number defined as: $P_R = (-1)^{3(B-L)+2s}$. B corresponds to the baryon number, L to the lepton number and s to the spin. All Standard Model particles have R-parity equal 1, and the MSSM superpartners have -1.

The minimal MSSM model using a gravity-mediated Supersymmetry Breaking is known as mSUGRA (minimal SuperGRavity). In this model, gravity mediates the breaking of SUSY through the existence of a hidden sector. This is one of the most widely experimentally explored models due to the low number of free parameters that determine the low energy phenomenology:

- Universal gaugino masses: $m_{1/2}$;
- Scalar masses: m_0 ;
- Soft breaking trilinear coupling constant (A_0) for Higgs-sfermion-sfermion;
- $\tan\beta$: this is the Vacuum Expectation Value ratio for the two Higgs;
- Sign of μ : it is the sign of the Higgsino mass parameter.

7.1.1 Dilepton and large missing transverse energy

At hadron colliders, charginos (χ^\pm) and neutralinos (χ^0) can be produced in pairs from parton collisions of electroweak strength:

$$q\bar{q} \rightarrow \tilde{\chi}_i^+ \tilde{\chi}_j^-, \quad q\bar{q} \rightarrow \tilde{\chi}_i^0 \tilde{\chi}_j^0, \quad u\bar{d} \rightarrow \tilde{\chi}_i^+ \tilde{\chi}_j^0, \quad d\bar{u} \rightarrow \tilde{\chi}_i^- \tilde{\chi}_j^0 \quad (7.6)$$

with $i, j > 0$. Some examples of the Feynman diagrams at tree-level of these processes are shown in Figure 7.1 for $d\bar{u} \rightarrow \tilde{\chi}_2^- \tilde{\chi}_1^0$. These production modes get contributions from electroweak vector bosons in the s-channel and also have t-channel squark-exchange contributions that are of lesser importance in most models. In models with R-parity conservation, the lightest neutralino (χ_1^0) is the lightest supersymmetric particle and it is stable and very weakly interacting.

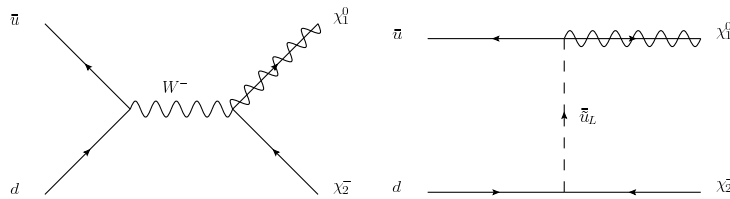


Figure 7.1: Tree-level Feynman diagrams for the process $d\bar{u} \rightarrow \tilde{\chi}_2^- \tilde{\chi}_1^0$.

The possible leptonic decays for charginos and neutralinos are:

- $\tilde{\chi}_i^0 \rightarrow l^\pm \nu \tilde{\chi}_j^\mp$
- $\tilde{\chi}_i^\pm \rightarrow l^\pm \nu \tilde{\chi}_j^0$
- $\tilde{\chi}_i^0 \rightarrow l^\pm l^\mp \tilde{\chi}_j^0$

- $\tilde{\chi}_i^\pm \rightarrow l^\pm l^\mp \tilde{\chi}_j^\pm$

where $i > j$, $i, j > 0$. The decay chains of the initial neutralinos and charginos result in final states with two lightest neutralino (χ_1^0) that escape the detector due to the weak nature of the interaction. These stable particles carry away an energy twice the mass of the neutralino, leading to a large missing transverse energy together with 2 or more leptons produced through the decay chain.

7.2 Object reconstruction

- Electrons:

Electron reconstruction is based on cluster and ID tracks matching. The *tight* definition is applied to select candidates. The final candidates have to be $p_T > 20$ GeV and $|\eta| < 2.47$. If the electron is the lepton with the highest p_T in the event, the momentum has to be $p_T > 25$ GeV to be in the plateau of the trigger efficiency.

Final electrons have to be isolated: the p_T sum of tracks inside a cone of $\Delta R < 0.2$ around each electron has to be less than 10 % of the transverse momentum of the electron. Electrons with $0.2 < \Delta R < 0.4$ with respect to a jet are rejected and if the jet is in $\Delta R < 0.2$ the jet is not accepted.

- Muons:

They are reconstructed from ID tracks and MS segments. For the ID track, a minimum number for Pixel, SCT and TRT hits are required. The ID track is extrapolated to the muon system. A good quality matching between ID track and MS segment is required. Muons must have $p_T > 10$ GeV and $|\eta| < 2.4$. In case a muon is the leading lepton of the event, i.e. the reconstructed lepton with largest transverse momentum, the requirement is $p_T > 20$ GeV. This is required to be in plateau of the trigger efficiency.

In order to reject cosmic muons, tight cuts are applied to select muons produced close to the primary vertex. In the transverse plane muons with $|d_0| < 0.2$ mm are selected, while in the longitudinal plane the cut $|z_0| < 1$ mm is applied. To reduce the amount of jets faking a muon, the candidates are required to be isolated. The p_T sum of tracks inside a cone of $\Delta R < 0.2$ around each muon has to be less than 1.8 GeV. Finally, if a jet is found around a muon in a cone of $\Delta R < 0.4$, the muon is discarded.

- Jets:

The anti- k_t jet clustering algorithm with radius 0.4 is used. The seeds are clusters formed from the energy deposits in the calorimeters. Final jets are required to have $p_T > 20$ GeV and $|\eta| < 2.8$. The final candidate cannot overlap with electrons or muons inside a cone of $\Delta R < 0.2$. A quality criterion is applied to remove noise and non-collisions backgrounds.

- Missing transverse energy E_T^{miss} :

This is the magnitude of the vector sum of the p_T of all jets with $p_T > 20$ GeV, electrons and leptons selected. Also additional non-isolated muons and calorimeter clusters in $|\eta| < 4.5$ are taken into account.

7.3 Event selection and signal regions

The primary vertex of the event is required to have 5 tracks. During some months of the data taking, events with a jet in the problematic region of the liquid argon calorimeter, are rejected [112]. The selected event must have exactly 2 leptons (ee , $e\mu$ or $\mu\mu$). In case of $e\mu$ event, if the electron $p_t > 25$ GeV, the event must satisfy the electron trigger. Events with no such electron must satisfy the muon trigger. To remove low-mass dilepton resonances, the invariant mass of the lepton pair must be greater than 12 GeV.

As shown in Figure 7.1.1, different possible SUSY final states can be studied, so different signal regions are defined in this analysis. For opposite-sign leptons, the signal regions to study are:

- OS-SR1: $E_T^{miss} > 250$ GeV.
- OS-SR2: 3-jets ($p_T > 80, 40, 40$ GeV), $E_T^{miss} > 220$ GeV
- OS-SR3: 4-jets ($p_T > 100, 70, 70, 70$ GeV), $E_T^{miss} > 100$ GeV

In case of same-sign leptons, 2 signal regions are defined:

- SS-SR1: $E_T^{miss} > 100$ GeV
- SS-SR2: 2-jets ($p_T > 50, 50$ GeV), $E_T^{miss} > 80$ GeV

The signal regions involving jets in the final state are designed to exploit the expected presence of jets in cascade decays from colored SUSY objects. These regions are optimized from mSUGRA and constrained MSSM models. In these models, the scalar and gaugino mass are free parameters. Fixed values of the universal trilinear coupling parameter, ratio of the vacuum expectation values of the two Higgs doublets and Higgs mixing parameter are used. Selection without minimal number of jets in the final state are designed to study R-parity conserving SUSY models with large missing transverse energy.

7.4 Background contributions

Different techniques have been applied depending on the background:

- Single top is based on Monte Carlo simulations
- Drell-Yan ($Z/\gamma^* + \text{jets}$) and $t\bar{t}$ backgrounds are evaluated from Monte Carlo after reweighting the samples to get agreement between data and MC in predefined control regions.

- Fake and non isolated leptons consisting on semi-leptonic $t\bar{t}$, single top, $W + \text{jets}$ and QCD light and heavy-flavor jet production are obtained using a *matrix method* data-driven technique.
- Diboson background is estimated directly from MC samples. A detailed study is presented in the next section.

7.5 Diboson background estimation

A review of the physics of pairs of electroweak gauge bosons (diboson) produced at high energy colliders is presented in [128]. In that paper a detailed overview of Tevatron and LHC measurements is shown together with the latest NLO calculations and Monte Carlo predictions and their agreement with data. Diboson production is an irreducible background for all Beyond Standard Model physics searches with two or more leptons in the final state and large missing transverse energy, in same and opposite-sign final states. This contribution is not just important for new physics searches, but also plays an important role in tests of electroweak theory. With the current data, as will be discussed later for each case, a remarkable agreement between Standard Model and the experiments is found.

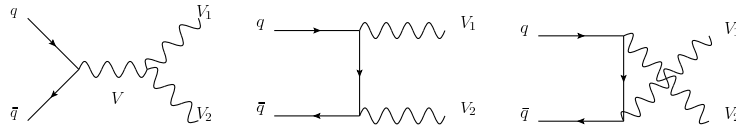


Figure 7.2: Tree-level Feynman diagrams for diboson production in the Standard Model in proton-proton colliders. $V, V_1, V_2 = W^\pm, Z, \gamma$. The left side plot corresponds to the s-channel, for which the trilinear gauge boson vertex only is valid for $WW\gamma$ and WWZ .

In Figure 7.2, the tree-level diagrams for diboson production in the Standard Model in proton-proton colliders are presented. In the SM, at leading order, neutral triple gauge boson couplings (nTGCs) are absent, hence there is not contribution from s-channel $q\bar{q}$ annihilation to ZZ , $Z\gamma$ and $\gamma\gamma$ production.

WW, WZ and ZZ

The production of a pair of bosons has been studied in detail at LEP and Tevatron and no deviations from the Standard Model expectations have been observed [128].

Also the ATLAS detector has recently measured ZZ to four leptons contribution [129] in proton-proton collisions. The measured cross-section is $\sigma_{ZZ}^{total} = 8.5_{-2.3}^{+2.7}$ (stat.) $\pm_{-0.3}^{+0.4}$ (syst.) ± 0.3 (lumi.) pb which is consistent with the SM at NLO: $\sigma_{ZZ}^{NLO} = 6.5 \pm_{-0.2}^{+0.3}$ pb. The measurement of the W^+W^- cross section [131] was done by ATLAS finding a value of: 40_{-16}^{+20} (stat) ± 7 (syst) pb. The NLO prediction is 44.9 ± 2.2 pb [130] and it is in agreement with the measurement. The last pair of massive boson production to look is $W^\pm Z$. It

was measured by ATLAS [132] getting a cross-section of: $\sigma_{WZ}^{total} = 21.1_{-2.8}^{+3.1}(\text{stat.}) \cdot {}_{-1.2}^{+1.2}(\text{syst.}) \cdot {}_{-0.8}^{+0.9}(\text{lumi.})$ pb in agreement with the SM expectation of $17.2_{-0.8}^{+1.2}$ pb.

Table 7.1: Cross-sections for WW, WZ and ZZ production for the different Monte-Carlo generators. The Cross-sections are corrected to NLO using k-factors.

Generator	Process	Cross-Section $\sigma \times \text{BR}$ [pb]
Herwig	W^+W^-	17.43916
Herwig	$W^\pm Z$	5.553
Herwig	ZZ	1.265308
McAtNlo	$W^+W^- \rightarrow e\nu e\nu$	$5.7 \cdot 10^{-1}$
McAtNlo	$W^+W^- \rightarrow e\nu\mu\nu$	$5.7 \cdot 10^{-1}$
McAtNlo	$W^+W^- \rightarrow e\nu\tau\nu$	$5.7 \cdot 10^{-1}$
McAtNlo	$W^+W^- \rightarrow \mu\nu\mu\nu$	$5.7 \cdot 10^{-1}$
McAtNlo	$W^+W^- \rightarrow \mu\nu e\nu$	$5.7 \cdot 10^{-1}$
McAtNlo	$W^+W^- \rightarrow \mu\nu\tau\nu$	$5.7 \cdot 10^{-1}$
McAtNlo	$W^+W^- \rightarrow \tau\nu\tau\nu$	$5.7 \cdot 10^{-1}$
McAtNlo	$W^+W^- \rightarrow \tau\nu e\nu$	$5.7 \cdot 10^{-1}$
McAtNlo	$W^+W^- \rightarrow \tau\nu\mu\nu$	$5.7 \cdot 10^{-1}$
McAtNlo	$ZZ \rightarrow llqq$	$5.3 \cdot 10^{-1}$
McAtNlo	$ZZ \rightarrow ll\nu\nu$	$1.5 \cdot 10^{-1}$
McAtNlo	$ZZ \rightarrow llll$	$2.5 \cdot 10^{-2}$
McAtNlo	$W^+Z \rightarrow l\nu qq$	1.7
McAtNlo	$W^+Z \rightarrow l\nu ll$	$1.6 \cdot 10^{-1}$
McAtNlo	$W^+Z \rightarrow qqll$	$5.0 \cdot 10^{-1}$
McAtNlo	$W^-Z \rightarrow l\nu qq$	$9.8 \cdot 10^{-1}$
McAtNlo	$W^-Z \rightarrow l\nu ll$	$8.0 \cdot 10^{-2}$
McAtNlo	$W^-Z \rightarrow qqll$	$2.7 \cdot 10^{-1}$
Alpgen	$W^+W^- \rightarrow l\nu l\nu$ 0 jets	2.6
Alpgen	$W^+W^- \rightarrow l\nu l\nu$ 1 jets	1.3
Alpgen	$W^+W^- \rightarrow l\nu l\nu$ 2 jets	$5.7 \cdot 10^{-1}$
Alpgen	$W^+W^- \rightarrow l\nu l\nu$ 3 jets	$2.2 \cdot 10^{-1}$
Alpgen	$W^\pm Z \rightarrow ll + 0$ jets	$8.6 \cdot 10^{-1}$
Alpgen	$W^\pm Z \rightarrow ll + 1$ jets	$5.3 \cdot 10^{-1}$
Alpgen	$W^\pm Z \rightarrow ll + 2$ jets	$2.9 \cdot 10^{-1}$
Alpgen	$W^\pm Z \rightarrow ll + 3$ jets	$1.2 \cdot 10^{-1}$
Alpgen	$ZZ \rightarrow ll + 0$ jets	$6.6 \cdot 10^{-1}$
Alpgen	$ZZ \rightarrow ll + 1$ jets	$3.0 \cdot 10^{-1}$
Alpgen	$ZZ \rightarrow ll + 2$ jets	$1.1 \cdot 10^{-1}$
Alpgen	$ZZ \rightarrow ll + 3$ jets	$4.1 \cdot 10^{-2}$

These cross sections, at the studied luminosity, provide low event rates, therefore data driven methods are difficult to apply and so this background is estimated from Monte Carlo simulations. The diboson background is one order of magnitude below the dominant background contribution ($t\bar{t}$). The central values contribution are computed with the

Herwig generator [116]. The samples are filtered for one lepton with $p_T > 10$ GeV and $|\eta| < 2.8$. This simulation is done at Leading-order (LO), therefore, k-factors are used so that the unfiltered Herwig cross-section agrees with the NLO prediction [130]. The final cross-sections for the WW, WZ and ZZ samples used to normalize the contribution to the amount of data analyzed are detailed in Table 7.1. The uncertainties on the cross-sections for normalization are of the order of 5%.

In order to study the kinematic predictions for different generators, two extra samples have been produced:

- LO generator Alpgen [134].
- NLO generator MC@NLO [120].

Both of them are interfaced to HERWIG and JIMMY [117] generators to add the parton shower and the underlying event. The cross-sections for these samples can be found in Table 7.1, where k-factors are used to correct the LO generators to NLO cross-sections.

The ATLAS software [121], based on a GEANT4 [122] simulation, has been used to simulate the detector response. All the samples have been weighted to match the number of interactions per bunch crossing measured in data. The same reconstruction and analysis chain as for data is applied to the samples.

In the Tables 7.2 and 7.3, the number of accepted events for the different signal regions for the three generators is shown. In these tables, the simulations are normalized to the same luminosity and only statistical uncertainties are included. Some differences between Herwig, Alpgen and MC@NLO for opposite and same sign leptons are presented.

All samples have the same p_T spectrum for the leading lepton as also shown in Figure 7.3. This shows that the kinematic properties of the production and decay of the weak bosons are very close in all generators. In Figure 7.4 the E_T^{miss} distribution is shown. The E_T^{miss} is dominated by the neutrinos created from the W decay and missed leptons due to acceptance. As shown, the E_T^{miss} distributions for all generators are in agreement for low energies, the main differences appear in the E_T^{miss} tail where the limited available statistics prevents firm conclusions. In this analysis, multi-jets signal regions are included. Figure 7.5 shows the number of jets with $p_T > 20$ GeV for both samples. Alpgen generates larger number of jets than Herwig. Furthermore, Alpgen produces higher transverse momentum jets as shown in Figure 7.6 where the sum of the 4 leading jets in the event is shown for both generators. These effects are expected due to different properties of both generators. In Herwig, additional partons are emitted from the leading partons using splitting functions. This effect is not fully included in Alpgen because of the matrix element - parton shower matching method used, so the p_T spectrum of leading jets is expected to be harder for Alpgen than Herwig as shown in Figures 7.6 and 7.7.

In Tables 7.4 and 7.5 the rate of Herwig versus Alpgen (MC@NLO) is presented. The rate is calculated as: $\frac{N_{\text{Herwig}} - N_{\text{Alpgen(MC@NLO)}}}{N_{\text{Herwig}}}$. For the signal regions, number of accepted events is very low. This increases the uncertainties for the rate. Also, the best agreement for the three generators is expected to be for the 2-lepton cut so the estimate generator uncertainty is 5.1% and this uncertainty is propagated to the different signal regions. It is

clear that in the future, for larger integrated luminosity, more events will be needed to be simulated to get a good description of the tails.

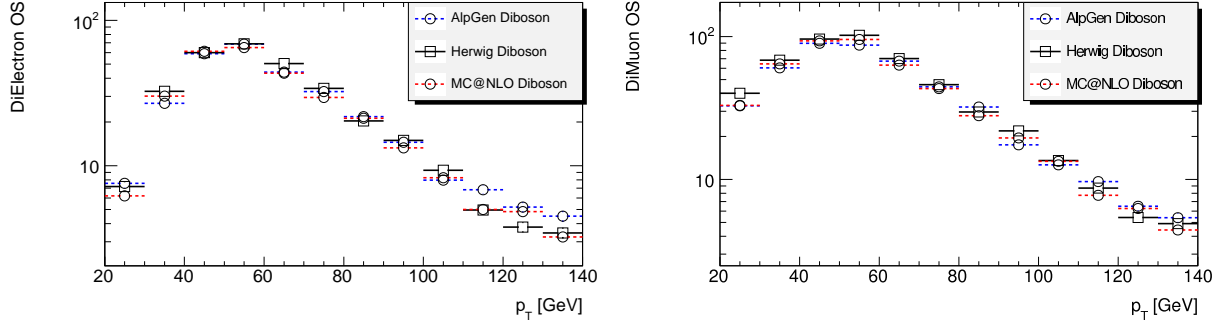


Figure 7.3: Transverse momentum of the leading lepton for events with 2 signal electrons (left) and 2 signal muons (right). Comparison between Herwig, Alpgen and MC@NLO for diboson background.

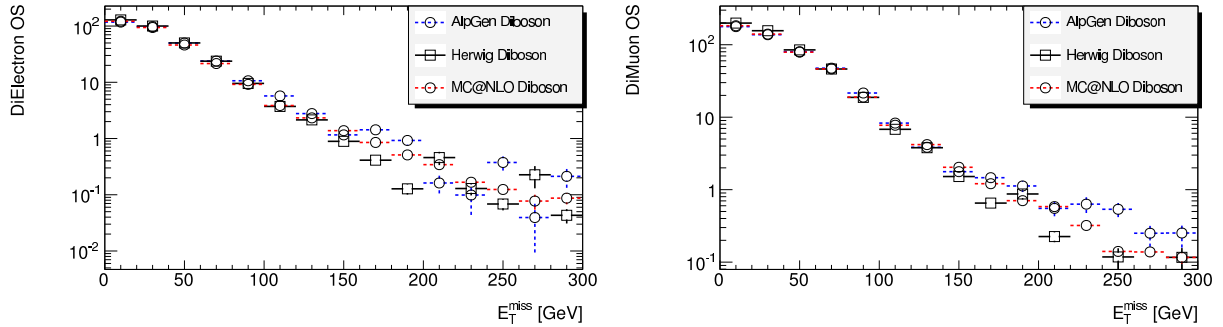


Figure 7.4: Missing transverse energy (E_T^{miss}) for events with 2 signal electrons (left) and 2 signal muons (right). Comparison between Herwig, Alpgen and MC@NLO for diboson background.

W^+W^++jj

During 2010, the collected data were very few and therefore, the production and decay of two same sign W bosons was not studied. In 2011, with increased luminosity accumulated, this background has been included. The LO cross-section for this process, is $2.2 \cdot 10^{-1}$ pb. Just single parton collisions have been included in this calculation. The contribution from double parton collisions has been neglected because expected cross-section is lower than for single parton interaction and in addition, like-sign W has not being measured yet in hadron colliders and this will require fine tuning of the generators [136]

Using MadGraph [135] for the matrix element interfaced to Pythia [75] for the parton shower and fragmentation, a sample of two same sign $W^+ + jj$ has been produced. In

Table 7.2: Comparison between diboson samples produced with Herwig, Alpgen and MC@NLO for opposite sign leptons. Samples are normalized to 689 pb^{-1} . Only statistical uncertainties are included.

MC Production Generator Channel	MCI0b											
	Herwig				AlpGen				MC@NLO			
	ee	$e\mu$	$\mu\mu$		ee	$e\mu$	$\mu\mu$		ee	$e\mu$	$\mu\mu$	
2 Leptons OS	320.33 ± 2.77	331.86 ± 3.92	525.55 ± 3.63		312.73 ± 3.410	317.05 ± 3.27	489.39 ± 4.24		302.56 ± 1.70	345.01 ± 1.004	484.65 ± 2.056	
$E_{\text{T}}^{\text{miss}} > 80 \text{ GeV}$	17.860 ± 0.721	26.065 ± 1.086	34.130 ± 1.006		23.846 ± 0.875	43.336 ± 1.136	40.855 ± 1.165		19.173 ± 0.248	37.410 ± 0.331	36.351 ± 0.321	
SR1 $E_{\text{T}}^{\text{miss}} > 250 \text{ GeV}$	0.362 ± 0.099	0.012 ± 0.010	0.443 ± 0.098		0.671 ± 0.149	0.964 ± 0.156	1.031 ± 0.167		0.487 ± 0.040	0.581 ± 0.041	0.561 ± 0.038	
SR2 3 jets (80,40,40)	5.155 ± 0.242	0.449 ± 0.133	6.892 ± 0.294		15.449 ± 0.663	3.248 ± 0.264	22.680 ± 0.826		9.091 ± 0.347	1.574 ± 0.068	12.079 ± 0.402	
$E_{\text{T}}^{\text{miss}} > 220 \text{ GeV}$	0 ± 0	0.012 ± 0.014	0.246 ± 0.093		0.019 ± 0.014	0.173 ± 0.062	0.432 ± 0.105		0.098 ± 0.015	0.132 ± 0.019	0.085 ± 0.015	
SR3 4 jets (100,70,70,70)	0.050 ± 0.027	0 ± 0	0.2391 ± 0.057		0.805 ± 0.147	0.051 ± 0.028	0.481 ± 0.113		0.323 ± 0.065	0.060 ± 0.013	0.216 ± 0.047	
$E_{\text{T}}^{\text{miss}} > 100 \text{ GeV}$	0 ± 0	0 ± 0	0 ± 0		0 ± 0	0 ± 0	0 ± 0		0.0001 ± 0.0005	0.041 ± 0.011	0.008 ± 0.005	

Table 7.3: Comparison between diboson samples produced with Herwig, Alpgen and MC@NLO for Same Sign leptons. Samples are normalized to 689 pb^{-1} . Only statistical uncertainties are included.

MC Production Generator Channel	MCI0b											
	Herwig				AlpGen				MC@NLO			
	ee	$e\mu$	$\mu\mu$		ee	$e\mu$	$\mu\mu$		ee	$e\mu$	$\mu\mu$	
2 Leptons SS	9.890 ± 0.4406	19.053 ± 0.601	10.109 ± 0.384		10.884 ± 0.618	19.131 ± 0.818	11.584 ± 0.648		7.37 ± 0.22	12.54 ± 0.28	4.51 ± 0.21	
$E_{\text{T}}^{\text{miss}} > 80 \text{ GeV}$	0.912 ± 0.154	2.459 ± 0.206	1.274 ± 0.136		1.781 ± 0.242	3.944 ± 0.332	1.484 ± 0.211		0.704 ± 0.053	1.894 ± 0.090	0.749 ± 0.054	
SR1 $E_{\text{T}}^{\text{miss}} > 100 \text{ GeV}$	0.332 ± 0.098	0.791 ± 0.109	0.517 ± 0.086		1.401 ± 0.218	2.579 ± 0.256	1.032 ± 0.171		0.377 ± 0.039	0.707 ± 0.054	0.190 ± 0.023	
SR2 2 jets (50,50)	0.731 ± 0.090	1.189 ± 0.180	0.331 ± 0.070		2.207 ± 0.234	3.884 ± 0.314	1.004 ± 0.152		0.475 ± 0.056	0.563 ± 0.076	0.139 ± 0.021	
$E_{\text{T}}^{\text{miss}} > 80 \text{ GeV}$	0.013 ± 0.014	0.153 ± 0.046	0.067 ± 0.031		0.381 ± 0.090	1.780 ± 0.199	0.419 ± 0.091		0.109 ± 0.020	0.181 ± 0.032	0.055 ± 0.013	

Table 7.4: Rate of Herwig versus AlgGen(MC@NLO) for Opposite Sign leptons. The rate is computed as $\frac{N_{\text{Herwig}} - N_{\text{AlgGen(MC@NLO)}}}{N_{\text{Herwig}}}$. Only statistical uncertainties are included.

MC Production Generator	MC10b			
	Herwig vs AlpGen		Herwig vs MC@NLO	
Channel	ee	$e\mu$	$\mu\mu$	$e\mu$
2 Leptons OS	0.024 ± 0.027	0.046 ± 0.036	0.0688 ± 0.021	0.055 ± 0.026
$E_{\text{T}}^{\text{miss}} > 80$ GeV	-0.34 ± 0.14	-0.66 ± 0.16	-0.19 ± 0.10	-0.07 ± 0.125
SR1 $E_{\text{T}}^{\text{miss}} > 250$ GeV	-0.85 ± 1.13	-76.12 ± 65	-1.33 ± 1.02	-0.34 ± 0.922
SR2 3 jets (80,40,40)	-2.00 ± 0.26	-6.23 ± 2.79	-2.29 ± 0.25	-0.76 ± 0.189
$E_{\text{T}}^{\text{miss}} > 220$ GeV	0 ± 0	-13.42 ± 19.83	-0.76 ± 1.48	0 ± 0
SR3 4 jets (100,70,70,70)	-15 ± 10.207	0 ± 0	-1.01 ± 1.06	-5.46 ± 4.75
$E_{\text{T}}^{\text{miss}} > 100$ GeV	0 ± 0	0 ± 0	0 ± 0	0 ± 0

Table 7.5: Rate of Herwig versus AlgGen (MC@NLO) for Same Sign leptons. The rate is computed as $\frac{N_{\text{Herwig}} - N_{\text{AlgGen(MC@NLO)}}}{N_{\text{Herwig}}}$. Only statistical uncertainties are included.

MC Production Generator	MC10b			
	Herwig vs AlpGen		Herwig vs MC@NLO	
Channel	ee	$e\mu$	$\mu\mu$	$e\mu$
2 Leptons SS	-0.100 ± 0.151	-0.004 ± 0.104	-0.146 ± 0.135	0.255 ± 0.124
$E_{\text{T}}^{\text{miss}} > 80$ GeV	-0.95 ± 0.71	-0.60 ± 0.33	-0.16 ± 0.37	0.22 ± 0.47
SR1 $E_{\text{T}}^{\text{miss}} > 100$ GeV	-3.22 ± 1.94	-2.26 ± 0.79	-0.99 ± 0.74	-0.13 ± 0.93
SR2 2 jets (50,50)	-2.02 ± 0.69	-2.27 ± 0.83	-2.03 ± 1.15	0.35 ± 0.33
$E_{\text{T}}^{\text{miss}} > 80$ GeV	-28.3 ± 34.41	-10.63 ± 4.30	-5.25 ± 4.05	0.22 ± 0.47

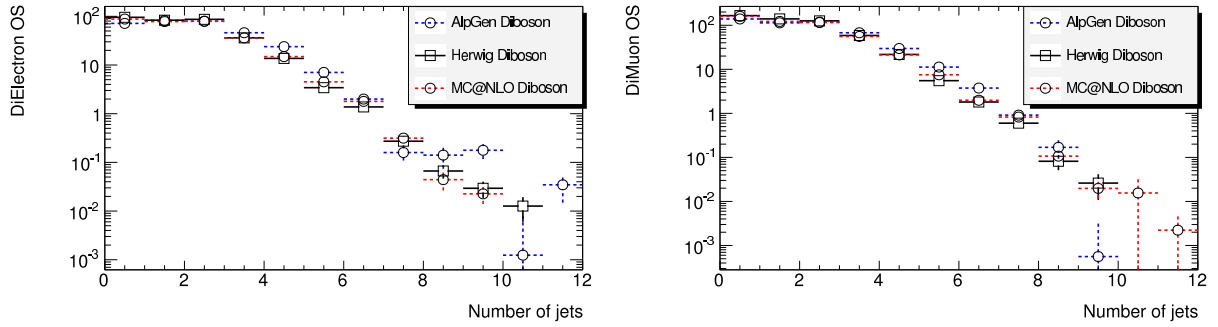


Figure 7.5: Number of jets ($p_T > 20$ GeV) for events with 2 signal electrons (left) and 2 signal muons (right). Comparison between Herwig, Alpgen and MC@NLO for diboson background.

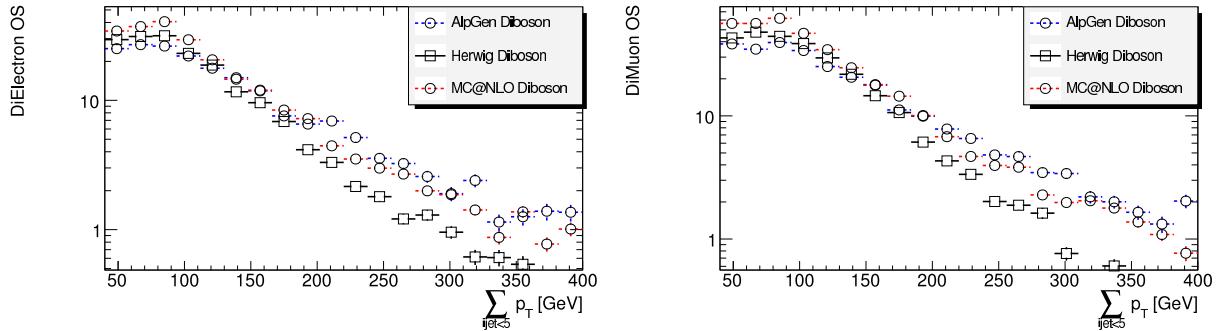


Figure 7.6: Total transverse momentum of the 4 most energetic jets ($p_T > 20$ GeV) for events with 2 signal electrons (left) and 2 signal muons (right). Comparison between Herwig, Alpgen and MC@NLO for diboson background.

Table 7.6 the results for same and opposite sign leptons are presented. This background, as expected, is negligible for opposite-sign signal regions. In the case of same sign leptons, the number of events expected with 2 leptons is 3.1 for an accumulated luminosity of 689 pb^{-1} . For the signal regions, this background is an order of magnitude lower than the general diboson estimation. This background is very small, but it is included in the final backgrounds for same-sign searches. When luminosity will increase, it will be important to keep control over this process and measure the cross-section for double parton scattering to make sure Monte Carlo generators describe it properly.

W/Z+ γ

The production of a weak boson together with a high momentum photon has also been studied. The cross-section at LO for $W^+ + \gamma$ is 28.8 pb. $W^- \gamma$ cross section is 18.9 pb and for $Z\gamma$ is 9.7 pb. MadGraph interfaced with Pythia has been used to simulate the events. For $W^\pm \gamma$ events, if the photon does not decay producing an electron-positron pair,

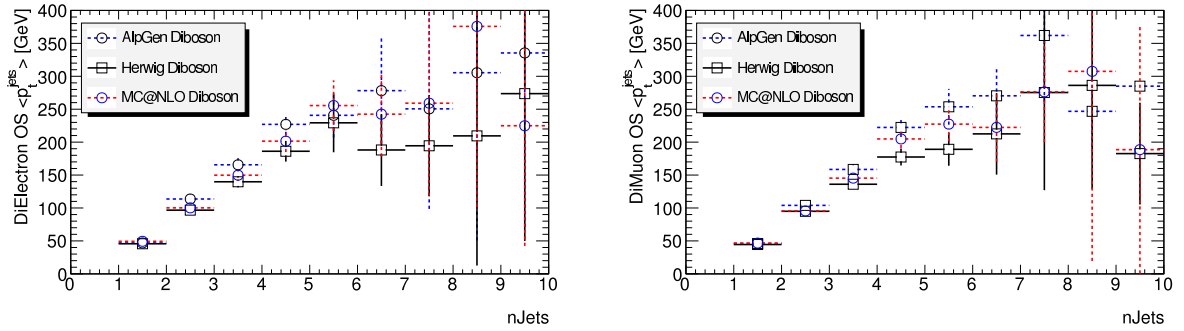


Figure 7.7: Total transverse momentum of the 4 leading p_T jets depending on the number of jets reconstructed for events with 2 signal electrons (left) and 2 signal muons (right). Comparison between Herwig, Alpgen and MC@NLO for diboson background.

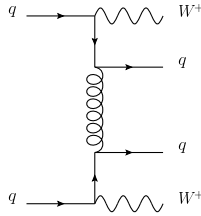


Figure 7.8: Tree-level Feynman diagrams for W^+W^+jj production in the Standard Model in proton-proton colliders.

only a single lepton will be measured, rejecting the event. In case the photon produces an electron-positron pair, the leptons will not point to the primary vertex and the event will have a great probability to be rejected. In the case of $Z\gamma$, events with two leptons are reconstructed. Once large E_T^{miss} is requested, the number of events accepted is negligible due to the very good calorimeter properties of the detector, that will reconstruct the photon and will not lead to missing transverse energy. In conclusion, the boson plus photon background does not have to be taken into account for the signal regions of the analysis.

7.6 Conclusion and results

A comparison of the latest Monte Carlo predictions for the SUSY analysis are presented together with a brief review on the different up to date measurements for diboson production in hadron colliders. At this stage, diboson background is very low and the systematic effects can be taken into account without affecting the sensitivity of the analysis. However, when the accumulated luminosity increases, a good control of the correct simulation is going to be crucial. In the same way, the same-sign W background will start to be important for the like sign lepton analysis. Finally, the production of a weak boson together with a

Table 7.6: Cut flow for $W^+W^+ + jj$. The sample is normalized to 689 pb^{-1} . Only statistical uncertainties are included.

MC Production	MC10b		
Generator	MadGraph		
Channel	ee	$e\mu$	$\mu\mu$
2 Leptons OS	0.0001 ± 0.0004	0.013 ± 0.005	0 ± 0
$E_T^{\text{miss}} > 80 \text{ GeV}$	0 ± 0	0 ± 0	0 ± 0
SR1 $E_T^{\text{miss}} > 250 \text{ GeV}$	0 ± 0	0 ± 0	0 ± 0
SR2 3 jets (80,40,40)	0 ± 0	0.0053 ± 0.0030	0 ± 0
$E_T^{\text{miss}} > 220 \text{ GeV}$	0 ± 0	0 ± 0	0 ± 0
SR3 4 jets (100,70,70,70)	0 ± 0	0 ± 0	0 ± 0
$E_T^{\text{miss}} > 100 \text{ GeV}$	0 ± 0	0 ± 0	0 ± 0
2 Leptons SS	0.569 ± 0.030	1.506 ± 0.050	1.046 ± 0.040
$E_T^{\text{miss}} > 80 \text{ GeV}$	0.274 ± 0.020	0.652 ± 0.032	0.46 ± 0.03
SR1 $E_T^{\text{miss}} > 100 \text{ GeV}$	0.174 ± 0.016	0.488 ± 0.028	0.31 ± 0.02
SR2 2 jets (50,50)	0.314 ± 0.022	0.958 ± 0.040	0.59 ± 0.03
$E_T^{\text{miss}} > 80 \text{ GeV}$	0.158 ± 0.015	0.444 ± 0.026	0.31 ± 0.02

large momentum photon, due to the high photon-electron ATLAS rejection, will be very low, even in the cases where the photon decays into electron-positron pairs.

The final SUSY analysis takes into account the contributions for diboson productions and the systematic differences between generators explained here. The expected number of events together with the data measured for the final analysis are shown in Table 7.8. With an accumulated luminosity of 1 fb^{-1} no deviations from the Standard Model are found. These results are used to set upper limits on $A \times \epsilon \times \sigma$, where A is the fraction of events passing geometrical and kinematic cuts at generator level, and ϵ is the detector efficiency for particle reconstruction and identification and σ is the cross-section for new phenomena.

Table 7.8: Predicted number of background events, observed number of events and the corresponding 95% CL upper limit on $A \times \epsilon \times \sigma$

	Background	Observed	95% C.L.
OS-SR1	15.5 ± 4.0	13	9.9 fb
OS-SR2	13.0 ± 4.0	17	14.4 fb
OS-SR3	5.7 ± 3.6	2	6.4 fb
SS-SR1	32.6 ± 7.9	25	14.8 fb
SS-SR2	24.9 ± 5.9	28	17.7 fb

Chapter 8

Summary and outlook

In this thesis the Transition Radiation Tracker performance and its calibration have been studied in detail. A very stable method has been developed and implemented, which allows to get the timing properties and the gas drift velocity with high accuracy. This method allowed to get an acceptable performance already for Cosmics rays. For proton-proton collisions, the calibration method was fine-tuned and the resolution measured is comparable to the design resolution. This makes the TRT a fundamental piece for the reconstruction of high momentum charged particles.

For the TRT Calibration, a great amount of attention has been devoted to study the calibration effects at different levels, in order to get the best compromise between resolution, stability and CPU performance. The method described in this thesis, shows that there is little room for improvement. Increasing the calibration granularity for the $r-t$ relations, the resolution can only be improved by few μms and will be included in the coming data-taking. Also, the application of straw corrections is under consideration.

The great tracking properties of ATLAS has been explored in Chapter 5 to measure the charged particle multiplicity and its correlations. A detailed study of the high order moments corrected to generator level has been done. This study shows in data the quasi-oscillations predicted by QCD. A comparison to several Monte Carlo generators has been done. All the Monte Carlo generators describe the quasy-oscillations, with some variations of the amplitude and the first minimum position. However, even the up to date recent tune of Pythia8, which describes reasonably well the multiplicity tail at 900 and 7 TeV, does not describe exactly the moments measured in data. Several parameters of the model can introduce these differences and in the future, a detailed study for the proton-proton collisions will be of great interest.

The attempt to measure the factorial moments for different pseudorapidity bins had the problem of large model depended corrections. This is caused by the low tracking efficiency in ATLAS at low momentum. A possible method able to perform model independent corrections, based on Bayesian unfolding, was introduced, however, due to time limitations could not be fully tested. The reconstructed level factorial moments were shown and compared to Pythia and Phojet. Qualitatively, all the generator and tunes are able to describe the rise on the factorial moments when increasing the number of bins. The normalization between different samples and data was very different, which makes impossible to draw

strong conclusion until the corrections to generator level are performed.

During 2012, LHC will deliver during few days dedicated collisions to study Minimum Bias data. Our current detector understanding is much better and the LHC efficiency also, and this will allow to get a large fraction of data to redo more accurately the studies presented here.

The last part of this thesis is about Searches Beyond Standard Model. In the Chapter 6 the search of same-sign top pairs production and forth family of b-like quarks is introduced. I worked on understanding the fraction of reconstructed leptons in which the charge measurement was wrongly assigned. For this, I developed two new methods for charge mis-identification studies: the direct extraction and the likelihood. I have proved that the former method, tag and probe, cannot be applied for our analysis because it may bias the kinematic distributions of the leptons. The use of the likelihood improves the charge mis-identification description, making the best use of the available statistics. Other good feature of the likelihood approach is that it can be easily extended to more than one dimension. The first attempt to measure the charge mis-identification in p_T and η has been done, however with the available luminosity the low number of leptons with high momentum produced by Z boson decay returns very large statistical uncertainties.

The charge mis-identification estimation described here was of main importance to the describe the $t\bar{t}$ contamination in the same-sign region with very good performance for the analysis. In combination with the rest of MC background estimations, a good agreement of our data and the Standard Model was found. Lower limits in the same-sign cross-section production were set. One remarkable result is that with the current result, is not possible to explain the $t\bar{t}$ forward-backward asymmetry observed at the Tevatron based on minimal Z' models. In the case of b-like quarks produced by a fourth family of quarks, minimum for the b-like quark mass of 450 GeV was set. The prospects for this analysis is to keep looking for at larger luminosity to exclude larger b' masses and smaller same-sign top cross sections, or in case the nature is producing them, claim the discovery.

Finally, in the Chapter 7, a detailed study of the MC generators for diboson production was done. This is one of the few irreducible backgrounds in the SUSY searches with 2 leptons and large missing transverse energy. Also, this background was not fully studied before the LHC era, so a good control on the MC systematics is important. This result have been used in the final ATLAS 2011 SUSY result, were, similarly as for the same-sign top analysis, a good agreement with the Standard Model was found.

The next years are going to be of crucial importance for the High Energy Physics community, with the Higgs boson at the finger tips (for discovery or exclusion) and LHC delivering data at very large rate. The analyses will become more and more sophisticated and a great understanding of the detector will be needed. In my thesis I tried to improve our detector understanding, focusing on the TRT and the electron and muon reconstruction. I used this information in the first 2010 data to study the minimum bias events and the 2011 data to search for new physics. *Unfortunately*, until now, the Standard Model and its detailed implementation in the MC generators has shown to model well the current LHC data, but new data will be delivered soon so we need to keep looking for.

Chapter 9

Acknowledgements

There are a seemingly uncountable number of people who supported me in this long journey in the world of particle physics and ATLAS.

Firstly, I want to express my sincere gratitude to my supervisor Oxana Smirnova for her continuous support and the opportunity she gave me to seek and define my own research interests and apply them in this thesis. I would like to thank Torsten Åkesson, my second supervisor, for always finding the time to discuss my work and have helpful discussions. Although he is not officially my supervisor, I am very grateful to Bernhard Meirose for introducing me to the exciting world of beyond Standard Model physics. He always provided great ideas, suggestions and support in backing me up in the hard environment that can be the ATLAS physics groups.

I am grateful to all my colleagues in the division. Lots of thanks go to Else Lytken for the extremely useful discussions about exotic searches. Thanks also to Evert Stenlund and Anders Oskarsson for the extensive proof-reading of this thesis. I am extraordinarily grateful to Bozena Wlosinska for helping me since the first day I arrived in Lund, settling everything from then until today.

Also from Lund, but in the other side of the building, my gratitude goes to all the theory colleagues for keeping always the door open to carry enlightenment discussions.

During those last four years, it was a great pleasure for me to be part of the TRT Offline group. The work I have done for the TRT was only possible thanks to the great team that the TRT is. I am very grateful to Saša Fratina and Jahred Adelman who spent countless hours discussing and helping me with calibration and performance studies. I am most grateful to the NBI group, especially to Johan Lundquist, Esben Klinkby and Peter Hansen. Their support and expertise were fundamental to accomplish my tasks. Furthermore, thanks to Christoph Rembser for appreciating my TRT contribution and for always supporting my work.

Thanks to Hulya Guler and Edward Sarkisyan-Grinbaum, my involvement in multi-particle correlations studies was only possible with their collaboration, support and the extremely rich discussions we had during these years around the coffee table.

Working with Ning Zhou has been a great experience, although most of the time the pressure was very high, he was always patient and always willing to help.

I would like to express my gratitude to my master supervisors: Pablo García and José

María Hernández. Thanks to them I had the opportunity to come to Sweden for the PhD.

Even if sometimes it gets tough during the PhD, in addition to work, a physicist must have a social life too, and Lund turns out to be a great environment for friendship. I want to thank you all for the dinners, the nights at Ariman, the gaming nights, the bike tours, the juggling, the coffee chats, the Lundaloppet training, the beach, the hiking, the time blaming ROOT, etc. The list is very long, so I am sure someone is missing, but thanks to you all: Weina, Philippe, Anthony, Alex, Florido, Simona, Nele, Richard, Jacob, Lisa, Antonio, Ilaria, Jose, Irene, Chris, Angela, Stefan, Francesca, Carlo, Fran, Xavi, Olga, Josep, Natalia, Audrius.... Even if Lund is for most of us a transition place, I really hope we will still be in contact for long long time.

Load and loads of thanks to my old friends: the Erasmus crew, the ones from Madrid and *los Gallegos*. Living abroad can be tricky, but we always found the time and the place to meet, to do cultural visits and to get updates of our current status. Great thanks for being always there!

My warmest thanks to my family, for keeping me posted of all the news happening at home, for taking care of me both from the distance and back in Madrid and for encouraging me to take the challenge of the PhD abroad.

Last but no the least, my deepest gratitude to my wonderful girlfriend, Lili. I know sometimes it has not been easy, but without your unwavering support this thesis would have not been possible. Thank you so much!!!

Lund, March 2012

Bibliography

- [1] A. Alonso *High p_T : Electroweak and QCD results from ATLAS*, contribution to the proceedings of 40th (XL) edition of the International Symposium on Multiparticle Dynamics, 978 90 5487 913 8, 2011.
- [2] A. Alonso *Commissioning and performance of the ATLAS transition radiation tracker with high energy collisions at LHC*, Nucl.Phys.Proc.Suppl. **215** (2011) 185-188.
- [3] The ATLAS Collaboration, *Calibration of the ATLAS Transition Radiation Tracker* ATLAS-CONF-2011-006.
- [4] J. Adelman, J. Alison, A. Alonso, S. Fratina, B. Jackson, J. Stahlman, *Tracking performance of the ATLAS Transition Radiation Tracker Under Preparation*.
- [5] A. Alonso, B. Meirose, *New data-driven methods for lepton charge mis-identification* ATL-COM-PHYS-2012-264, to be approved as internal note.
- [6] The ATLAS Collaboration, *Search for same-sign top quark production and fourth generation quarks in pp collisions, at $\sqrt{s} = 7$ TeV with the ATLAS detector* [arXiv: 1202.5520 [hep-ph]], submitted to JHEP.
- [7] The ATLAS Collaboration, *Searches for supersymmetry with the ATLAS detector using final states with two leptons and missing transverse momentum in $\sqrt{s} = 7$ TeV proton-proton collisions*, [arXiv: 1110.6189 [hep-ph]], 2011, accepted by PLB.
- [8] The ATLAS collaboration, *ATLAS Detector and Physics Performance Technical Design Report* (CERN/LHCC/2003-022).
- [9] *The LHC Design Report*, CERN-2004-003.
- [10] *LEP design report*, CERN-LEP,1, 1984.
- [11] www-bdnew.fnal.gov/tevatron.
- [12] CMS Collaboration *CMS Physics TDR* CERN-LHCC-2006-001 P. W. Higgs, *Broken symmetries, massless particles and gauge fields*, Phys. Lett. **12** (1964) 132.
- [13] CMS Collaboration *CMS Physics TDR* CERN-LHCC-2006-001.

-
- [14] ALICE Collaboration *Technical Proposal for A Large Ion Collider Experiment at the CERN LHC* CERN / LHCC / 95-71, 1995.
- [15] LHCb Collaboration *LHCb: Technical Proposal* CERN-LHCC-98-004, 1998.
- [16] The ATLAS Collaboration, *Expected Performance of the ATLAS Experiment*, CERN-OPEN-2008-020.
- [17] The ATLAS collaboration *The ATLAS Experiment at the CERN Large Hadron Collider* JINST **3** (2008) S08003.
- [18] W. Blub, W. Rieger, L. Rolandi *Particle detection with Drift Chambers* Springer (2008).
- [19] W.R. Leo *Techniques for Nuclear and Particle Physics Experiments* Springer-Verlag (1994).
- [20] C. Driouichi, *B-physics potential of the ATLAS experiment, and, performance of the ATLAS transition radiation tracker*, LUNFD6-NFFL-7220-2004.
- [21] V.L. Ginzburg and V.N. Tsytovich, *Transition Radiation and Transition Scattering*, Publisher: Taylor and Francis, (1990).
- [22] R. Veenhof, *Garfield - A drift chamber simulation program* , CERN Program Library W5050, 1984.
- [23] Nakamura et al. (Particle Data Group), *J. Phys. G* **37**, 075021 (2010).
- [24] W. W. M. Allison and J. H. Cobb, *Relativistic Charged Particle Identification By Energy Loss*, *Ann. Rev. Nucl. Part. Sci.* **30** (1980) 253.
- [25] The ALICE Collaboration, *Technical Design Report of the Time Projection Chamber*, CERN-OPEN-2000-183.
- [26] The ATLAS Collaboration, *The ATLAS Experiment at the CERN Large Hadron Collider*, JINST **3** (2008) S08003.
- [27] The ATLAS Collaboration, *Expected Performance of the ATLAS Experiment - Detector, Trigger and Physics*, arXiv:0901.0512 [hep-ex].
- [28] The ATLAS Collaboration, *The ATLAS Inner Detector commissioning and calibration*, *Eur. Phys. J. C* **70** (2010) 787-821.
- [29] The ATLAS Collaboration, *Particle Identification Performance of the ATLAS Transition Radiation Tracker*, ATLAS-CONF-2011-128.
- [30] The TRT ATLAS Collaboration, *The ATLAS Transition Radiation Tracker(TRT) proportional drift tube: design and performance*, JINST **3** (2008) P02013.

-
- [31] The TRT ATLAS Collaboration, *The ATLAS TRT barrel detector*, JINST **3** (2008) P02014.
- [32] The TRT ATLAS Collaboration, *The ATLAS TRT end-cap detectors*”, JINST, **3**, (2008), P10003.
- [33] The TRT ATLAS Collaboration, *The ATLAS TRT Electronics*, JINST **3** (2008) P06007.
- [34] P. Cwetanski, *Straw performance studies and quality assurance for the ATLAS transition radiation tracker*, CERN-THESIS-2006-025.
- [35] E. B. Klinkby, *W mass measurement and simulation of the transition radiation tracker at the ATLAS experiment*, CERN-THESIS-2008-071.
- [36] T. Akesson *et al.* [RD6 Collaboration], *Study of straw proportional tubes for a transition radiation detector tracker at LHC*, Nucl. Instrum. Meth. A **361**, 440 (1995).
- [37] T. Akesson *et al.* [RD6 Collaboration], *The ATLAS TRT straw proportional tubes: Performance at very high counting rate*, Nucl. Instrum. Meth. A **367** (1995) 143.
- [38] The TRT ATLAS Collaboration, *Straw tube drift-time properties and electronics parameters for the ATLAS TRT detector*, Nucl. Instrum. Meth. A **449** (2000) 446.
- [39] <http://atlas.ch/photos/inner-detector-trt.html>.
- [40] S. Fratina, E. Klinkby *The Geometry of the ATLAS Transition Radiation Tracker* ATL-COM-INDET-2010-002.
- [41] The ATLAS Collaboration, *Alignment Performance of the ATLAS Inner Detector Tracking System in 7 TeV proton-proton collisions at the LHC* ATLAS-CONF-2010-067.
- [42] The ATLAS Collaboration, *Alignment of the ATLAS Inner Detector Tracking System with 2010 LHC proton-proton collisions at $\sqrt{s} = 7$ TeV* ATLAS-CONF-2011-012.
- [43] T. Cornelissen, M. Elsing, S. Fleischmann, W. Liebig, E. Moyse, A. Salzburger *Concepts, Design and Implementation of the ATLAS New Tracking (NEWT)*, ATL-SOFT-PUB-2007-007.
- [44] T. Cornelissen, M. Elsing, A Wildauer, N. van Eldik, E. Moyse, W. Liebig, N. Picquadio, K. Prokoev, A. Salzburger *Updates of the ATLAS Tracking Event Data Model* soft-pub-2007-003.
- [45] F. Akesson, M.J. Costa, D. Dobos, M. Elsing, S. Fleischmann, A. Gaponenko, K. Gnanvo, P.T. Keener, W. Liebig, E. Moyse, A. Salzburger, M. Siebel, A. Wildauer *ATLAS Inner Detector Event Data Model* soft-pub-2007-006.
- [46] T. Cornelissen *Track Fitting in the ATLAS Experiment* CERN-THESIS-2006-062.

- [47] R. Frhwirth, *Application of Kalman filtering to track and vertex fittings* Nucl. Instrum. Methods Phys. Res., A **262** (1987) 444.
- [48] The ATLAS Collaboration, *Particle Identification Performance of the ATLAS Transition Radiation Tracker*, ATLAS-CONF-2011-128.
- [49] R.L. Gluckstern *Uncertainties in track momentum and direction, due to multiple scattering and measurement errors* Nuclear Instruments and Methods **24** (1963) 381-389.
- [50] D. Olivitio *Calibration Studies for the ATLAS Transition Radiation Tracker* ATLAS-COM-INDET-2009-008.
- [51] D. Charlton, C. Guyot, M. Hauschild, A. Hcker *Sign-off Procedure for Bulk Data Reconstruction* ATL-COM-GEN-2008-002.
- [52] <https://twiki.cern.ch/twiki/bin/viewauth/Atlas/ExpressStream>.
- [53] G. Dimitrov, R. Hawkings, F. Viegas *COOL schema organization for replicated conditions databases*, http://atlas.web.cern.ch/Atlas/GROUPS/DATABASE/project/online/doc/cool_schema.pdf
http://atlas.web.cern.ch/Atlas/GROUPS/DATABASE/project/online/doc/coolrefwork_002.pdf
- [54] <https://twiki.cern.ch/twiki/bin/viewauth/Atlas/AtlasCalibration>.
- [55] <https://atlas-trt-web.cern.ch/cgi-bin/default.cgi>
- [56] P. Wagner et al *The TRT Fast-OR Trigger* ATL-COM-INDET-2009-042
<https://twiki.cern.ch/twiki/bin/viewauth/Atlas/TrtTrigger>
- [57] S. Fratina et al *The Measurement of Cosmic-Ray Time with the Transition Radiation Tracker* ATL-COM-INDET-2010-045.
- [58] M. Hance *Readout of the ATLAS Transition Radiation Tracker: Timing Parameters and Constraints* ATL-COM-INDET-2008-002.
- [59] E. Klinkby *Private Communication*.
- [60] C. Ohm, T. Pauly *The ATLAS beam pick-up based timing system* Nucl. Instrum. Meth. A **623** 558-560 (2010).
- [61] R. Ellis, W. Stirling, and B. Webber, *QCD and Collider Physics*, Cambridge University Press (1996).
- [62] S. Bethke, *The 2009 World Average of $\alpha(s)$* , Eur. Phys. J. C **64**, 689 (2009) [arXiv:0908.1135 [hep-ph]].
- [63] D. J. Gross, *Twenty five years of asymptotic freedom*, Nucl. Phys. Proc. Suppl. **74**, 426 (1999) [hep-th/9809060].

- [64] R. G. Newton, *Optical theorem and beyond*, American Journal of Physics **44** (1976) no. 7, 639-642.
- [65] A. Donnachie and P. V. Landsho, *Total cross sections*, Physics Letters B **296** (1992) no. 1-2, 227.
- [66] G. A. Schuler and T. Sjostrand, *Hadronic diffractive cross sections and the rise of the total cross section*, Phys. Rev. D **49** (1994) no. 5.
- [67] V.N. Gribov, L.N. Lipatov. Sov.J.Nucl.Phys. **15**: 438 (1972)
G. Altarelli and G. Parisi. Nucl. Phys. B **126**: 298 (1977)
Yu. L. Dokshitzer. Sov.Phys. JETP **46**:641 (1977).
- [68] P.M Nadolsky, H.L Lai, Q.-H Cao, J. Huston, J. Pumplin, D. Stump, W.K. Tung and C.P. Yuan *Implications of the CTEQ global analysis for collider observables*. Phys. Rev. D **78**: 013004, 2008.
- [69] A.D. Martin, R. G. Roberts, W. J. Stirling and R.S. Thorne. *Physical gluons and High ET Jets*. Phys. Lett. B **604**: 61-68, 2004.
- [70] T. Sjostrand and P. Z. Skands, *Transverse-momentum-ordered showers and interleaved multiple interactions*, The European Physical Journal C - Particles and Fields **39** (2005) no. 2, 129.
- [71] B. Anderson, G. Gustafson, G. Ingelman and T. Sjostrand, *Parton Fragmentation and String Dynamics*, Phys. Rept., **97**: 31-145, 1983.
- [72] R.D. Field and S. Wolfram. *A QCD model for e^+e^- annihilation* Nucl. Phys. B **213**: 65-84, 1983.
- [73] A. Buckley et al., (2011), ArXiv:1101.2599, Accepted for publication in Physics Reports.
- [74] A. Moraes, C. Buttar, I. Dawson *Prediction for minimum bias and the underlying event at LHC energies* Eur. Phys. J. C **50**, 435-466 (2007).
- [75] T. Sjöstrand, S. Mrenna and P. Skands, *JHEP* **05** (2006) 026, LU TP 06-13, FERMILAB-PUB-06-052-CD, [arxiv:hep-ph/0603175].
- [76] R. Engel *Photoproduction within the two component dual parton model. 1 Amplitudes and cross-sections* Z. Phys. C **66** (1995) 539.
- [77] I. M. Dremin and J. W. Gary, *Hadron multiplicities*, Phys. Rept. **349** (2001) 301 [hep-ph/0004215].
- [78] I.M Dremin, Phys. Lett. B **313** (1993) 209; I.M Dremin, V.A. Nechitailo, JETP Lett. **58** (1993) 881.
- [79] J. F. Grosse-Oetringhaus and K. Reygers, *Charged-Particle Multiplicity in Proton-Proton Collisions*, J. Phys. G G **37**, 083001 (2010) [arXiv:0912.0023 [hep-ex]].
- [80] A. Giovannini and L. Van Hove, Z. Phys. C **30** 391 (1986).

- [81] C. Fuglesand, *La Thuile Multipart. Dyn.* 1989 193.
- [82] A. Giovannini and R. Ugoccioni, *Phys. Rev. D* **59** 094020 (1999). hep-ph/9810446.
- [83] A. Białas and R. Peschanski, *Moments of Rapidity Distributions as a Measure of Short-Range Fluctuations in High-Energy Collisions*, *Nuclear Physics B* **273** (1986) 703-718.
- [84] C. Albajar and others, *Intermittency Studies in $\bar{p}p$ Collisions at $\sqrt{s} = 630$ GeV*, *Nuclear Physics B* **345** (1990) 1-21.
- [85] P. Lipa and H. C. Eggers and F. Botterweck and M. Charlet, *Intermittency, the empty bin effect and uncertainty* *ZPC* **54** (1992) 115-125.
- [86] W. Kittel and E. A. De Wolf, *Soft Multihadron Dynamics*, World Scientific, Singapore, 2005.
- [87] The ATLAS Collaboration, *ATLAS Monte Carlo tunes for MC09*, ATL-PHYS-PUB-2010-002.
- [88] The ATLAS Collaboration, *Charged-particle multiplicities in pp interactions measured with the ATLAS detector at the LHC*, *New J. Phys.* **13** (2011) 053033 [arXiv:1012.5104 [hep-ex]].
- [89] P. Z. Skands, *The Perugia Tunes*, 2009. [arXiv: 0905.3418v1 [hep-ex]].
- [90] M. G. Albrow, et al., *Tevatron-for-LHC Report of the QCD Working Group*, 2006. [arXiv: 0610012 [hep-ex]].
- [91] R. Corke and T. Sjöstrand, *Interleaved Parton Showers and Tuning Prospects* *JHEP* 1103 (2011) 032 [arXiv:1011.1759 [hep-ph]].
- [92] G. D'Agostini, *A Multidimensional unfolding method based on Bayes' theorem*, *Nucl. Instrum. Meth. A* **362** 487-498 (1995).
- [93] I. M. Dremin and V. A. Nechitailo, *Soft multiple parton interactions as seen in multiplicity distributions at Tevatron and LHC*, *Phys. Rev. D* **84**, 034026 (2011) [arXiv:1106.4959 [hep-ph]].
- [94] W. J. Metzger, *Estimating the Uncertainties of Factorial Moments*, 2010.
- [95] The ATLAS Collaboration <https://twiki.cern.ch/twiki/bin/view/AtlasPublic/LuminosityPublicResults>
- [96] The ATLAS Collaboration, *Electron performance measurements with the ATLAS detector using the 2010 LHC proton-proton collision data*, [arXiv: 1110.3174 [hep-ex]].
- [97] TH. Lagouri, et al., *A muon identification and combined reconstruction procedure for the ATLAS detector at the LHC at CERN* *IEEE Trans. Nucl. Sci.* **51** (2004) 3030-3033.
- [98] S. Jung, H. Murayama, A. Pierce and J. D. Wells, *Phys. Rev. D* **81** (2010) 015004 [arXiv: 0907.4112 [hep-ex]]. J. Cao, Z. Heng, L. Wu and J. M. Yang, *Phys. Rev. D* **81**, 014016 (2010) [arXiv: 0912.1447 [hep-ex]]; D. Choudhury, R. M. Godbole, S. D. Rindani and P. Saha, [arXiv: 1012.4750 [hep-ex]]; J. Cao, L. Wang, L. Wu and J. M. Yang, [arXiv: 1101.4456 [hep-ex]]; B. Bhattacharjee, S. S. Biswal and D. Ghosh, [arXiv: 1102.0545 [hep-ex]]; E. L. Berger, Q. H. Cao, C. R. Chen, C. S. Li and H. Zhang, [arXiv: 1101.5625 [hep-ex]].

- [99] J. A. Aguilar-Saavedra, Nucl. Phys. B **843** (2011) 638 [arXiv:1008.3562 [hep-ph]].
- [100] J. A. Aguilar-Saavedra and M. Perez-Victoria, arXiv:1104.1385 [hep-ph].
- [101] CDF Collaboration, *Evidence for a Mass Dependent Forward-Backward Asymmetry in Top Quark Pair Production*, Phys. Rev. D **83**, 112003 (2011) [arXiv:1101.0034 [hep-ex]].
- [102] D0 Collaboration, *Forward-backward asymmetry in top quark-antiquark production*, [arXiv:1107.4995 [hep-ex]].
- [103] CDF Collaboration, *Search for like-sign top quark pair production at CDF with 6.1 fb^{-1}* CDF/PHYS/EXO/PUBLIC/10466.
- [104] CMS Collaboration, *Search for Same-Sign Top-Quark Pair Production at $\sqrt{s} = 7 \text{ TeV}$ and Limits on Flavour Changing Neutral Currents in the Top Sector*, JHEP **1108**, 005 (2011) [arXiv:1106.2142 [hep-ex]].
- [105] Particle Data Group Collaboration, *Review of particle physics*, Phys. Lett. B **667** (2008).
- [106] G. Eilam, B. Melic, and J. Trampetic, *CP violation and the 4th generation*, Phys. Rev. D **80** (2009) 116003, [arXiv: 0909.3227 [hep-ex]].
- [107] W.-S. Hou, *Source of CP Violation for the Baryon Asymmetry of the Universe*, Chin.J.Phys. **47** (2009) 134, [arXiv: 0803.1234 [hep-ex]].
- [108] G. D. Kribs, T. Plehn, M. Spannowsky, and T. M. Tait, *Four generations and Higgs physics*, Phys.Rev. **D76** (2007) [arXiv: 0706.3718 [hep-ex]].
- [109] CDF Collaboration: *Search for New Bottomlike Quark Pair Decays $Q\bar{Q} \rightarrow (tW^{pm})(\bar{t}W^{mp})$ in Same-Charge Dilepton Events*, Phys. Rev. Lett. **104**, 091801 (2010).
- [110] CMS Collaboration, *Search for a Heavy Bottom-like Quark*, CMS-EXO-11-036 (2011).
- [111] D0 Collaboration *Search for Long-Lived Particles Decaying into Z bosons*, Phys. Rev. Lett. **104** .091801 **5454** (2007) 091801, [arXiv: 0912.1057 [hep-ex]].
- [112] The ATLAS Collaboration, *Data-Quality Requirements and Event Cleaning for Jets and Missing Transverse Energy Reconstruction with the ATLAS Detector in Proton-Proton Collisions at a Center-of-Mass Energy of $\sqrt{s} = 7 \text{ TeV}$* ATLAS-CONF-2010-038.
- [113] The ATLAS Collaboration, *Measurement of the top quark pair production cross section in pp collisions at $\sqrt{s} = 7 \text{ TeV}$ in dilepton final states with ATLAS*, [arXiv: 1108.3699 [hep-ex]].
- [114] M. L. Mangano, M. Moretti, F. Piccinini, R. Pittau and A. D. Polosa, *ALPGEN, a generator for hard multiparton processes in hadronic collisions*, JHEP **0307**, 001 (2003) [arXiv: 0206293 [hep-ph]].
- [115] P. M. Nadolsky *et al.*, *Implications of CTEQ global analysis for collider observables*, Phys. Rev. D **78**, 013004 (2008) [arXiv: 0802.0007 [hep-ph]].

- [116] G. Corcella, I.G. Knowles, G. Marchesini, S. Moretti, K. Odagiri, P. Richardson, M.H. Seymour & B.R. Webber, *HERWIG 6: an event generator for hadron emission reactions with interfering gluons* JHEP **0101** (2001) 010.
- [117] J. M. Butterworth, J. R. Forshaw and M. H. Seymour, *Multiparton interactions in photo-production at HERA*, Z. Phys. C **72**, 637 (1996) [arXiv: 9601371 [hep-ph]].
- [118] The ATLAS Collaboration, *First tuning of HERWIG/JIMMY to ATLAS data* ATL-PHYS-PUB-2010-014.
- [119] T. Gleisberg and S. Hoche and F. Krauss and M. Schonherr and S. Schumann and F. Siegert and J. Winter, *Event generation with Sherpa 1.1* JHEP **02** (2009) 007 [arXiv: 0811.4622 [hep-ph]].
- [120] S. Frixione and B.R. Webber, *Matching NLO QCD computations and parton shower simulations*, JHEP **0603**, 092 (2006) [arXiv: 0512250 [hep-ph]].
- [121] The ATLAS Collaboration, *The ATLAS Simulation Infrastructure* Eur.Phys.J.C **70** (2010) 823-874 [arXiv: 1005.4568 [hep-ex]].
- [122] V. N. Ivanchenko *et al.*, *Geant4: a simulation toolkit* Nucl. Instrum. Meth. A **506** (2003) 250-303.
- [123] F. James and M. Roos, *Minuit: A System For Function Minimization And Analysis Of The Parameter Errors And Correlations*, Comput. Phys. Commun. **10** (1975) 343.
- [124] D0 Collaboration Collaboration, T. Aaltonen *et al.*, *Search for Long-Lived Particles Decaying into Z bosons*, Conf. Note **5454** (2007) 091801, [arXiv: 0912.1057 [hep-ex]].
- [125] E. Gaiser, *Appendix-F Charmonium Spectroscopy from Radiative Decays of the J/Psi and Psi-Prime*, Ph.D. Thesis, SLAC-R-255 (1982).
- [126] A. Read, *Presentation of search results: The CL(s) technique*. J. Phys., **G28**, (2002), 2693-2704.
- [127] S. P. Martin, *A Supersymmetry Primer* [arXiv: 9709356 [hep-ph]].
- [128] Mark S. Neubauer, *Diboson Production at Colliders*, Annual Review of Nuclear and Particle Science. **61** (2011) 223-250.
- [129] The ATLAS Collaboration, *Measurement of the ZZ production cross section and limits on anomalous neutral triple gauge couplings in proton-proton collisions at $\sqrt{s} = 7$ TeV with the ATLAS detector* [arXiv: 1110.5016 [hep-ex]].
- [130] J. Butterworth and E. Dobson and U. Klein and B. Mellado Garcia and T. Nunnemann and J. Qian and D. Rebuzzi and R. Tanaka *Single Boson and Diboson Production Cross Sections in pp Collisions at $\sqrt{s}=7$ TeV*, ATL-COM-PHYS-2010-695, Aug 2010.
- [131] The ATLAS Collaboration, *Measurement of the WW production cross section in proton-proton collisions at $\sqrt{s} = 7$ TeV with the ATLAS detector*, ATLAS-CONF-2011-015, Mar 2011.

-
- [132] The ATLAS Collaboration, *Measurement of the WZ production cross section in proton-proton collisions at $\sqrt{s} = 7$ TeV with the ATLAS detector*, ATLAS-CONF-2011-099, Jul 2011.
- [133] The ATLAS Collaboration, *Measurement of the production cross section of $W + \gamma$ and $Z + \gamma$ at $\sqrt{s} = 7$ TeV with the ATLAS Detector*, ATLAS-CONF-2011-013, Mar 2011.
- [134] Mangano, Michelangelo L. and Moretti, Mauro and Piccinini, Fulvio and Pittau, Roberto and Polosa, Antonio D. *ALPGEN, a generator for hard multiparton processes in hadronic collisions*, JHEP **07** (2003) 001 [arXiv: 0206293 [hep-ph]].
- [135] F. Maltoni and T. Stelzer, JHEP 0302:027, 2003 *MadEvent: Automatic event generation with MadGraph*, JHEP **02** (2003) 027, [arXiv: 0208156 [hep-ph]].
- [136] J. R. Gaunt, C. H. Kom, A. Kulesza and W. J. Stirling, *Same-sign W pair production as a probe of double parton scattering at the LHC*, Eur. Phys. J. C **69**, 53 (2010) [arXiv:1003.3953 [hep-ph]].